UQAC
Université du Québec
à Chicoutimi

Behaviour of alumina powder fed into molten electrolytic bath

by
Csilla Kaszas

Under the supervision of Laszlo Kiss and Sandor Poncsak

Dissertation submitted at the University of Québec at Chicoutimi, Département des Sciences Appliquées, in fulfillment of the requirements for PhD in Engineering

Defended on 25th November 2020

Jury:

Dilip Sarkar, professor, UQAC, chairman

Robert Chahine, project manager, Rio Tinto, France, external member

Gervais Soucy, professor, Sherbrook University, external member

Québec, Canada

Acknowledgements

First and foremost, I would like to express my gratitude to Laszlo Kiss, my supervisor, for his support, patience and guidance that ensured the completion of my thesis. I would also like to extend my thanks to every present and former member of GRIPS who contributed to my work in any way: Patrice Paquette, for his technical support that ensured the realisation of the envisioned experiments, Anthony le Noc, who conducted a large number of experiments in the analog setup on my behalf, Thomas Roger, who prepared and analysed dozens of compressed alumina discs and continued to assist me in various experiments as a fellow student, Sandor Poncsak for accepting the responsibility of becoming my co-supervisor, and many others.

For the execution of the porosity analysis, I owe thanks to Houshang Alamdari and Francois Chevarin from University Laval.

I would like to thank the Natural Sciences Engineering Research Council of Canada and Rio Tinto Aluminium for their financial support. A part of the research presented was financed by the Fonds de recherche du Québec -Nature et technologies by the intermediary of the Aluminium Research Centre – REGAL.

Last but not least, I am grateful for the moral support of my friends in Quebec.

Résumé

La dissolution de l'alumine (oxyde d'aluminium) dans l'électrolyte est un procédé essentiel dans la production d'aluminium, le deuxième métal le plus utilisé sur Terre. Dans les cellules actuelles de réduction d'aluminium, la poudre d'alumine de fonderie est ajoutée à la surface du bain cryolitique fondu à des doses variant entre 0,5 et 2 kg. Bien que la dissolution d'une poudre dans son solvant puisse sembler anodine, ce processus présente plusieurs particularités qui entravent la dispersion rapide de l'alumine. La dissolution douteuse peut saper le contrôle cellulaire, et l'alumine non dissoute peut former des agglomérats qui peuvent diminuer l'efficacité et la durée de vie de la cellule.

L'objectif de cette thèse était d'analyser les mécanismes qui favorisent la formation d'agglomérats, et d'entraver ainsi la dispersion rapide de l'alumine ajoutée dans le bain cryolitique, en se concentrant principalement sur:

• la formation du radeau: l'étalement de la poudre, injectée sur la surface du bain;

• l'évolution des radeaux d'alumine, en ce qui concerne la flottation du radeau à la surface du bain;

• le comportement à la flottation des agglomérats à l'interface bain-métal.

Les méthodes utilisées dans ce travail comprennent la modélisation mathématique, des expériences en bain cryolitique, l'analyse de radeaux d'alumine et des expériences dans des systèmes analogiques poudre-liquide.

Un modèle mathématique a été développé pour analyser les conditions de flottation en régime permanent d'objets axisymétriques sur une surface liquide. Le modèle a été appliqué à la surface du bain électrolytique. Pour l'interface bain-métal, le modèle statique a été étendu pour prendre en compte la vitesse initiale de l'agglomérat et la dynamique de la pénétration de l'interface.

L'angle de contact entre l'alumine et le bain cryolitique (un paramètre d'entrée important pour le modèle de flottation) a été mesuré par la méthode Wilhelmy.

Des expériences ont été menées dans le bain cryolitique pour étudier et analyser la formation de radeaux. La teneur en humidité a été identifiée comme une propriété importante de l'alumine qui influence la forme, la structure et la microstructure du radeau d'alumine, se formant lors de l'injection. Des échantillons de radeau ont été préparés par lixiviation pour éliminer la cryolite, révélant la structure d'alumine sous-jacente, puis la porosité était analysée.

Des disques d'alumine compressés en tant que radeaux d'alumine artificiels ont été préparés pour obtenir des radeaux de forme et de taille contrôlée, tout en laissant les principaux processus inchangés. L'uniformité des radeaux artificiels a permis de comparer facilement les échantillons prélevés après différentes étapes et de suivre l'évolution de la ligne d'infiltration

dans le temps. La densité des radeaux, ainsi que les séquences vidéo des expériences ont prouvé que la tension superficielle peut contribuer à la flottation des radeaux d'alumine.

Un modèle bidimensionnel de radeaux d'alumine a été créé pour prédire la solidification du bain, l'infiltration et la densité apparente, donc la possibilité de flottation pour le radeau. Les propriétés thermiques de l'alumine primaire de fonderie ont été mesurées par un dispositif de chauffage à rampe monotone, et en raison de la structure complexe de la porosité de l'alumine, un modèle à deux niveaux a été appliqué pour pouvoir estimer sa conductivité thermique avec différentes densités.

Le détachement des grains saturés ou des amas du radeau principal diminuerait sa taille ainsi que sa densité apparente. La désintégration d'un radeau est dictée par les effets concurrents et la dynamique du frittage et de la dissolution. Bien que la dissolution soit souvent considérée comme le but ultime de la recherche concernant le comportement de l'alumine dans l'électrolyte, elle devrait plutôt être considérée comme un processus parallèle mais opposé au frittage, et enquêter simultanément sur les deux. Dans le cadre de ce travail, la teneur en carbone a été identifiée comme un facteur favorisant la désintégration en affaiblissant le frittage.

Des injections de poudre dans des systèmes liquide-liquide analogiques à basse température ont été effectuées pour mieux comprendre leurs interactions. Alors que dans de nombreux aspects, les systèmes analogiques ne représentent pas fidèlement le système alumine-bain-aluminium, certains phénomènes peuvent s'appliquer à la cellule d'électrolyse. Ces observations sont d'une importance particulière pour l'interface bain-métal.

Abstract

The dissolution of alumina (aluminium-oxide) in an electrolyte is an essential process in the production of aluminium, the second most commonly used metal on Earth. In the state-of-the-art aluminium reduction cells, smelter grade alumina powder is added on the surface of the molten cryolitic bath in doses varying between 0.5-2 kg. While dissolving a powder in its solvent might seem trivial, there are several particularities to this process that hinder the rapid dispersion of alumina. The dubious dissolution may undermine the cell control, and the undissolved alumina could form agglomerates that can decrease the efficiency and lifetime of the cell.

The objective of this PhD was to analyse the mechanisms that promote the formation of agglomerates, and hinder the fast dispersion of alumina added into cryolitic bath, mostly focusing on:

- the raft formation: the spreading of the powder, injected onto the bath surface;
- the evolution of alumina rafts, with regard to the flotation of the raft on the bath surface;

- the flotation behaviour of agglomerates on the bath-metal interface.

The methods used in this work include mathematical modelling, experiments in cryolitic bath, analysis of alumina rafts, and experiments in analog powder-liquid systems.

A mathematical model was developed to analyse the conditions of steady-state flotation of axisymmetric objects on a liquid surface. The model was applied to the surface of the electrolytic bath. For the bath-metal interface, the static model was extended, to consider the initial velocity of the agglomerate and dynamics of the interface penetration.

The contact angle between alumina and cryolitic bath (an important input parameter for the flotation model) was measured by Wilhelmy method.

Experiments were conducted in the cryolitic bath to study and analyse raft formation. Moisture content was identified as an important property of alumina that influences the shape, structure, and microstructure of the alumina raft, forming upon injection. Raft samples were prepared by leaching to remove cryolite, revealing the underlying alumina structure, then the pore structure analysed.

Compressed alumina discs as artificial alumina rafts were prepared to obtain rafts with controlled shape and size, while leaving the main processes (bath solidification, infiltration, sintering and dissolution) unchanged. The uniformity of the artificial rafts permitted the easy comparison between samples removed after different stages, and to follow the advancement of the line of infiltration in time. The density of the rafts, along with the video footage of the experiments proved that the surface tension can contribute to the flotation of alumina rafts.

Two-dimensional thermal model of alumina rafts was created to predict bath solidification, infiltration and apparent density – therefore possibility of flotation for the raft. Thermal properties of primary smelter grade alumina were measured by monotonic ramp heating device, and due to the complex pore structure of the alumina, a two-level model was applied to be able to estimate its thermal conductivity with different packing densities.

The detachment of infiltrated grains or clumps from the main body of the raft decreases its size and also its apparent density. The disintegration of a raft is controlled by the opposing effects and the dynamics of sintering and dissolution. While dissolution is often considered as the main goal of research concerning the behaviour of alumina in the electrolyte, it should rather be considered as an opposing but parallel process to sintering, and should be investigated simultaneously. In the frame of this work, carbon content was identified as a factor that aids disintegration via weakened sintering.

Powder injections in low-temperature analog liquid-liquid systems were conducted to gain insight on their interactions. While in many aspects, the analog systems fail to represent faithfully the alumina-bath-aluminium system, certain phenomena may apply for the electrolysis cell. These observations are of special importance for the liquid-liquid interface.

Table of contents

List of tables

List of figures

List of equations

Notation

a	Capillary length [m]
b	Radius of axisymmetric object at the triple line [m]
Ca	Associated mass coefficient
C_d	Drag coefficient
F_b	Buoyant force [N]
F_d	Drag force [N]
F_g	Gravitational force [N]
F_s	Resultant force of the surface tension [N]
g	Gravitational acceleration [m/s^2]
H	Thickness [m]
h/d	Height-diameter ratio for disc geometry
h_m	Meniscus height [m]
K	Mean surface curvature [1/m]
k_e	Effective thermal conductivity [W/mK]
m	Mass [g]
m_a	Associated mass [g]
R	Radius of sphere or disc [m]
r', r''	First and second derivatives of r(h)
r=r(h)	Liquid interface profile, radius as a function of height
R_x, R_y	Radius of curvature in two perpendicular axes in the tangent plane to the surface [m]
v	Velocity [m/s]
V	Volume [m^3]
v'	Acceleration [m/s^2]
V_d	Displaced volume [m^3]
V_f	Volume of displaced fluid [m^3]
V_l	Volume of displaced liquid [m^3]
x	Relative immersion of the sphere: the vertical distance between the triple line and the bottom of the sphere, in relation to its diameter
Δp	Laplace pressure [Pa]

γ	Surface tension [N/m]
$\gamma_{sg,sl,lg}$	Interfacial energy, solid-gas, solid-liquid, liquid-gas [N/m]
δ	Angle of interface at the triple line, compared to vertical [°]
α	Contact angle [°]
β	Angle of solid [°]
β_0	Angle of corner of solid body [°]
ρ_s	Density of solid [kg/m^3]
ρ_l	Density of liquid [kg/m^3]

ρ^*	Equivalent density [kg/m^3]
ρ_{bulk}	bulk density [kg/m^3]
ρ_{sk}	Skeletal density [kg/m^3]
η	Viscosity [Pas]

BET: Surface area determined by Brunauer-Emmett-Teller theory
BMI: Bath-metal interface
MSG: Monosodium-glutamate
SEM: Scanning electron microscope
SGA: Smelter grade alumina

Introduction

Aluminium, the second most commonly used metal on Earth is, produced from alumina (aluminium oxide), via the Hall-Héroult process (Figure 1). In aluminium smelters, cryolite (Na_3AlF_6) and additives are melted in a carbon crucible, also serving as cathode for electrolysis. The cryolitic bath serves as a solvent for alumina, and permits bringing it into a liquid phase, 1000°C below its melting point, making the production of aluminium economic. Carbon anodes are inserted into the electrolyte, conducting direct current.

As a result of the electrolysis, liquid aluminium accumulates in the bottom of the cell, while the oxygen from the alumina consumes the carbon of the anodes, creating carbon-dioxide, the bulk of the so-called anode gas. The liquid metal is syphoned at regular intervals. The prebaked anodes, consumed by the process, also get replaced regularly. The anode gas is collected and cleaned by the dry scrubbers, using primary alumina to adsorb the fluorides escaping from the bath. This process prevents fluoride emission into the environment, and also saves on supplementing the evaporating fluorides.

Another function of alumina is the thermal insulation. The top of the anodes are covered with a mixture of alumina and crushed bath material, which solidifies over time and forms a crust on the anode and the top of the bath, to prevent thermal losses. The sides of the cathodes are also covered with frozen bath. The side ledge protects the cell from the highly corrosive molten cryolite.

Historically, alumina was shoveled into the cell on the sides. Modern smelters use point-feeding systems to add the alumina into the bath. The powder is placed in hoppers above the cells, and a small batch of alumina (0.5-2 kg) is added at a time, between the anodes. To ensure that the alumina reaches the bath, crust-breakers are integrated with the feeding systems, so the crust could be crushed if it were to close over the holes below the feeders.

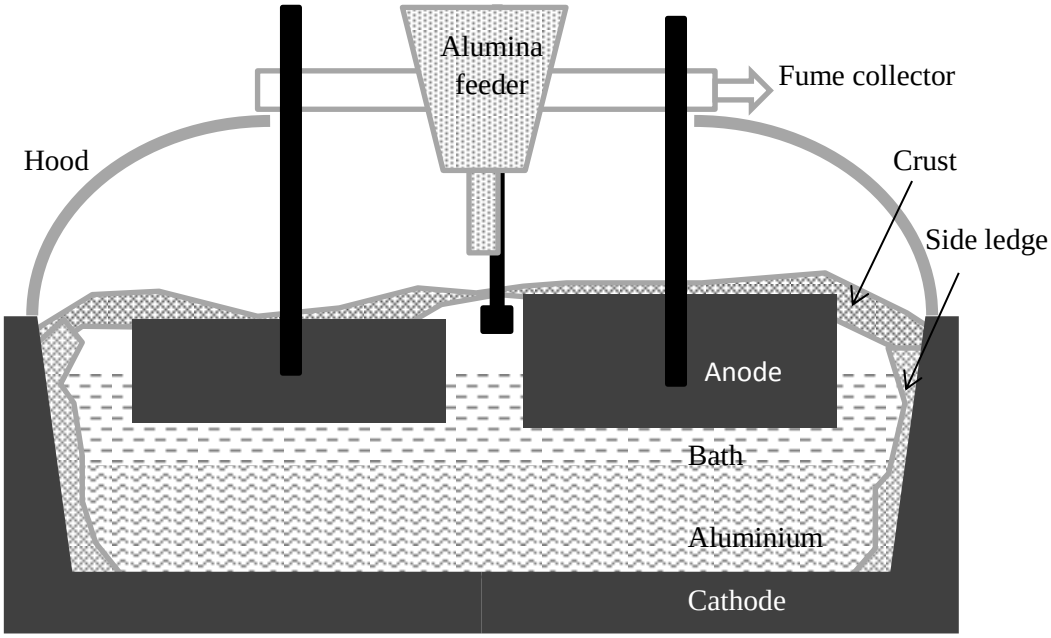

Figure 1: Schematic drawing of an aluminium electrolysis cell ©Csilla Kaszas

Research problem

The rapid and complete dissolution of alumina would be desirable for the efficient operation of the cell, but the dispersion, and as a consequence, the dissolution of the powder is hindered by raft-formation and agglomeration. While the end goal is the dissolution, many various thermal, mechanical and chemical processes occur beforehand, influencing each other along the way. First, the moisture, evaporating from the alumina due to the rapid temperature increase, spreads the powder on the surface. The bath, in counter effect, is solidifying around the cold alumina, hindering the infiltration. The behaviour of the electrolyte is complicated by the fact that it has additives, and between the solidus and liquidus temperature some components crystallise. By the time the solidified bath completely re-melts, another issue arises obstructing the dispersion of alumina: the sintering, resulting from the recrystallization into alpha-alumina. The particles can get attached to each other and will not let go until the dissolution weakens the bond so the currents of the bath and the gravity manage to tear clusters of particles from the main mass, that end up sinking like leaves are falling in the autumn. All the while the main raft may remain afloat – or sink as well.

Sinking is a milestone in the life of smelter grade alumina. It marks the end of its life as an alumina raft, and becomes full-fledged alumina agglomerate (Figure 2). While it is afloat, only the bottom of the raft is exposed to the cryolitic bath, limiting the possible contact surface with the bath, and also the rate of heating. Being fully surrounded by the agitated bath improves upon these conditions; however this blissful state is only temporary. Unless the agglomerate is consumed by the bath during its journey, it will meet the bath-metal interface (BMI). The BMI

may or may not stop the agglomerate in its downward spiral. If it does, the exposure to the fresh bath will be limited once again. If it does not, the exposure to fresh bath will be impossible for a long time, if not forever.

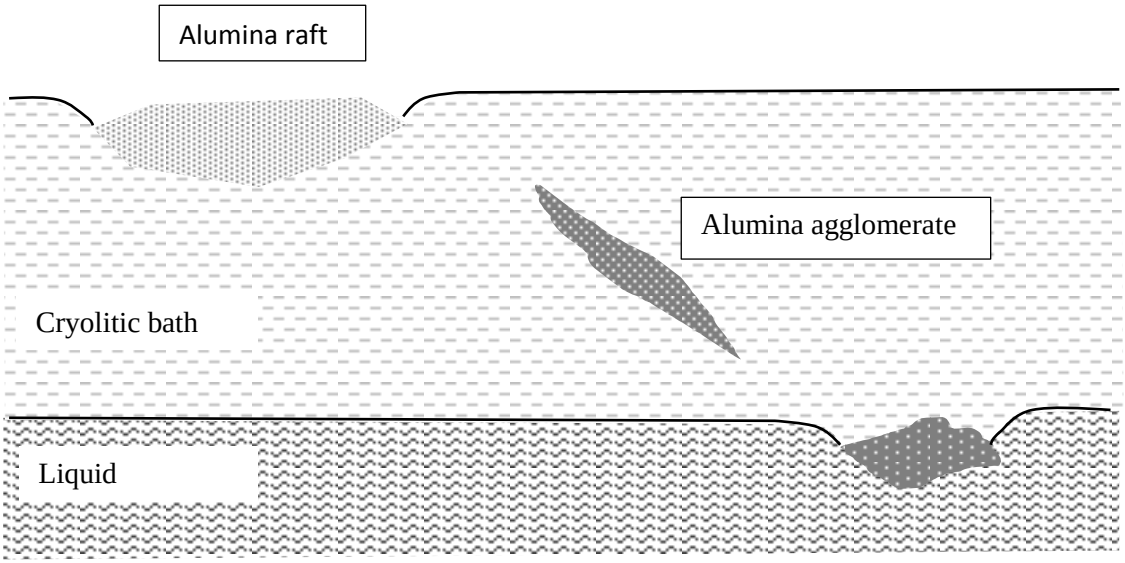

Figure 2: Different phases in the life of alumina raft/agglomerate ©Csilla Kaszas

Originality

Raft formation and flotation occurs most of the time when alumina is injected into the electrolyte, however, the phenomena has usually only merited a few honorary mentions in scientific papers, but did not attract much attention in the field of research. As flotation has a (formerly neglected) effect on the possibility of dissolution, it was selected as the roadmap/arranging principle of this work, the study of the behaviour of alumina in the electrolysis cell.

Objectives

The objective of this PhD was to analyse the mechanisms that promote the formation of agglomerates, and hinder the fast dispersion of alumina added into cryolitic bath, mostly focusing on:

- the raft formation: the spreading of the powder, injected onto the bath surface;
- the evolution of alumina rafts, with regard to the flotation of the raft on the bath surface;
- the flotation behaviour of agglomerates on the bath-metal interface.

Methodology

Several methods have been applied to study the behavior of alumina injected into the bath, including the development of mathematical models, experiments with different alumina powders and objects in the cryolitic bath, and analog experiments.

After the injection of alumina powder, the majority of the powder stays afloat, that is called an alumina raft. It is exposed to the bath at the bottom, and to the anode gas on the top, containing gradually less and less powder unaffected by the bath. If it does not disperse on the surface, but sinks, it will be further referred to as agglomerate, surrounded completely by the cryolitic bath. This work mainly focuses on the first part of the process, the development of alumina raft. As sinking is usually the natural end of the raft's life, its condition was a key viewpoint (/organising principle), and the models and experiments are grouped here by the mechanism, through which they influence the flotation behavior of the raft. When a factor influences the flotation in more than one way, it is mentioned in several chapters, but the detailed description of each related experiment is written only at the most pertinent section, the one indicated below.

The following list summarises the methods with short descriptions and links the corresponding chapters.

- Mathematical models
  - The mathematical model on the static conditions of flotation of spherical and cylindrical objects on liquid surface and liquid-liquid interface determines the floatability of alumina particles, rafts and agglomerates on bath surface and bath-metal interface as a function of size, density, and shape.
  - The mathematical model on the penetration of liquid surface and liquid-liquid interface determines the penetration depth of alumina in the bath, and the critical velocity of agglomerates on the bath-metal interface as a function of size and density.
  - The thermal model of alumina rafts includes bath solidification and infiltration, predicts flotation time, with a possibility of integrating sintering and disintegration of raft. Corresponding experiments were executed with regularly shaped artificial alumina rafts.
- Experiments in analog low-temperature systems
  - To study the powder-liquid interactions in more general, cost-effective, and easily observable ways, experiments were conducted with water, oil, molten paraffin as 'bath' and salts, alimentary and other accessible powders as 'alumina'.
- Experiments in cryolitic bath:
  - Injection of alumina powder, analysis of video recordings
  - Compressed alumina discs as artificial alumina rafts
  - Contact angle measurement with capillary rising method
  - Contact angle measurement with gravimetric system

- Methods to analyse alumina raft samples:
  - Leaching
  - Porosity analysis
  - Optic and scanning electron microscope imaging
  - Measurement with monotonic ramp heating device

Structure of document

The model on the static conditions of flotation shall be presented first, given that most alumina powders reach close to steady state flotation before sinking or disintegration.

Several phenomena occur between alumina and bath, and they influence the flotation behavior in one way or another. These phenomena are organized in this document by the parameter, through which they influence flotation the most:

- Surface tension
- Shape
- Apparent density

Since these processes are interconnected, the following figure is intended to help the comprehension and orientation in this document. (Figure 3). The explanations are presented in the related chapters.

In the last chapter, the dynamic interface penetration model is presented with the corresponding experiments.

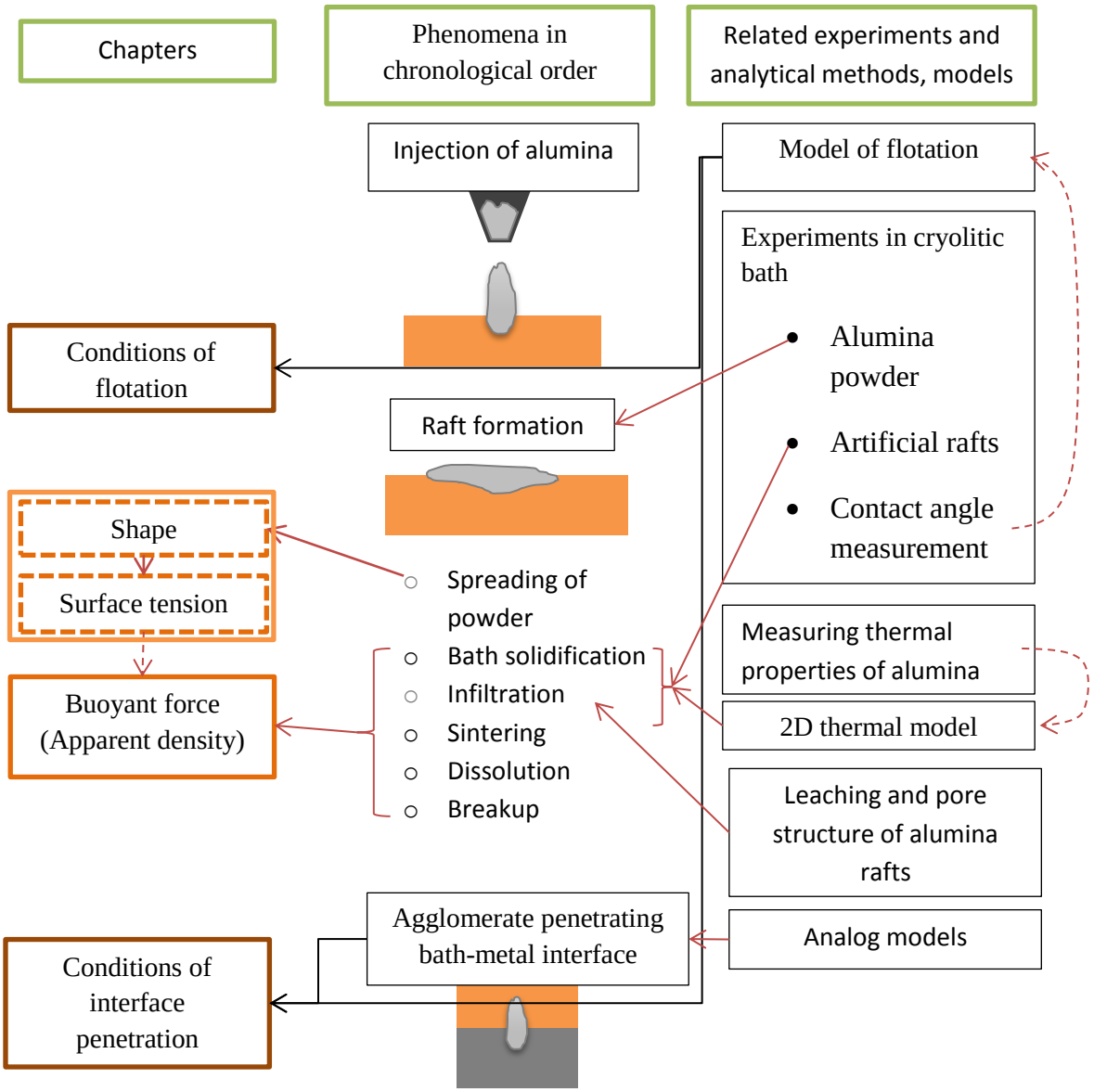

Figure 3 Structure of the document ©Csilla Kaszas

1 Context of research problem

This chapter focuses mainly on smelter grade alumina (SGA) and its interaction with the electrolytic bath, but due to the diverse nature of this work, several other articles from various fields will be mentioned in the forthcoming chapters as well.

1.1 Smelter grade alumina

Alumina is used as refractory material, desiccant, it is used in ceramics, composites, even toothpaste – but most importantly, it is the raw material of aluminium production.

1.1.1 Production of SGA

Alumina is produced by the Bayer process from bauxite. Crushed bauxite is digested in a caustic solution at high pressure and temperature; the alumina is brought into the solution while the impurities remain solid, and are disposed of as red mud (bauxite residues). From the clarified solution, gibbsite ($Al(OH)_3$) crystals are precipitated. During the last step of the Bayer process, calcination, aluminum-hydroxide grains are heated to a high temperature and the material transforms into alumina. Transformation to the stable corundum phase (alpha alumina), requires a temperature above 1200 °C. Depending on the calcination technology, temperature and retention time, the properties of the resulting SGA may vary.

Primary alumina can be fed directly into the aluminium electrolysis cell, or processed further by the dry scrubbing. The main purpose of dry scrubbing is to remove fluorides from the anode gas, for both environmental and economic reasons, but it also has a significant effect on the alumina, which is used in the process – referred to as secondary alumina. By adsorbing the anode gas, the alumina is replenishing fluorides lost by evaporation, into the bath. Due to the mechanical impact of the process, the particles can break up, decreasing the average particle size, increasing the percentage of fines.

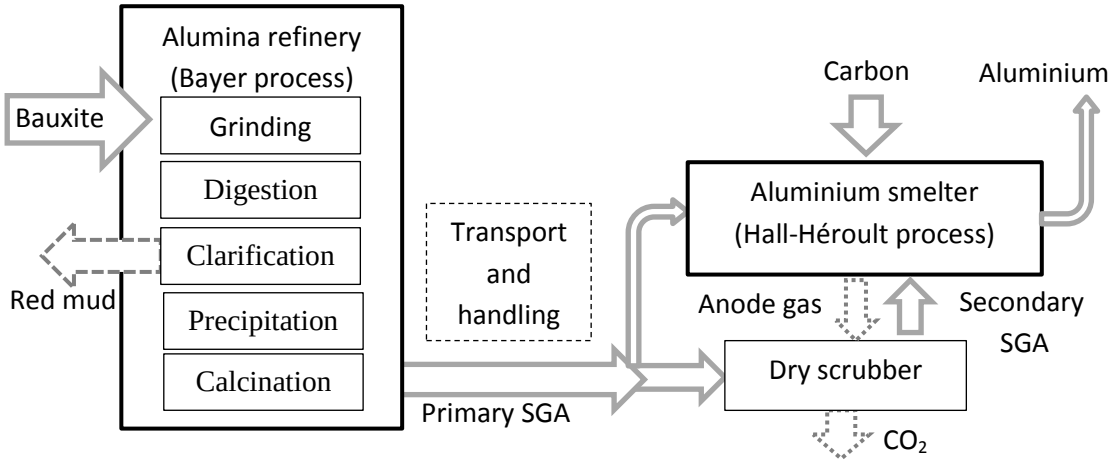

Figure 4: Main processes and material flow of aluminium production ©Csilla Kaszas

Specifications also differ between companies, and since easily measurable properties do not translate well/directly into preferred behavior in the smelter, this is unlikely to change in the future [1] [2] [3] [4]. [5] [6]. Many of the properties are not independent, and it could be challenging, if not impossible to change only one, which can make drawing conclusions from experiments difficult [7] [8].

1.1.2 Structure

Historically, two kinds of SGA were used, sandy and floury, the latter having a high alpha alumina content and small particle size. With the environmental and economic need to clean anode gas and recuperate fluorides via dry scrubbing, floury alumina got out of use, as it is less efficient in the adsorption of HF. Generally, SGA is expected to contain less than 5% alpha alumina (corundum) these days [1] [9]. The alpha phase is located on the surface of the particles and along the cracks in the grains, the parts exposed most to the high temperature during calcination. The bulk of SGA consists of transitional phases of alumina: gamma, gamma-prime phases and theta [10] [11]. As these transitional phases are in low-crystalline form, unlike corundum, they cannot be clearly distinguished by X-ray diffraction, and as consequence, they are usually grouped together under the gamma category in the industry, without further distinction. Residual hydroxides are tolerated at some extent, impurities may be also present [2] [12].

SGA is a polydisperse powder, the majority of particles range between 40 and 100 µm. The quantity of larger and smaller particles are controlled, especially the ultra-fines (<20 µm). The structure of particles resembles the structure of aluminum-hydroxyl, with cracks on their surface [13].

1.1.3 Density

The bulk density, an easily measurable characteristic of SGA, can vary between 0.9-1.15 g/cm^3. The skeletal density depends on the phase distribution, around 3.5-3.7 g/cm3, larger with higher alpha content (alpha: 3.99, theta: 3.6, gamma: 3.2-3.7 g/cm^3) [14]. As the ratio of bulk density and skeletal density shows, the porosity of the SGA is quite high; this is due to the intra-particle porosity in the transitional phases of alumina.

1.1.4 Moisture content

The moisture content of alumina is usually characterized by the loss on ignition (LOI), the weight loss of the material when heated to a specific temperature. Humidity can be bound to alumina at different levels, influenced by its structure. The alpha phase in SGA cannot adsorb water, but the transitional phases, the majority of SGA, can. The first layer of adsorption is chemisorption, `dissociative addition of water molecules on aluminium oxide surface sites`, then several layer of water can be bonded by physisorption via Van der Waals forces, and finally, capillary condensation in the pores. Most of the moisture escape the alumina at around 150 °C, which is also the approximate temperature of alumina fed into the electrolysis cell, but for complete drying, temperature over 200 °C is needed, in vacuum or dry gas [15] [16].

Another source of water in SGA can be attributed to residual hydroxyls. Gibbsite ($Al(OH)_3$) and boehmite (AlOOH) can be present in SGA, due to incomplete calcination process [9] [17] [11]. Despite the misleading terms: alumina hydrate, crystalline water, dehydration sometimes seen in the literature [12] [18], alumina does not contain lattice water [9]. While water is result of the transformation, it is not present in the material as H_2O. Gibbsite transforms to boehmite at around 300 °C, but the transformation of boehmite into gamma alumina is not so clear cut. According to different sources, gamma alumina occurs at 400 °C [10], the 'residual hydrate' leaves by 500 °C [12], or the transformation to alumina occurs only above 700°C [18]– while the gamma-delta phase transformation is also set at 700-800 °C [14]. Gamma alumina itself may contain hydrogen atoms, randomly distributed in the structure, which would leave only above 1000 °C [10], at the transformation to corundum.

For secondary alumina, the desorption of fluorides also occurs at high temperatures, contributing to the LOI. Haverkamp found that there was no desorption below 500°C, with a peak around 700 °C [19]. This finding is in accordance with Gillespie, who observed no fluoride loss of secondary alumina below 440 °C [20]. Young found that around half of the fluorides escaped as HF below 740 °C with H_2O, while the rest desorbed as chiolite between 740-1100 °C [21].

The moisture content of alumina is known to have beneficial effect on its dissolution rate to up to a certain point, but excess moisture delays dissolution, as the surplus energy demand of evaporation freezes more bath in the vicinity of the injected powder. [22]

1.1.5 Thermal properties of alumina powder

The thermal properties of solid, pore-less corundum have been measured numerous times [23] [24] [25] [26]. As alumina is used by multiple industries for various purposes, the thermal conductivity of alumina powder, other than SGA, can also be found in the literature [27] [28].

Regarding thermal properties of smelter grade alumina, research usually focused on the top crust, covering the anodes, providing thermal insulation and reducing heat loss. Related to these studies, thermal properties of smelter grade alumina have also been measured, however the characteristics of the alumina used for these measurements are lacking or vague (Table 1).

Table 1 : Literature on the thermal properties of SGA

	Method	Alumina used	Temperature	Results [W/mK]
Llavona [12] only crust: [29] [30]	Hot wire method	Several types, characteristics not specified, correlation with packing density and hydrate content	at 600°C	0,131+9,542·10^-5·$\rho_{bulk[kg/m3]}$ (for SGA without hydrate)
Ostvold [31] (crust)	Transient hot strip method	Hydro Aluminium A/S Norway, 24-27% alpha	20 - 700 °C	0.18-0.25 monotonically increasing with temperature
Rye [32] (crust)	Vertical heat flux, thermocouples placed at different depths of alumina/crust	Primary, 'normal', sandy SGA	Average value for alumina between 200-700 °C	'Loose cover': 0.15-0.2 W/mK

1.1.6 Other properties; interconnectedness

There are several common ways to characterise SGA.

The angle of repose, or the flow funnel time are indicators of the tendency of the powder to jam in the feeders. Better performance is expected from alumina with low fine content.

The attrition index (measured by non-standardised test, just like flow funnel time) predicts how much the particles will break during dry scrubbing and handling in general; it depends on the microstructure of the alumina grains.

BET surface area is considered a very important parameter for dry scrubbing.

These specifications often correlate somewhat with the alpha-content of the alumina; however it is usually not a decisive factor. Two SGAs from different sources can have the same alpha-content, similar particle size distribution and BET surface area, and still behave differently. Alpha content is easily measured – but smelter grade alumina has a complex structure that is hard to characterise and measure. Tests, like flow funnel time, are practical but superficial, and if someone expects to find the whys and hows of the behaviour of alumina, studies on the microstructure and phase distribution of alumina are of great importance.

1.2 Properties of electrolytic bath

1.2.1 Composition

The electrolytic bath consists mainly of cryolite, the only known solvent of alumina. The melting point of pure cryolite is 1010 °C, but any additive (including alumina) reduces the liquidus

temperature. This permits lowering operating temperature of the cell. On the other hand, additives decrease the solubility and dissolution rate of alumina.

Aluminium fluoride is primary additive of the electrolyte. The bath is often characterised by the bath ratio, the mass ratio of NaF and AlF_3 content of the bath.

Other additives are calcium fluoride and lithium fluoride, the bath can also contain magnesium fluoride from the impurities of dissolved alumina. The additives influence the chemical and physical properties of the mixture, from electrical conductivity to interfacial tension. There is not one ideal bath composition; it depends on the priorities and preferences of smelters.

The electrolyte is a complex, multicomponent molten salt system, with the composition constantly changing in space and time with the addition of alumina between the anodes, the consumption of alumina under the anodes, and the evaporation of certain components of the bath on the surface.

1.2.2 Temperature

The composition determines the liquidus temperature of the bath, above which, the entire bath is in liquid phase. The superheat is the difference between the actual temperature and the liquidus, which influences the cell`s current efficiency, the thickness of the side ledge, and also the behavior of alumina powder.

The actual values in industrial cells might vary. Walker reported 965°C operation temperature and around 10 °C superheat [33].

1.2.3 Density

The density of the electrolytic bath depends on its temperature and composition. To maintain good separation between the bath and liquid aluminium, the latter having a density of 2.3 g/cm^3, the bath density is usually kept around 2.1 g/cm^3 or below. Several empirical equations are available and have been presented in well-known reference books in the industry [34] [35] (Equation 1), where the bath ratio is the mass ratio of NaF and AlF_3.

$$\boldsymbol{\rho_{bath}}\left[\frac{\boldsymbol{g}}{\boldsymbol{cm^3}}\right] = \mathbf{2.64} - \mathbf{0.0008}(\boldsymbol{temperature\ in}\ ℃) + \mathbf{0.18}(\boldsymbol{bath\ ratio}) - \mathbf{0.008}(\boldsymbol{w\%\ Al_2O_3}) + \mathbf{0.005}(\boldsymbol{w\%\ CaF_2}) + \mathbf{0.008}(\boldsymbol{w\%MgF_2}) - \mathbf{0.004}(\boldsymbol{w\%LiF})$$

Equation 1: Density of cryolitic bath [35]

The above-mentioned values represent well the parameters of the experimental setup used in the present work and shall be used in the calculations shown in the following chapters.

1.2.4 Surface tension

Surface tension, interfacial tension and contact angle not only influence flotation behavior, they have an impact on bubble formation on the anodes, and the possible penetration of carbon by

the bath. The surface tension of cryolitic melts has been measured by several research groups by pin detachment method [36] or maximum bubble pressure methods [37]. Model equations were fitted to the experimental data (Equation 2). The validity of these empirical equations is limited to a certain temperature range where the experiments were conducted. As the alumina fed into the bath tends to be several hundred degrees cooler than the bath itself, surface tension values at low temperature hold particular interest in the flotation of alumina rafts. Beside measurements, a theoretical approach to predict the surface tension of molten salt mixtures is also available [38].

$$\gamma_{bath}\left[\frac{mN}{m}\right] = 266.69 - 0.1257(temperature\ ℃) - 4.754(w\%AlF_3) + 1.546 \cdot 10^{-3} AlF_3 \cdot t + 3.002 \cdot 10^{-2} \cdot {AlF_3}^2 + 2.078 \cdot 10^{-5} \cdot AlF_3 \cdot CaF_2 \cdot t + 2.702 \cdot 10^{-5} \cdot AlF_3 \cdot Al_2O_3 \cdot t - 3.507 \cdot 10^{-4} \cdot CaF_2 \cdot Al_2O_3 \cdot t$$

Equation 2: Surface tension of cryolitic bath [36]

The equation (Equation 2) predicts the surface tension to be 145 mN/m; with the chemical composition and the temperature of the bath during our experiments. For the bath-metal interfacial tension, 450 mN/m was used in the later calculations [39].

For future reference, the capillary length (a) at the upper bath surface is 2.6 mm and 15 mm at the bath-metal interface (Equation 3).

$$a = \sqrt{\frac{\gamma}{\Delta\rho g}}$$

Equation 3: Capillary length

Where ϒ is the interfacial tension and Δρ is the density difference between the upper fluid and the lower liquid.

The contact angle between alumina and aluminium on the BMI was measured by Utigard [39] and was found to be between 150-170°. As the electrolytic bath dissolves alumina, it is expected that alumina is wetted by the bath. However, the actual contact angle between these substances has not been found in the literature.

1.3 Behavior of alumina in the bath

1.3.1 Dissolution

Regarding the dissolution of alumina, one should differentiate between the solubility of alumina in the cryolitic bath (with certain composition and temperature), or its dissolution rate. The latter of the two is of most interest in regard to this work.

Experimental studies may focus on the influencing of alumina and bath properties on the dissolution. A difficulty of these investigations is that there is not one commonly accepted method to measure the dissolution of alumina. Visual observation is not easily quantifiable and some argue that alumina crystals become transparent when heated to the temperature of the bath. Electrochemical methods (voltametry) can be unreliable and sampling the bath results in interfering with the experiment. Bath temperature is often monitored and used as part of the analysis.

In these studies, the form of alumina is often controlled, and the natural raft formation and flotation are prevented.

The general conclusions are summarized below. [40] [41] [42] [43]

- Secondary alumina dissolves faster than primary alumina.

- Dissolution time decreases with
  - increasing particle size – optimum size is supposed to be between 40 and 100 µm,
  - Increasing volatile content.

- Effect of bath:
  - Vigorous stirring ensures dispersion and dissolution.
  - High concentration of alumina and other additives decreases dissolution rate and increases chance of agglomeration formation.
  - High superheat increases the rate of dissolution.

Mathematical modeling on this field mostly aim to determine and predict the dissolution rate of alumina and the dominant driving mechanism behind it: heat transfer or mass transfer.

Haverkamp created a model for the dissolution of individual grains [42], Walker for the infiltration of cylindrical agglomerates [33], Dassylva for spherical agglomerates [43].

In some models, the alumina is separated in two parts, the rapidly dispersing individual grains, and the rest that agglomerates [44] [45] [46].

1.3.2 Crusting, agglomeration and sintering

Top crust is a mixture of alumina and crushed bath, solidified over time that covers the anodes and the top of the bath, providing thermal insulation. However, some researchers refer to raft formation as crusting, as the alumina, injected into the bath, forms a hard shell with the frozen bath on the bath surface. While some of the alumina fed into the cell might end up as part of the top crust – and some of the top crust might end up falling into the bath later, it is important

to separate the two, as the circumstances of the interaction between alumina and bath are different. The top crust contains a limited amount of bath at a lower temperature, but the alumina is exposed to it for a long period of time – while alumina on the bath surface gets in contact with a large amount of hot bath in a matter of minutes.

Agglomeration, the tendency of alumina powder to form clumps is also a subject of research. While it is most often a natural part of the life cycle of alumina injected onto the bath, in research, artificial agglomerates are often created in a way that differs from their formation in an industrial cell.

Either top crust, or agglomerate; what holds the particles together and prevents dispersion in either the cryolitic bath, or above it, is sintering. Sintering is a blanket term, may be used to describe different mechanisms for different materials. For smelter grade alumina and cryolitic bath, it is understood that the recrystallization of transitional alumina phases into alpha alumina that results in the growth of alpha-alumina platelets, which may interlock or fuse together neighbouring particles. Sintering of alumina is of interest in other fields than aluminium production; however, SEM images of alumina sintered at 1300-1600 °C, low heating rate and without the presence of fluorides, show a different picture of the structure of the particles, therefore indicates a different mechanism [47] [48].

Less was the first who reported that the gamma-alpha phase transition, catalysed by fluorides, results in interlocking alpha-alumina platelets, effectively sintering the particles together. Townsend proposed: “Crust is formed because gamma-alumina dissolves faster in the bath than alpha-alumina, causing local supersaturation. Gamma-alumina continues to dissolve, whereas alpha-alumina crystallizes to cement ore into crust.” [49] This theory was debated by Gerlach [50]. Oedegard described sintering as the result of “’necking’ between adjacent grains and simultaneous grain growth” [51]; while Johnston and Richards wrote “rapid growth of alpha alumina to cross link or fuse together adjacent grains of alumina ore to fuse crust” [52]

Even though the phenomenon has been investigated, there is still much to be learned.

A method often used is to create samples is to melt a batch of cryolitic bath and then fill the rest of the crucible with alumina and let the bath infiltrate the powder from below, to replicate the formation of top crust [52] [50] [53]. Walker created and analysed artificial agglomerates by plunging alumina powder in cylindrical aluminium canisters into cryolitic bath. He distinguished the two infiltration layers in these samples as well, the inner layer being of pink-peach colored with harder and more compact structure [33]. Kobbeltveld followed in tow with a cylinder 8 cm high and 5 cm of diameter [54]. Ostbo also replicated these experiments and, in some cases, he also could identify the layer structure described by Walker – however, not in all cases. He considered the results to be intermediate and moved to another direction.

Ostbo studied two types of alumina, and created artificial agglomerates in well-controlled conditions (temperature, time span, exposure to certain quantities and types of catalyzers). In his dissertation, he theorises that few nucleation sites and `ample conditions for mass transport`

lead to large (15µm) platelets, which lead to strong connections between the particles, therefore to a hard and solid agglomerate [55]. Doping the alumina with fluorides or bath is often used as a tool to create and analyse samples [51] [31], in spite of the fact that these conditions do not reflect well the industrial conditions of agglomeration.

Johnson found that increased LOI lead to increased crusting, presumably through lower alpha content [52]. This finding is in accordance with the observation of many other researchers that alumina with high alpha content forms weak crust [49] [50] [52] [56]. Alpha content correlates negatively with BET surface area, and as the alpha content increase, there are less transitional phases that would recrystallize to form the strong bond of alpha platelets.

According to Gerlach, fines reduce the penetration rate of the bath into the alumina powder [50]. Johnson found that fines do not influence crusting behavior, up to 30%, above which increased fines content lead to poorer crusting [52]– and poorer crusting leads to better dissolution.

Becker measured the strength of crusts; they found that primary alumina formed 10% stronger crust. They theorised that carbon in secondary alumina lowers the fluoride wetting capacity, and the lower median pore size of primary alumina makes fluoride adsorption more favourable [56]. Oedegard found that dry scrubber alumina sintered at around 785 °C, sandy alumina with AlF_3 (the most effective at sintering from all the additives) at 800 °C, while pure primary alumina at 1040 °C [51].

1.3.3 Flotation on the bath surface

The phenomena of alumina raft formation – the observation that smelter grade alumina (SGA) tends to stay afloat on the surface of the electrolyte due to its low bulk density and the relatively low temperature of the injected powder, combined with the low superheat of the extremely hot bath, leading to delayed infiltration of the pores – has been reported by various researchers and witnessed by those working with electrolysis cells since the dawn of the aluminium industry.

Although most researchers kept only a written record about their visual observations [49], for the purpose of studying and understanding the behavior of alumina on the bath surface, visualisation of alumina injections are invaluable. Coincidentally, researchers recording alumina in the bath comment more on its flotation. Visual observation of alumina dissolution is not a novelty, the quality of the recordings used to be quite low [57] [58]. Recently, Yang and his team presented several papers about alumina injections into electrolytic bath in a transparent quartz crucible with superior images [59] [60] [61].

Utigard used X-ray radiography and hot-stage microscope to observe the injected (0.5g) alumina to drop into the bath than resurface. Qiu, Liu and Yang observed and recorded alumina in see-through cells. Qiu, using 1.5 g sandy and intermediate type of alumina, named three stages of alumina dissolution procedures, the first being “formation of bath/alumina agglomerates on the bath surface” [62]. They may have been the first to liken the agglomerates from disintegrating

raft to “snow-flakes”. Liu commented on the flotation of gamma alumina (20 g batch), and how it forms thin and large pieces of agglomerates in the bath that are difficult to dissolve [57]. Yang, who experimented with 2 g and 5 g doses, remarked the “boat-like” crust formation of primary alumina [63] [60] [59].

Townsend experimented with four types of smelter grade alumina (8 g), primary and secondary, and provided written record of the wetting time, sinking time, time to complete dissolution and the characteristic crusting and dissolution behavior [49]. Johnson also made video recording of 3g injected alumina, and provided data without imaging on the flotation time and dissolution time and categorised rafts as hard/moderately hard/soft [64].

Walker [33] recovered raft samples from industrial cells, 15-60 seconds after injection of 8 kg alumina powder. He found that his samples were mushy, and had a layered structure, with frozen bath on the bottom, two different types of infiltrated layers, and alumina powder on top. He explained the difference between the first and second infiltration layer by fact that while some components at the electrolyte solidifies at a higher temperature, some part of it high in fluoride content may stay or become liquid at a lower temperature, around 700 °C – while liquid closer to the bath composition in the main volume of the crucible would follow above 900 °C. He discovered clusters of alumina with hard frozen bath layer around, in the removed rafts, which were of ellipsoid shape, with 50mm of diameter and 10 mm of height. The average bulk density of his samples was 2462 kg/m^3. The density of industrial alumina rafts measured by Walker exceeds the density of the cryolitic bath, which may show that their flotation was aided not only by buoyant force [33].

The flotation of carbon particles on the bath, and their interference with the measurement of the surface tension, noted by Kucharic [37] is worth mentioning as the same issue was encountered by the author of this work, and industrial cells are contaminated with carbon dust even more than experimental setups.

1.3.4 Flotation on BMI

The possibility of flotation of alumina agglomerates on the bath-metal interface is of more direct importance to the industry. A flotation model of disc-shaped agglomerates has been presented by Solheim [65], and a simple estimation for the flotation limit of spherical agglomerates by Thonstad: 1.5 cm diameter for a solid alumina sphere [66]. Both of them focused mainly on the possibility of an alumina particle layer on the interface. They theorize that the alumina layer on the interface impedes mass transfer of aluminium, therefore decreases the re-oxidation of the metal by the anode gas and increases current efficiency. Solheim proved the possibility of alumina and cryolite precipitation on the interface through theoretical investigation of bath chemistry [67], though he later pointed out that Marangoni convection might clear the interface of those particles [65].

Interestingly, both Walker and Ostbo dedicated a section to the flotation of agglomerates on the BMI in their dissertations – one of them referencing Solheim, the other Thonstad, however they do not expand on their works.

Based on the equation formerly applied by Thonstad, Keller calculated the flotation limit for accumulation of alumina particles and agglomerates on the bath-metal interface, with different estimated densities [68].

1.3.5 Sludge

Sludge is a semi-solid deposit/mixture of alumina (≈40%), bath and other impurities, under the metal pad of industrial cells [69]. It causes operational problems and cathode wear, and it is a direct proof that alumina penetrates the bath-metal interface in some form. While some people work under the assumption that sludge is the result of undissolved alumina particles sinking to the bottom of the cell [70] [71], Thonstad theorised that it is caused by pieces of the top crust falling into the bath, and not from the feeding of alumina [72]. Large quantity of sludge can be found under feeding holes, but it does not support any of the concepts more than the other.

Taylor made a distinction between “soft sludge” and “hard sludge”, the latter containing corundum up to 70% [34].

1.3.6 Alumina phases

Comparing the behavior of alpha and gamma alumina, Liu found that alpha alumina sunk to the bottom of the crucible in a non-agitated cryolitic bath, however, the clumps disintegrated with relative ease when the stirring of the bath started. Gamma alumina formed a raft on the bath surface and disintegrated faster, with the exception of the remaining agglomerate that was proved hard to dissolve even with stirring [57]. They also theorised that the evaporating moisture breaks up the gamma particles from the inside, and shattering of grains increases the contact surface, therefore aid the dissolution process.

Jain found that highly calcined alumina with high alpha content would decrease the dissolution rate, and that it is more sensible to the thermal influences. The dissolution of gamma alumina requires 20% less heat than the dissolution of alpha, due to the exothermic nature of the gamma-alpha transformation that occurs in the bath [7]. Isaeva came to the same conclusion regarding the alpha content’s effect on the dissolution rate, however she also claimed that grains above 150 micron (mostly gamma), dissolve slower [73].

Bagshaw suggested that the delta-phase content of SGA, and the morphology of the original hydrate might have an effect on its dissolution rate [74].

1.3.7 Secondary alumina

Haverkamp observed that secondary alumina dissolves 30-40% faster than primary alumina. Bagshaw attributed the difference to the volatile content [74]. Haverkamp claimed that the fluoride content does not appear to enhance the dissolution rate in and of itself, but it is the adsorbed moisture in the dry scrubber that has an effect [22]. Yang presented alumina

injections in see-though cells, they theorized that rafts of secondary alumina disintegrate faster because of the carbon content: according to them, the carbon particles burn out and the flash-off gas agitates the raft. They treated the secondary alumina at high temperature, and measured the carbon content of the samples. For alumina treated above 600 °C, the carbon was burned out, and there were no visible bubbles in the raft. Coincidentally, the high temperature treatment would also decrease the volatile content, but it was unaccounted for in the publications [61] [63].

After experiments with four kinds of alumina (virgin and reacted), Townsend noted that secondary alumina is wetted faster than primary alumina [49]. In his characterisation of the forming raft he differentiated between soft and hard crust, the former mostly formed by secondary, and the latter by primary alumina. While this observation was pointed out, there was no explanation or theory provided.

1.3.8 Feeding

Beside the characteristics of the alumina and the bath, the method of feeding also influences the behavior of alumina. Over the decades, alumina batch sizes shrunk considerably, as smaller doses would consequently lead to smaller agglomerates [75].

Tessier tested a modified feeder design for four months in an industrial cell. They restricted feeder pipe diameter to ensure an elongated injection and a thinner raft, as the forming raft would drift along with the bath's currents [76].

Solheim played with the idea of an agglomerate-free alumina feeding strategy that would require sprinkling individual grains on the bath surface, eliminating contact between particles, therefore eliminating the possibility of sintering [77].

Bagshaw emphasized the importance of flowability of alumina in relation to feeder design [74].

Kobbeltvedt pointed out that dissolution rate of alumina decreased when the feeding hole was plugged, compared to an open feeding hole [78].

2 Conditions of steady-state flotation on bath surface

A mathematical model was developed, based on the force balance of an axisymmetric solid object (disc or sphere) floating in equilibrium on gas-liquid and liquid-liquid interfaces, to determine the conditions of flotation of alumina on the bath surface, and agglomerates on bath-metal interface. The model has been extended into a dynamic model with the addition of the drag force and virtual mass, mostly relevant to the penetration of bath-metal interface (BMI) by agglomerates. The dynamic model and the results concerning the bath-metal interface will be presented in chapter 5.

When a batch of alumina powder is added into the bath, it will float due to its high porosity, low bulk density, in addition to its low temperature that results in bath solidification and prevents rapid infiltration. An alumina raft formed this way can stay afloat on the bath surface for several minutes. By the time it sunk, effects of the initial impact had been diminished, which justifies the use of a static model of flotation to predict the floatability of rafts on the bath surface.

2.1 Mathematical model

2.1.1 Force balance of a floating axisymmetric object in equilibrium

According to Newton's first law, an object at rest will stay at rest as long as the sum of all forces acting upon it is zero. It is known since Archimedes that a floating object is subjected to a buoyant force, equivalent to the weight of the displaced fluid. Large objects, such as boats, depend on the buoyant force to stay afloat, and the surface tension will not make or break their flotation. On the other hand, the surface tension may play an important role in the flotation of small objects (Figure 5: Forces acting on a floating axisymmetric object).

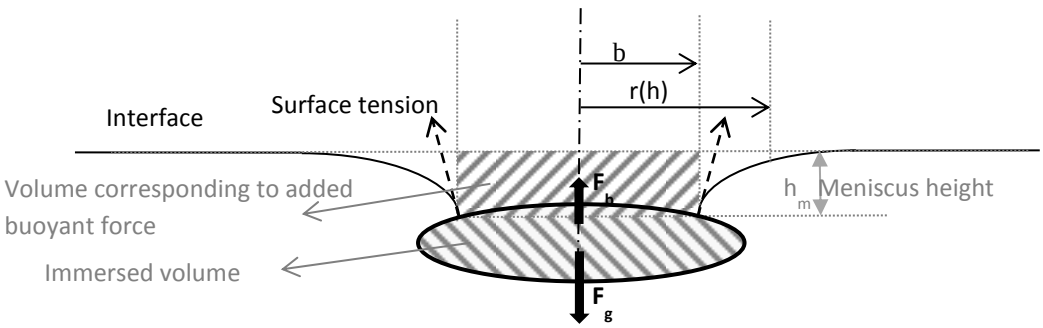

Figure 5: Forces acting on a floating axisymmetric object ©Csilla Kaszas

The force balance of a floating object at equilibrium can be expressed with the following form:

$$\boldsymbol{F_g + F_b + F_s = 0}$$

Equation 4: Force balance of a floating object

Where F_g is the gravitational force, F_b is the buoyant force, F_s is resultant force of the surface tension.

The surface tension can aid the flotation but it can hinder it as well, depending on the wetting characteristics of the liquid-solid system. The surface tension may influence the flotation in two ways: directly, via the resultant force of the surface tension, and indirectly, by forming the meniscus (curved surface). The vertical component of the surface tension acting along the triple line is influenced by the shape of the object and the contact angle of the liquid surface at the triple line. The meniscus around a floating object is also the result of the surface tension and it influences the hydrostatic pressure, therefore the buoyant force acting on the object. In another way, the displaced volume of liquid can be expressed as a sum of the object`s volume below the triple line, plus the volume of a cylinder with the radius of the triple line, and the height of h_m, the meniscus height.

2.1.2 Meniscus height

The inclusion of the meniscus height in a flotation model can be done in various ways. The simplest solution is to neglect the meniscus height altogether, and consider the buoyant force corresponding to the volume of the object below the triple line [79] or below the undisturbed surface [80]. It is a pragmatic solution, which results in a negligible inaccuracy for the flotation of particles significantly smaller than the capillary length, as is the case with the flotation of individual smelter grade alumina particles on the surface of the electrolyte. Solheim applied the meniscus height calculated beside a plane wall to determine the flotation limit of disc-shaped alumina agglomerates on the bath-metal interface [65]. The meniscus height around a cylinder approaches that around a plane wall as the radius increases, which makes this estimation appropriate for large objects. The most precise method would be to solve the Young-Laplace equation. Singh used direct numerical simulation of the water-air interface to determine the behavior of floating particles, and as he pointed out, the required computational capacity increases unfeasibly when there are several objects on the surface [81].

In this work, the equation describing liquid surface around axisymmetric objects (Equation 5) [82] was solved numerically to obtain the meniscus height:

$$\boldsymbol{K = \frac{r''}{(1 + r'^2)^{3/2}} - \frac{r'}{(b + r)(1 + r'^2)^{1/2}}}$$

Equation 5: Liquid surface curvature around axisymmetric objects

Where:
K: mean surface curvature
b: radius of axisymmetric object at the triple line
r=r(h): interface profile, (see Figure 5: Forces acting on a floating axisymmetric object)
r', r'': first and second derivatives of r(h)
h: meniscus height/depth, axial (vertical) coordinate

It should be noted, that the independent variable is h and the dependent variable is r. While it is customary to represent the independent variable on the horizontal axis, the meniscus shape is illustrated in the direction one encounters it in reality, with r on the horizontal, and h on the vertical axis (Figure 11). The meniscus profile approaches h=0 at r=inf, where the interface flattens out and the mean curvature is zero. The meniscus is shown curving downwards around the axis (or the floating object). As the focus of this work is on the circumstances when the surface tension aids flotation, the resultant force of surface tension is pointing upwards and the meniscus is negative. The equations are equally applicable to the meniscus curving upwards around the center, the profile being the mirror image of its equivalent.

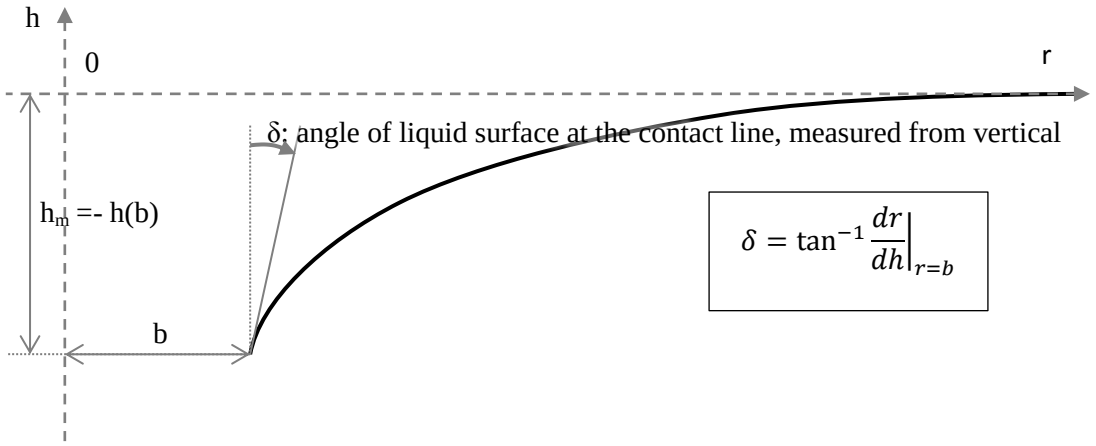

Figure 6: Meniscus profile, illustration of variables ©Csilla Kaszas

The mean surface curvature corresponds to the capillary pressure, according to the Young-Laplace equation (Equation 6), which is proportional to the meniscus height and the density of the liquid:

$$\Delta \boldsymbol{p} = \boldsymbol{\gamma}\left(\frac{\mathbf{1}}{\boldsymbol{R_x}} + \frac{\mathbf{1}}{\boldsymbol{R_y}}\right) = \boldsymbol{\gamma 2 K}$$

Equation 6: Young-Laplace equation

Δp: Laplace (or capillary) pressure
ϒ: surface tension
R_x, R_y radius of curvature in two perpendicular axes in the tangent plane to the surface.
K: mean surface curvature

Matlab ordinary differential equation solvers can only solve fist order equations; therefore, the second order equation was rewritten as an equivalent system of first order equations.

$$r' = r_2$$

$$r'' = r_2' = -\frac{h}{a^2}\left(1 + {r_2}^2\right)^{\frac{3}{2}} + \frac{r_2}{b + r}\left(1 + {r_2}^2\right)$$

Equation 7: Meniscus profile as a system of first order differential equations

The following boundary conditions should apply, assuming a single floating object on an otherwise undisturbed infinitely large surface:

$$\lim_{h \to 0} r(h) = \infty$$

$$\left.\frac{dr}{dh}\right|_{h=-h_m} = \tan\delta$$

Equation 8: Boundary conditions for meniscus profile

Due to the limitations of Matlab, and the fact that h_m was the parameter sought for, a trial and error method was applied, and the meniscus height gradually decreased until the solution fulfilled (or rather, approached) the first boundary condition. Solutions for a few different values of the angle of surface are presented below (Figure 7).

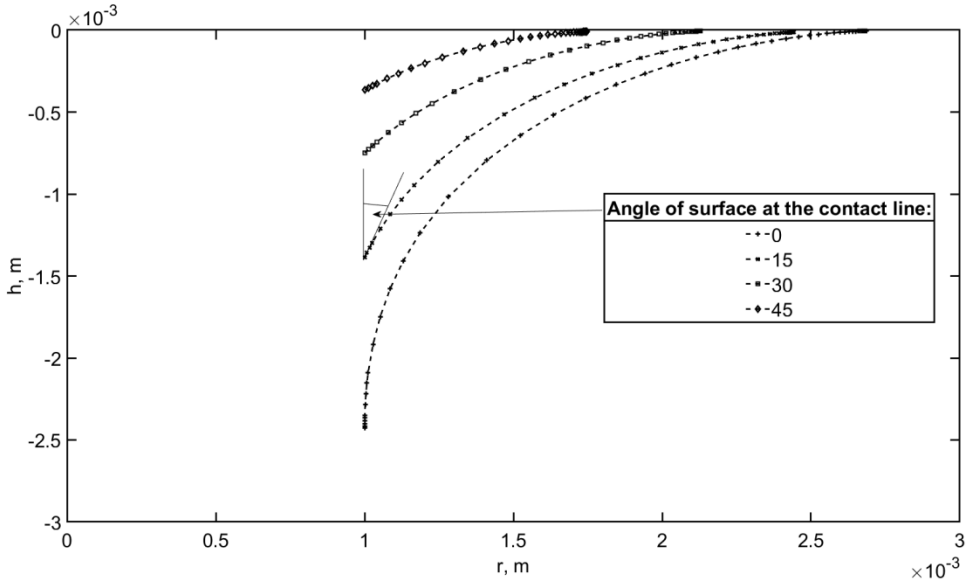

Figure 7: Numerical solutions for meniscus profile at the surface of cryolitic bath

The meniscus profile was calculated using the surface tension and density of the cryolitic bath, discussed in previous chapter (1.2). The results can be presented in a dimensionless form by dividing the radius and height by the capillary length (h_m/a, b/a) (Equation 3).

Regardless of the radius of the triple line (b), the meniscus height is zero when delta is 90° that is the surface is horizontal. The meniscus height increases with decreasing delta, but at a different rate depending on the radius of the triple line. When b is larger than the capillary length, the meniscus height changes more rapidly when delta is small. The influence of the radius on the meniscus height is significant below the capillary length, but decreases gradually and it eventually peters out (Figure 8).

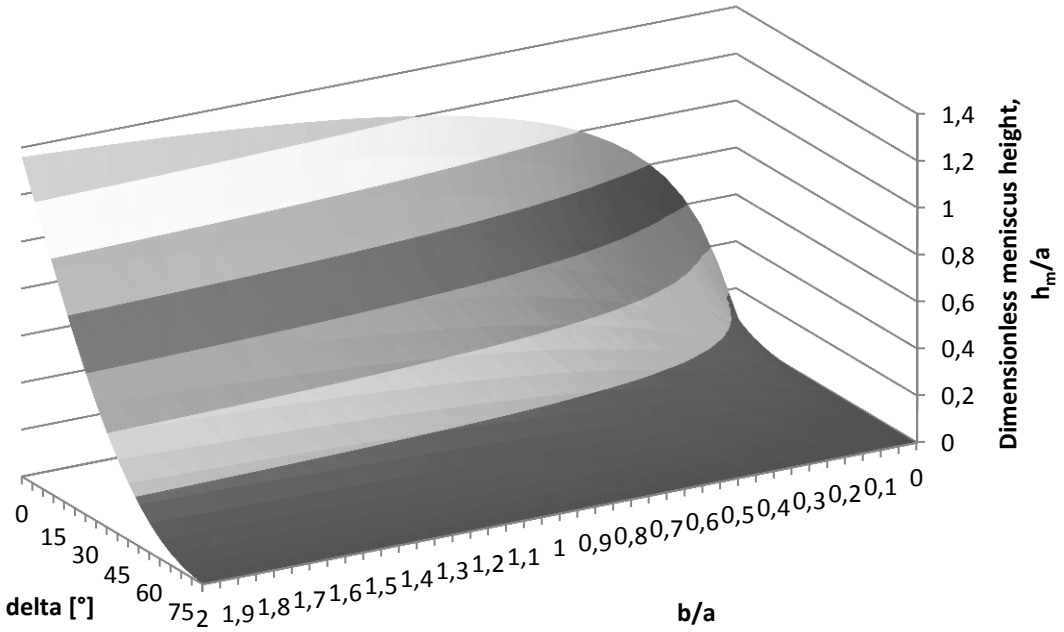

Figure 8: Dimensionless meniscus height as a function of triple line radius and angle of the interface

The angle of the liquid surface at the triple line (δ) could also potentially become negative, so the interface would bulge over the floating object. This does not hinder the solution of the differential equation (i.e. finding the shape of the interface) for larger diameters, but as the radius of the triple line fell below the capillary length, the range of angles for which acceptable solutions were found, became limited (Figure 9). For large diameters, the solution approaches that beside a plane wall. Delta below -90° was not considered, as the floating object would interfere with the liquid surface.

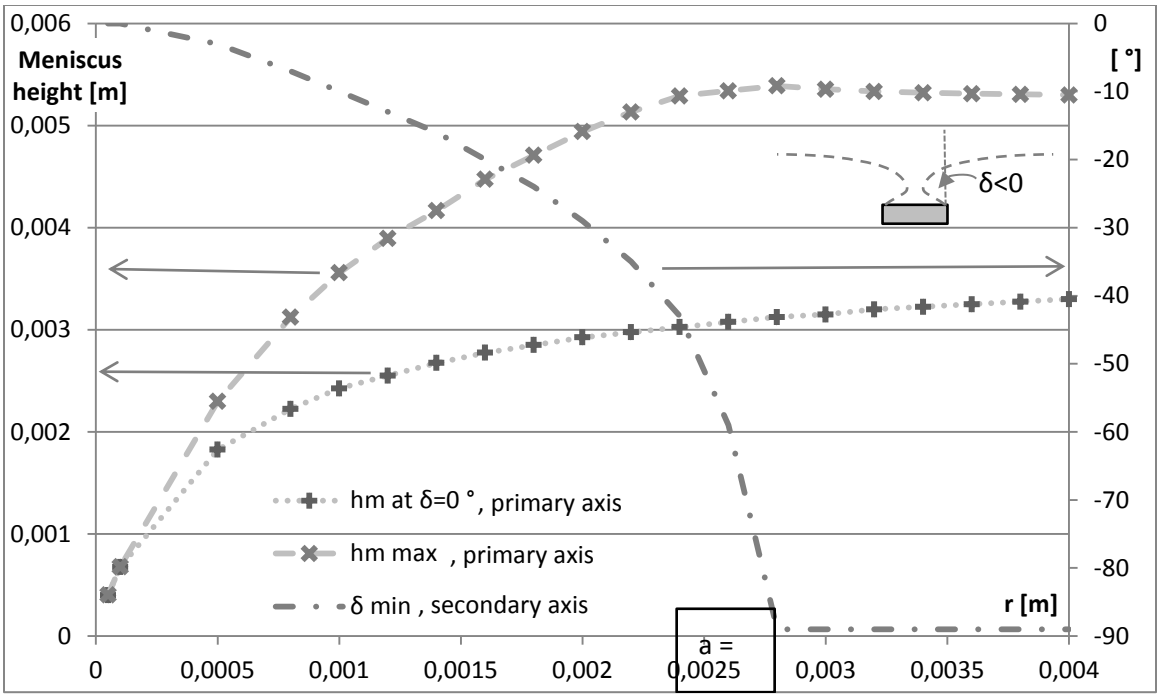

Figure 9: Maximum meniscus height, minimum angle of interface, as a function of radius, on the bath surface

2.1.3 Angle of interface at the triple line

The angle of the interface at the triple line is necessary to find the vertical component of the surface tension force, and also as a boundary condition to determine the meniscus height. For smooth, homogenous surfaces, the Young-Dupré equation shows the connection between the interfacial energies and the equilibrium contact angle (Equation 9). If the floating object has a smooth surface, the angle of the object at the triple line and the contact angle determine the angle of the liquid surface (Figure 10).

$$\gamma_{SG} - \gamma_{SL} = \gamma_{LG} \cos \alpha_0$$

Equation 9: Young-Dupré law

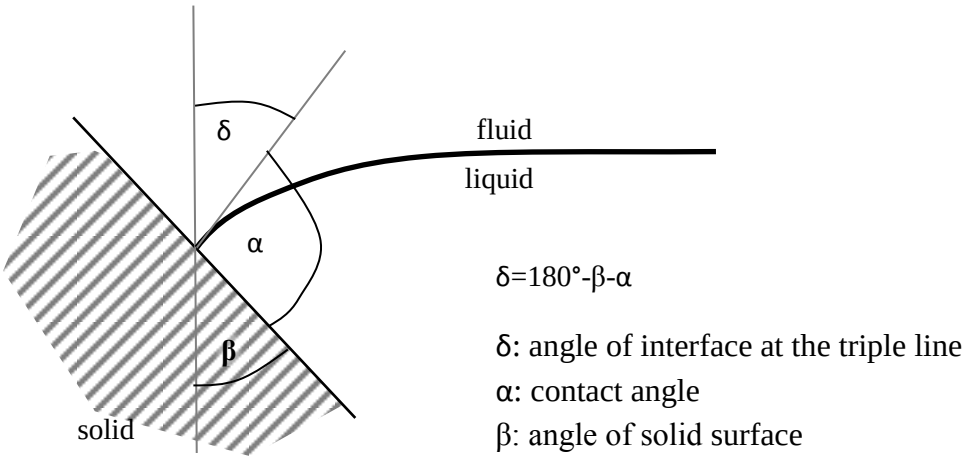

Figure 10: Determination of the angle of interface at the triple line, on smooth solid surface ©Csilla Kaszas

The contact angle (α) has a significant influence on the flotation. A large contact angle will permit the floating object to descend deeper below the line of the undisturbed surface without sinking than an object wetted by the liquid could. But that is not to say flotation of an object denser than the liquid is not possible even if the contact angle defined by the Young-Dupré equation would reach 0°, as the shape and surface quality of the solid would also influence the angle of the interface at the contact line (δ). The contact angle at an edge can vary between the range specified by Gibbs [80] (Equation 10).

$$\boldsymbol{\alpha_0 < \alpha < 180 - \beta_0 + \alpha_0}$$

Equation 10: Gibb`s extension of Young-Dupré law

Where α_0 is the static equilibrium contact angle and β_0 is the angle of the corner of the solid body as shown in Figure 11.

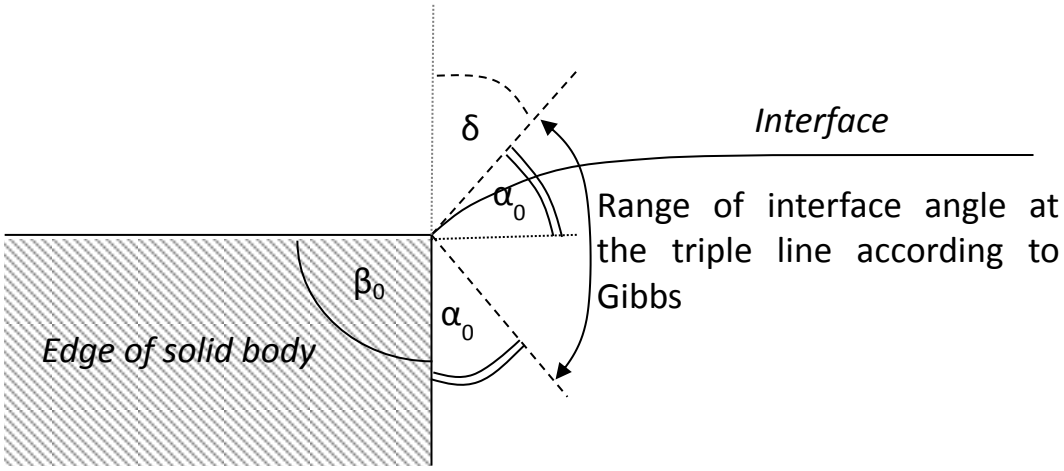

Figure 11: Illustration for Gibbs extension to the Young-Dupré law ©Csilla Kaszas

On rough or heterogeneous surfaces, the Young equation is only locally applicable. The influence of surface roughness on flotation can be estimated by increasing the contact angle in the flotation model. The Wenzel and the Cassie-Baxter equations offer estimations for the apparent contact angle (α) for different wetted states [82].

The angle of interface at the flotation limit (the last stable floating position) will be determined by the shape of the floating object and the contact angle. The contact angle between alumina and the cryolitic bath has not been found in the published literature; it was measured in the frame of this work, and will be presented at a later point (3.3.1).

2.1.4 Shape of the floating object

The mathematical model was developed for two shapes: spheres and circular disks. The former is used as a universal shape; it can represent a single alumina particle, or agglomerate on the bath-metal interface. The disk form holds more interest with small height-diameter ratio, as alumina tends to spread on the bath surface, a disc is a reasonably good representation of an alumina raft. Theoretically, the same equation can be applied for large height-diameter ratio, such as a rod, floating vertically. This, admittedly, is an unlikely, mostly unstable scenario to occur naturally, and since it has no relevance for the studied phenomena either, the height-diameter ratio in this study was limited to 1 and under.

The different terms of the governing equations of flotation are presented below, along with the corresponding shapes (Figure 12).

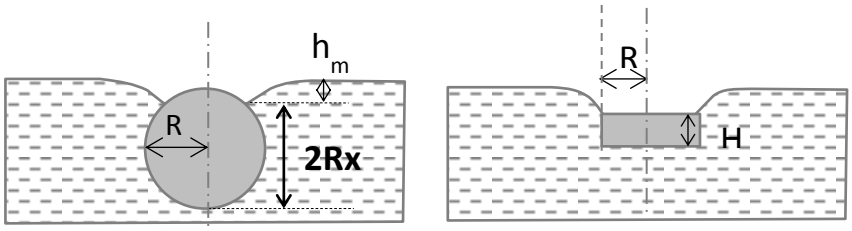

Gravity	$-\rho_s \cdot g \cdot \frac{4}{3} R^3 \pi$	$-\rho_s \cdot g \cdot R^2 \pi H \cdot$
Buoyancy	$\rho_l g 4 R^2 \pi x \left\lfloor \frac{x}{3}(3R - 2Rx) + h_m(1-x) \right\rfloor$	$\rho_l \cdot g \cdot R^2 \pi \cdot (H + h_m)$
Surface tension	$2\sqrt{R^2 - (2Rx - R)^2}\, \pi \cdot \gamma \cdot \cos(\delta(x))$	$2R\pi \cdot \gamma \cdot \cos \delta$

Figure 12: Geometries and corresponding force terms used in the present flotation model ©Csilla Kaszas

Where ρ_s is the density of solid,
ρ_l is the density of liquid,
R is the radius of the sphere or the disc, respectively
H is the thickness of the disc
x is the relative immersion of the sphere: the vertical distance between the triple line and the bottom of the sphere, in relation to its diameter
and h_m is the meniscus height.

For disc geometry, the position of the triple line at the flotation limit is evidently at the top rim of the disc. As delta decreases from 90° to 0°, both the resultant force of the surface tension and the meniscus height increase, therefore at this range, the contact angle determines delta at the flotation limit, according to Gibb's extension to the Young-Dupré law (Figure 11). However, when the contact angle exceeds 90°, delta may become negative, with the liquid surface bending over the top of the disc (Figure 13). In this case, the meniscus height still increases with decreasing delta, however the resultant force of the surface tension reached its maximum at δ=0. Therefore, even though a deeper immersion on the liquid surface is theoretically possible, it might not correspond with the position in which the maximal upward force may be exerted on the floating disc.

Figure 13: Contact angle limiting the position of a floating disc ©Csilla Kaszas

It should be noted, that researchers who attempted solving the problem of meniscus shape, did not succeed achieving negative interface angles with floating discs in reality, supposedly due to instability [80]. It stands to reason, that a position with negative surface angle would be unstable, and a slight tilt of the floating disc could swing the disc out of balance. As one side of the disc gets closer to the surface, the angle of the liquid surface at the contact line at that side gets closer to vertical, escalating the tilt. For this reason, the minimal angle of the surface for discs in the model was limited to 0 degree (Figure 10).

Figure 14: Surface tension stabilizing tilted disc with $\delta>0$, opposite effect on disc with $\delta<0$ ©Csilla Kaszas

While there is no possibility of stable floating position when the density of the solid exceeds the density of the liquid, metastable (or conditionally stable) states exist, where depending on the magnitude of the disturbance, the degree of tilting or displacement from the equilibrium position, the floating object might return to its original floating position, or sink.

Whereas the length of the triple line is constant in case of disc geometry, regardless of the immersion, when the floating object is a sphere, the length of the triple line changes with the relative immersion (x), and so does the angle of the interface and the meniscus height (Figure 15).

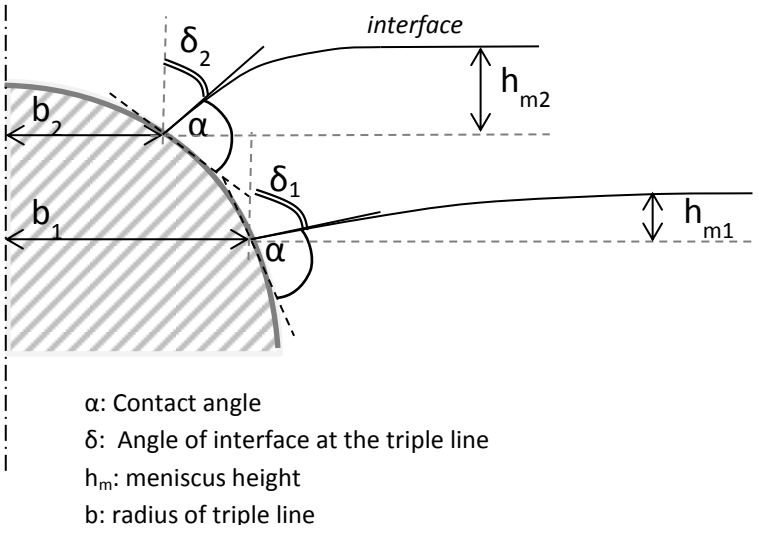

Figure 15: Dependence of the angle of interface, meniscus height and triple line length on the relative immersion of a floating sphere ©Csilla Kaszas

Based on the relative immersion of a sphere (x), and the contact angle (α), the angle of the interface at the triple line can be expressed by the following equation.

$$\boldsymbol{\delta(x) = 2\pi - \arccos(1 - 2x) - \frac{\pi}{2} - \alpha}$$

Equation 11: Angle of liquid surface at the triple line as a function of relative immersion and contact angle, for spheres

The contact angle provides a minimum immersion, where the direction of the resultant force of the surface tension flips (Figure 16). Below that point, the surface pulls downwards the sphere, and its density could not exceed the density of the liquid. However, the variables interconnected as they are, there is no clear, evident answer to the question: at which immersion rate, above the formerly determined limit, will be the maximum upward force exerted. Therefore, to determine the maximum density of a floating sphere with variable parameters, the force balance was calculated for relative immersions above the formerly determined limit with 1% increments until total immersion, and the highest density was selected from the lot.

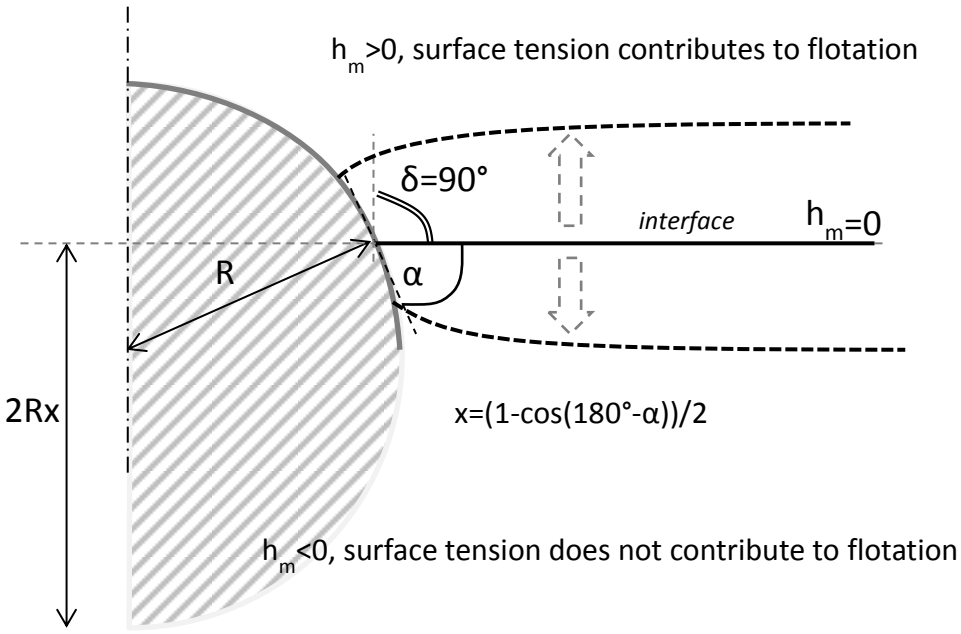

Figure 16: Minimum immersion of interest, determined by contact angle ©Csilla Kaszas

2.1.5 Dimensionless equations

To conclude the description of the mathematical model, the dimensionless forms of the force balance for a disc and sphere are presented below (Equation 12) and (Equation 13).

$$\frac{(\boldsymbol{H}+\boldsymbol{h_m})\boldsymbol{\rho_l}}{\boldsymbol{H}\cdot\boldsymbol{\rho_s}}+\frac{\mathbf{2}\cdot\boldsymbol{\gamma}\cdot\mathbf{cos}\,\boldsymbol{\delta}}{\boldsymbol{R}\cdot\boldsymbol{H}\cdot\boldsymbol{\rho_s}\cdot\boldsymbol{g}}=\mathbf{1}$$

Equation 12: Dimensionless force balance of a floating disc

$$\frac{\boldsymbol{\gamma}*{}^{\mathbf{3}}\!/_{\mathbf{2}}\sqrt{\mathbf{4}\boldsymbol{x}-\mathbf{4}\boldsymbol{x}^{\mathbf{2}}}*\mathbf{cos}(\boldsymbol{\delta}(\boldsymbol{x}))}{\boldsymbol{\rho_s}\boldsymbol{R}^{\mathbf{2}}\boldsymbol{g}}+\frac{\boldsymbol{\rho_l}\boldsymbol{x}^{\mathbf{2}}(\mathbf{3}-\mathbf{2}\boldsymbol{x})}{\boldsymbol{\rho_s}}+\frac{\mathbf{3}\boldsymbol{\rho_l}\boldsymbol{h_m}\boldsymbol{x}(\mathbf{1}-\boldsymbol{x})}{\boldsymbol{\rho_s}\boldsymbol{R}}=\mathbf{1}$$

Equation 13: Dimensionless force balance of a floating sphere

The dimensionless form reveals which ratios of properties should be respected in case of an analog model (5.3.1). The most influential parameters for the possibility of flotation that can be pinpointed are: the density ratio (ρ_l/ρ_s), the ratio of characteristic size and capillary length, the angle of interface at the contact line, influenced by the shape and contact angle.

2.2 Results

2.2.1 General (dimensionless, contact angle dependent)

Firstly, the model results for the flotation limit are presented in a general, dimensionless form (Figure 17). The contact angle has an immense effect on the flotation limit of spheres. While in case of perfect wetting, the density of a floating sphere could not exceed the density of the liquid, the maximal density gradually increases with increasing contact angle, with a more rapid rate in case of smaller dimensions (when the radius of the spherical object is at the same scale as the capillary length).

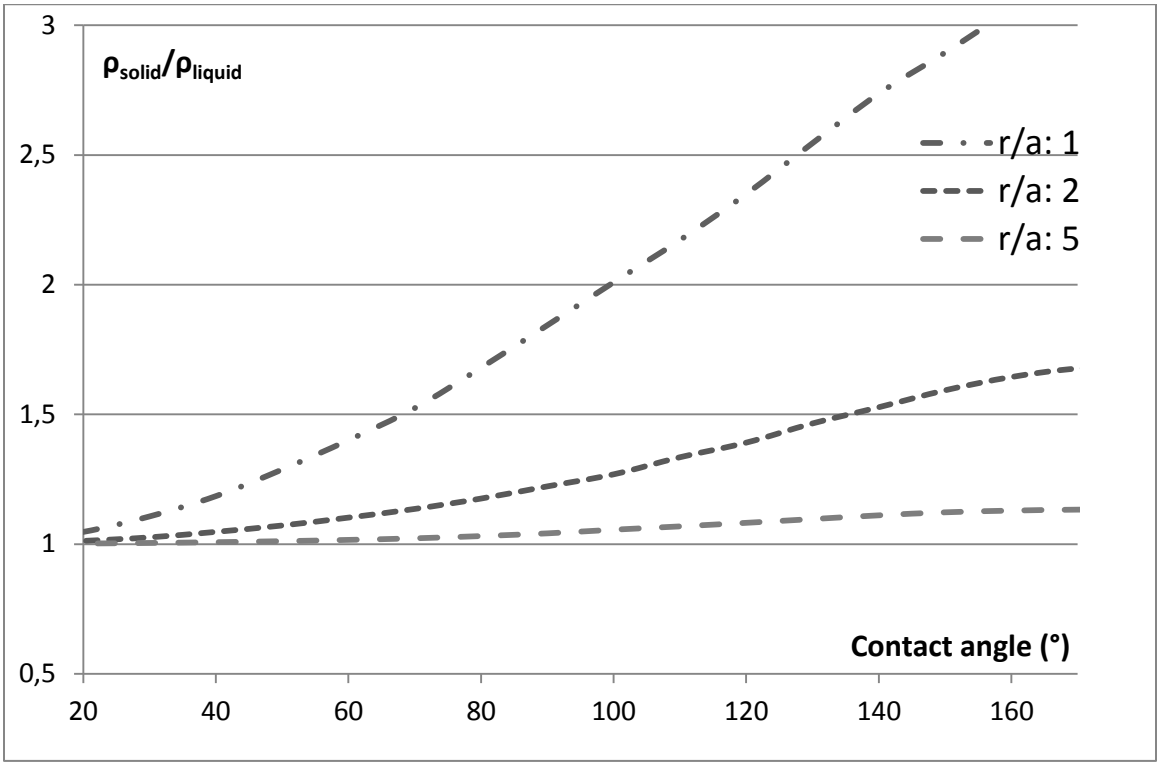

Figure 17: Dimensionless flotation limit of spheres

To compare with spheres, discs with the same radius and same volume were chosen, in other words, discs with 0.67 height-diameter ratio (Figure 18). Disc geometry is more advantageous to flotation. The flotation limit increases almost linearly for contact angles between 0 and 90°. As discussed before, because of stability issues, the angle at the triple line was limited at 0° (dashed line), in which case the flotation limit with 90° contact angle is the flotation limit for any contact angles above that value.

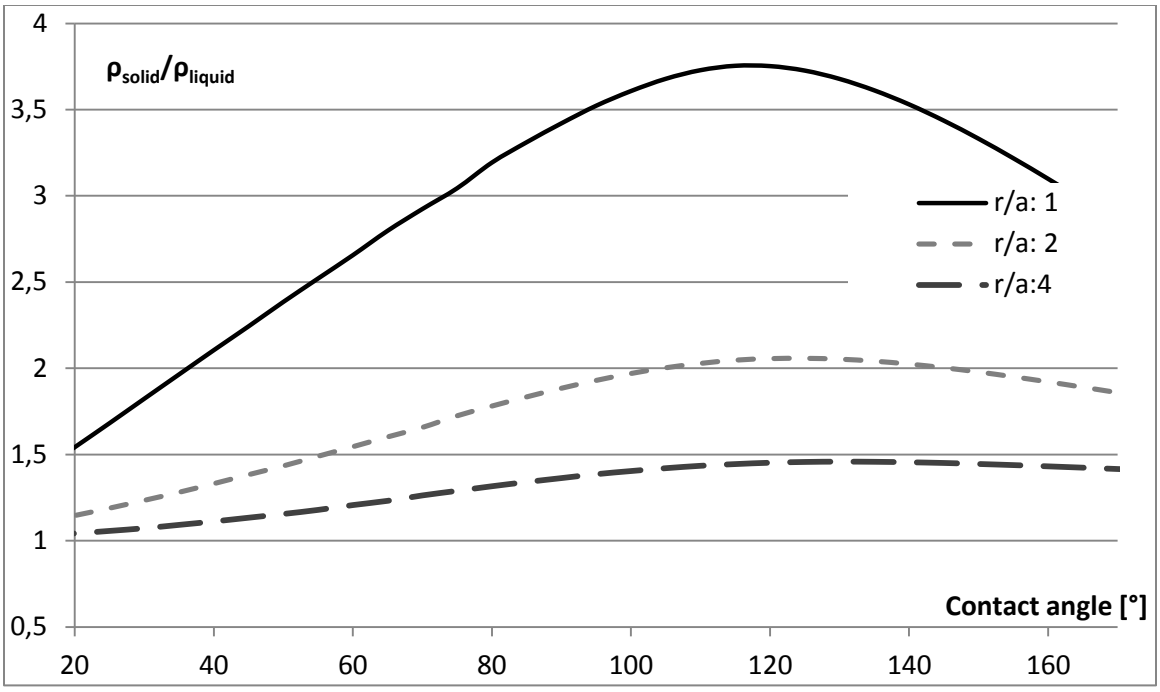

Figure 18: Dimensionless flotation limit of discs, h/d=2/3; dashed line: the angle delta limited at 0

While often the flotation limit is presented as the maximal density of a floating object with certain geometry, the question may be asked another way as well: what is the maximal size of an object that permits the flotation of an object with a certain density (Figure 19).

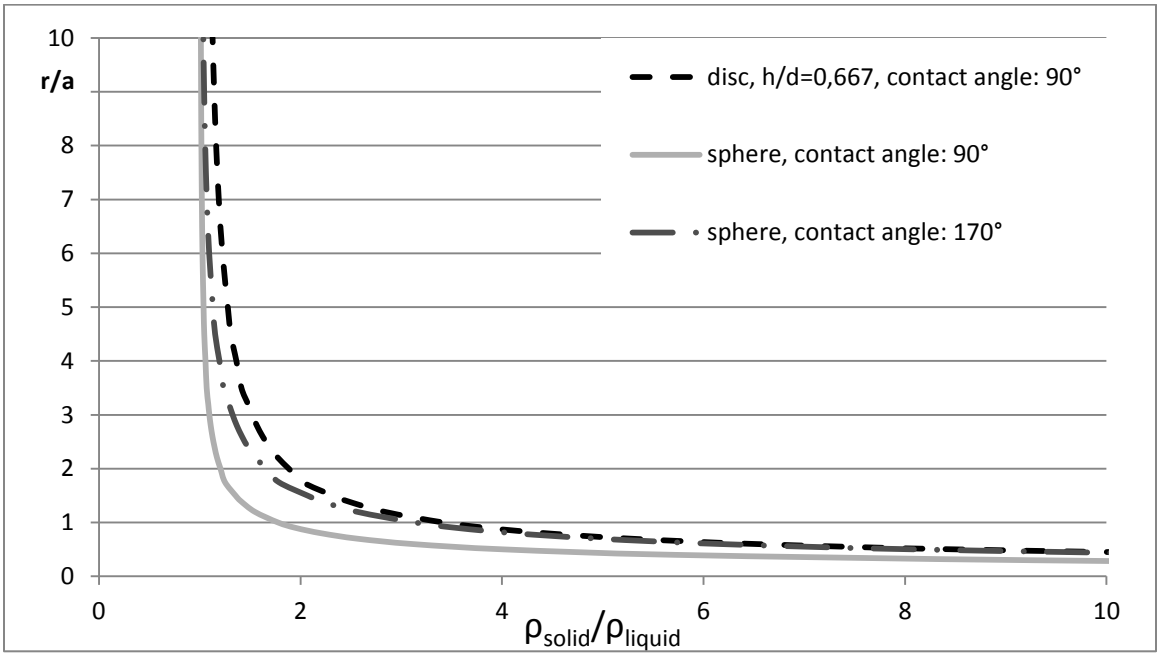

Figure 19: Dimensionless flotation limit, as maximal radius, with different contact angles and geometries

A sphere with 90 °contact angle is closer to a sphere with larger contact angles at low density. For larger spheres with higher densities, the flotation limit is closer to a disc with the same volume and contact angle.

2.2.2 Flotation limit on cryolitic bath surface

For predicting the behavior of solid disks and spheres on the upper surface of the bath, the flotation limit was calculated for 30° contact angle (link chapter with contact angle measurement). The effect of the small contact angle is more prominent for the flotation limit of spheres than for discs. Discs would always have a higher flotation limit than spheres with the same volume and diameter. As the height-diameter ratio decreases, the discs get thinner, the curved surface's contribution to the buoyant force becomes more prominent, as can be seen in the increase of flotation limit with decreasing height-diameter ratio (Figure 20).

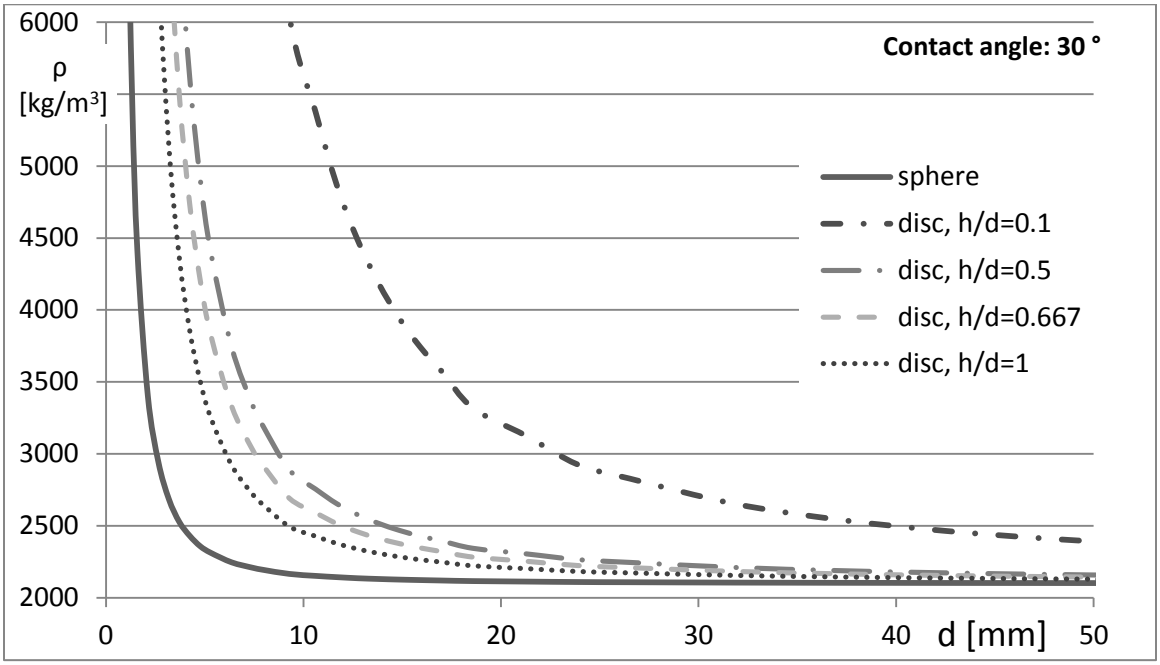

Figure 20: Flotation limit on bath surface, contact angle: 30°

Alumina powder tends to spread widely on the bath surface due to its moisture content that evaporates when it gets in contact with the molten electrolyte (link the part in next chapter). Therefore, discs with small thickness-diameter ratios hold the most interest. The bulk density of alumina powder is around 1 g/cm^3, while the skeletal density of alpha alumina is almost 4 g/cm^3. While cylindrical agglomerates with large height-diameter ratio could be expected to float if they are only a few mm in diameter, thin rafts could theoretically stay afloat easily.

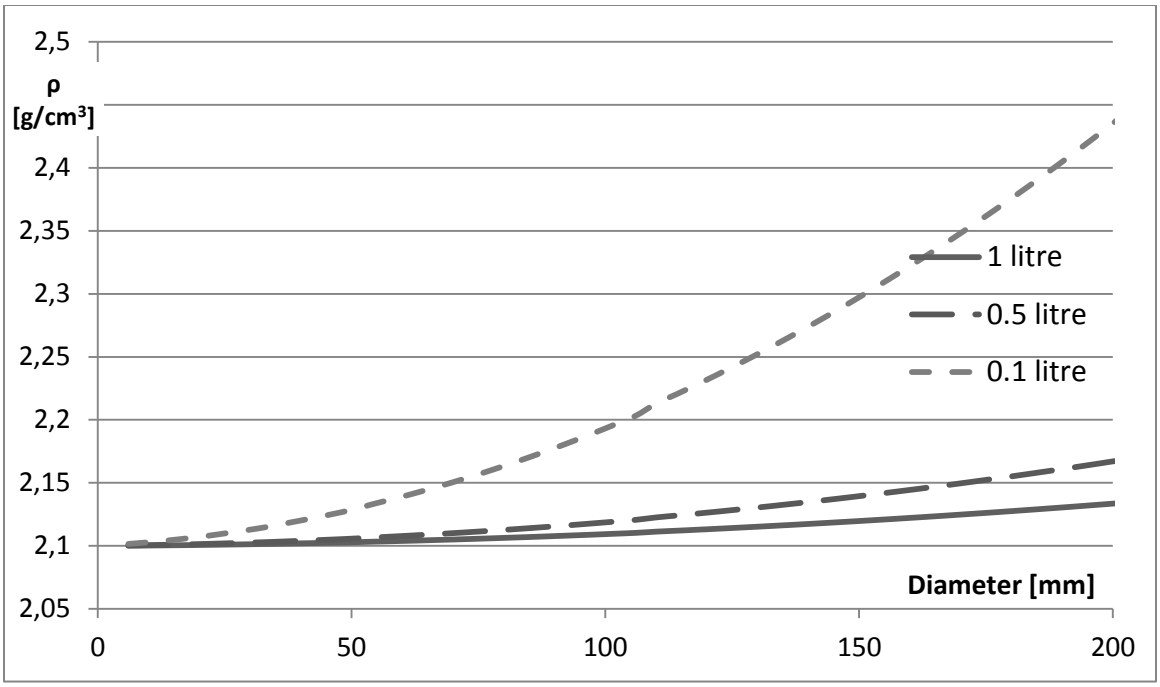

Figure 21: Density limit of a fixed volume of alumina raft, assuming spreading to disc-shape

In industrial electrolysis cells a certain quantity of alumina powder is injected to the bath surface at a time, usually between 0.5 and 2 kg, which corresponds to 0.5-2 l of volume. This powder tends to spread on the available surface, limited by the anodes. With these considerations, the density limit of flotation was calculated for disc-shaped alumina rafts (Figure 21). While the density of larger rafts could only slightly exceed the density of the bath before sinking, with smaller batch-sizes, the maximal density increases rapidly with the available surface for spreading.

Due to the asymmetrical shape of a real raft and the disturbances in the bath, the flotation limit predicted by the model is only theoretical, except for one certainty: the raft cannot sink until its density reaches the density of the bath (2.1 g/cm^3) which corresponds to 50% of the pore volume infiltrated; assuming the packing and the skeletal density did not change. 100% infiltration with the same conditions would result in a density of 2.6 g/cm^3. In this range, the diameter and thickness both have a significant effect on floatability.

The contact angle has less effect on the flotation limit of discs than on spheres, because the discs would hang on the liquid surface at the same triple line, the contact angle would only influence the curvature of the surface at that point. The shape of the meniscus at the flotation limit of a disc with a certain diameter is not influenced by its thickness, therefore the density limit increases with decreasing thickness. Even if the resultant force of the surface tension is neglected, if the thickness of a disc equals the meniscus height, the buoyant force is doubled, so its density can be two times of the density of the liquid.

2.3 Comparison of model with experiments on bath surface

The experimental setup and detailed description and analysis of different phenomena, regarding the flotation of alumina rafts on the cryolitic bath surface, are discussed in the following chapters.

2.3.1 Compressed alumina discs

The experiments proved that alumina discs can float on the surface of the cryolitic bath, even when their density became larger than the density of the bath, therefore the surface tension can play a role in the delayed dispersion of alumina in the bath. In the evaluation of the experiments, the mathematical model of flotation is used reversibly. When modeling the flotation, the maximal density of a floating object was calculated, based on its size and the contact angle. For the experiments, the density and dimensions of the floating discs are known, which, with the help of the mathematical model, provides the angle of the surface at the contact line, at the moment the disc was removed from the bath – and that points to the minimal contact angle (Figure 14). The discrepancy between the estimated and measured density are due to the fact that the discs were covered with an uneven layer of frozen bath, partly due to the removal process. As the estimated volume was based on the diameter and thickness of the discs at their bottom corners, the volume was underestimated. While for the measurement of the volume with Archimedes method, the total volume was measured, including the added frozen bath, which adds to the volume, and, at that point of infiltration, decreases the overall density.

While the contact angle between alumina and bath was measured to be around 30° (3.3.1) using the Wilhelmy method with an alumina rod, with the discs, only 10° was reached at best. This could be explained by several factors relating to the realities of experimentation, such as the lack of a well-defined, sharp edge of the discs, slight asymmetries in either the alumina discs or the setup, and the continued exposure to disturbances, the convection in the bath, and manipulations around the setup.

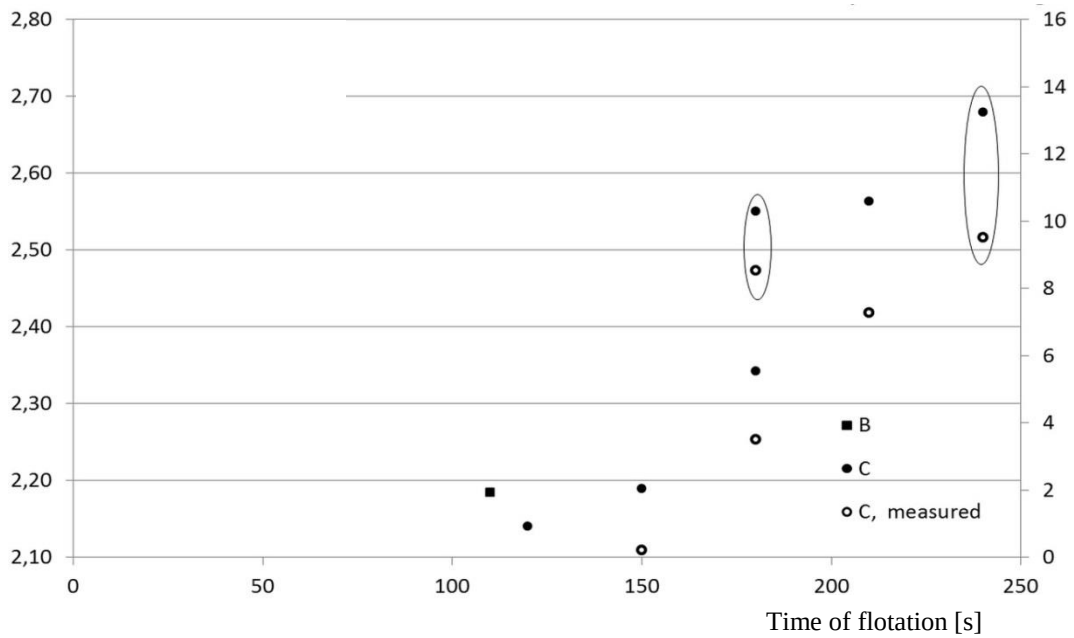

Figure 22: Density of samples, results from repeated experiments B and C

The experiments with compressed alumina discs are presented in greater detail later (4.1.1).

2.3.2 Alumina spheres

Attempts have been made to validate the flotation limit of alumina spheres on the bath surface. Porous alumina spheres had been successfully placed on the bath surface on stable floating position (Figure 23). However, the tests with solid alumina spheres failed, probably due to the lack of precision of movement, required to place a dense sphere to its stable floating position. The bath solidification at insertion and removal also made manipulation difficult, and this line of study has been abandoned.

Figure 23: Placement and flotation of porous alumina sphere (desiccant) on cryolitic bath surface ©Csilla Kaszas

2.3.3 Gravimetric tests

The gravimetric system is decribed in the next chapter (3.1.4), along with certain results (contact angle measurement, effect of frozen bath).

While in the flotation model, the sought paramters are those at the limit of flotation (largest density, largest size), for the gravimetric system, the test object's parameters are known. But using the same equations, the forces acting on the object, depending on its level of immersion can be calculated. And the measured apparent mass of an object, gradually descended into a liquid can be compared to the resultant force calculated by an adapted form of the flotation model.

3 Alumina raft formation– shape and role of surface tension

The shape of an alumina raft has an immense effect on its floatability. As the immersion progresses, the shape determines the length of the triple line, the angle of the liquid surface and the buoyant force.

Experiments with alumina powder and cryolitic bath had been conducted in the laboratory of GRIPS UQAC. The description of the set-up is the first part of the present chapter. The results are discussed in the present and the following chapters, according to the structure of the document.

The second part of the chapter discusses the injection of powder into liquid, specifically alumina powder into cryolitic bath, to analyse the governing effects in the process of raft formation and in the shape that a raft ultimately takes.

The third part concerns the surface tension-related aspects of flotation, including the contact angle measurement between alumina and cryolitic bath.

3.1 Description of the experimental setup

As several experiments were conducted in very similar conditions, the setup for the high temperature experiments in the cryolitic bath is presented here. The same setup with the same conditions were used for most of these tests – if not, it shall be indicated.

The high temperature experiments were conducted at the laboratory of GRIPS, UQAC, in a carbon crucible. The free surface of the bath was 7.6 cm x 7.6 cm square with rounded corners. The depth of the bath was 3,8 cm. The prepared bath contained 83% cryolite, 11,5% AlF_3 and 5,5% CaF_2. Due to initial impurities and the sequence of the experiments, the content of alumina varied, usually between 1.5 and 6%. The increasing alumina concentration, as a natural consequence of experimentation with alumina injections, resulted in the decrease of the liquidus temperature (Figure 24). In the early stages, a furnace fabricated by our technician was used, until it was upgraded to a kiln manufactured by Paragon Industries. The rectangular carbon crucible was heated from two (or later, three) sides, the thermocouple for the temperature control placed under the crucible. The insulated cover from the top was removed during experiments, and replaced between tests so the temperature could stabilize. For longer experiments, to reduce the heat loss towards the open surface of the bath, the opening was covered with a quartz plate between manipulations to be able to observe the test object on the bath surface. The control temperature usually was set to 980 °C, which decreased after the removal of the cover. Occasionally a thermocouple was inserted in the bath and it showed approximately 10°C less than the controller.

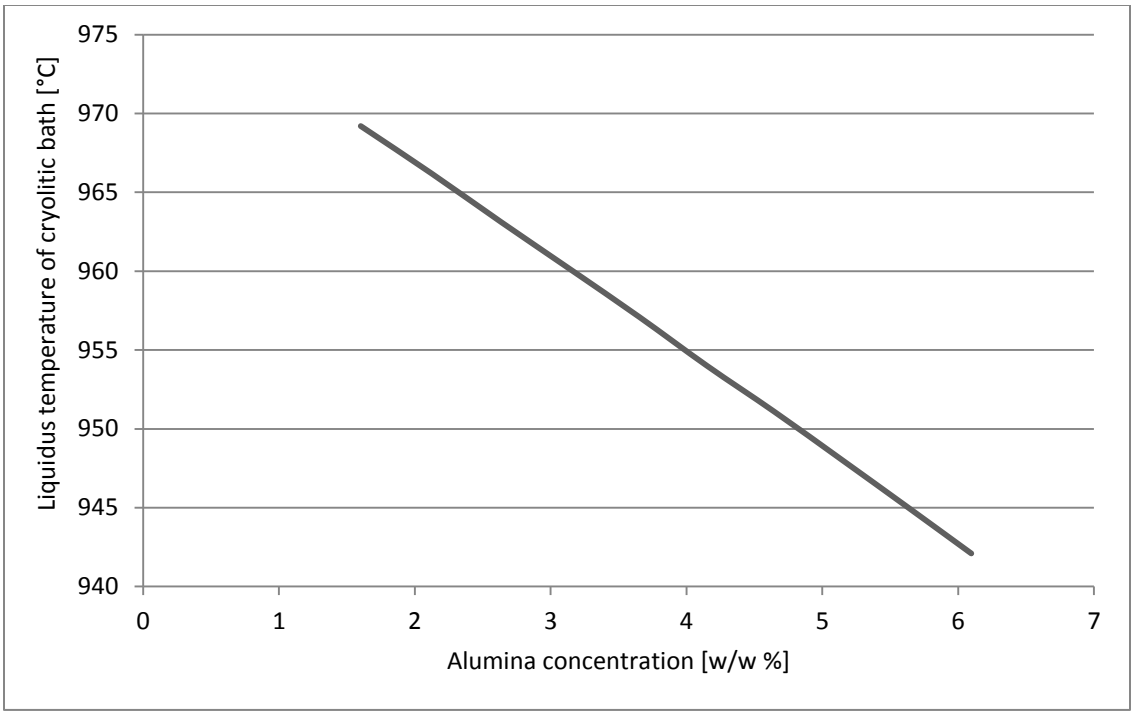

Figure 24: Liquidus temperature in the experimental setup (FactSage)

Despite the troublesome temperature instability of these small-scale experiments, this size provided a cost-effective way to observe alumina on the surface of cryolitic bath, an opportunity to conduct various experiments in relatively large number, and easy access for the manipulation of the samples in the bath. Even if we cannot give the exact value of the superheat, the experiments were conducted in very similar conditions.

3.1.1 Smelter grade alumina

Unless indicated, primary smelter grade alumina (SGA) was used in the cryolitic bath, provided by Rio Tinto. The alpha-alumina content of the SGA was measured to be 2-4%, in the laboratory of Rio Tinto. The content of impurities is presented in the table below, determined by XRF analysis (Table 2: Impurities of SGA). The grain size distribution was determined by sieving in the GRIPS laboratory (Figure 25).

Table 2: Impurities of SGA

Impurities of tested SGA,w/w %								
SiO_2	Fe_2O_3	Na_2O	ZnO	CaO	V_2O_5	TiO_2	P_2O_5	F
0.0184	0.0137	0.3709	0.0006	0.0404	0.0007	0.0023	0.0006	<0.0806

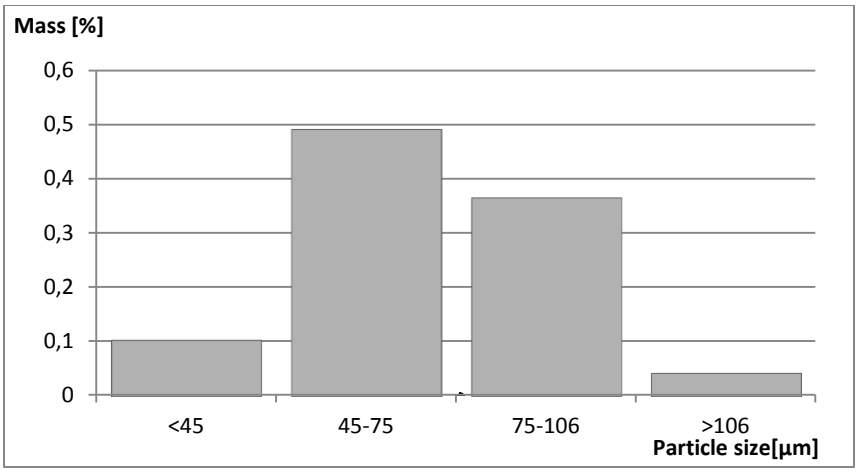

Figure 25: Particle size distribution of smelter grade alumina

The BET surface area was measured at 75 m^2/g; determined with nitrogen adsorption with a Tristar II Porosity Analyzer, at Laval University.

3.1.2 Alumina injections with video recording

Alumina powder was injected onto the cryolitic bath surface from a conic steel feeder, constructed for this task. The diameter of the drop tube was 11 mm, the injection height 5 cm.

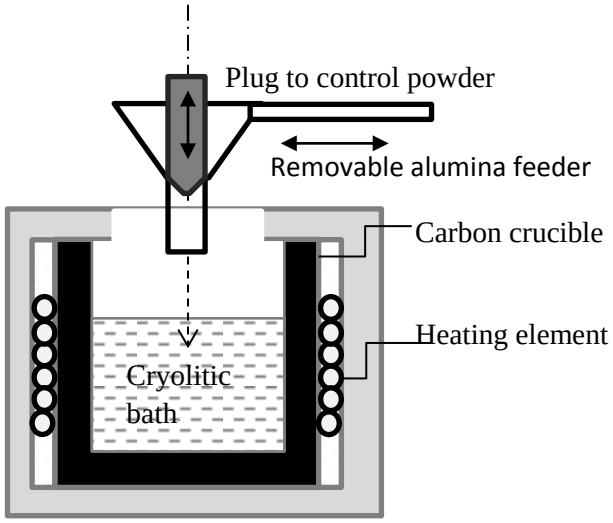

Figure 26: Sketch of experimental setup for alumina powder injections ©Csilla Kaszas

The injections and their aftermath were recorded with a camera installed above the crucible. This setup permitted full view of the bath surface after the removal of the feeder. On certain occasions the alumina rafts were removed and subjected to further analysis.

3.1.3 Compressed alumina discs as artificial rafts

Primary alumina discs (with 40mm diameter and 8.6 mm thickness) were prepared using a Struers Labo-Press 3 machine. 12.5 ml powder was fed into a steel mold, and exposed to 50 kN for 15 minutes which included a 3 minutes initial period where the powder was heated to 180 °C. The produced discs were very fragile, they crumbled easily and some powder got lost every time they were handled. For this reason, a separate batch of discs was prepared only for the statistical analysis of the properties of the discs. The average mass of a dozen discs was 13.4g, with a deviation of +/- 0.2 g. The average mass loss after four manipulations (for example: taking it up and putting it on a scale would count as one manipulation) was 1.2%. The average thickness of the discs is 8,6 mm, with a deviation of +/- 0.1 mm. The apparent density derived from these measurements was 1.25 g/cm^3 – while the measured bulk density of non-compressed alumina powder used for the preparation of discs was 1.03 g/cm^3, calculated by measuring the mass of a given volume of powder.

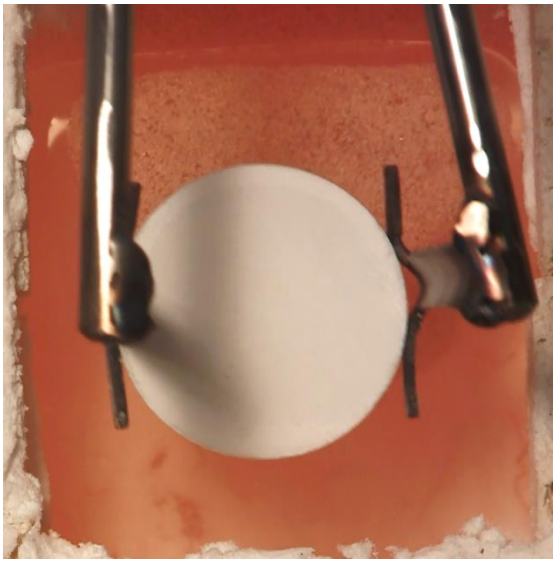

Figure 27: Insertion of alumina disc onto the bath surface ©Csilla Kaszas

3.1.3.1 Course of experiments

The compressed discs were carefully placed on the surface of cryolitic bath, and after a certain period of time, they were recovered. Both the insertion and the recovery were executed with tongs specially designed for this task. The quartz plate covering the top of the crucible became hazy rapidly after the insertion due to the deposition of vapor emitted by the bath, so it was changed frequently to maintain the visibility of the floating discs. Recovery was the most challenging part of the experiment. A careless movement could cause premature sinking of the disc, or it could slip and fall back into the bath.

The samples obtained this way have been weighed and broken or cut up along the diameter for observing the infiltration front with a Digital Microscope. Some of the samples were analyzed with a Scanning Electron Microscope (SEM JEOL JSM 6480 LV with EDS Oxford SiLi detector and

Inca software). The apparent density was estimated by measuring the thickness and diameter of the discs, assuming a perfect cylindrical form; while in some cases, samples were covered with a silicon-based spray to obtain density with Archimedes method.

3.1.3.2 Reasoning

Using compressed alumina discs as artificial rafts eliminates the dynamic effects of the injection and provides slightly denser rafts, but it results in easily comparable samples. The physical and chemical processes after the insertion are essentially the same in both the artificial and the real rafts. The main difference is that the particles are mechanically locked from the beginning. Although there is not a strong bond between the particles, the discs are quite fragile and disintegrate easily during careless manipulation. In spite of their fragility, the conversion of moisture content into vapour did not have an effect on the raft's shape and integrity. In the compressed discs, the rate of vapour escape is slowed down by the diffusion through the porous structure. Due to the compaction of the particles, the bonds are stronger than it would be in a real raft after sintering. That being said – since the initial mass, density and geometrical form of these artificial rafts are well known – they are excellent for the verification of models of the evolution of rafts, aiding the development of models towards a more realistic representation of describing looser and more irregular rafts.

3.1.4 Gravimetric system

A gravimetric system was developed by GRIPS at UQAC to analyse different aspects of the behavior of alumina in the cryolitic bath. Different test objects were suspended above the bath. These samples were descended at a predetermined velocity into the bath while their apparent mass was measured via a load cell. Both the position and the apparent mass were recorded simultaneously. Due to the high temperature of the bath, the load cell was placed at a significant height, and it was also protected by heat shields. On the other hand, the heat loss from the bath did not preheat sufficiently the samples, therefore in certain cases a heating coil was installed above the bath surface to prevent bath deposition on the test objects, biasing the analysis.

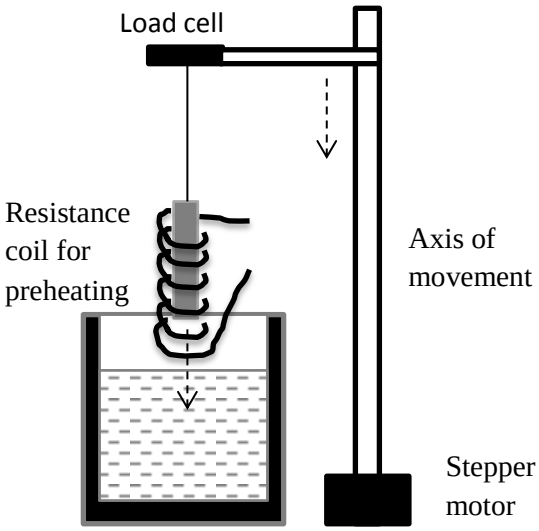

Figure 28: Schema of gravimetric system ©Csilla Kaszas

The apparent mass corresponds to the resultant force acting on the test object. It is equal to its mass before the object reaches the surface, and then, the buoyant force and the resultant force of surface tension influence the measurements, as seen in the flotation model. Furthermore, the mass gained by bath solidification or deposition on the test object, and mass loss caused by dissolution or disintegration of the samples also influences the measured apparent force.

The history of position and apparent mass evolution in time had been analysed to extract information.

3.2 Injection of SGA – Raft formation and shape

In a pot room, the alumina powder is dumped from a hopper above the cell. The feeder design might vary; it might let the powder fall down vertically or have a slanted lower section to direct the powder to the hole below the crust breaker. SGA arrives onto the surface as a jet of powder. Like a solid object, the powder may float or sink, but unlike a solid object, a batch of powder will change its shape like a fluid, according to the forces and pressure it is subjected to. It can also change its apparent density due to infiltration, and size due to disintegration even before all of the powder could reach the surface.

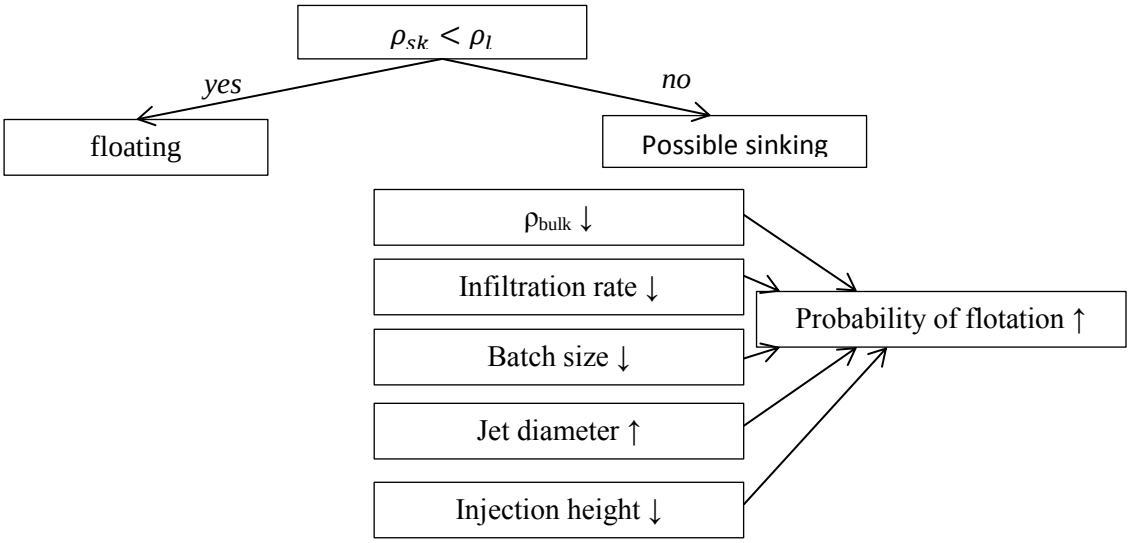

Figure 29: Schematic description of flotation behaviour of powders on the surface of liquids ©Csilla Kaszas

A powder would only surely float if its skeletal density ρ_{sk} is less than the density of the liquid it is fed into. Otherwise, the characteristics of the injection and other properties of the powder would influence the outcome (Figure 29). Smelter grade alumina has a low bulk density which favours flotation; and the low superheat of the bath and the low temperature of the alumina ensure bath solidification in the vicinity of the added powder that hinders infiltration.

Slow infiltration rate can be a result of large contact angle: cocoa powder for example has a high fat content therefore it is not wetted by water and does not mix readily with it – hence the popularity of instant cocoa powders that can achieve rapid dispersion with additives. Another well-known example for the clumping of powders is flour. Starches expand when they absorb water, effectively blocking the pathway for the liquid.

Bath solidification if different in two important ways:

- it hinders the infiltration only temporarily, when the raft warms up the infiltration continues;
- it preserves the shape of the raft.

Experiments with analog models, including different injection temperatures of the powders to simulate bath solidification are presented in detail in chapter 5.3.

Although shape-preservation is started by bath solidification, it is consolidated later on by sintering in SGA. Another peculiarity of SGA is the evaporating moisture content of alumina that expands and fluidises the powder upon injection.

3.2.1 Injection of alpha alumina – effect of bulk density

Historically, floury alumina with high alpha alumina content had been used in European smelters. Nowadays, high gamma content is the norm for the industry, the differences between the behaviour of alpha and the transitional phases still merit a discussion in the field of research.

The density of alpha alumina is almost 4 g/cm^3. It forms solid particles without internal porosity. Therefore, if we assume 40%-45% void fraction, the bulk density of alpha powder is 2.4-2.2 g/cm^3.

Alpha alumina is known to sink in the cryolitic bath (1.3), and undoubtedly, a density higher than the density of cryolitic bath (2.1 g/cm^3) would favour sinking, while SGA with a bulk density around 1 g/cm^3 would favour flotation. If a jet of powder with sufficiently large velocity pierces the bath surface and submerges, the apparent density of the agglomerate would determine if the agglomerate would sink or resurface (Figure 30). Alpha alumina would sink, gamma would likely resurface, and if the feeding continued, it could stop the fall of the following batch and prevent submersion altogether. This phenomenon was observed in an analog setup (5.3.3).

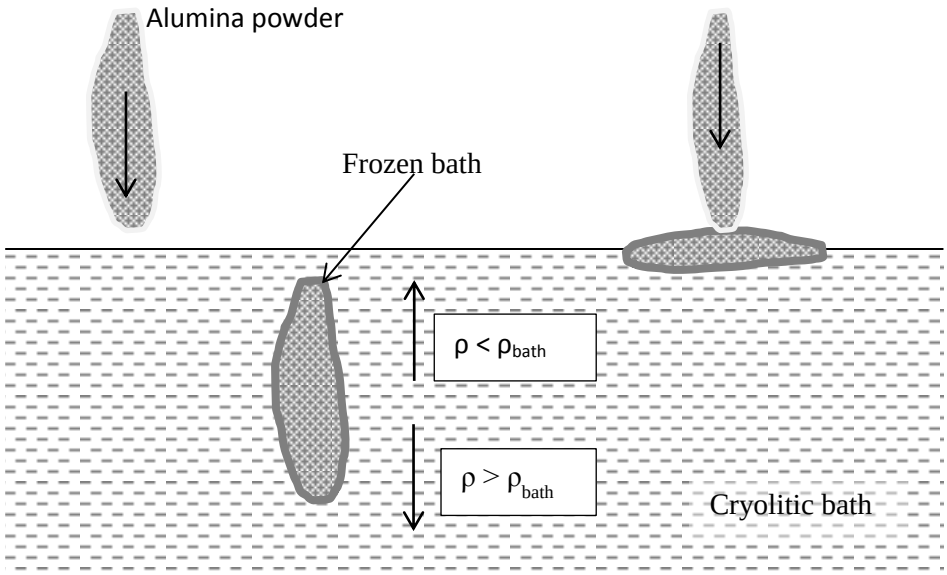

Figure 30: Powder injection, effect of density ©Csilla Kaszas

However, that it is not to say, alpha alumina could not float. Small quantity of alpha alumina powder fed from a low injection height could and would float on the bath surface, if not as long a raft of SGA (Figure 31).

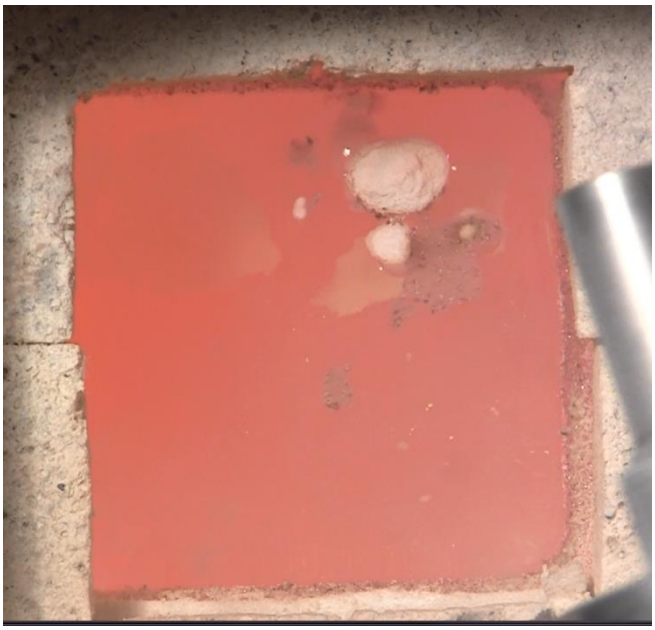

Figure 31: Alpha alumina raft on cryolitic bath surface (2.5g) ©Csilla Kaszas

When the kinetic effect of the impact is not prominent, and there are no additional forces at work, the shape of a raft can be described as shown below (Figure 32). As the powder reaches the surface, it sinks deeper in it and spreads to the side, forming a heap like on a flat surface. A powder with a larger bulk density would exert more pressure on the bottom of the raft, similarly to a liquid droplet on a liquid surface; the increasing density would push the middle of the raft deeper in the surface.

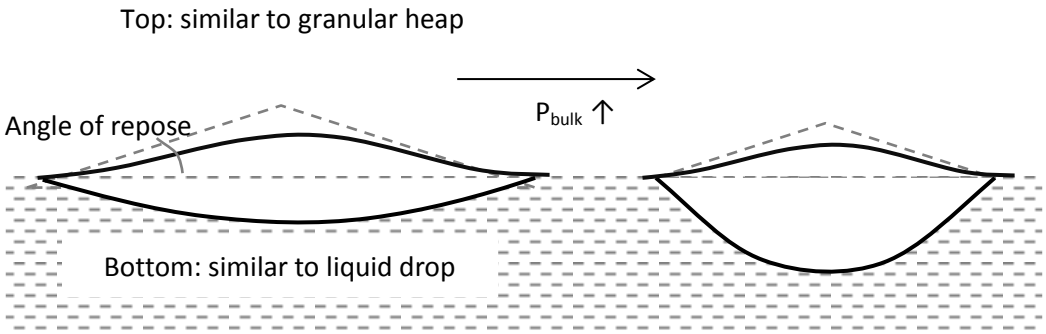

Figure 32: Shape of powder on liquid surface, effect of bulk density ©Csilla Kaszas

For free-flowing powders, the edge of the raft is spread thinly. In the early stages of raft flotation, the liquid surface would attach itself to these sharp edges where the angle of the surface has a degree of freedom. The surface tension acts along these extremities and the shape

of the raft has little effect on the flotation behaviour – this explains why we use the disc geometry in the flotation model.

3.2.2 Particle size/fines

Alpha alumina however, does not differ from sandy alumina only in their bulk density. The particle size distribution of primary smelter grade alumina is obtained during its production. Longer, higher temperature calcination results in higher alpha alumina content and finer particles – but it is not to say that high content of fines necessarily indicates high alpha content – it can also be the result of the attrition of large particles of transitional phases, which occurs during transportation and the dry scrubbing process. Another possible reason for high fine content is segregation; the separation of granular material induced by variance in size and density of particles, which can lead to the accumulation of fines at certain locations.

Smaller particle size leads to larger surface area, and the cohesive forces between the particles are more prominent. Even if not all the particles are small, the fines can jam and block the movement of larger granules, effectively increasing the angle of repose. Increasing angle of repose reduces spreading of the injected powder, resulting in smaller raft surface, shorter triple line, larger relative thickness, ultimately less floatability.

The influence of particle size will also be presented in an analog model at a later chapter (5.3.2).

3.2.3 Effect of moisture content on the shape of alumina rafts

A phenomenon, disregarded in the previous sections, is the evaporation of the moisture content of the alumina.

The volatile content of SGA has been discussed in chapter 1.1.4. Besides moisture and structural hydrogen, secondary smelter grade alumina also contains fluorides. Hydrogen-fluoride desorption occurs at a high temperature, therefore it is expected to effect the structure of the alumina raft, but not their shape; to be discussed in the next chapter (4.2).

For the images presented below, alumina powder was fed onto cryolitic bath surface, in 14 g doses. Some of the alumina had been dried beforehand at different temperatures for 16 hours (overnight), then covered, cooled and stored in airtight containers at room temperature until the experiment. The injections were filmed from a top view; the rafts were recovered from the bath 45 seconds after the injection. The experiments with each type of powder were conducted consecutively, in a saturated bath.

Water desorption occurs in two waves, first physically adsorbed water around 100 °C, then chemisorbed water around 300 °C. This is in accordance with observations in a separate set of experiments (4.1.2). The differences between the behaviour of alumina that had not been dried previously and alumina dried at 150 °C, cannot be observed at full extent, due to the limited size of the surface of the bath. Both of these powders spread completely over the available surface.

In both cases, some dusting was observed as the rapidly escaping vapour blows the alumina in every direction and the fines settle at a slower rate. This effect is more prominent in the case of non-dried alumina (Figure 33). The vapour practically flattened out the rafts both on their tops and bottoms (Figure 34).

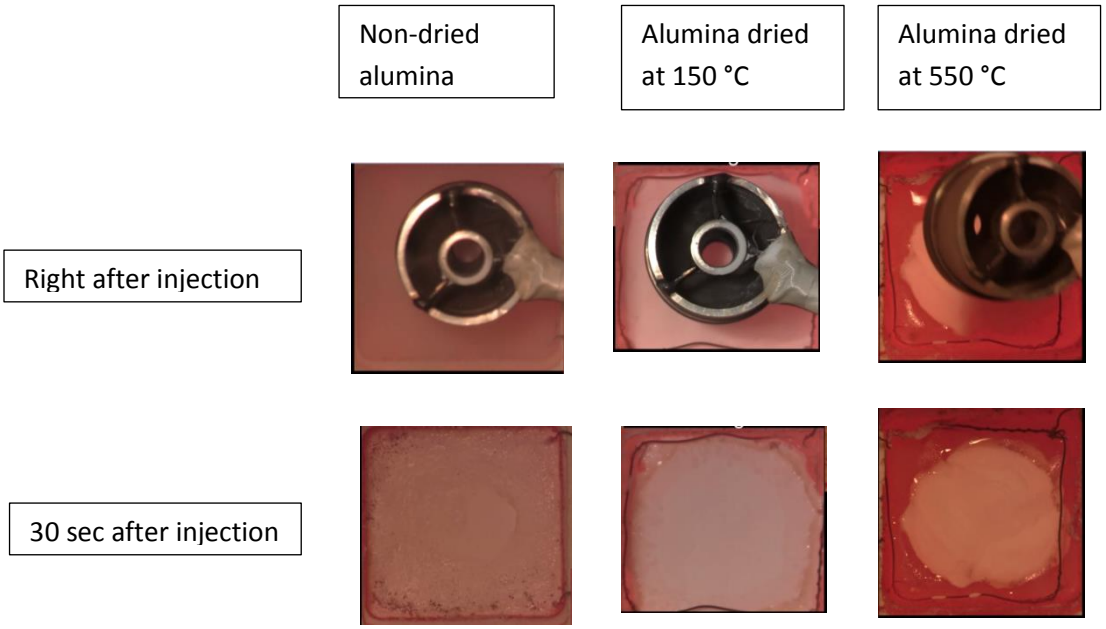

Figure 33: Alumina rafts on bath surface, influence of moisture content ©Csilla Kaszas

Alumina, dried at a higher temperature, spread the way it had been formerly discussed, the bottom sunk into the liquid surface as a saucer, while the top formed a heap. On the presented photo (Figure 34), the raft floated sideways during the injection of alumina powder, therefore not one but two depressions can be observed on the raft's bottom. Besides the shape of the raft, the moisture content also influenced their structure, which shall be discussed in the next chapter (4.2).

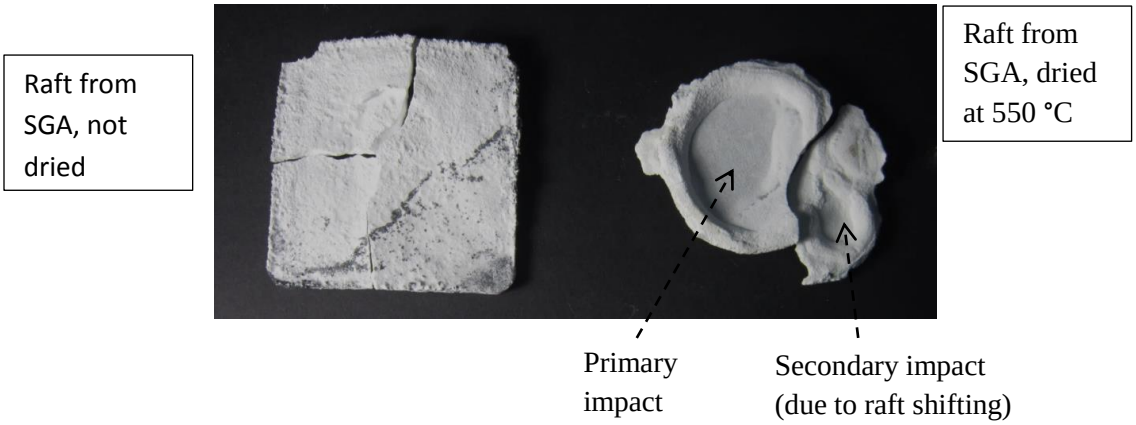

Figure 34: Alumina rafts removed from bath after 45 seconds retention time, (Loose alumina powder from dried alumina rafts was removed) ©Csilla Kaszas

Although it could not have been observed directly in the present experimental setup, the formation of a cloud of alumina particles below the bath surface can be observed upon the injection of powder in transparent crucibles. The phenomenon was also recorded by a former student member of GRIPS, Antoine Molin, though it remained unpublished. This initial rapid dispersion in part might be attributed to the dynamic effect of the injection. However, it also stands to reason that just as the escaping vapour moves alumina particles above the liquid surface, it would send other particles downwards and sideways, towards the bath simultaneously to bath solidification (Figure 35).

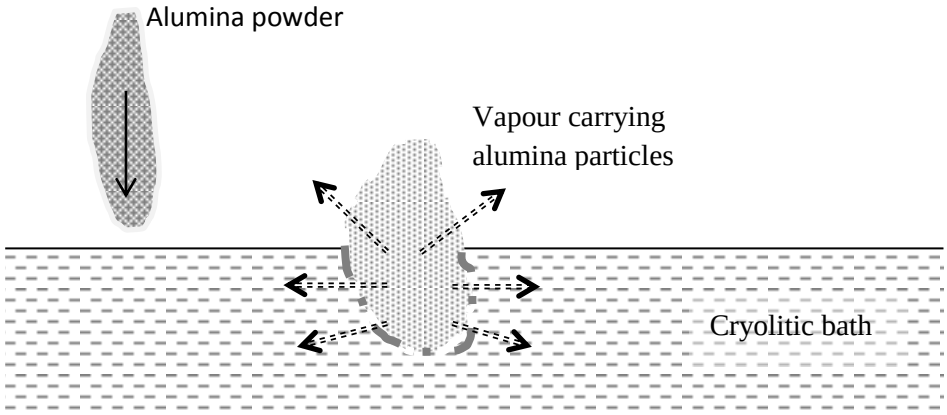

Figure 35: Effect of moisture content of alumina upon injection into cryolitic bath ©Csilla Kaszas

If the evaporation were slow, the steam would travel by diffusion in the pores and leave the batch of powder without disturbing a particle. If it were faster, but still relatively weak, the

pressure would build up to a level that it would displace the powder at the point of least resistance and some gas would escape relieving the pressure. This can be observed as the so-called geysers or volcano effect in industrial cells: around a blocked feeder hole, the steam from below blows the powder upward from at a few unchanging locations, either continuously, or as the quantity of volatiles and the rate of evaporation decreases, periodically (Figure 36).

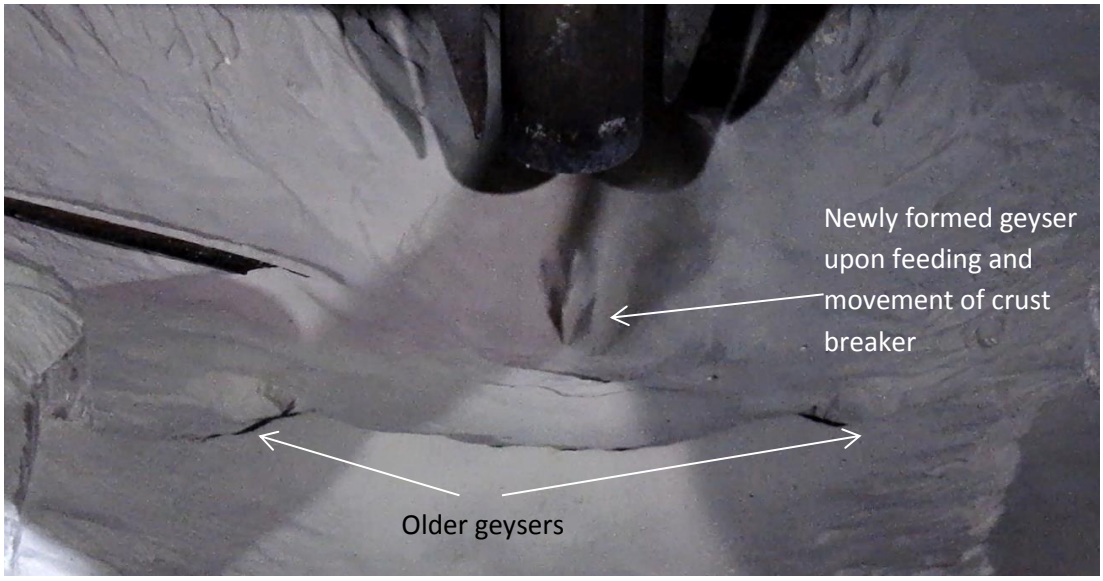

Figure 36: Geysers around a plugged feeder hole, image from a video taken at RTA plant by an employee, 2011

At the few seconds following the injection, the evaporation is so rapid that the gas cannot be released fast enough upwards only, the vapour escapes in all directions, even though through the liquid, sending the batch of powder both upward and below the liquid surface. This means that the moisture content does not only influence the shape of the raft, but also results in the instant dispersion of some of the powder, and the resulting raft contain less alumina than that was initially added.

It should be noted that during the experiments with artificial rafts (3.1.3), the discs were not damaged by the escaping vapour. After placing the compressed alumina discs onto the bath surface, they kept their shape, even though they were quite fragile and crumbled easily when handled carelessly. The evaporating moisture was present and the escaping jets moved the disc around in the bath vigorously after insertion, but did not break the integrity of the discs (Figure 37). Although some experts might refer to the effect of vapor as `explosive` as it certainly can blow apart or fluidise loose powder and agitate the bath and the disc, according to our observations, its effect is not as strong as that expression would suggest.

Intense bubbling right after insertion Occasional bubbles 10 s after insertion

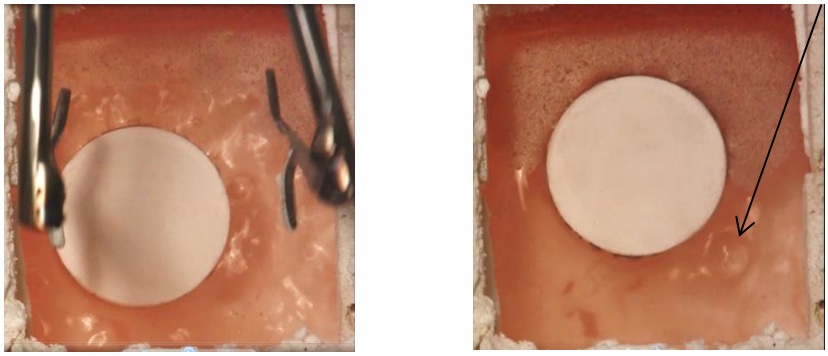

Figure 37: Compressed alumina disc on bath surface ©Csilla Kaszas

Unlike with alumina powder, the vapour was not only leaving on the top surface of the discs, bubbling was noticeable around the artificial rafts as well. The presence of these bubbles in the bath suggests that the evaporating moisture was escaping through the bottom, disturbing or preventing the formation of solidified bath at certain locations.

Figure 38: Sinking of artificial raft
left: view right after sinking - right: removal of disc, top detached ©Csilla Kaszas

The alumina disc presented in Figure 38 sunk without intervention after 4 minutes of flotation time, which is representative for the majority of these experiments. The gas from the un-infiltrated top-center part of the discs burst out from the disc in a second after the sinking, blasting off the top layer (Figure 38). “Explosion” might be an adequate expression for this incident, but since the disc spent 4 minutes on the bath surface, the gas leaving the alumina is unlikely to contain moisture; this explosion was probably caused by the rapid infiltration of the porous material below the bath surface.

3.2.4 Bath solidification

Cryolitic bath with low superheat solidifies readily around the injected cold alumina. The frozen layer not only conserves, but modifies the shape of the raft as well. Its influence on the apparent

density of the raft shall be discussed in the next chapter. Here the focus is on the way the bath solidifies on the bath surface and affects the resultant force of the surface tension.

3.2.4.1 Frozen bath collar

The photo below shows a compressed alumina disc removed from the surface of cryolitic bath (Figure 39). Due to the low superheat and the heat loss at the top of the crucible, the bath froze around the inserted disc, especially at the free surface where a heat loss occurs naturally in the setup. The freezing surface preserves the shape of the meniscus and creates a rim that can be higher than the top of the raft itself. This collar increases the length of the triple line, aiding flotation via increasing surface tension force; but more importantly, the additional volume increases the buoyant force.

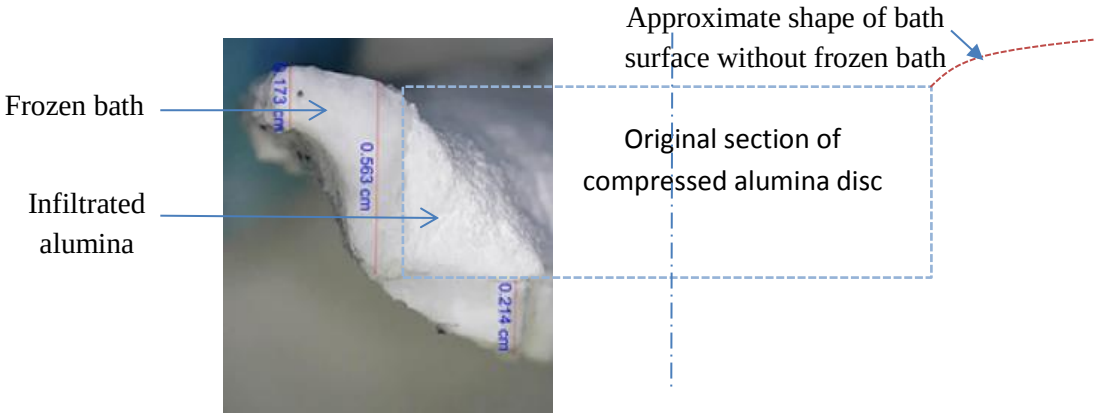

Figure 39: Frozen bath around compressed alumina disc (low superheat) ©Csilla Kaszas

Similar phenomena can also be observed with rafts, created with dried alumina powder, but the separation line between frozen bath and alumina was not as well visible.

3.2.4.2 Effect of bath solidification shown by gravimetric analysis

During gravimetric analysis (3.1.4), when the test object, an alumina rod, was not preheated before the descent into the cryolitic bath, the effect of the bath solidification resulted in a jagged line in the diagram (Figure 40). The bath froze around the object, the liquid held onto the solid collar for a while, until the object was descended too far, and the surface of the liquid jumped up, resulting in a sudden increase in apparent mass (similar to a “stick-and-slip” movement in case of solids). As long as the object was still cold enough, the solidification started again with the free surface sticking to the edge of the frozen bath.

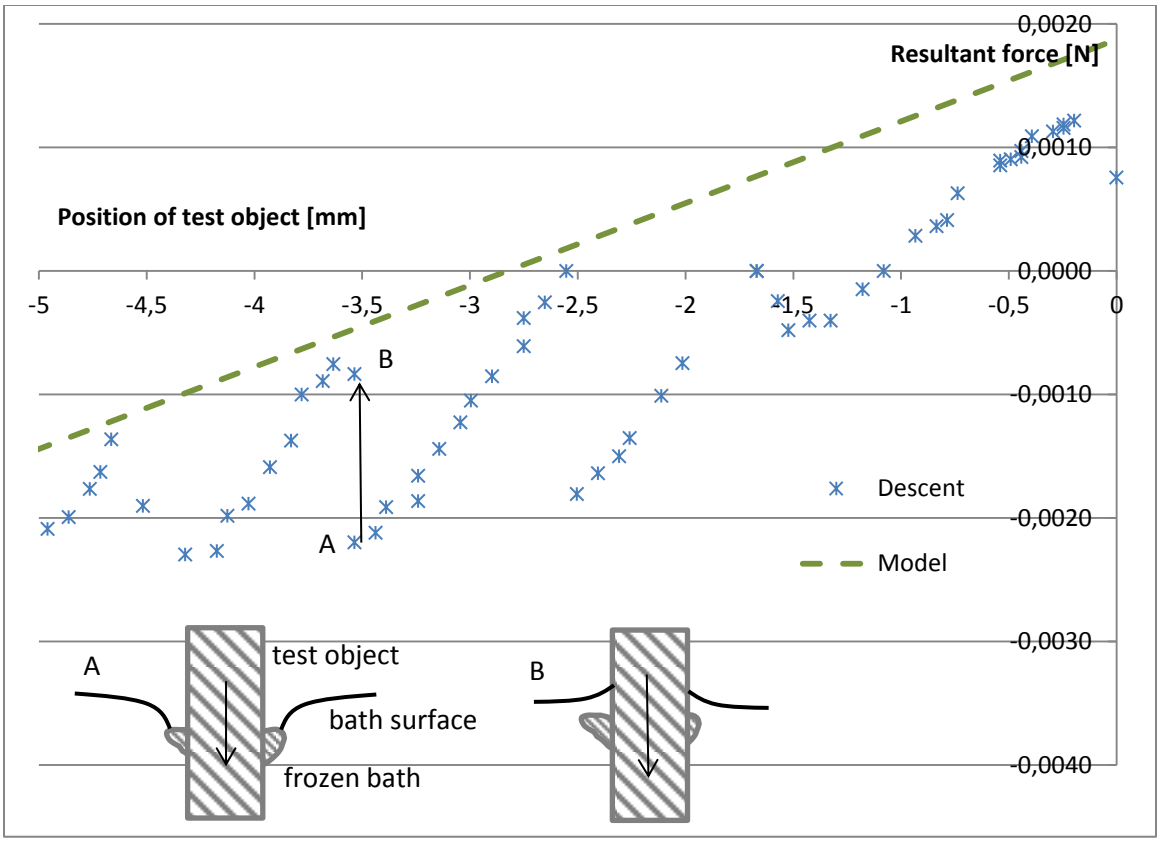

Figure 40 Gravimetric test on alumina rod in cryolitic bath, result vs expected behaviour without solidification

Although the aim of gravimetric analysis was not the demonstration of this phenomenon, since we observed it, we judged it worth for discussion.

3.3 Surface tension

One might assume that as alumina is wetted by the electrolytic bath, the surface tension cannot contribute to the flotation, only the buoyant force keeps the raft on the surface. Undeniably, the low bulk density of alumina powder contributes greatly to the flotation of rafts, but that does not mean that the surface tension does not have part in it, especially in the later stages in the raft's life.

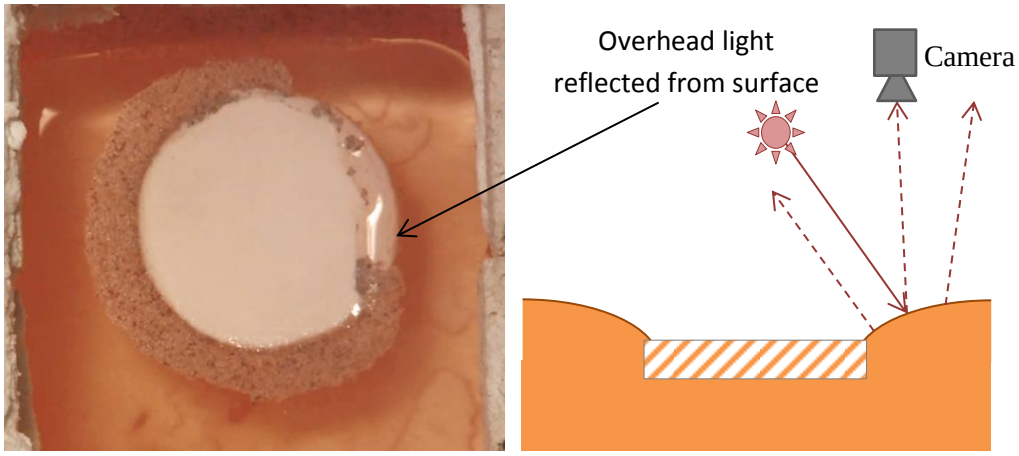

Figure 41: Surface tension of bath can contribute to the flotation of artificial raft ©Csilla Kaszas

The present sub-chapter contains phenomena related to the bath-gas interface – or lack thereof, but first and most importantly, the determination of the contact angle between alumina and electrolyte.

3.3.1 Contact angle

Contact angle is used to quantify wettability; it is measured on the liquid side – 0° if the liquid wets the solid perfectly, 180° for the case of perfect non-wetting. While it is expected that cryolitic bath wets the alumina, the value of the contact angle has not been found in the literature, even though it has a significant influence on the limit of flotation. There are numerous methods to measure the contact angle but the high temperature of the bath poses a significant challenge to them.

Several tests were conducted, trying to place alumina balls on the bath surface to estimate the contact angle with the flotation model based on the floatability of these balls. Dense, slightly deformed alumina balls sunk – but since their diameter was around 5 mm, it could only be concluded that the bath wets the alumina – the contact angle is smaller than 90°. Due to the encountered difficulties in the execution of these tests, other methods were considered to measure the contact angle.

3.3.1.1 Contact angle measurement by capillary rise

In the capillary rise method of contact angle measurement, a tube of small internal diameter is dipped into a liquid vertically. If the liquid wets the solid, it rises into the tube to a certain height, driven by the surface tension at the triple line. In equilibrium, the surface tension holds up the weight of the liquid above the undisturbed surface. The relationship can be described by the equation below.

$$\rho_l \cdot g \cdot H_c \cdot r^2 \cdot \pi = 2 \cdot r \cdot \pi \cdot \gamma \cdot \cos(\alpha_0)$$

Equation 14: Force balance of a liquid column in a capillary tube

Where, H_c is the capillary rise of the liquid in a vertical tube, r is the inner radius of the tube. If all the other properties are known, and the height of the liquid is measured, the contact angle can be calculated as:

$$\cos(\alpha_0) = \frac{\rho_l \cdot g \cdot H_c \cdot r}{2 \cdot \gamma}$$

Equation 15: Contact angle based on force balance in a capillary tube

The capillary rising was tested in ceramic alumina tubes produced by extrusion, with different internal diameters. These tubes are not transparent; therefore, the direct visual determination of capillary rise in the bath was not possible. To counteract this weakness, translucent sapphire (also Al_2O_3) tubes were also tested, in order to be able to adjust and improve the experimentation process. Sapphire is a crystalline form of aluminium oxide; it is more structured and more expensive than regular alumina. Presumably, the wetting properties should be similar.

Composition of test tubes from AdValue Technologies:

Alumina tube: 99.6% alumina, porosity <0.5%

Sapphire tube: >99.98% Al_2O_3 ; polycrystalline sapphire

The capillary rise experiments were conducted with fresh bath (3% alumina concentration) to avoid the interference by carbon particles produced by the degradation of the carbon crucible during the tests.

Another verification method was considered: the insertion of a thin metal wire with the measurement of electrical resistivity between the bath and the wire – which would decrease drastically when the bath reaches the end of the wire. After consideration, this was ruled out because of foreseen precision issues due to wire bending in the tube, and because the wire would have interfered with the capillary rising once the liquid touched it. It was decided that the tube should be cooling with the liquid inside, leaving it to solidify and determining the capillary rise after, at room temperature.

The final setup consisted of a resistance heating wire around the capillary, above the bath surface as shown in Figure 42. The dimensions of the coil were 1 cm of outer diameter, 10 cm of length, and an adjustable support for the alumina tube. The tube was inserted into the spiral, the end dipped below the liquid bath surface, heated for 10 minutes, and then it was descended

deeper in case the bottom was dissolved and the contact between the liquid and the tube needed to be re-established. After another minute, the heating was turned off and the tube was let cooled for the bath to solidify.

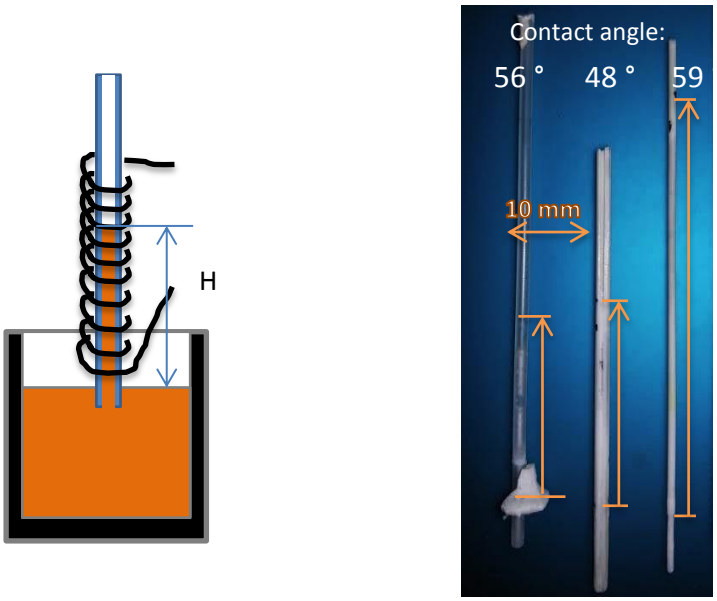

Figure 42: Schema of capillary rising measurement and results of successful experiments ©Csilla Kaszas

Table 3: Capillary rise in alumina/sapphire tubes; calculated contact angle

	Date	Internal diameter [mm]	Capillary rise [mm]	Contact angle
Sapphire	2016.08.23.	0.685	18	64.0
			23	56.0
Alumina	2016.09.07.	0.64	27	52.1
			29	48.8
Alumina	2016.10.25.	0.26	55	59.5
Alumina	2017.12.19.	0.64	30	47.0
			26	53.8

The density and surface tension of the cryolitic bath are known from literature, although they vary with composition and temperature.

Table 4: Bath properties used for the calculation at 960 °C

Surface tension of bath	0,145	N/m
Density	2100	kg/m^3

The capillary rise measurement has certain drawbacks, particularly under the conditions of our interest. The potential errors are the following:

- angle of tube during experiment – if the tube was not vertically inserted, the measured capillary rise is larger than the real value
- Determination of the level of undisturbed liquid – bath curves up around the outside of the tube, undisturbed level is lower than what can be observed on the tube, the measured capillary rise is lower than the actual value
- Properties of tube (uniformity of internal diameter, surface roughness, straightness) – roughness of the surface can result in a higher apparent contact angle and lower capillary rise than the theoretical value for smooth surface
- Shrinking of bath during solidification and cooling – measured capillary rise is lower than the real value
- Exact knowledge of temperature and composition of bath in the tube, influencing density and surface tension

While there is a certain scattering between the results, the effect of most of the potential errors underestimate the capillary rise, so we estimate that the contact angle is most likely below 50 degrees.

Table 5: Sensitivity analysis for contact angle measurement with capillary rise method

Sensitivity analysis		$\frac{\Delta\alpha/\alpha}{\Delta\rho/\rho'}$ $\frac{\Delta\alpha/\alpha}{\Delta H/H'}$ $\frac{\Delta\alpha/\alpha}{\Delta r/r'}$	$\frac{\Delta\alpha/\alpha}{\Delta\gamma/\gamma}$
Date	Capillary rise [mm]	+1% $\boldsymbol{\rho, H, r}$	+1% γ
2016.08.23.	18	-0.44	0.43
	23	-0.69	0.68
2016.09.07.	27	-0.86	0.84
	29	-1.03	1.02
2016.10.25.	55	-0.57	0.56
2017.12.19.	30	-1.14	1.12
	26	-0.78	0.77

3.3.1.2 Contact angle measurement with gravimetric analysis

The gravimetric system was developed to analyze different aspects of the behavior of alumina in the cryolitic bath (3.1.4).

An alumina rod of ¼ inch diameter was suspended by a nichrome wire above the bath surface, preheated to avoid bath solidification upon insertion, and then descended with a velocity of 0.5 mm/s. The position and resultant force were recorded at 1 second intervals.

Before the test object touched the liquid surface (position larger than p_0 - the position where the bottom of the object touches the horizontal liquid surface), the measured force corresponds to its weight. When the object reaches the surface, the resultant force increases rapidly (ΔF),

due to the effect of the surface tension. With further descent into the liquid (position below p_0) the resultant force is reduced by the buoyant force.

$$\boldsymbol{F = m \cdot g + \begin{cases} 0 \; if \; p = position > p_0 \\ d\pi\gamma \cdot \cos\alpha + \frac{d^2\pi}{4}\rho_l \cdot (p - p_0) g \; if \; p \leq p_0 \end{cases}}$$

$$\boldsymbol{\cos\alpha = \frac{\Delta F|_{p_0}}{d \cdot \pi \cdot \gamma}}$$

Equation 16: Resultant force on test object of gravimetric analysis, and resulting formula for contact angle

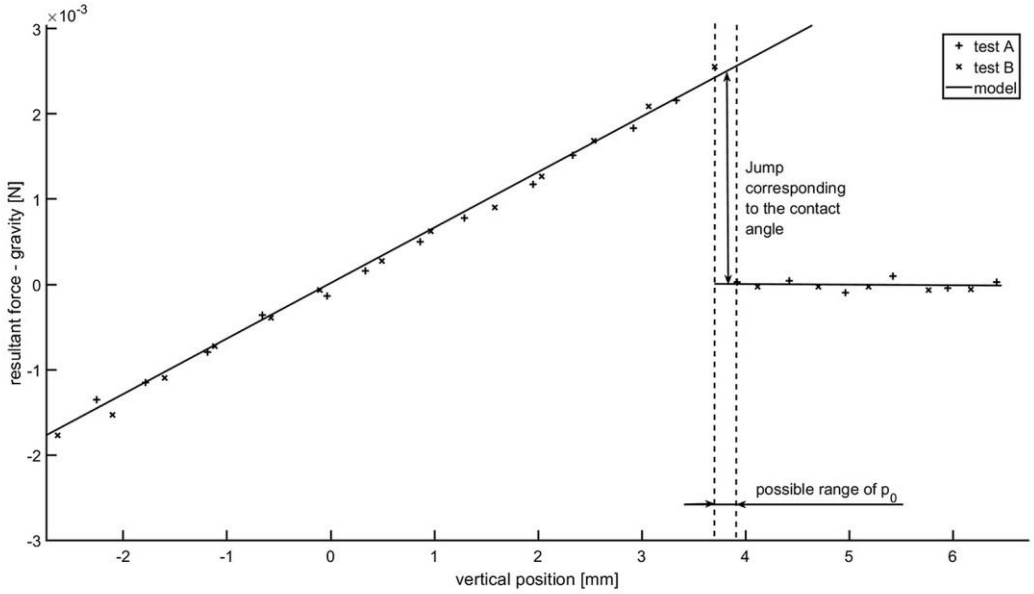

Figure 43: Buoyant and surface tension forces acting on an alumina rod, immersed into cryolitic bath

Theoretically, the contact angle can be calculated from the jump in the resultant force when the rod first touches the surface (p_0, position 0). However, as the data recording is not continuous, the detection of the jump may be delayed by almost a full-time step. To decrease this uncertainty, the results of two tests (A and B) were superposed (Figure 43). Note that as we cannot produce perfectly identical samples, both the resultant force and the zero position need to be adjusted for the superposition. Vertically, one set of results was shifted by the force corresponding to the difference between the initial masses of the samples, while the horizontal shift aligned the left edge of the diagram. This process did not only provide better visual representation, but the exact position of zero was narrowed down significantly. There is a slight noise in the data, but the test results correspond well to the model, and it narrows down the range of the contact angle to an interval of 29-34°.

3.3.2 Roughness of smelter grade alumina

Although the contact angle is an important factor in the flotation limit of alumina rafts, the contact angle between a smooth alumina surface and the cryolitic bath is not necessarily the same as the apparent contact angle between a raft and the bath.

Since alumina is a powder, the roughness can be observed at multiple levels. Alumina rafts exhibit a roughness corresponding to the particle size, so even if the individual particles were smooth, agglomerates at the beginning of their life are not. Furthermore, the shape and roughness of the particles themselves may provide edges for the liquid surface to cling to.

Scanning electron microscope images of alumina particles show that large particles, over 100 microns, have a blackberry-like structure. They seem to be formed as a cluster of smaller (5-50 micron) crystals with hexagonal shape and sharp edges. Fine particles, less than 1 micron, probably mostly alpha alumina, can be observed clinging to the surface of the large particles, that had not been removed by compressed air in the preparation of the sample. (Figure 44)

On the surface of the large particles, cracks or slits can be found, where the evaporating moisture left during the calcination process: the opening of intra-particle pores.

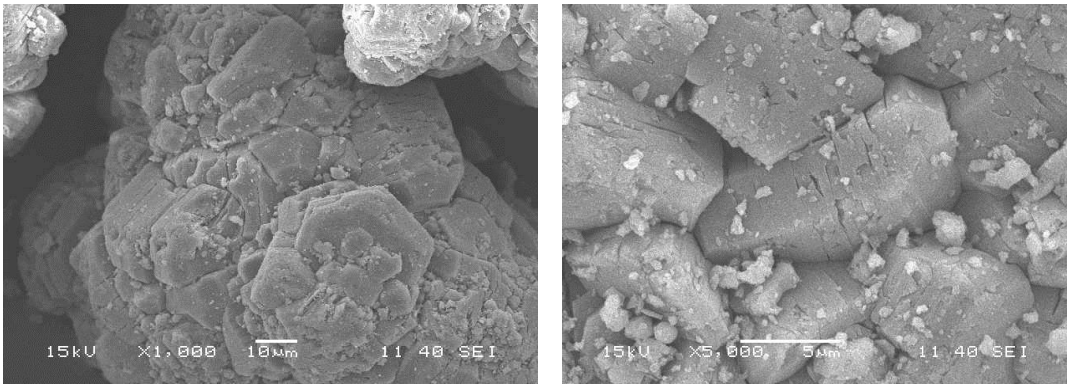

Figure 44.: SEM Images of primary smelter grade alumina ©Csilla Kaszas

The former photos show particles prior to injection. When the hot liquid bath gets in contact with the alumina, it initiates the recrystallization of transitional phases to alpha. The following image shows the edge of an infiltrated artificial raft, with recrystallized alpha-alumina platelets (1-3 micron in diameter, less than 1 micron in thickness) (Figure 45). The blackberry-shape is still recognizable, but the surface is distinctly different. The protruding platelets could provide contact points to the liquid surface to cling onto, increasing the apparent contact angle.

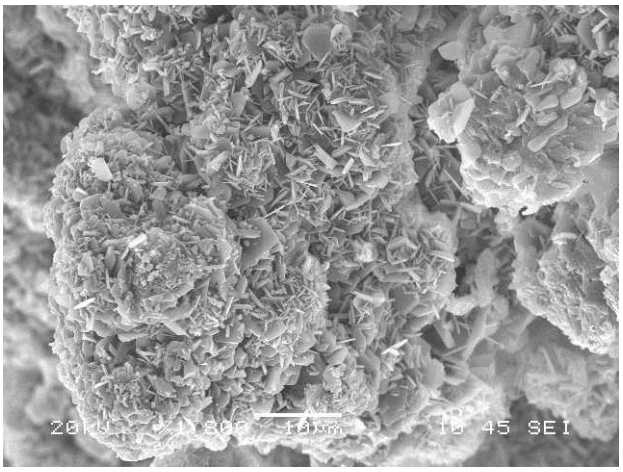

Figure 45.: Scanning electron microscope image of recrystallized alumina at the front of infiltration of a compressed alumina disc ©Csilla Kaszas

The structure of the rafts and recrystallized alumina would be discussed further in the next chapter (4.2). The electron microscope images were made at the UQAC's laboratory (3.1.3.1).

3.3.3 Influence of foreign particles on the bath surface

3.3.3.1 Capillary rafts – general review

Sometimes, when a powder is sprinkled on a liquid surface or interface, rapid spreading can be observed aided by the lateral capillary forces that carry particles with surprising velocity. A similar phenomenon could happen when a liquid droplet is placed on a powder: the droplet might lift particles to its free surface. The effect is possibly due to the asymmetric initial wetting of the particles that causes that the surface tension acts mainly in one, horizontal direction, and the capillary force big enough to remove the particles from the bulk. Publications on this phenomenon are mainly experimental [83] [84] [85] [86]. Although it was suspected that this phenomenon is also responsible for the rapid spreading of alumina on the bath surface, our experiments proved otherwise.

A seemingly contradictory phenomenon is the gathering of particles on a surface. The attraction between small floating objects is sometimes referred to as the cheerios effect [87]. These particles deform the liquid surface around them; and the combined effect of two or more objects on the surface in each other vicinity creates an asymmetry. In consequence, the resultant force of the surface tension may get a horizontal component. For a few floating objects, the surface and the resulting movement can be calculated, but the computational demand increases rapidly with each new element disturbing the free surface [88] [89] [81] [90] [91] [92].

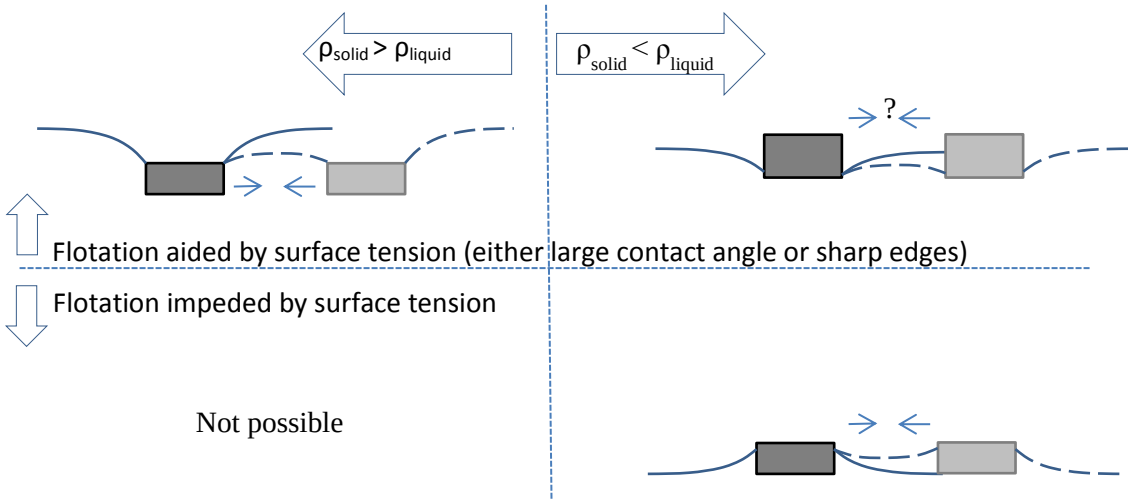

Figure 46: Approximate shape of meniscus around a single floating object (solid line), and around two identical floating objects (dashed line) ©Csilla Kaszas

Either by spreading from a clump of powder, or the gathering of lone floaters, a monolayer of particles can form, which is called a granular or capillary raft. These rafts are flexible, similarly to a liquid interface, but they can also wrinkle, fold, and support more weight than the free surface [93] [87] [94].

3.3.3.2 Foreign particles on the surface of cryolitic bath

In an industrial electrolysis cell, the main source of foreign particles littering the free surface is the carbon from the anodes. While most of the carbon is used up in the electrolysis process, some particles escape. Since amorphous carbon has a skeletal density of 1.9 g/cm, lower than that of the bath, it would inevitably resurface. In experimental cells with carbon crucibles, the walls can also degrade, leading to the same effect.

During our experiments, the surface of the bath was rarely entirely clean. While the black carbon particles can be identified with certainty, the overall appearance of this scum was of a light grey color (Figure 47). When the overhead lighting was turned off, the raft formed by these particles appeared as a dark spot on the glowing bath, with darker and lighter parts swirling underneath (Figure 48). While the composition of these raft were not analysed, we can speculate that the cold air breaking in from opening above might locally cool the surface of the bath enough for some solidification to happen. In experimental setups, the degradation of refractory material above the opening could also taint the bath surface.

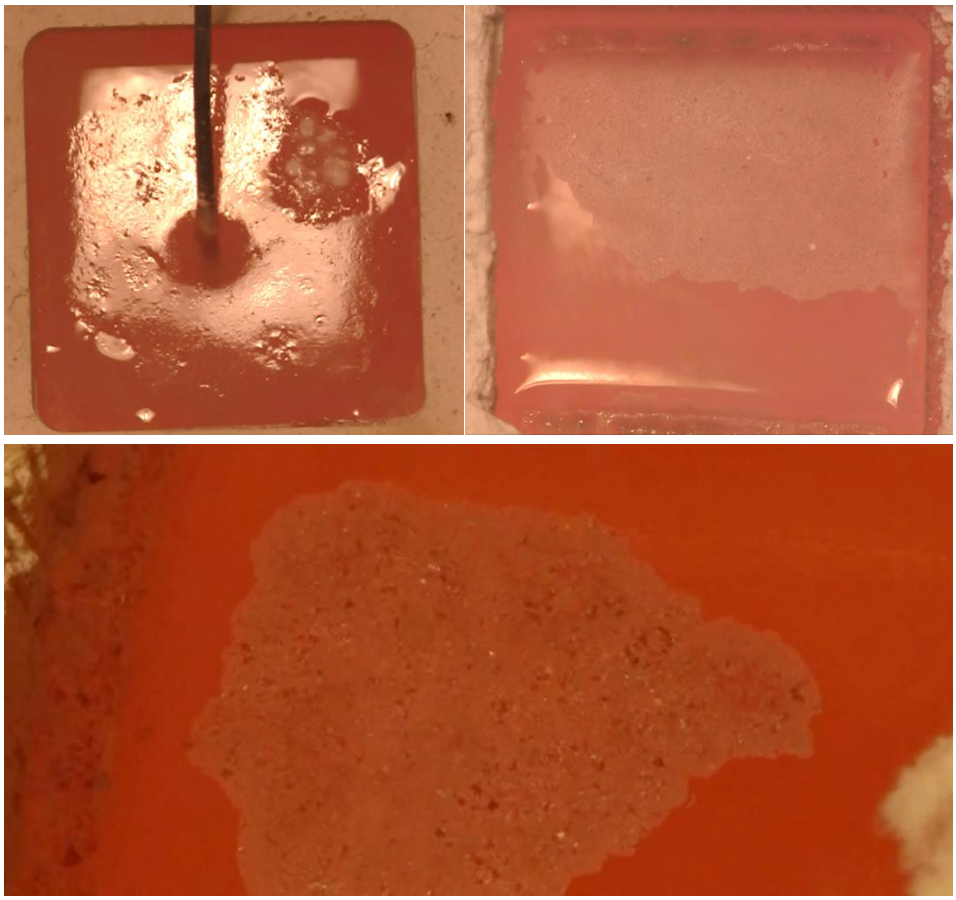

Figure 47: Different foreign particles on bath surface ©Csilla Kaszas

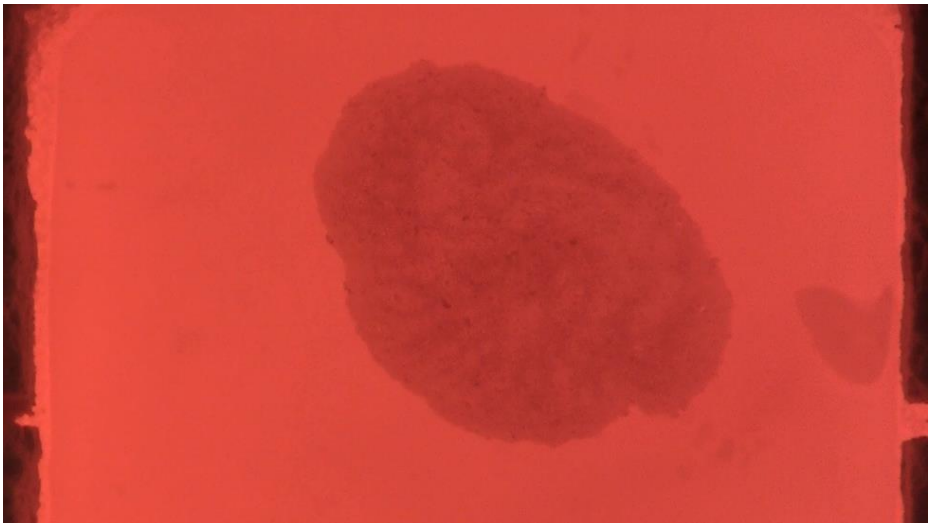

Figure 48: Particle raft on bath surface without overhead light, the lighter patches seemingly swirling under the surface ©Csilla Kaszas

While the surface tension does not change with particles on the bath surface per se, the achievable meniscus height might increase. Particles attached to the bath surface, give some degree of freedom to the surface around them especially if they are not wetted by the liquid. The presented experiment shows an artificial raft surrounded asymmetrically by scum (Figure 49). On the right side, relatively free of particles, the surface starts creeping on the top of the disc, leading to its sinking, while the meniscus is hold stable on the left where carbon particles surround the disc.

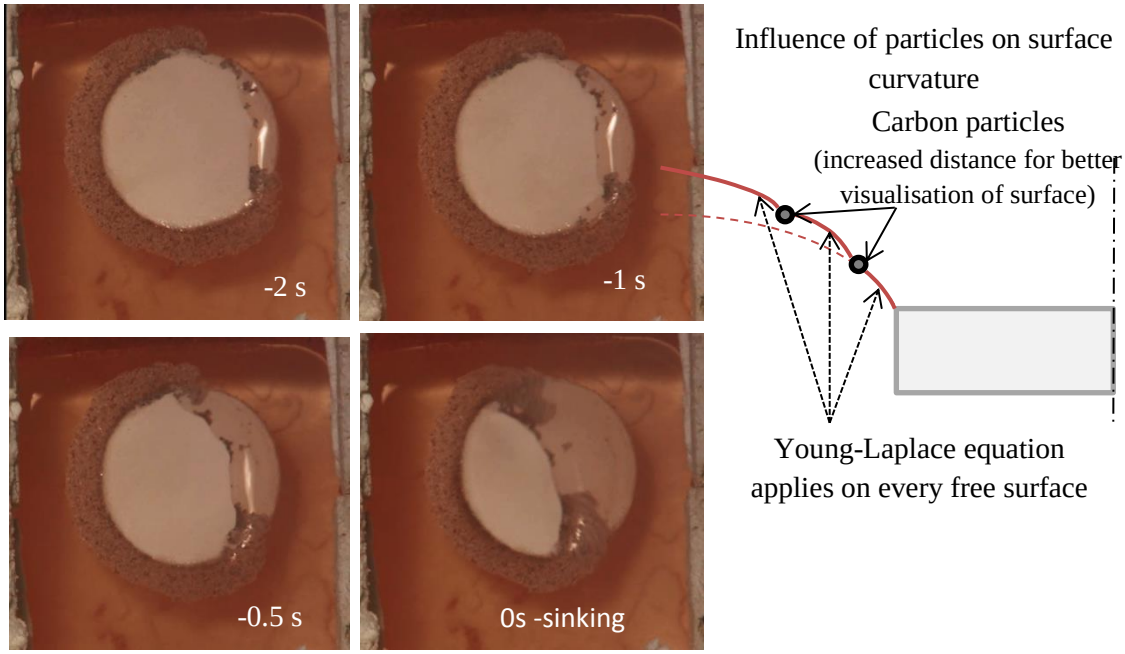

Figure 49: Contaminated surface around compressed alumina disc, process of sinking ©Csilla Kaszas

3.3.4 Raft contacting carbon wall/anode during formation

In the mathematical model for flotation, infinite free surface was assumed. It is obviously not the case, but as long as the available surface is sufficiently large, it should make no difference. However, as it was shown, the evaporating moisture content from alumina could spread the powder apart so it could fill up the limited available space. This eliminates the triple line and the surface tension force, but another effect can take place that would nevertheless hinder the sinking of the raft.

During experiments, it has been observed several times, that a raft could descend below the surface level, without sinking to the bottom. Instead, it would stay suspended just below the bath surface. Two cases were selected for discussion. For the first series of images, the crucible was covered with quartz glass to prevent heat loss; hence the misty image, but the unprompted collapse of the raft had been immortalized (Figure 50). The second series is presented from an angle, which provides a view of the carbon wall, as well as the raft (Figure 51). In both cases, the

powder spread to the walls of the crucible upon injection. There is not one single moment that can be pointed out as sinking. The liquid gradually infiltrates the raft, which weighs down and bends downward. The process can best be observed by the appearance and advancement of surface scum. The raft can stay in that position below the surface, until dissolution weakens its structure enough that it breaks under its own weight.

2.5 g primary alumina (15.10.13)

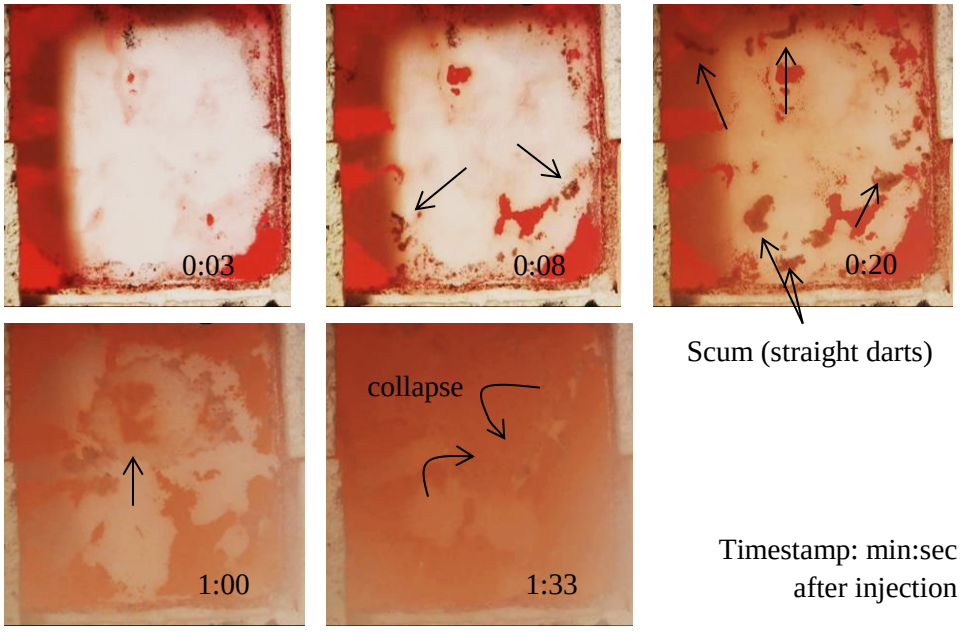

Figure 50: Suspended alumina raft, top view 2.5 g (10.13, 3rd) ©Csilla Kaszas

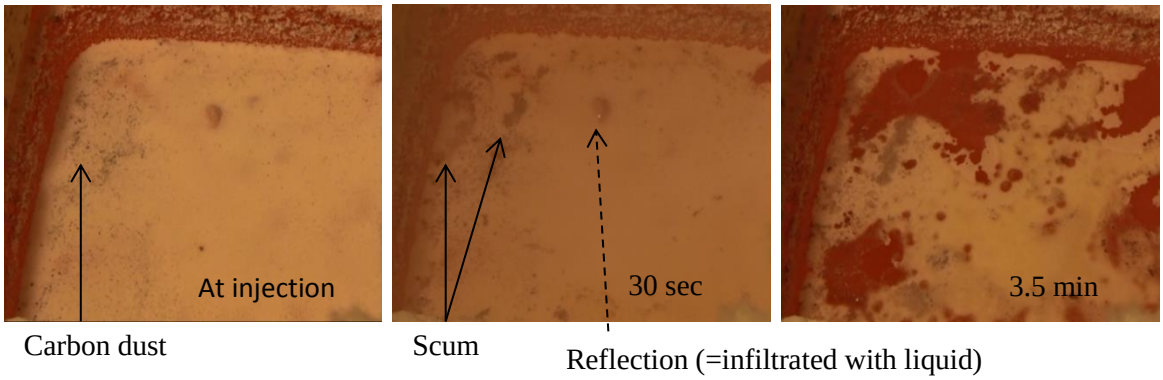

Figure 51: Suspended alumina raft, angled view 5g (10.22, 3rd) ©Csilla Kaszas

Raft holds up lodged between the walls due to sintering. Upon contact with the liquid bath, alumina sinters and achieves a good mechanical strength. As a powder, it could fill in the nooks and crannies of the coarse carbon wall, providing the raft with similarly rough edges. As long as the raft is structurally sound and is supported on both sides, it would not tilt and sink.

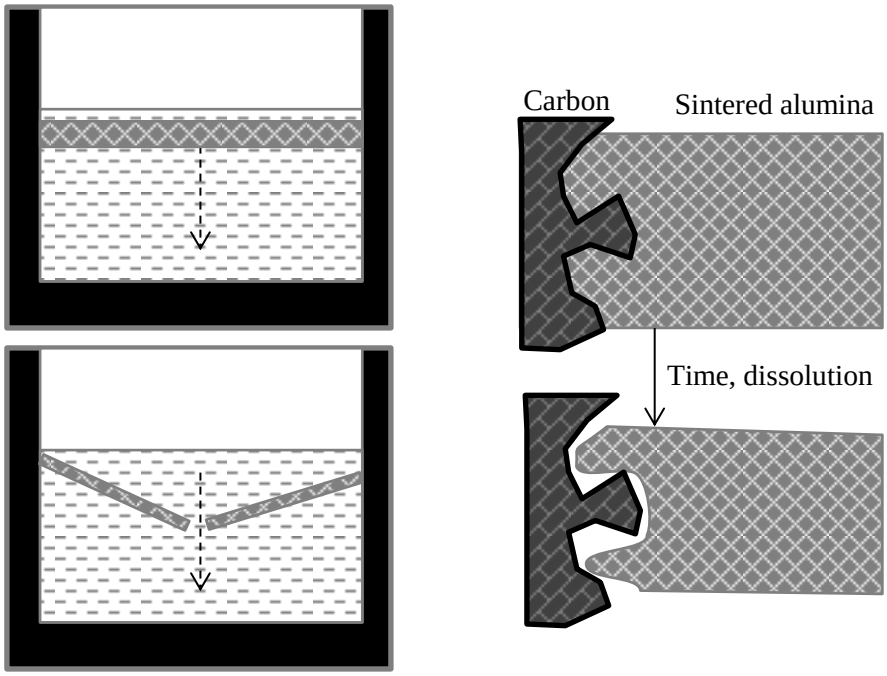

Figure 52: Sketch of suspended alumina raft ©Csilla Kaszas

3.3.5 Agitation of bath surface

In the experimental setup, the bath is not intentionally agitated, but that is not to say, it is not in motion. The liquid is heated through the walls of the container that creates a natural convection in the bath. The carbon of the crucibles disintegrates with use, and occasional bubbles and flashes might be observed during the tests (Figure 53).

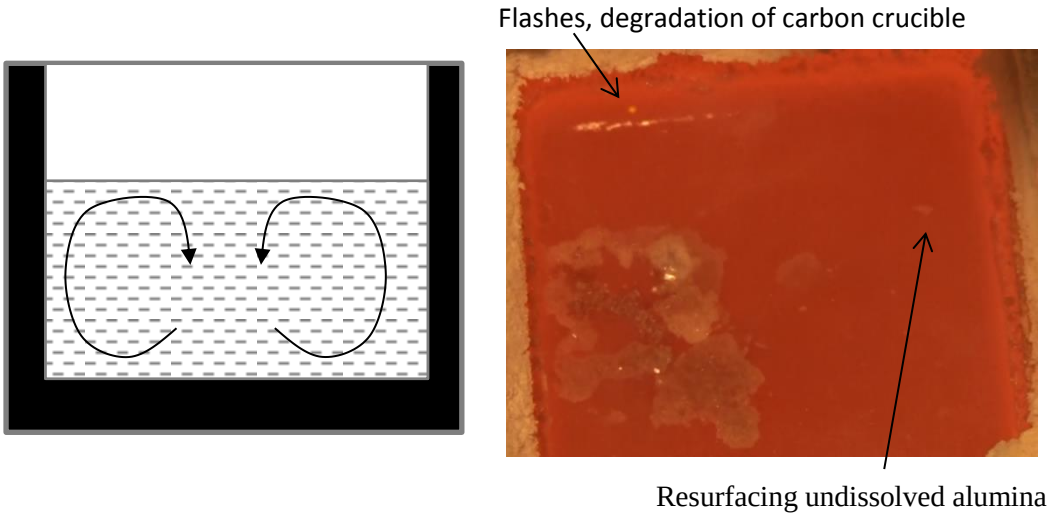

Figure 53: Disturbances of the bath surface in the experimental setup ©Csilla Kaszas

In the mathematical model of static flotation, the liquid was assumed to be undisturbed. While the bath in the experimental setup is slightly disturbed, the bath in an industrial cell is even more so agitated by the generation of carbon-dioxide under the anodes. This movement increases the chance of offsetting an alumina raft into a metastable floating position, therefore, it reduces the influence the surface tension it has on flotation in reality.

4 Evolution of raft's apparent density

Although the shape of an alumina raft, and consequently, the surface tension force acting along the triple line, has an influence on flotation, the more dominant factor on floatability is undeniably its apparent density. This chapter incorporates different elements in the life cycle of an alumina raft that influences its mass and volume, therefore its apparent density.

A raft is an alumina based solid object floating on the surface of a cryolitic bath. It can consist of different phases of alumina, frozen and liquid bath of different local composition and temperature, and a multiscale pore-structure that can be filled with gas (may that be air, anode gas, water vapour or hydrogen fluoride) or infiltrated by bath. The apparent density of the raft is the result of its composition, morphology and granulometry of the grains, and the skeletal density of the materials it contains. As long as the raft is one solid unit, its apparent density can ensure flotation as long as it is lower than the density of the cryolitic bath. When the density surpasses this limit, the raft could either sink or stay afloat depending on the disturbances it has to endure. After its density reaches the theoretical limit of flotation, defined and calculated in chapter 2, it surely sinks.

Several different factors influence the evolution of the apparent density of an alumina raft, some in more ways than one (Figure 54). The solidification of bath around the raft is driven by the heat transfer between the cold alumina and the cryolitic bath with a low superheat. As long as there is a solid frozen layer on the bottom of a raft, the infiltration is hindered. The moisture content not only influences the process by the energy consumption of evaporation, it also changes the structure of the raft, blurring the line between frozen bath and infiltrated powder through mixing.

When the frozen bath has re-melted and the powder is thoroughly infiltrated, the raft could disperse, even without dissolution. However, the recrystallization of gamma phase alumina results in binding the adjacent particles together. The strength of this bond may vary, and the gravity and bath currents may not suffice to break the grains from the bottom of a raft, until it is weakened by dissolution.

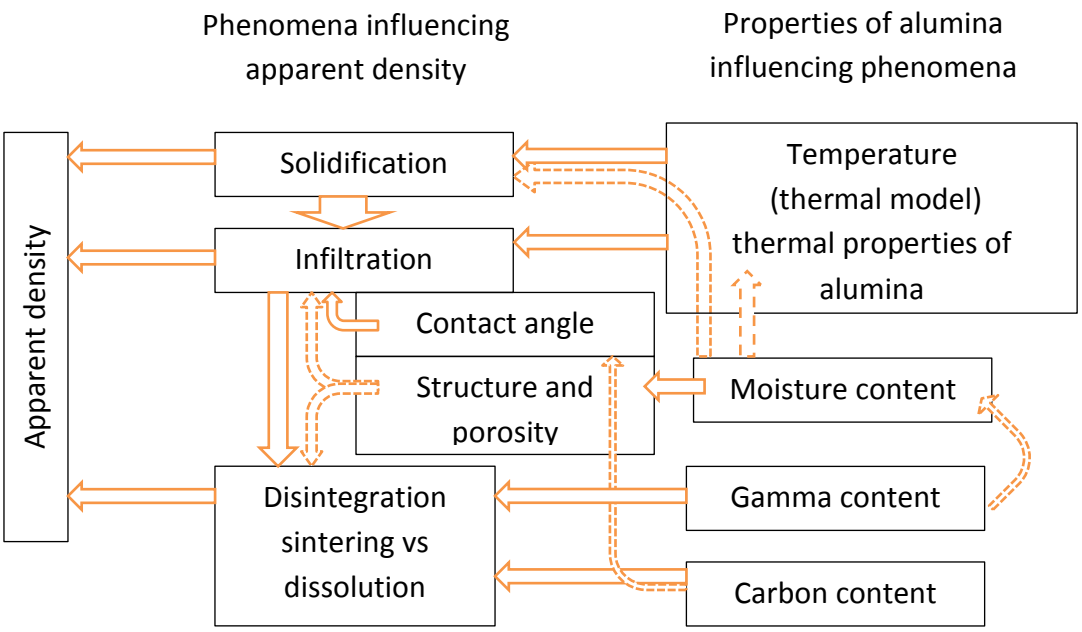

Figure 54: Structure of chapter ©Csilla Kaszas

4.1 Thermal behaviour of alumina rafts

4.1.1 Compressed discs as artificial rafts

The description of the preparation of the artificial rafts and the course of the experiments has been presented earlier (3.1.3), along with some of the results to compare with the static flotation model (2.3.1).

4.1.1.1 Sets of experiments

The following table contains the list of experiments where the compressed alumina discs were placed on the surface of cryolitic bath and removed after a certain period of time. The relative uniformity of these rafts permits the better comparison of the samples than naturally formed rafts would.

Table 6: Compressed disc removals

	Retention time [s]
A	30, 30, 60, 60, 90, 90
B (day 1)	40, 90, 20, 70, 120, 60
B (day2)	110, 30, 80, 10, 50, 100
C	120, 210, 30, 150, 60, 240, 90, 180

The disc insertions and removals started using a bath with 4% alumina content. As the discs did not disintegrate, it was assumed that most of the dissolved alumina would be contained in the

disc and would not get into the main volume of bath. Still, to avoid systematic error, the order of the retention time was randomised after the first set of experiments.

4.1.1.2 Structure of samples

A photo of the cross section of an artificial raft removed from bath had been presented previously (Figure 39).

The samples from series A were analyzed by scanning electron microscope (SEM). While with optical microscope the porosity of the infiltrated powder was not very apparent, on the SEM images it was clearly seen that the infiltration was not uniform. The corner was very dense and compact while porosity increased towards the zone formed by loose powder. It can also be seen on the upper part of the photo, which was the bottom of the disc, how the frozen layer started to erode due to the preparation of the sample (Figure 55).

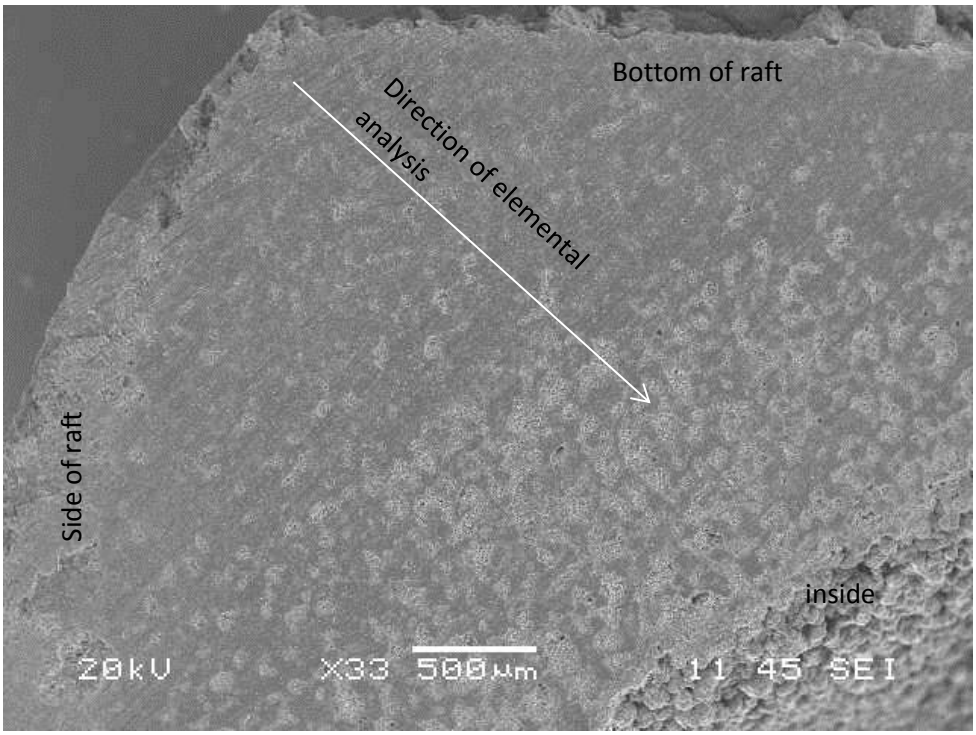

Figure 55:SEM image of alumina disc infiltrated by bath
(sample upside-down; 30 s retention time) ©Csilla Kaszas

Using the elemental analysis from the electron microscope, and assuming that all oxygen belonged to alumina, the saturation of the powder (the volume occupied by the bath over the original pore volume) can be estimated (Figure 56). The elemental composition and atomic mass of the elements permits to calculate the mass composition of the samples. Assuming all oxygen is bond as alumina (Al_2O_3), leaves the rest of the aluminium and the other elements (Na, F, Ca) as bath. Assuming the 28% volume fraction of alumina did not change, that leaves the remaining 72% of volume for the bath to potentially fill.

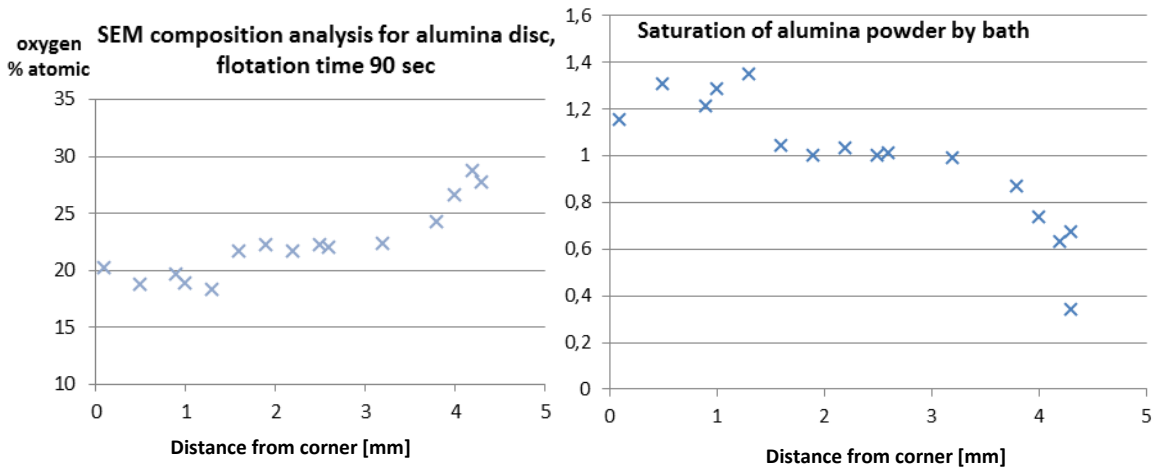

Figure 56: Saturation of alumina by bath in compressed disc, flotation time: 90 sec

The low oxygen content in the corners can be explained by the dissolution of alumina. The corners were exposed to the bath, hence this is where the dissolution started and reached a more advance state – and the initial porosity of the alumina increased with the dissolution, the bath filling out the pores.

4.1.1.3 Infiltration front of compressed discs

Conducting a large set of experiments shows the general tendency of the evolution of the infiltration front (Figure 57).

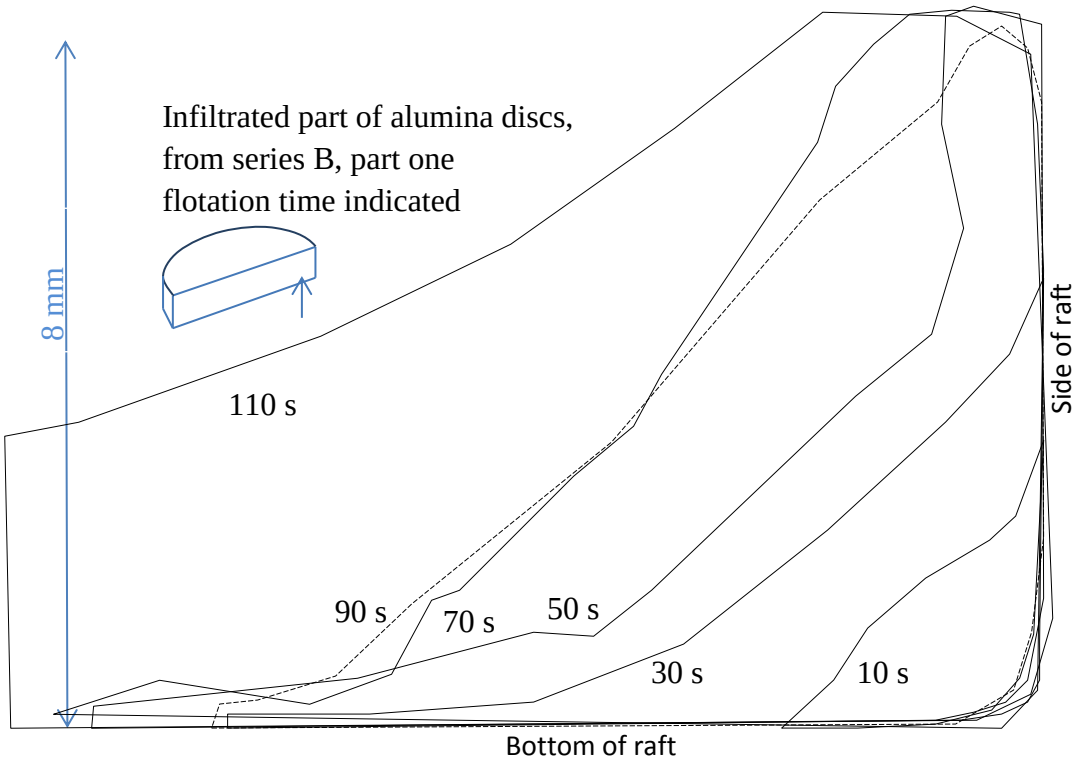
Infiltrated part of alumina discs,
from series B, part one
flotation time indicated
8 mm
110 s
90 s
70 s
50 s
30 s
10 s
Side of raft
Bottom of raft

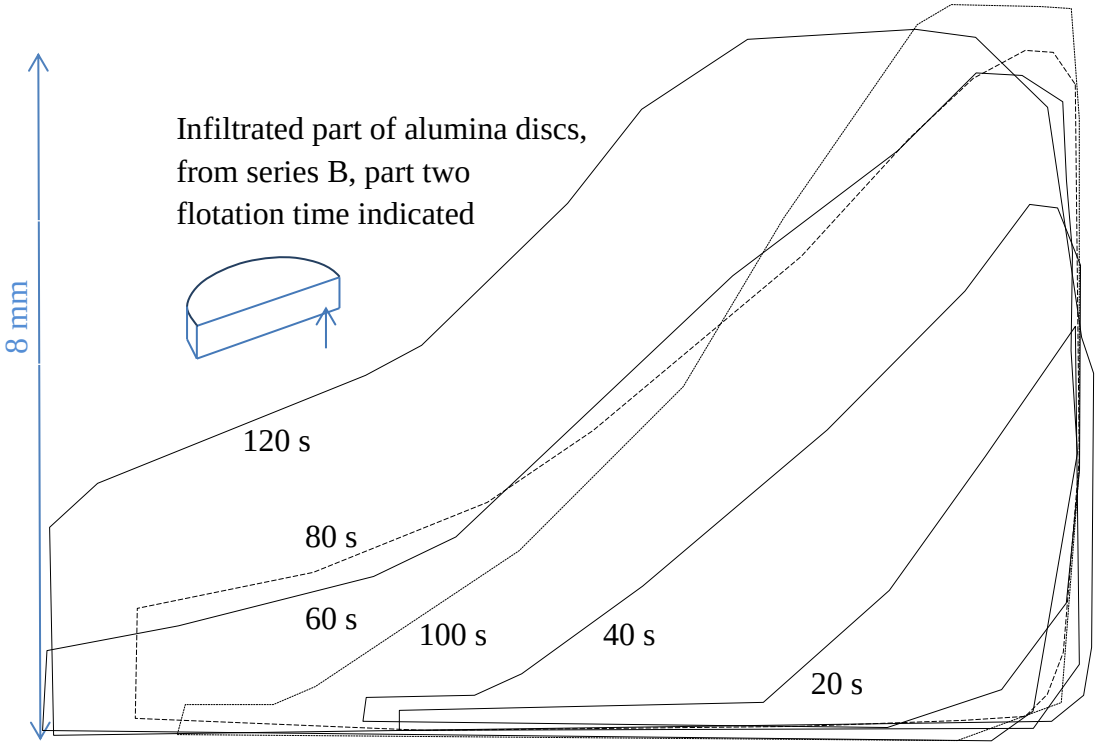
Infiltrated part of alumina discs,
from series B, part two
flotation time indicated
8 mm
120 s
80 s
60 s
100 s
40 s
20 s

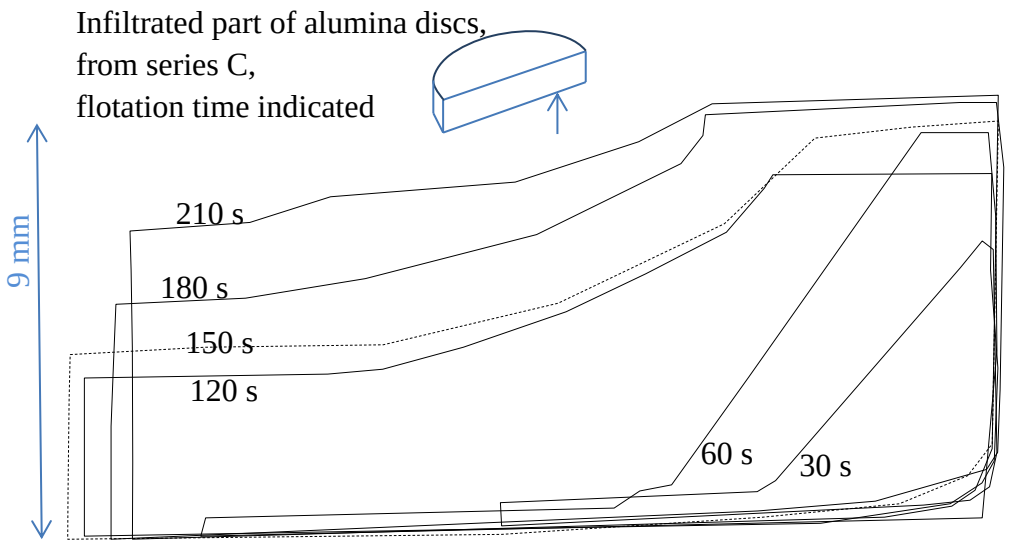

Figure 57: Infiltration front in artificial alumina rafts, series B and C ©Csilla Kaszas

Since the bottom corners of the discs were exposed most to the bath, they warmed up faster and that is where the infiltration started. The front of infiltration gradually extended both horizontally and vertically.

The roundness of the corners could have come from the abrasion due to handling before insertion but also could be the result of dissolution. The fresh bath entered the discs from the corners; it could have dissolved some of the alumina and got saturated by the time it reached the middle of the disc.

Some variation of the shape of the infiltration front starts to show around the one minute mark. For the disc with 50 seconds retention time, the infiltration occurred along the full height of the disc around the cylindrical surface, while for the disc with 70 seconds retention time, the infiltration did not reach the top of the disc. This is likely due to an imperfect insertion of the object. At the time of insertion, fresh compressed discs could float on the bath with the triple line around halfway to their height, sinking deeper into the surface as infiltration progresses. However, if the discs are not placed precisely and gently on the surface to their equilibrium position, they might dip under that position and their sides could get a coat of bath. Some of the other samples show the same tendency, with more advanced infiltration rate on the top (70, 100, 120 s). Other differences, like a difference in porosity might have contributed to the advanced infiltration rate of the disc with 60 seconds retention time.

The infiltration normally reached the top of the discs in 1.5 minutes. It should be noted though, that at this time, the triple line stayed on the edge of the disc, it did not creep over the wetted alumina.

Some characteristic distances were measured in an attempt to better quantify the infiltrated zone (Figure 58). The infiltration at the corners was measured diagonally from the corners, the shortest distance to the un-infiltrated powder. The height of infiltration was the maximal height from the bottom where the bath penetrated the raft along the sides.

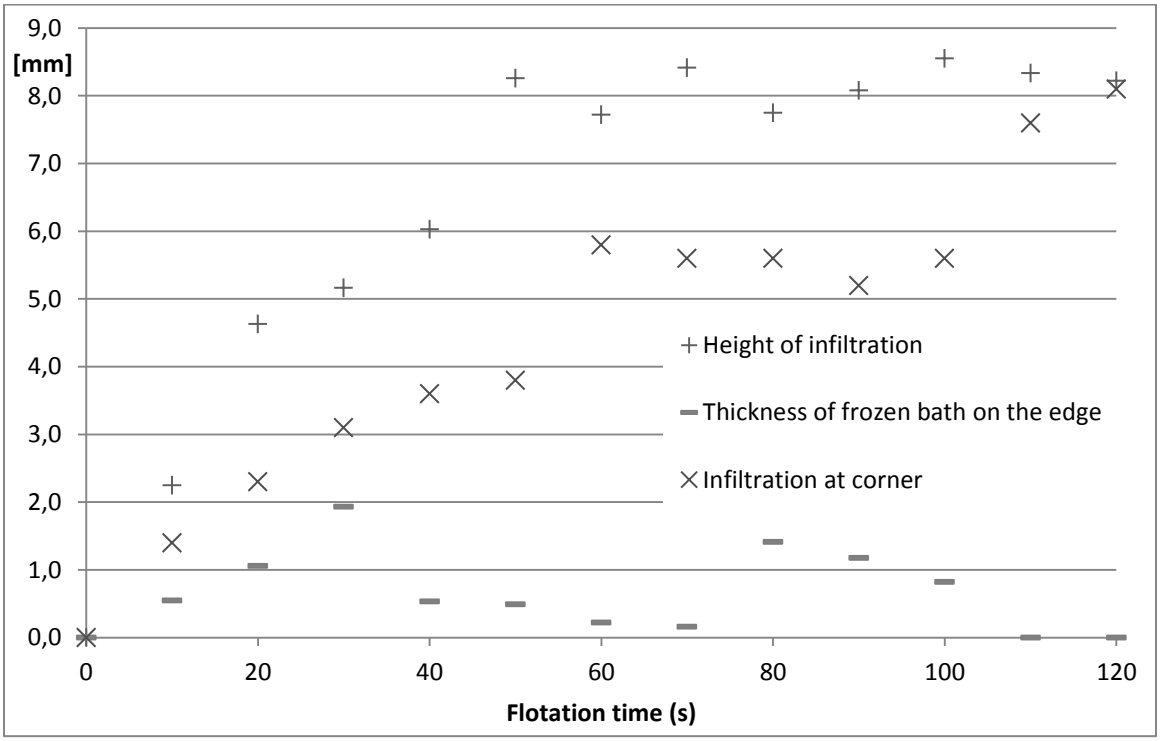

Figure 58: Characteristics of infiltrated artificial raft, series B

4.1.1.4 Mass and density of samples

The discs were weighted after they have been recovered from the bath and cooled down. After that, the non-wetted part of the powder by the bath has been removed, and the rest of the sample, namely the infiltrated zone together with the remaining frozen layer of bath (on the edges and under the bottom of the disc) has been measured. Assuming that the initial mass of the discs was the average mass (as the individual discs were not measured to prevent damage), the mass of the bath can be estimated (Figure 59).

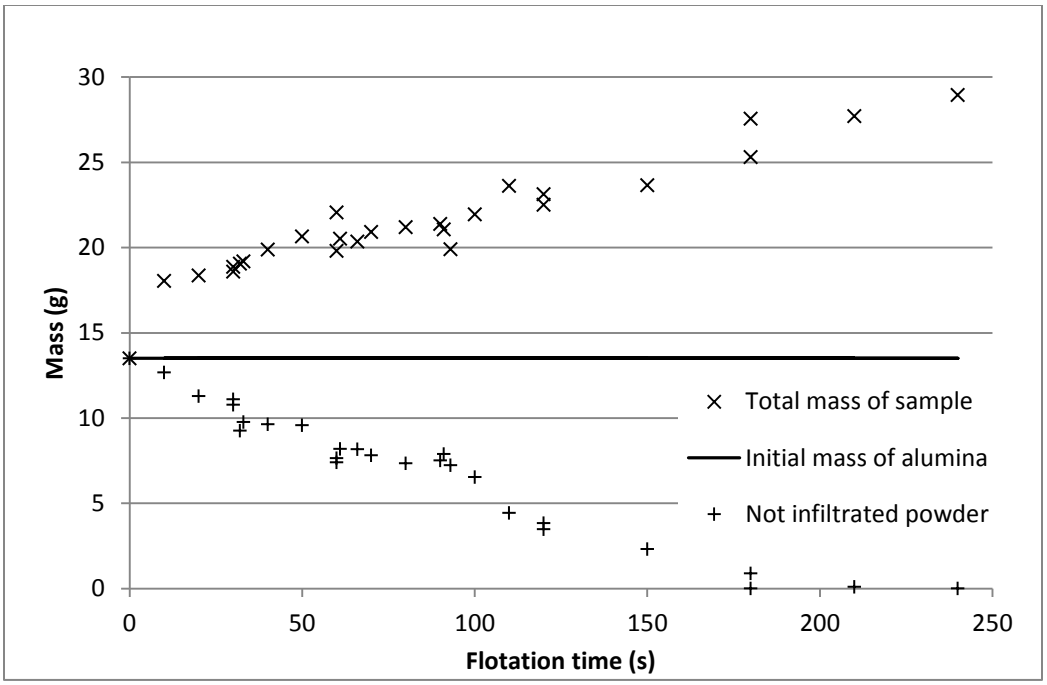

Figure 59: Evolution of the mass of artificial rafts

The insertion resulted in the sudden solidification of the bath around the disc. After an initial sudden increase of the mass due to the rapidly freezing bath, the mass growth was almost linear. Soon after that, the frozen layer started melting back rapidly while the infiltration began. Later, the infiltration front approached the center and at the same time, the porosity around the corners was decreasing, as it got soaked by the bath. Plotting the mass growth of the whole disc sample versus the mass of infiltrated powder, the correlation is more evident (Figure 60). The theoretical limit for the mass growth of the disc was calculated based on the assumption that the all the available void fraction of the disc was filled with bath with 2.1 g/cm^3 density.

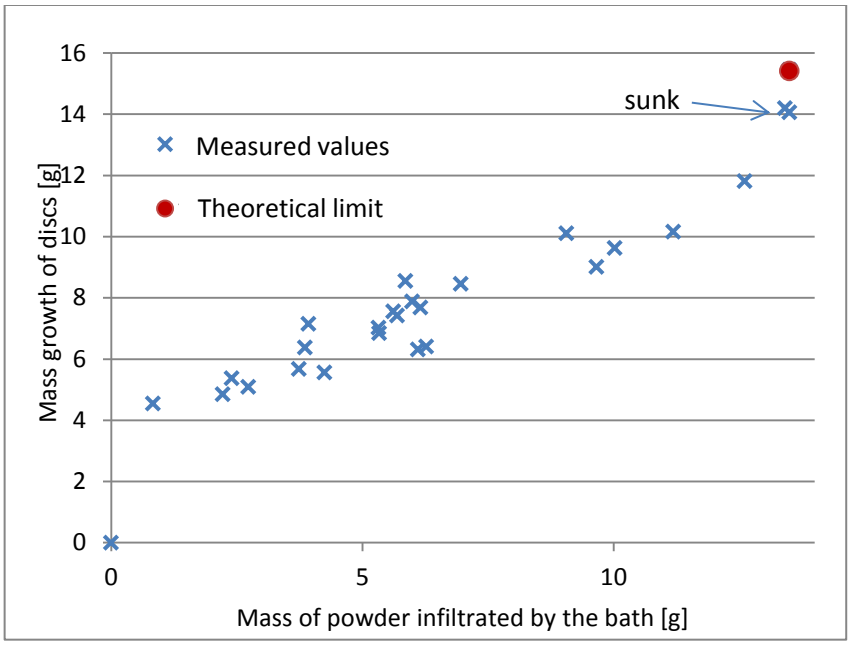

Figure 60: Correlation between mass growth of discs and infiltration

Assuming that the volume of the discs did not change during the flotation and applying the average thickness of the alumina discs from on our measurements, the density of the samples could be estimated (Figure 61). For comparison, the volume of the discs from series C was measured by the Archimedes method. They were covered with hydrophobic silicon spray to prevent infiltration by water.

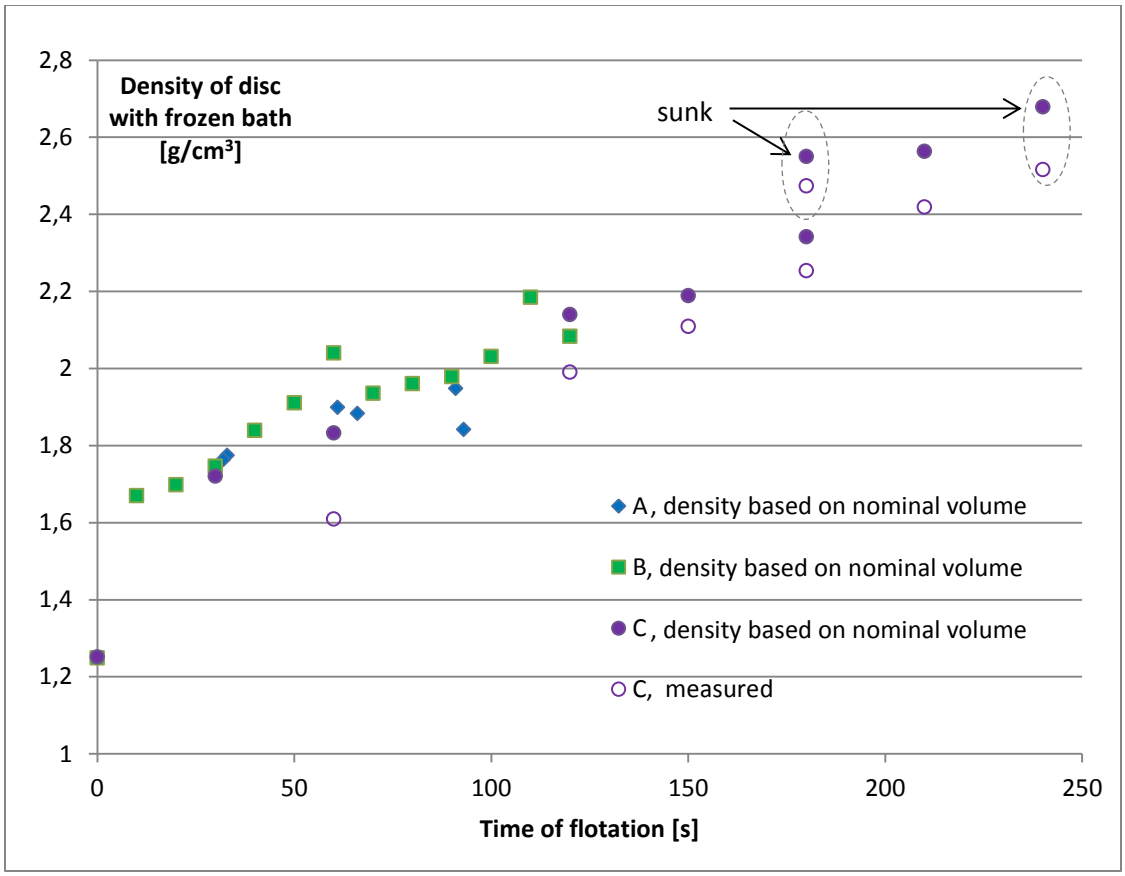

Figure 61: Density of samples, series A, B and C

The density of the rafts reached the density of the bath after approximately two minutes and continued to increase. After that moment, beside the buoyancy, the surface tension kept the raft on the surface and flotation became sensitive to any disturbances. It was concluded by calculations, density measurements and visual observation that the raft could stay afloat after its density exceeded the density of the bath with more than 20%.

4.1.1.5 Infrared temperature measurement of compressed discs

On separate occasions, disc insertions were filmed with a FLIR infrared camera (Figure 62).

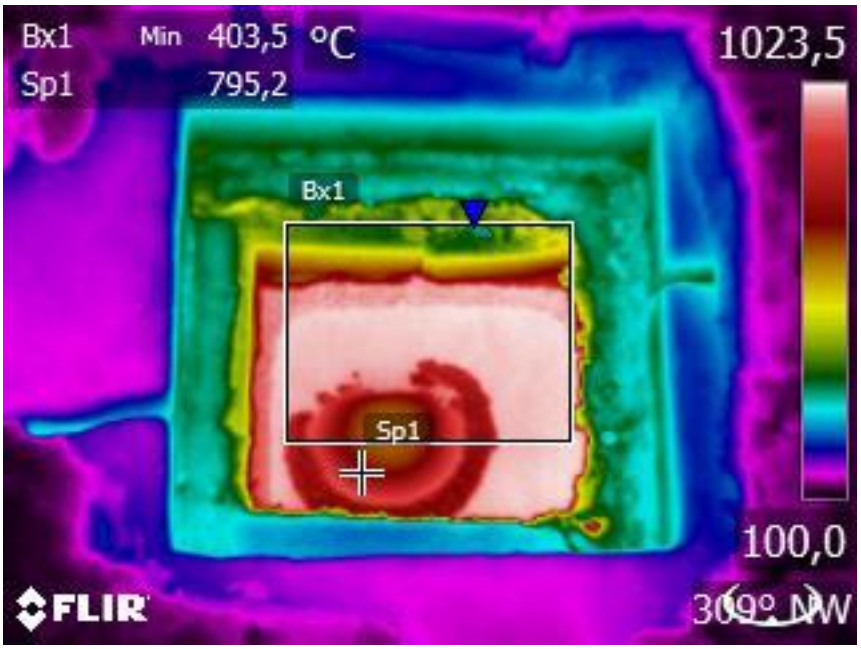

Figure 62: Artificial raft on bath surface via FLIR infrared camera ©Csilla Kaszas

The camera does not only provide colourful images, but can also be used to extract temperature values. However, as the emissivity of alumina is highly dependent on the wavelength, therefore of temperature, the readings are not reliable. To counteract this problem, the center of the top of the disc was sprayed with carbon paint. T min signifies the lowest indicated temperature on the top of the disc (Figure 63). Naturally, the coldest spot would be (and was indeed) the center of the disc. However, due to the black spot in the middle, the lowest measured temperature was a few millimeters off center, where the clear surface of low emissivity alumina showed. The temperature increased logarithmically, and flattened out around 750 °C, where the gap closed between the two series of data.

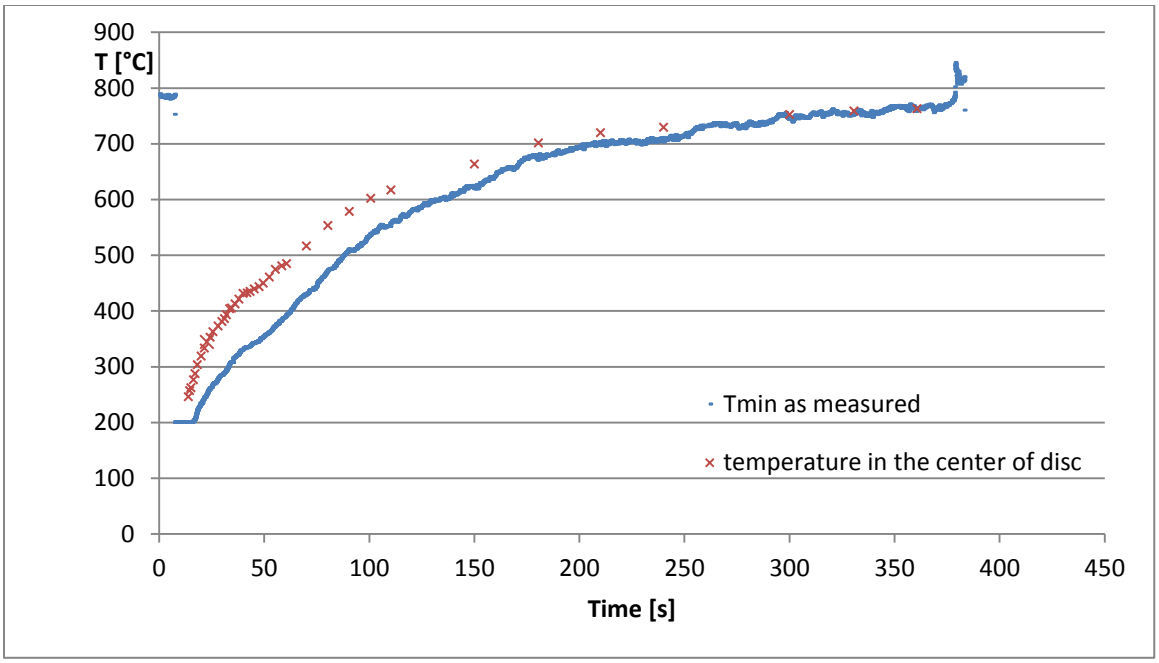

Figure 63: Temperature of the top of alumina disc on bath surface with FLIR camera

In spite of reliability issues due to varying emissivity, the infrared camera permitted temperature measurements with little effect to the experiment. To provide an unobstructed view, the opening was not covered with a quartz sheet, unlike it was usually done, to reduce heat loss. The excess cooling could explain the 6 minutes long flotation time, which usually barely exceeded above 4 minutes.

4.1.2 Measurement of thermal properties of alumina

4.1.2.1 Low temperature thermal conductivity measurements

For low temperature thermal conductivity measurements, a Quickline 30 thermo-physical instrument was used, with a needle probe. The device is suitable for thermal conductivity measurement between 0.015-0.2 W/mK and uses transient hot wire method.

A cylindrical glass container, 0.4 l of volume, 14 cm of height, was used to hold the SGA. It was covered all around with 2.4 cm insulating wool. As the sieving yielded enough powder between the 45-75 and 75-106 micron particle size range, those were selected for testing.

The powder was filled in the container, the container tapped to eliminate air pockets, and the needle probe was inserted in the center. The probe was removed, and then re-inserted for each measurement. The instrument was certified for up to 80 °C; therefore the container containing the powder was heated inside a furnace for a day to 60 °C, assuring even temperature distribution in the sample. After testing the powder at this higher temperature, to investigate the effect of moisture content (or lack thereof) in the SGA, the sample was heated to 500 °C. The estimated mass loss, and therefore the LOI of the SGA at its initial state, was 3%, based on

separate measurements. The containers were covered, to avoid rehydration of the powder from the moisture of air. The samples were left in the furnace to cool down, and the tests were repeated at different temperatures on the dried alumina.

4.1.2.2 Monotonic/ramp heating apparatus

An apparatus, developed at GRIPS, UQAC, based on the principle of monotonic heating was used to determine the thermal properties of SGA for up to 900 °C [95].

SGA was filled in a cylindrical stainless steel container, 0.1 m of diameter, and 0.4 m of height. The cylinder was heated on the side; the temperature of the wall was increased linearly in time (rate of increase m, K/s). The sample heater was separated into three zones vertically; each was controlled individually, to ensure one-dimensional (radial) heat transfer in the middle zone. After the regular regime sets, the temperature increases with the same rate as it was imposed on the surface, anywhere in the sample. In case of constant properties, this is equivalent to a second-type boundary condition: constant heat flux on the surface.

Two different modifications of the apparatus were used. In the two-point design, the container was filled with SGA only, two thermocouples were placed in the middle zone of the sample, one in the center (T_1, R_1=0) and one beside the wall (T_2, R_2). In the three-point design, a stainless-steel core was also used with a diameter of 13 mm, alumina powder filling out the place between the centered core and the wall of the cylindrical container. Three thermocouples were placed in the middle zone of the sample, one within the core (T_1, R_1), one on the inside of the cylinder's wall (T_3, R_3), the third in-between (T_2, R_2). The simpler, two-point design is suitable to determine thermal diffusivity (α) only, while with the three-point design, the core with known properties is used as a reference, and thermal conductivity (k) and specific heat capacity (c) can also be evaluated, along with thermal diffusivity.

Table 7: Equations for monotonic (ramp) heating measurements

	Two-point	Three-point
Base of calculations	Heat conduction equation of the suitable form, $$\alpha\frac{1}{r}\frac{\partial}{\partial r}\left(r\frac{\partial T}{\partial r}\right)=\frac{\partial T}{\partial t}=m$$ was solved.	
Boundary conditions	No heat flux at r=0 T_2 at R_2 known	$$R_1{}^2\pi\rho_0 c_0\frac{\partial T}{\partial t}=-k2R_1\pi\frac{\partial T}{\partial r}\Big\vert_{R_1}$$ T_1 at R_1 known
Solution of differential equation: T(r) in the powder	$$\frac{m}{4\alpha}r^2-\frac{m}{4\alpha}R_2{}^2+T_2$$	$$T_1+\frac{mR_1{}^2}{4\alpha}\left(\left(\frac{r}{R_1}\right)^2-1\right)+\frac{mR_1{}^2}{2\alpha}(\gamma-1)ln\frac{r}{R_1}$$
	Properties are expressed with the help of all the measured points (T, r)	
Thermal diffusivity (α)	$$\frac{m\cdot R_2{}^2}{4(T_2-T_1)}$$	$$\frac{mR_1{}^2}{4}\frac{(\eta_2{}^2-1)ln\eta_3-(\eta_3{}^2-1)ln\eta_2}{\Delta T_2 ln\eta_3-\Delta T_3 ln\eta_2}$$
Thermal conductivity (k)	-	$$\frac{mR_1{}^2\rho_0 c_0}{2}\frac{(\eta_2{}^2-1)ln\eta_3-(\eta_3{}^2-1)ln\eta_2}{\Delta T_2(2ln\eta_3-(\eta_3{}^2-1))-\Delta T_3(2ln\eta_2-(\eta_2{}^2-1))}$$
Specific heat capacity (c)	-	$$\frac{2\rho_0 c_0}{\rho}\left(\frac{\Delta T_3 ln\eta_2-\Delta T_2 ln\eta_3}{\Delta T_2\left((\eta_3{}^2-1)-2ln\eta_3\right)-\Delta T_3\left((\eta_2{}^2-1)-2ln\eta_2\right)}\right)$$

Where:

ρ_0, c_0: density and specific heat capacity of the core material

ρ, c: (bulk) density and specific heat capacity of the powder

ϒ: $\frac{\rho_0 c_0}{\rho c}$

η: r/R_1

ΔT_2: T_2-T_1

ΔT_3: T_3-T_1

One series of measurements with the three-point design, and one series with the two-point design are presented. Both series were started with fresh SGA, which remained in the container after each test, and let to cool down for 3-5 days. In the C series, the alumina was pre-dried, while in the D series, it was not, and after the third run, 2 dl tap water was dispersed in the powder with a syringe. The apparatus was closed and two days of waiting period followed so the adsorption equilibrium would set before the fourth run of the series.

Table 8: Series of measurements for thermal properties of SGA

Series /number of tests	Design	Thermocouple placement /distance from center [m]	Rate of temperature increase [°C/min]
C /	3 point	R_1 (for T_1): 0.0064 R_2 (for T_2): 0.0252 R_3 (for T_3): 0.0464	0.5
D /	2 point	0 0.0487	0.5

4.1.2.3 Evaluation of results

4.1.2.3.1 Conductivity by particle size

The results of the measurements with Quickline 30 are summarized in the table below (Table 9).

Table 9: Equivalent thermal conductivity of SGA [W/mK]

	24 °C	~60 °C	Drying	~60 °C	24 °C
Particle size					
75-106 µm	0.132	0.144		0.126	0.118
45-75 µm	0.128	0.14		0.122	0.119

The conductivity increases with the temperature, the 9% difference at the powder's original state, decreased after drying. While the thermal conductivity of solid alumina decreases with the temperature [26], the thermal conductivity of air increases; the results suggesting the latter to be the dominating influence. Furthermore, the effective conductivity due to radiation is proportional to the third power of the temperature, which contributes to the increasing tendency as well.

The equivalent thermal conductivity of the SGA between 75-106 µm was higher than that of the smaller particle size, in all except the last case. This tendency fits the expectations, as larger particles lead to fewer contact points, therefore less contact resistance per unit length. However, the difference in conductivity is only 3% at average, while the increase in mean particle size is 50%, which renders the importance of this is aspect less substantial.

A significant change (7-13% decrease) in conductivity may be attributed to drying. Due to the meniscus forming in tight corners and gaps, the water concentrates at those places, occupying the smaller pores in the particles and increasing the contact areas at the contact points of neighbouring particles. The absence of this moisture therefore leads to a more remarkable change in conductivity than the mere 3%, the moisture content of the original samples.

4.1.2.3.2 Results with monotonic heating method

The results are presented as a function of the mean temperature of the powder – the arithmetic average of the measured temperatures in the sample at any given moment. The beginning and the ending of each series were cropped to contain only valid data; the beginning at the point

where the rate of temperature increase on the inside of the sample reached the average rate (monotonic heating regime sets), the end when the heating turned off, as the outside temperature reached 900 °C.

The setup was run five consecutive times with the two point design, and three times with the three-point design (Figure 64). As the three-point design is very sensitive to the displacement of the thermocouples, which can shift during tests due to high temperature, the results were adjusted to fit the result of the more reliable 2-point design on the stable 400-800 °C interval.

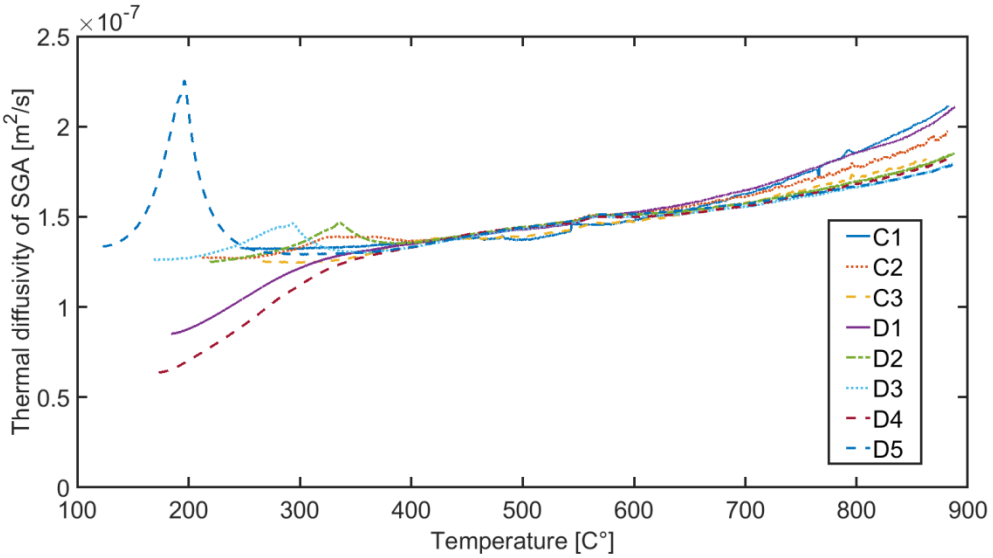

Figure 64: Adjusted results for series C and D

At the low temperature range, significant differences can be observed in the apparent thermal diffusivity, depending on the moisture content. The powder was not dried prior to the tests, and moisture was reintroduced before D4; therefore, in case of D1 and D4, the alumina had high moisture content. That is not to say however that the moisture content was zero during the other tests. After each test, it took days for hot alumina to cool down to close to room temperature so a new test could be done. During this period, the powder was exposed to air and could re-adsorb some moisture.

The effect of moisture content on the apparent diffusivity is twofold. The evaporation is an endothermic reaction, so the apparent heat capacity of the powder increases with moisture. However, as the moisture evaporates, the vapour can travel between the pores, increasing the apparent thermal conductivity. The results suggests that the increase of apparent heat capacity by the activation energy for desorption is more significant for larger quantity of moisture; while

with relatively dry powders, the increased conductivity is more prominent and the desorption manifests itself as a positive peak on the diagram of thermal diffusivity.

Between 300 and 700 °C, the results are similar. Above 700 °C, the plots fan out. This is probably due to the deformation of the thermocouples at high temperature

According to our measurements, the effective thermal conductivity of SGA increases linearly from 0.15 to 0.3 W/mK on the 350 – 850 °C interval (Figure 65).

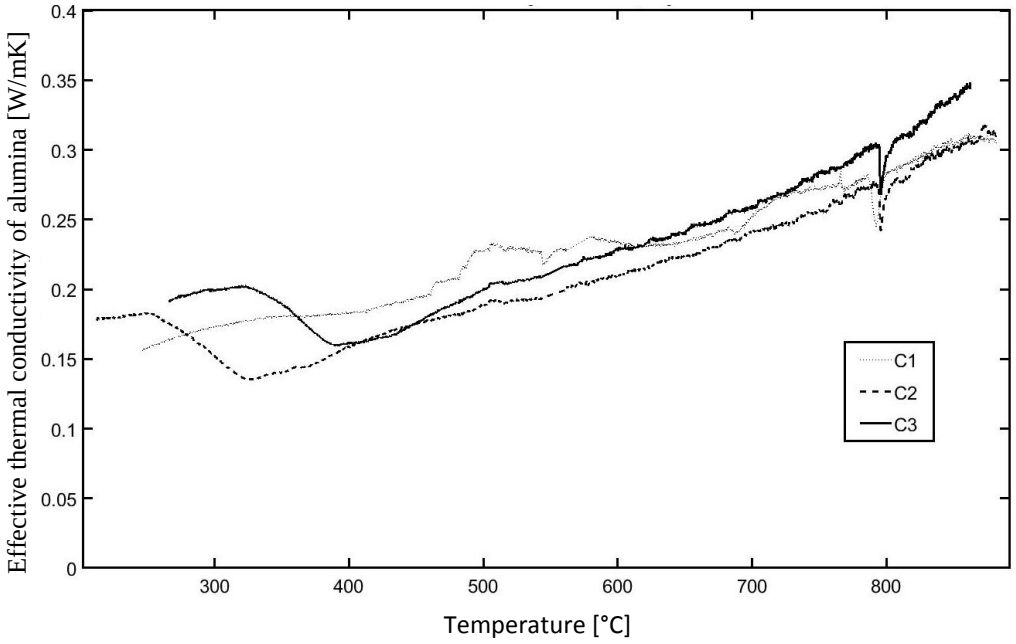

Figure 65: Thermal conductivity (three-point measurements)

4.1.2.4 Thermal conductivity model

Models and equations to estimate the equivalent thermal conductivity of porous media are available since Rayleigh [96]. These are applicable to certain geometries; in case of powders, mostly uniform, spherical particles are used in organized packing. In all cases, the thermal conductivity of the particle is part of the equation. While replacing the conductivity of the particle with the conductivity of the solid is acceptable if the particle has low porosity, it would be ill-advised to directly apply a model developed for solid particles to the highly porous SGA particles. There is the possibility for a two-level model: separating the intra-particle and inter-particle porosity, calculating the equivalent conductivity of the porous particle, embedding it in the model of the powder (Figure 66). The porosity of the particle can be estimated based on bulk density, skeletal density, and the possible packing density of a polydisperse powder. The estimation was also aided by a paper concerning the porosity of SGA [97]. The authors

measured the micro- and macroporosity of alumina, 6.8 µm being the border between the two. As tighter gaps between particles would manifest as microporosity, along with the intraparticle porosity, the measurements cannot be applied directly in the model, but it was used as an indicator, to make a sound assumption on the matter (Table 10).

Table 10: Connection between the different levels of SGA porosity, and estimated values

Intraparticle level	Interparticle level	Total
$\boldsymbol{P_I = 1 - \frac{\rho_p}{\rho_s}}$	$\boldsymbol{P_{II} = 1 - \frac{\rho_b}{\rho_p}}$	$\boldsymbol{P_{tot} = 1 - \frac{\rho_b}{\rho_s}}$
		$\boldsymbol{P_{tot} = 1-(1-P_I)(1-P_{II})}$
40%	50%	70%

Where ρ_s, ρ_p and ρ_b are the density of the solid, the particle and bulk density [kg/m^3]

The Krischer model (Figure 66) (Equation 17) is a generalized model, dependent on the porosity and containing a characteristic number to account for given geometry and pore structure. Due to its adaptability, the Krischer model was applied to both the intra- and the interparticle level to determine the overall effective conductivity of SGA. For characteristic number, which is descriptive of the unit cell geometry and represents the ratio of parallel and serial sub-elements, a_{II}=0.2 was used for the interparticle level, applicable for spherical particles, while a_I=0.15 was assumed for the intraparticle level, as the solid fraction is supposedly more connected inside the particle, than between the particles.

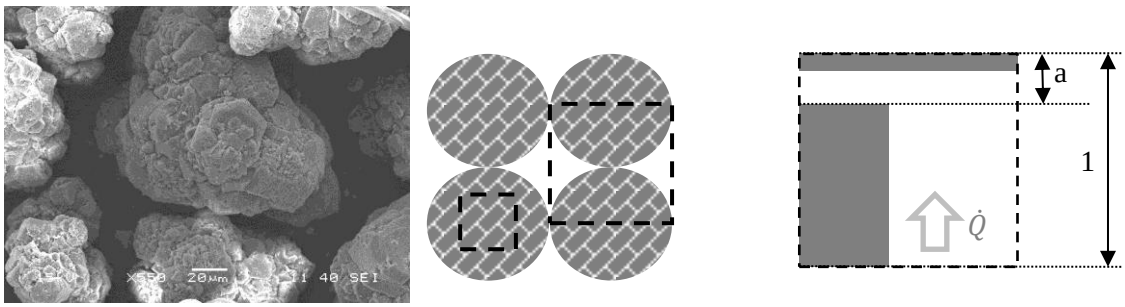

Alumina particles | Two-level model | Krischer model

Figure 66: Alumina powder (SEM image) and model geometry ©Csilla Kaszas

$$k_e = \frac{k_g}{\frac{1-a}{P+(1-P)\frac{k_s}{k_g}} + a\left(P+(1-P)\frac{k_g}{k_s}\right)}$$

Equation 17: Krischer model for effective thermal conductivity

Where

k_e: effective conductivity of powder [W/mK]

k_s and k_g: thermal conductivity of solid phase and gas phase [W/mK]

a: characteristic number for geometry

P: porosity.

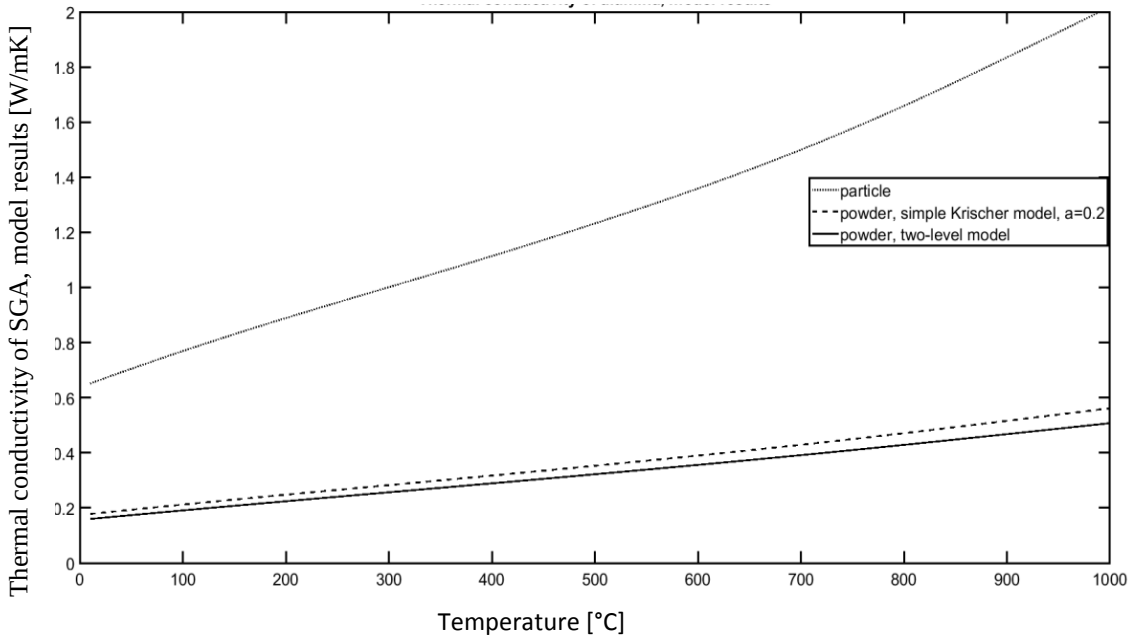

Figure 67: Effective thermal conductivity of alumina, model results

Compared to a simple Krischer model, the two-level model provides effective thermal conductivity closer to the measurements (Figure 67).

For high temperatures, the effect of radiation is more prominent, and should be taken into consideration.

$$k_r = 4\sigma dFT^3$$

Equation 18: Equivalent conductivity of powder for radiation

σ: Stephan-Boltzmann constant,
F: radiation exchange factor

The radiation exchange factor, could be a constant, or dependent of emissivity and other optical parameters of the powder, its various forms have been collected by Sih [98]. In the present case, the emissivity will be used for F.

The temperature dependence of emissivity has been calculated based of the work of Demange [99] (Figure 68).

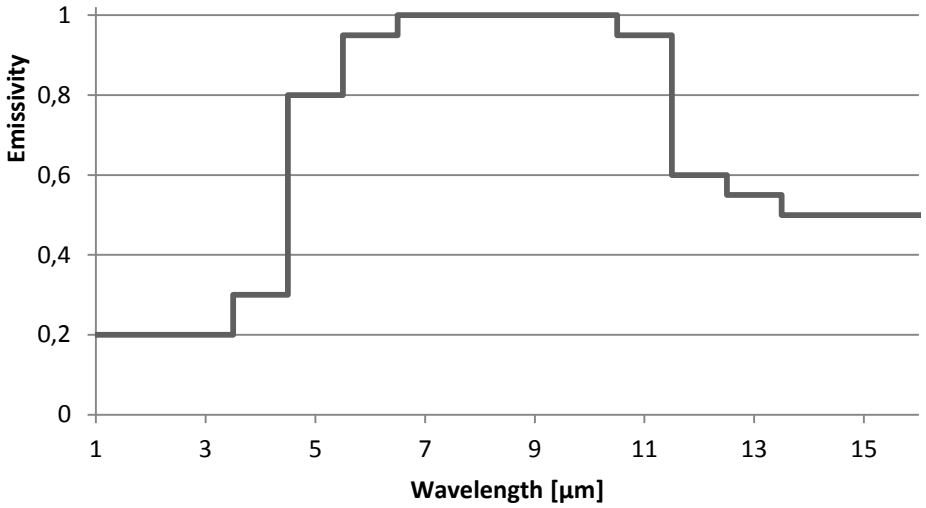

Figure 68: Approximate emissivity of alumina (25% porosity)

The scale order of magnitude of the results (Figure 69) shows that even at high temperature, the radiation has little influence on the overall effective conductivity of the powder, as it is representing only 2.4% of the conductivity calculated by the two-level Krischner model at 900 °C. For this reason, the radiation between the particles were neglected in the following model.

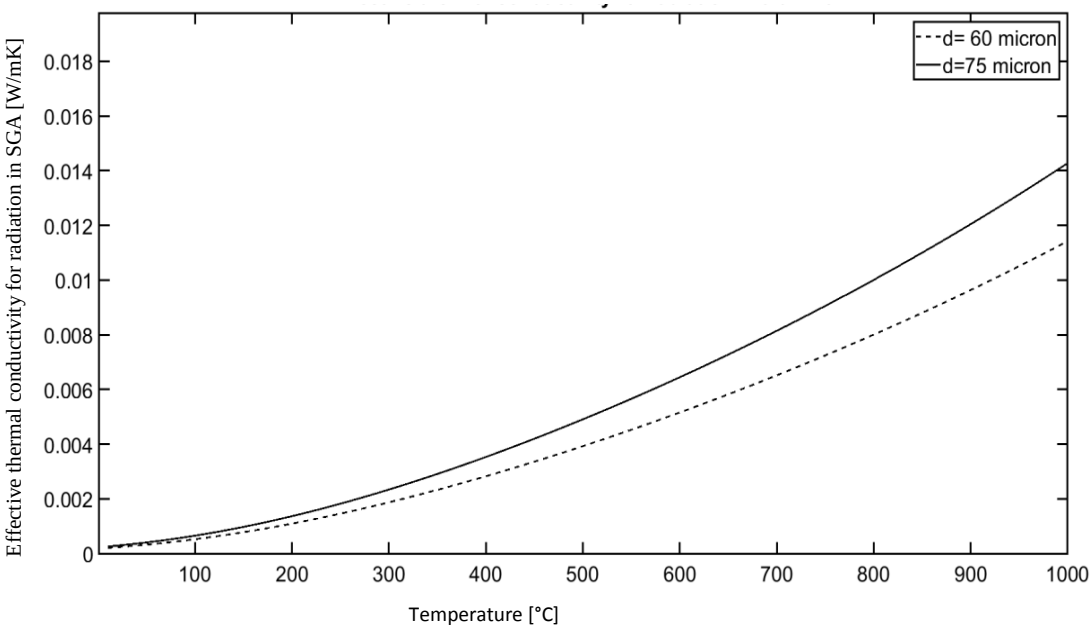

Figure 69: Effective thermal conductivity for radiation in function of temperature

4.1.2.5 Discussion and conclusions

Thermal properties of primary smelter grade alumina were measured at room temperature, 60 °C, and at high temperatures for up to 900 °C. It was found that the moisture content has significant effect on the thermal properties of alumina at room temperature, and even more so at 100-300 °C temperature range. While at room temperature, the effect can be described in a straightforward fashion: moisture content increases effective conductivity, at higher temperature range the effect of the moisture content depends not only on its quantity, but the type it is bonded to the alumina.

It should be noted for this particular temperature range that due to the difference between the industrial application and the circumstances of the test (slow rate of heating and samples contained in a closed space as packed bed in the monotonic ramp heating device), the results cannot be directly applied to alumina injections, as in that case, the rapidly evaporating moisture throws the powder apart, spreads it on the bath surface and mixing the particles of different temperatures, and even the liquid at some extent.

While the room temperature measurements can be applied to investigate the preheating of alumina in the feeder, and the 300-700 °C range to model the upper part of an already formed alumina raft, above 700 °C another effects should be considered as well: the early infiltration of the bath, and the sintering that may occur between the particles in the presence of fluoride.

The two-level porosity model gives comparable results to the measurements. The advantage of a two-level model is that it gives the flexibility to predict the conductivity with different packing

density – such as looser packing in a raft that was created by alumina with high moisture content, blowing the powder apart and settling; or compressed alumina discs, used by the authors to represent artificial rafts, investigating raft behaviour while keeping control on its shape.

4.1.3 Two-dimensional thermal model of raft

A two-dimensional thermal model was developed with finite difference method, explicit scheme, front tracking method, control volume approach. The model includes convection and radiation on the top surface of the disc top, axial and radial (in 2D) heat conduction in the powder and the frozen bath, solidification of bath in both directions, convection on the bath side. For the selected spatial and time steps, the model fulfilled the von Neumann stability criteria.

The image below shows the different zones in the model, the dark red being the alumina raft, the orange the frozen bath, the dark blue the liquid bath, with yellow and the lighter shade of blues are the transitional zones where the frozen bath layer grows or re-melts (Figure 70).

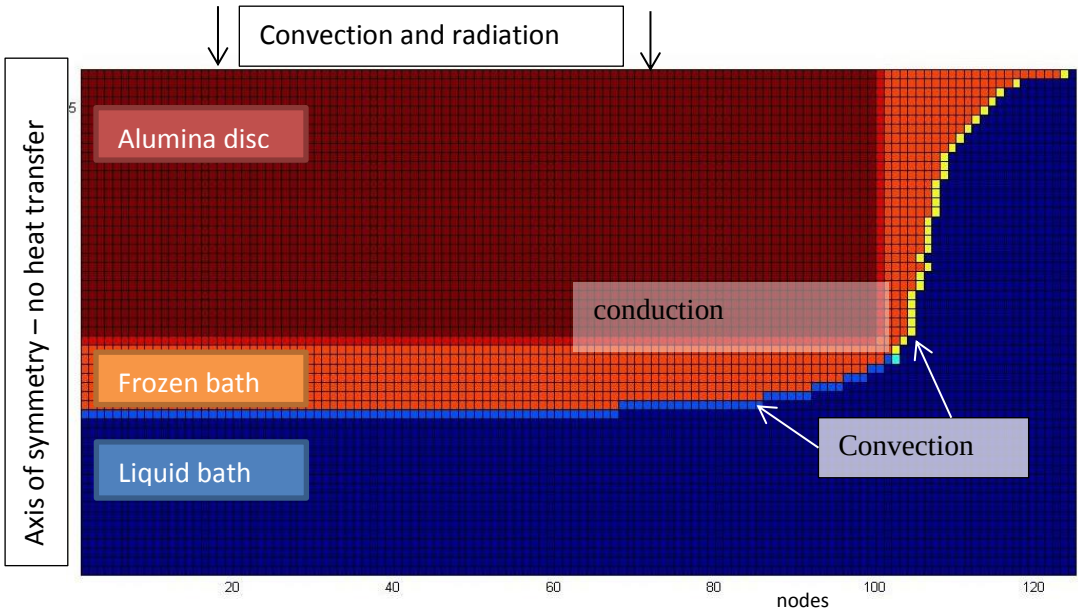

Figure 70.: Shape of frozen bath around an alumina disc, different zones of mathematical model ©Csilla Kaszas

On the front of phase change, the temperature of the cells is liquidus temperature. In each time-step, the outer radius (yellow zone) or the thickness (light blue zone) of the cell changes according to the heat balance, the enthalpy of the phase change and the previous size of the cell. If the size of the border cell exceeds the size of two regular cells, they get divided; if the cell

would shrink under the size of a regular cell, it gets merged with its neighbour. The phase change occurs at one (the liquidus) temperature in the model.

As the model results are to be compared with the compressed discs, the conductivity of the alumina was adjusted accordingly, the inter-particle porosity in the conductivity model was decreased by 10% compared to loose alumina powder. While the infiltration is driven by capillary forces, in the circumstances, the limiting effect of temperature is dominant, therefore the infiltration in the model is related to temperature only, the capillary forces were not considered. To account for the effect of the infiltration, above 800 °C, the pores were assumed to be filled with bath, with a thermal conductivity of 1 W/mK. Between 700 and 800 °C a zone of partial infiltration was assumed with linearly increasing conductivity (Figure 71).

The density of the compressed disc is also calculated based on this assumption, the density increases linearly from 1.3 to 2.7 g/cm^3 between 700 and 800 °C. The skeletal density of solid cryolite is 2.8 g/cm^3, however the measured values of frozen bath move around 2.3-2.4 g/cm^3. In the model 2.5 g/cm^3 was used.

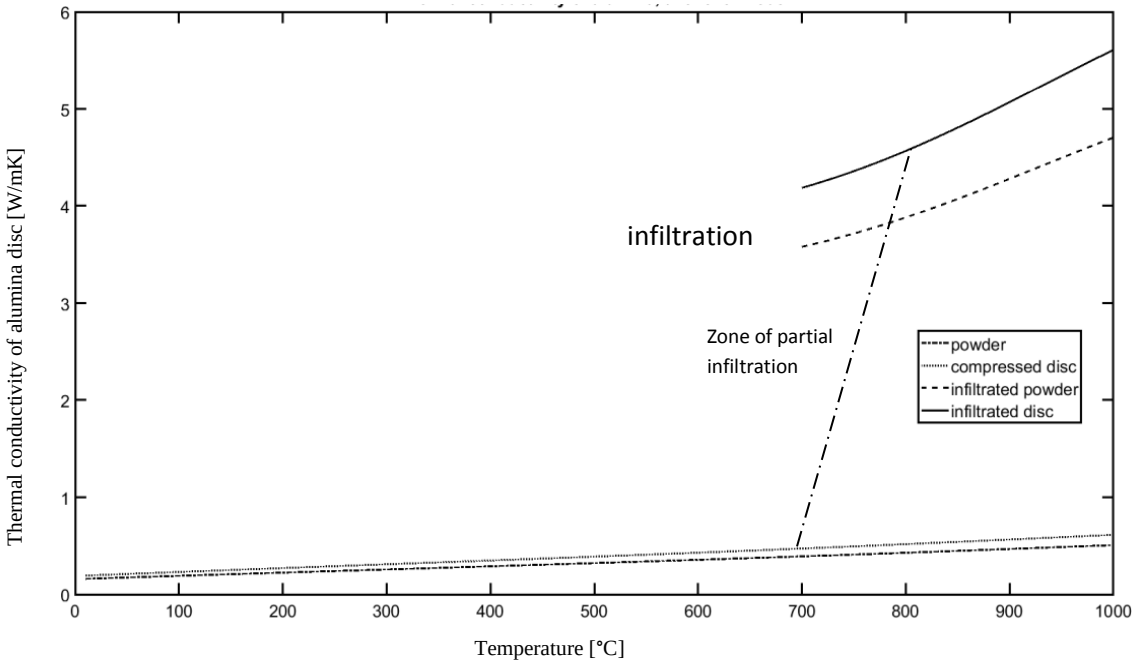

Figure 71: Thermal conductivity of alumina disc in thermal model

Walker [33] used 0.6 W/mK for the conductivity of the frozen layer. He might have taken room temperature measurements as his basis. Dassylva [43] presented measurements at 600 °C where the conductivity of frozen bath reached 1.5 W/mK. In the present model, 1 W/mK is used throughout. Walker assumed that the thermal conductivity of the infiltrated agglomerate would

approach that of the frozen layer; however, the conductivity of alumina is significantly higher, not to mention the effect of sintering on the improvement of conductivity.

The convective heat transfer coefficient was imposed as 800W/m^{2}K [43] on the bottom and side of the disc, neglecting the partial immersion at insertion, and 100 W/m^{2}K on the top surface. Radiation between the top and the room temperature environment though the opening was considered with 0.4 view factor. The same view factor was given to the radiation between the disc and the carbon walls of the crucible; the surface temperature of the latter was assumed to be equal to the liquidus temperature. Radiative heat transfer below the bath surface was not considered. The heat of solidification was 550 kJ/kgK. To account for the evaporation, the initial temperature of the disc was set to 100 °C.

4.1.3.1 Results

The 700 °C isotherms show similar tendencies as the measured infiltration fronts in the compressed disc (Figure 57, Figure 72). The apparently slower infiltration in the model can be attributed to the lack of the exothermic energy of alpha-gamma transformation, which is not included in the present model. Also, the thermal conductivity in the infiltration zone could have been ramped up in a shorter interval of temperature.

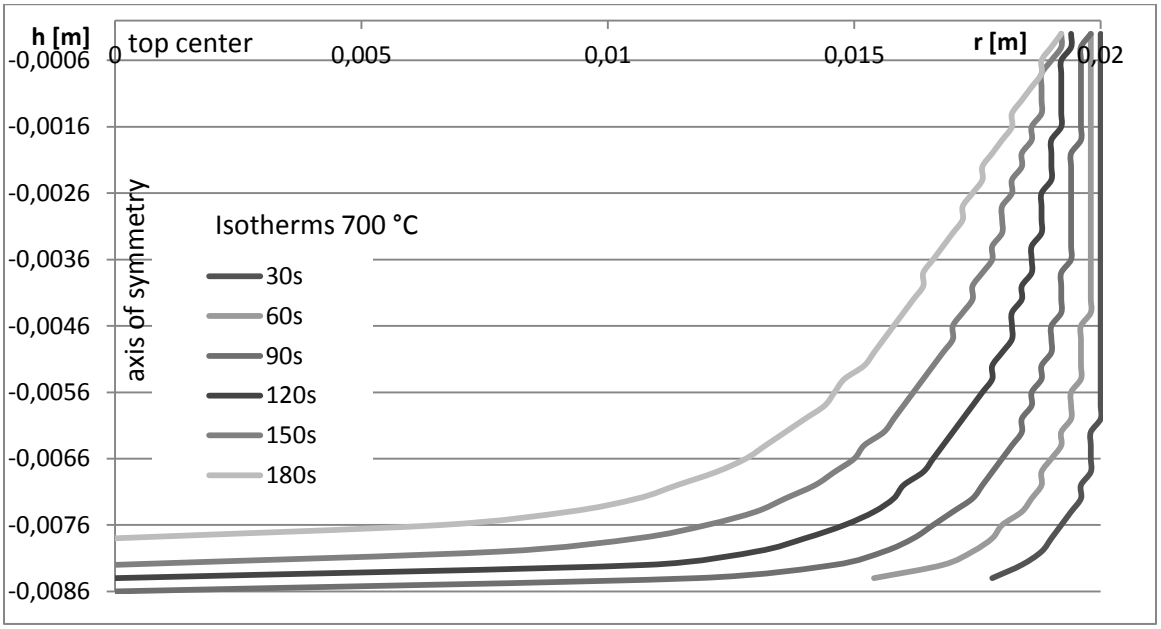

Figure 72: 700°C isotherms in discs, for 35°C superheat and 500 °C temperature above disc

The temperature distribution in the disc shows that, although the effect of heat transfer is less pronounced on the top of the disc, it is still present (Figure 73). After two minutes the temperature on the top is higher than a few millimetres below, closer to the center.

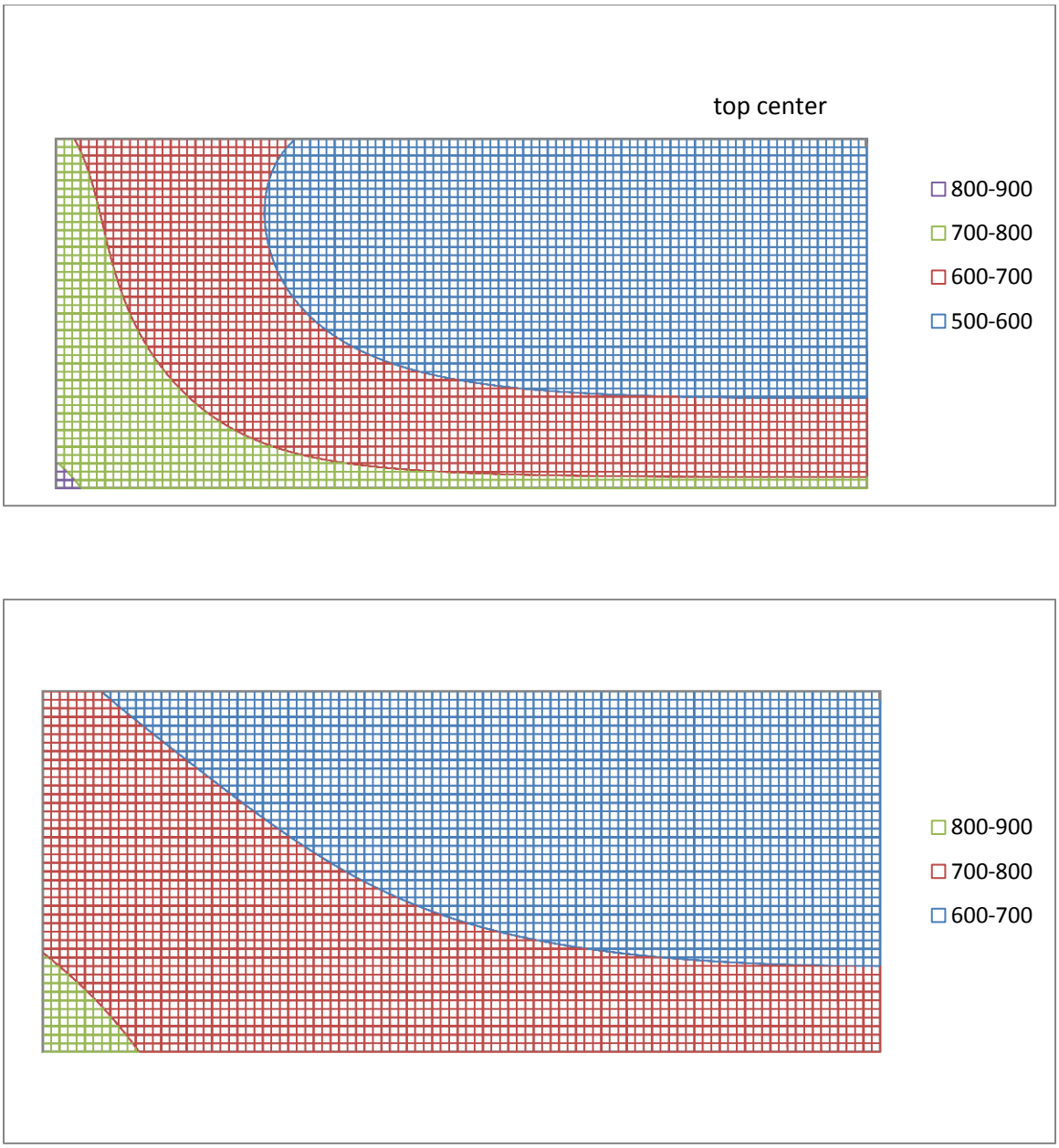

Figure 73: Temperature distribution in disc after 120 and 240 seconds

The temperature of the air, or rather, of the gas above the disc has significant effect on the temperature on the top of the disc, and this eventually translates into the increase of apparent density when the infiltration starts (Figure 74). The apparent density of the discs was calculated based on the mass and volume of compressed disc and solidified bath. The temperature-dependence of the disc's density was following the same assumption as the determination of the effective thermal conductivity: linear increase between 700 and 800 °C, at which point the bath fills out the available pore volume.

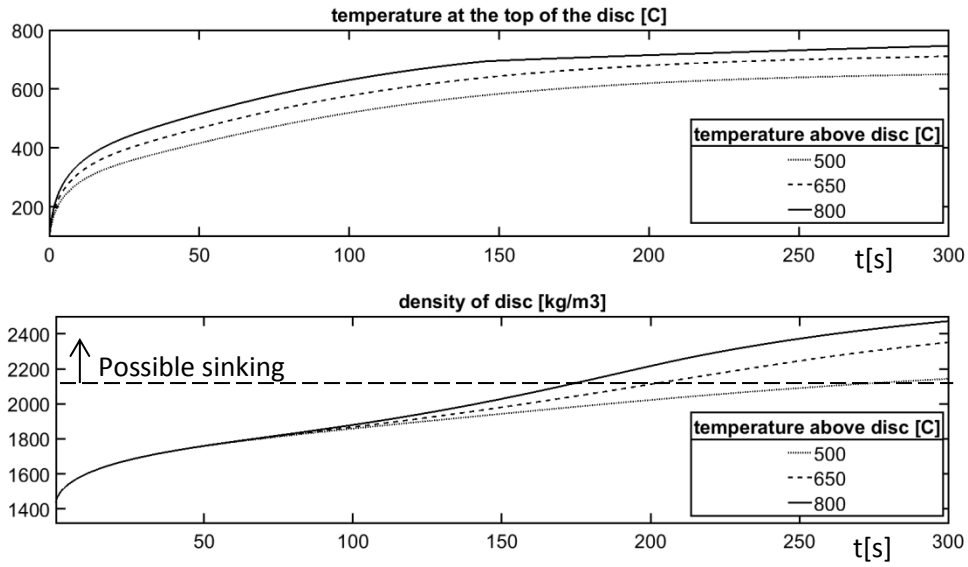

Figure 74 Evolution of temperature and density of compressed disc, result of model, superheat: 35 °C

Meanwhile, the temperature of the gas had little effect on the thickness of the frozen bath layer on the bottom. Similarly, the superheat does not influence much the temperature at the top of the disc even if we use unrealistic high values in the simulation (Figure 75).

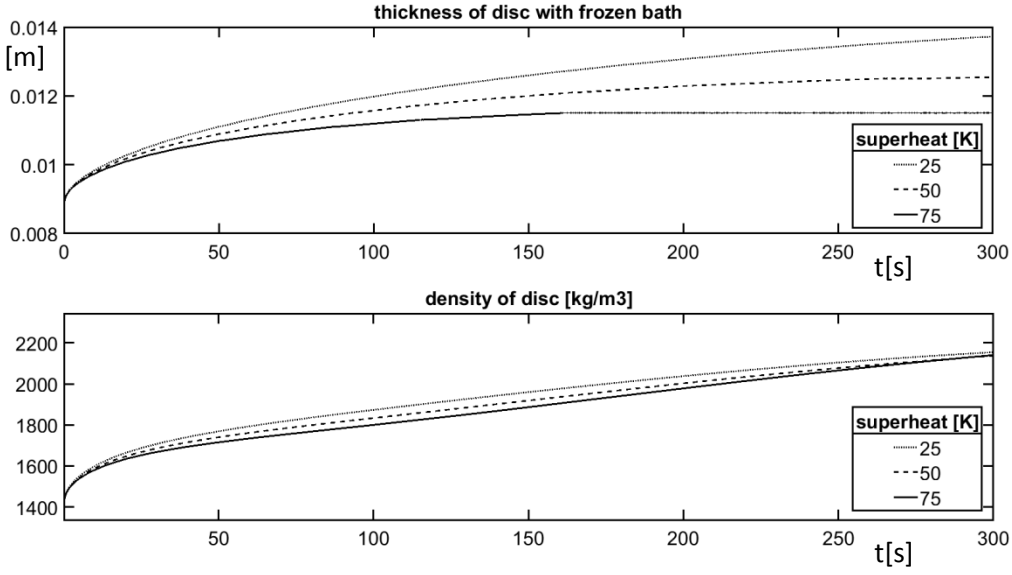

Figure 75: Evolution of the thickness of frozen layer and density of compressed disc, result of model, air temperature: 500 °C

With 75 °C superheat, the bath solidification in the center stops in around two minutes. As there was less frozen bath, the increase in apparent density as slower in those two first minutes, however the disc warms up faster, and due to the infiltration, the apparent density reaches the discs with lower superheat five minutes after insertion.

The two-dimensional model could be improved with the integration of the heat, generated by the gamma-alpha recrystallization, and a more precise estimation for the boundary conditions. However there are two other aspects that are even more crucial: the initial conditions and the disintegration of the raft. In the model and the corresponding experiments, compressed alumina discs were used with known dimensions and mass. If the same mass of powder would be fed into the bath, the raft would already contain somewhat less alumina, due to the initial dispersion. The powder would also mix at some extent with the bath, leaving the boundary layer not well defined, and we should account for that in the model as well. More importantly: the disintegration of alumina rafts is hindered by sintering. While sintering has been researched by many, as of yet there is not a model that would predict the force and strength of the bonds created by sintering, therefore there is also no predicting how much those bonds should be dissolved that would permit the disintegration locally. Dissolution in the model could be applied to the outer surface (bottom and side) of the disc, while on the inside the penetrating bath would soon become saturated and would only exchange matter with the main body of bath via diffusion through the tight pores of the alumina raft. In reality, the detachment of the saturated bottom layers of the rafts drive the dissolution process, and for the moment, the inclusion of that in this model could only happen by giving arbitrary condition for the detachment.

4.2 Influence of moisture content on the structure of alumina rafts

The previous sub-chapter presented a model for the evolution of the apparent density of alumina. In the model and the experiments with compressed alumina discs, the initial parameters of the rafts are known and unchanged; the powder remains a “fixed bed”.

In the previous chapter, the influence of moisture content on the shape of the alumina raft had been presented (3.2.3), but the influence of moisture content extends beyond the macroscopic shape of the raft: it also affects its internal structure.

4.2.1 Experimental

Primary smelter grade alumina was pre-dried overnight at 150°C and 550 °C temperature, then let cool down in hermetic containers, or alternately, left undisturbed to adsorb humidity from the environment. During the tests, 14 g of powder was injected onto the cryolitic bath surface in the setup previously described (3.1.2). The rafts were removed 45 seconds after injection, and weighted at room temperature. The bath had been previously enriched with alumina to prevent dissolution.

The cryolitic bath was removed from the samples by leaching. The samples were broken into pieces less than a millimeter of size. 5 g of each type of raft was boiled in 100 ml aqueous $AlCl_3$ solution (200g/l) for 6 hours. The solution was changed every 2 hours. As the solution dissolves

cryolite, the leaching procedure results in the sintered alumina skeleton of the raft, without the bath that previously filled the pores. The remains were filtered through glass microfiber filters (grade 169, 1 micron retention), and dried at 300 °C.

The leaching process was loosely based on Rio Tinto's documentation, describing a method to determine alumina content of the bath (method 538). The document stated that alpha alumina is not soluble in the aluminium chloride solution, but did not mention other phases, that could possibly still have been present in the raft samples. To verify that the $AlCl_3$ has no significant effect on the structure of alumina, primary alumina was also subjected to leaching.

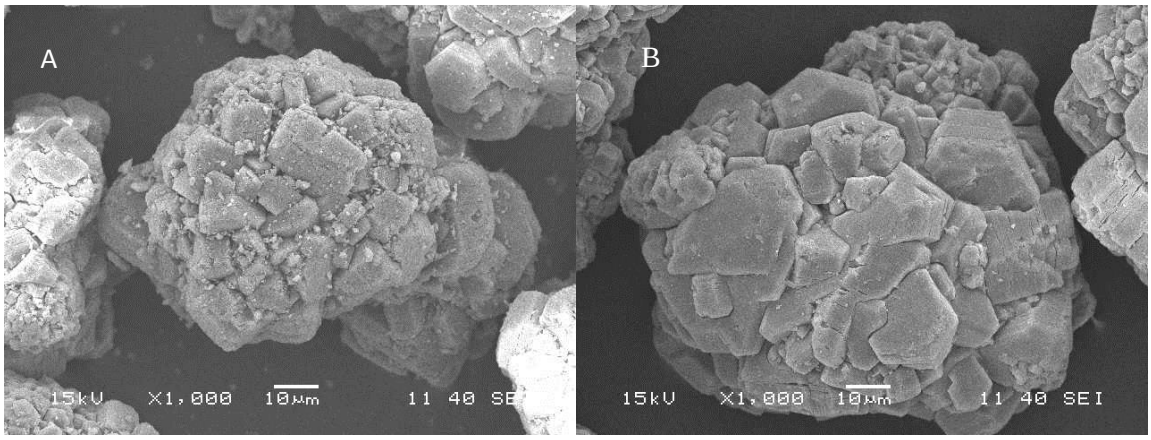

Figure 76: SEM imaging of untreated (left) and leached (right) primary alumina (x1000) ©Csilla Kaszas

As the SEM imaging shows (Figure 76), the leaching did not change the overall shape and structure of large alumina particles. The apparent difference is that the untreated alumina contains fines, presumably mostly alpha-phase alumina, covering the surface of the large particles, despite the fact that the sample has been blown with compressed air during preparation for the electron microscope imaging. The fines were discarded during the leaching process, albeit it was probably due to the washing of the powder, and not the effect of the aluminium chloride itself.

Leached and untreated samples were subjected to porosity analysis at the Laval University. The samples were degassed at 150 °C in flowing nitrogen for 16h before the measurements. The surface area and pore size distributions were characterised by nitrogen adsorption and desorption, obtained at 77K on a Micromeritics Tristar II 3020 porosimeter. The specific surface area was calculated using the BET (Brunauer-Emmett-Teller) equation [100]. The pore-size distribution was calculated from the desorption branch of the isotherm using density functional theory (DFT) and BJH (Barrett, Joyner, and Halenda) method [100]. Besides samples from the infiltrated part of the rafts, discussed in this sub-chapter, another sample was analysed: powder was scratched with a spoon from the front of infiltration of compressed alumina discs (Figure 77), where the recrystallization had already started, but the infiltration by the bath had not been complete. As a large number of these partially infiltrated discs were available, it was possible to collect enough powder for the porosity analysis.

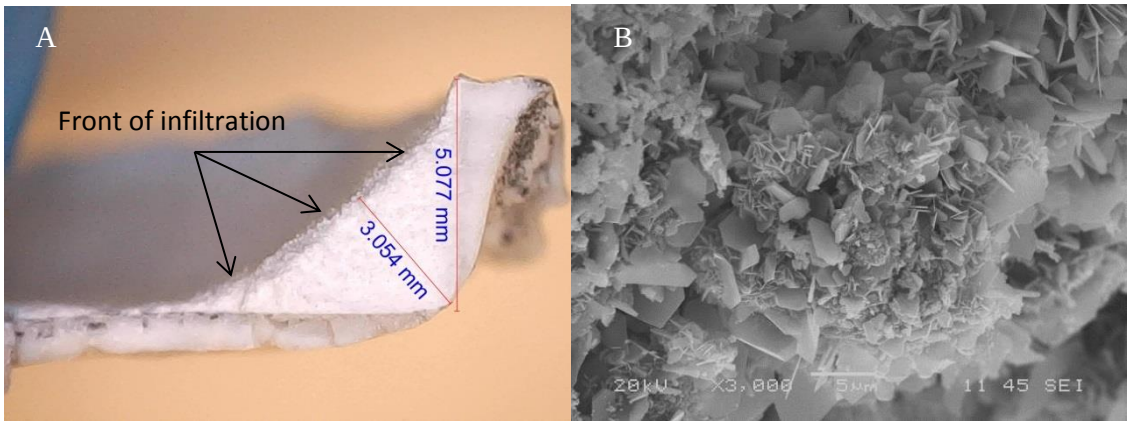

Figure 77: Front of infiltration for compressed alumina disc,
'A' photo with digital microscope, 'B' SEM imaging ©Csilla Kaszas

4.2.2 Composition of rafts

Alumina that had not been subjected to drying, and alumina, dried at 150 °C spread flatly over the entire available bath surface. The infiltration rate of the former was the fastest, closely followed by the latter. Alumina dried at 550 °C did not spread as the others, and its infiltration was far from complete at the time of raft removal.

Upon inspection of the cooled samples, rafts made with alumina containing moisture were less dense, more porous, while the infiltrated and solidified parts of the raft made with dry alumina were harder and denser. This is due to the evaporating moisture, agitating and partially freezing the bath at the same time, which leads to enclosed bubbles and non-infiltrated particles, or clusters of particles getting trapped below the bath level.

The rafts were weighed after removal, the loose powder separated from the infiltrated part. Assuming that there had been no dispersion upon injection, the mass composition of raft samples is presented in the next diagram (Figure 78).

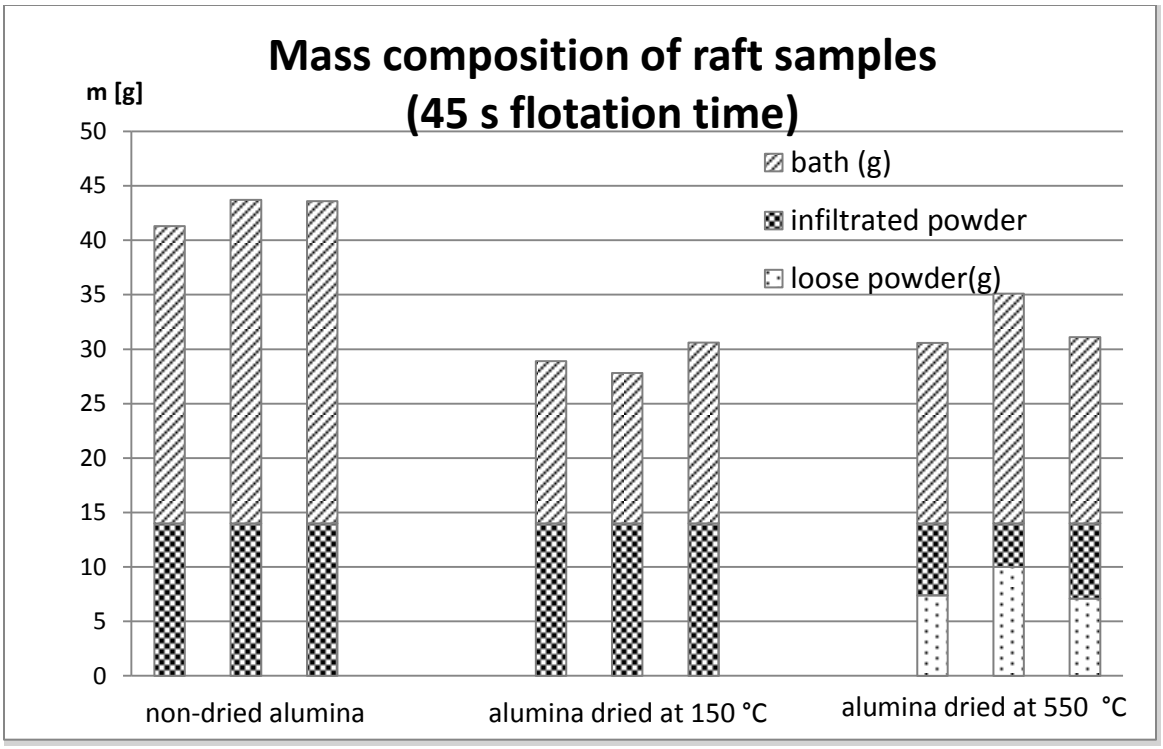

Figure 78: Composition of raft samples, assuming no dispersion occurred upon injection

The alumina containing the most moisture gained the most mass during raft formation. Since the heat demand of evaporation is significant, this is not surprising.

There is little difference in the final mass of the other samples. Alumina containing chemisorbed water formed slightly lighter rafts during the given period of time than that without moisture. It is somewhat curious for a number of reasons. The energy demand of desorption should increase the mass of frozen bath. Due to the agitation by volatiles the heat transfer is faster. The infiltration suggests that all of the powder in the alumina containing volatiles had warmed up to at least 700 °C before removal, while the dry alumina still contained loose, relatively cold powder. What might be the reason for this discrepancy then?

One possibility is that due to the increased heat transfer, the gamma-alpha recrystallization was faster in the alumina containing humidity, and this exothermic reaction provided more than enough heat for the evaporation of the moisture.

Another explanation might be a theory discussed in the previous chapter: that the evaporating moisture is at least partially responsible for the initial dispersion of a portion of the injected powder. This would mean that the infiltrated powder in the two first types of samples is less than the injected 14 g, and there is actually more frozen bath than it was assumed.

The alumina content of the solidified samples was estimated based on the previous assumption and weighing, and it was also measured by leaching (Figure 79).

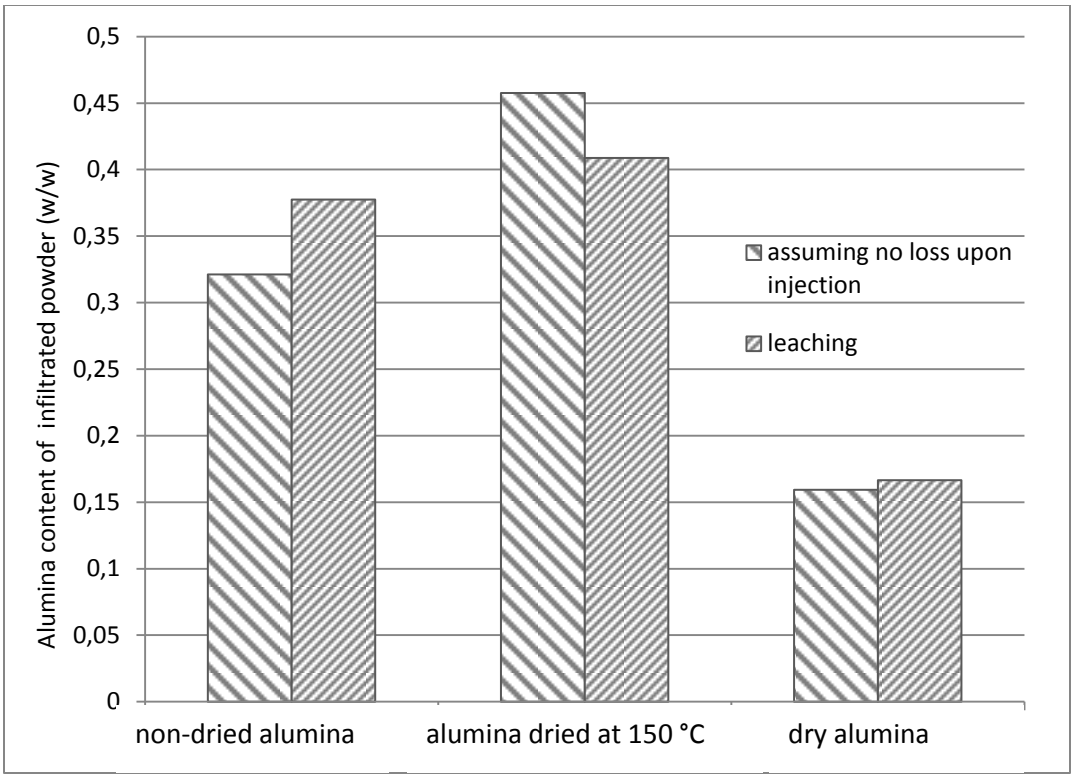

Figure 79: Alumina content of infiltrated powder

Leaching had been historically used as a method to determine alumina concentration of bath; however it was not its purpose in the frame of this work. The rafts samples were broken up to pieces, but were not ground, to preserve the underlying structure. There could have been still bath in the middle of some pieces, and fines could have been washed away and run through the filter. Another observation was made when the samples were removed from the warm furnace and taken to weighing: the cooling alumina on the scale was visibly gaining weight via adsorption of humidity from air. For these reasons, high precision could not be expected from this data.

In comparison with the previous calculations, leaching gives a similar value for alumina dried at 550 °C. The alumina content for non-treated alumina was shown higher by leaching, while for alumina dried at 150 °C, the one most at question, the alumina concentration was found to be lower.

4.2.3 Porosity analysis

To see the change of the pore structure during infiltration, samples from the experiments were sent to porosity analysis to University Laval, courtesy of Houshang Alamdari and his group, who specialises in another area of aluminium production [101] [102].

Porosity analysis of smelter grade alumina has been done for decades; however, the only data of interest was the BET surface area of the powder. In a simplistic way of thinking, larger surface area means larger contact surface between alumina and bath, therefore faster dissolution. As

we know already, it is not as simple as that, partly because alumina does not keep its pore structure once it gets in contact with the hot bath.

Table 11: BET surface area of samples

Sample	Treatment	BET surface area (m^2/g)
Primary alumina		75,07
	leached	78,00
Front of infiltration		42,27
Raft from undried alumina		2,18
	leached	16,36
Raft from alumina dried at 150 °C		2,41
	leached	17,52
Raft from alumina dried at 550 °C		1,00
	leached	13,51

Leaching increased the surface area of alumina by 4% (Table 11). It is not a significant change and easily explicable by the lack of fines in the leached samples (Figure 76). As the smaller particles would have contained more alpha phase alumina, and therefore less porosity, the remaining larger particles would have larger specific surface area as a consequence (1.1.2).

The untreated (not leached) raft samples had a small surface, since most of the pores would have been blocked or filled with frozen bath. The rafts made with dry alumina, which was the densest, had less than half the pore surface than the other untreated samples. The fact that there was, even a little surface area to be measured is likely due to the circumstance that the raft had cooled below 900 °C and the materials shrunk.

Leaching opened up the pores by removing the solidified cryolite. The BET surface area of primary alumina decreases from 75 to 42 m^2/g at the front of infiltration, and further to 13.5-17.5 m^2/g after 45 seconds contact with the bath.

Although it is not commonly investigated, in the recent years the porosity of smelter grade alumina has been studied to shed light on its fluoride adsorption capacity. The pore size distribution of the primary alumina, provided by Rio Tinto (Figure 80) and presented below, is comparable to that in the work of Dando and Lindsey [103].

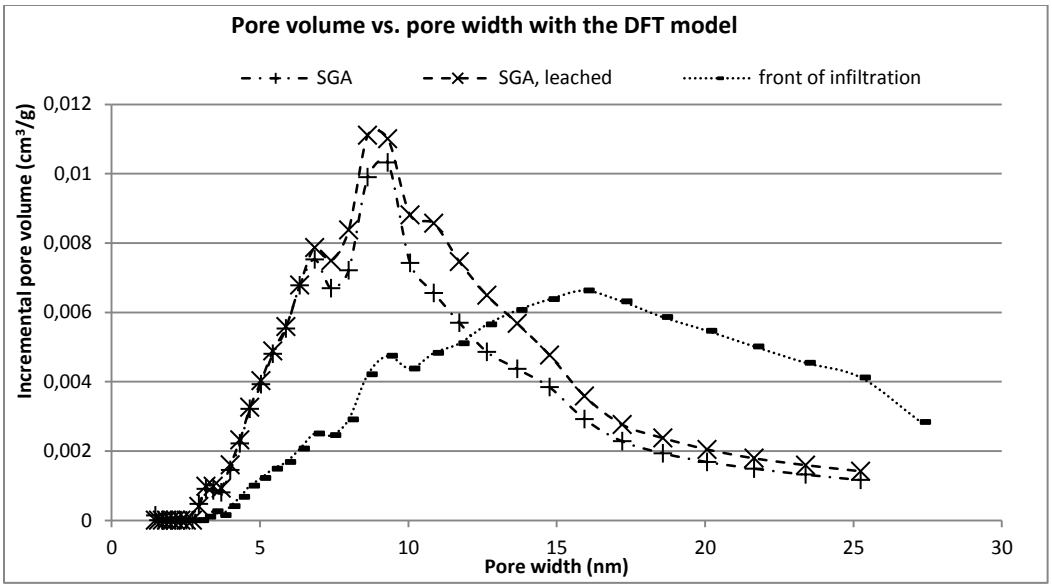

Figure 80: Porosity analysis of SGA

The leaching had no significant effect on the pore structure of primary alumina.

The specific surface area decreased as the alumina got in contact with the bath and started recrystallization, while the pore volume and the mean pore diameter increased. The pore size distribution is multimodal in SGA, and less prominently, but also in the alumina at the front of the infiltration. This indicates three different pore types in SGA, with the averages of 3, 7 and 9 nm – possibly related to three different transitional alumina phases. While these peaks are still present at the front of infiltration, their pore volume is halved while another peak appeared at 16 nm.

For the analysis of larger pores in the raft samples, the BJH model was applied (Figure 81).

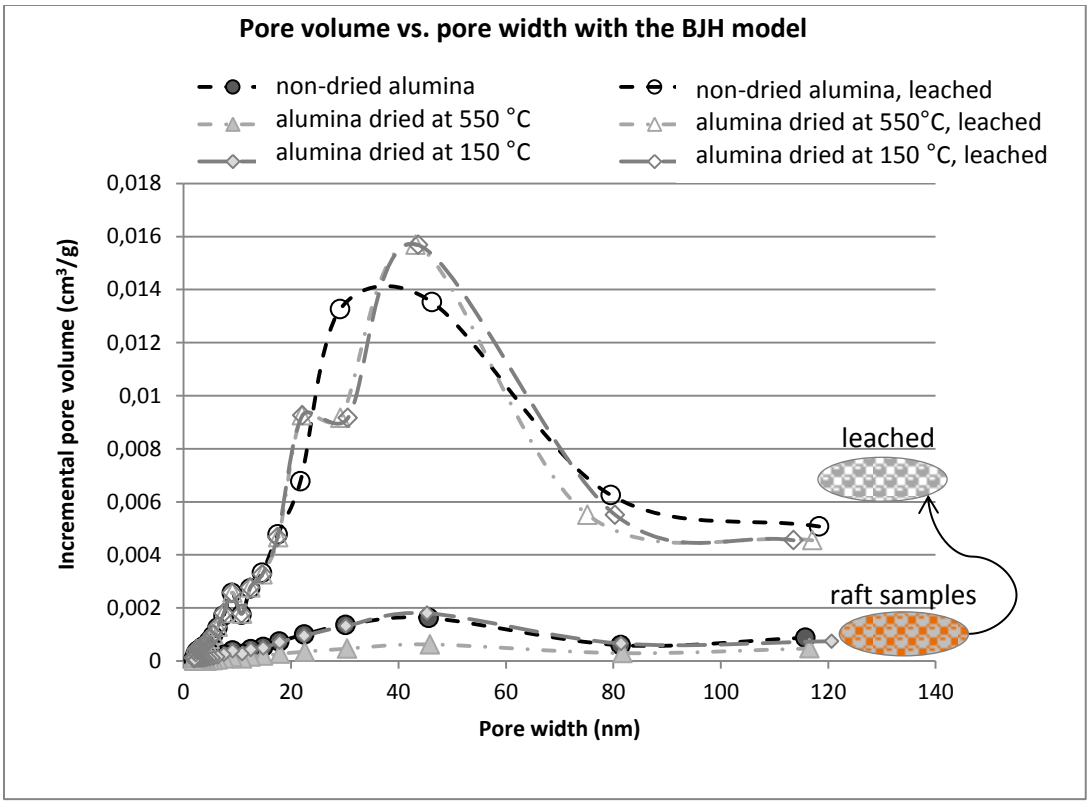

Figure 81: Pore size distribution of alumina rafts (BJH)

Raft samples before leaching show a low porosity, as the bath occupying or blocking the pores was still present. The pore size distribution was similar in these samples, with a peak at 45 nm. The pore volume of the raft made with dry alumina was proportionally lower along the different pore widths.

After leaching, the pores opened up for analysis. The pore size distribution has two peaks at 22 and 44 nm when the alumina contained no, or very little water. This suggests that these changes in the pore structure are the results of recrystallization. While a little humidity has big effect on the large scale behaviour of alumina fed into the bath, and on the distance and relation between alumina particles, the evaporation of chemisorbed water does not have a significant effect on the pore structure inside an alumina particle exposed to cryolitic bath. Interestingly however, the pore size distribution of the sample made with non-dried alumina was a little bit different. The two peaks present with the other samples are not distinct, which indicates that the evaporation of the larger quantity of moisture might have cracked those pores wider.

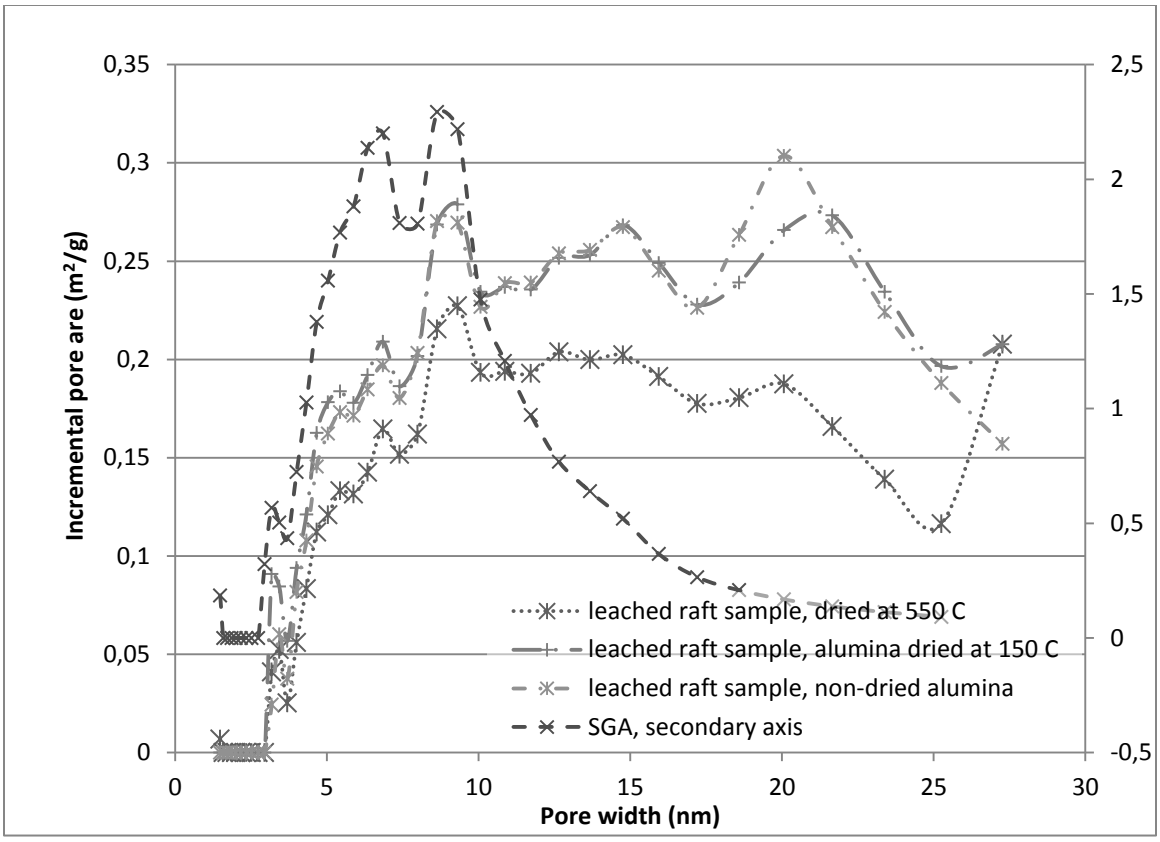

Figure 82: Pore size distribution of leached raft samples and alumina (DFT)

Concerning the smaller pore sizes (Figure 82), the peaks at 3, 7 and 9 nm are present in all leached raft samples, as well as the original SGA. Another peak appeared at 5.5 nm in the rafts that was not distinguishable in SGA, because of the proximity of the larger peak at 7nm. The incremental pore area in the rafts belonging to these pore sizes is 10% in SGA, meaning approximately 10% of the structure was still unchanged. The larger relative decrease at 7 nm indicates that the related phase corresponding to that pore diameter changed faster than the rest of the alumina.

The raft made with completely dry alumina showed less porosity at lower pore sizes, indicating that more of the original structure has been changed. How is that possible? All of the rafts were removed 45 seconds after injection; however that does not mean that each and every particle had spent 45 seconds in contact with the bath. Rafts made with not, or not completely dried alumina were infiltrated just below 45 seconds, so some parts were only recrystallizing for a second before the raft was removed and the liquid bath frozen. For rafts made with dry alumina, some of the powder got in contact with the bath right away but more than half of it was still not wetted by the time the raft was removed. Therefore, it is possible that particles in the infiltrated part of the dry alumina raft spent on average more time exposed to the bath than those in the rafts made with non-dried alumina.

4.2.4 Other possible effects for larger quantities of powder

The experiments in the previous sections had been conducted with 14 g alumina, which is only a fraction of the dosage in an industrial cell. Admittedly, there should be differences, but also, similarities.

If the injected powder is dry, it exerts an impact on the particles on the bottom with a high velocity and has a compressing effect on the powder. Evaporating moisture lifts the particles and they settle more evenly with a lower speed, which would have a loosening effect on the raft as a whole, even with larger batch-sizes (Figure 83).

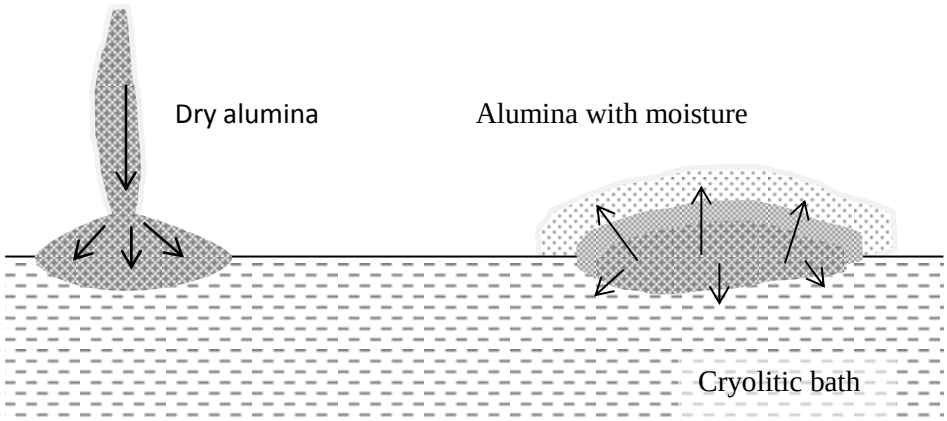

Figure 83: Structure of alumina raft with or without moisture ©Csilla Kaszas

Larger batch size means thicker rafts with equal available surface. The thicker the raft, the higher the pressure could build up due to evaporating moisture before a vapour bubble could escape by displacing the powder. The small rafts in our experimental cell appeared to be homogenous, but those that other researchers, like Walker [33], had removed from industrial cells were not. Clusters of powders enveloped in frozen baths were found. The raft's disintegration in the form of large and thin flakes also indicates that the structure is generally not homogeneous. The proposed mechanism for the local behaviour of thick alumina rafts is presented below (Figure 84). When the raft is thin, the evaporating moisture can escape rapidly. In a thick raft however, the powder above limits the vapour flow and the pressure increases locally, at the bottom of the raft where the vaporisation is the most prominent. The pressure builds up until it can displace and lift some of the powder to permit a gas bubble to rise to the surface. The escaping gas pushes some powder along to the surface and into the air, manifesting as a so-called geyser on the top of the alumina. Meanwhile, the pressure drops in the bottom, making it possible for bath or fresh powder to enter into the void.

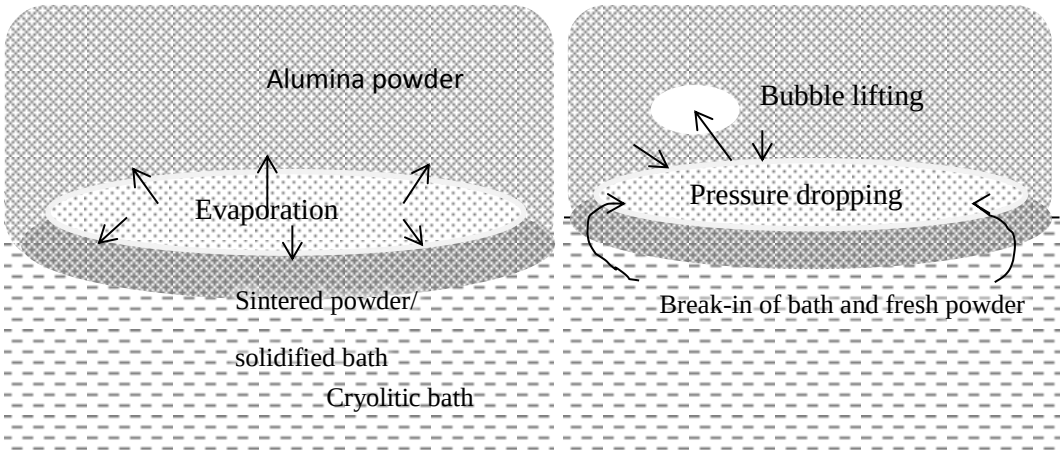

Figure 84: Proposed mechanism for local behaviour of thick alumina raft ©Csilla Kaszas

4.3 Infiltration experiments in steel tubes

Infiltration of SGA can be blocked by the solidification of the liquid, due to the low temperature of the alumina and low superheat of the bath; however, when the thermal conditions allow, it is still driven by surface tension, and at a lesser extent, hydrostatic pressure. The contact angle and the pore-structure of the powder play an important role in the rate of infiltration. The following experiments were prepared to investigate the process of upward infiltration of the powder, in a one-dimensional setting.

4.3.1 Experimental

The experiments were not conducted at the usual experimental setup but a larger furnace to permit the high temperature for a larger depth of powder. A Pyradia furnace was used with 34 cm width and depth and 27 A nominal amperage. Stainless-steel tubes of 30 mm inner diameter were filled with alumina powder, inserted vertically into the bath, the bottom 1 centimeter submerged. The large crucible/tube diameter ratio ensures that the bath level does not decrease significantly as the infiltration progresses; also, that only the capillary (surface tension) force drives the infiltration, not the hydrostatic pressure.

Different methods were used to keep the powder in the tubes during insertion. Firstly, before filling the tubes with the SGA, the empty tube was placed on the bath level and a small quantity of alumina was added to form a raft, and effectively, plug the tube. While this worked to hold the powder, during the time spent in bath some of the alumina dissolved and dispersed, possibly severing the connection between bath and the rest of the alumina, stopping the infiltration. For this later, in the last set of experiments, a 50 micron mesh was used to keep the powder in the tubes.

The tubes were removed after a certain interval of time, the remaining loose powder poured out and the steel tubes cut. For the first set of experiments (A), thermocouples were placed at 15 cm from the bottom in the center of the tube and on the side. In the last set of experiments

(C) the front of infiltration was also followed by electrical conductivity measurements. Wires were set in place in two-bore thermocouple protective tubes, the resistance measured at the ends. As the front of infiltration reached the wires, the resistance dropped rapidly. Three sets of sensors were placed in different positions in two tubes in the C series.

For series A, one tube was inserted into the bath at a time, while later on three tubes were placed on the setup at the same time, parallel to each other (Figure 85). The tubes were removed at different intervals. Series B constituted of two consecutive sets of three tubes: BI, BII.

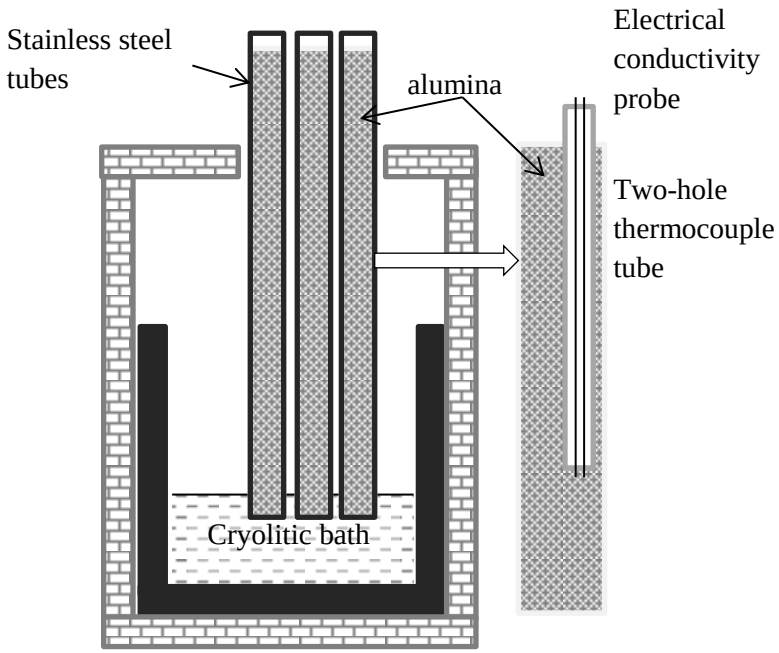

Figure 85: Schema of experimental setup for infiltration experiments ©Csilla Kaszas

With one exception, primary alumina was used, preheated to 500 °C, to make the manipulations manageable.

4.3.2 Results

4.3.2.1 Infiltration height

The conductivity measurements (C cond) indicate a linear increase in infiltration height during the first 25 minutes after insertion of the tube (Figure 86). For most of the samples, there is little increase between 30 and 45 minutes of retention time, it seems to tend to an asymptotic value about 200 mm. However, there is one outlier data above 300 mm that should not be disregarded. While during test B the top of the furnace and the tubes were covered well with insulating ceramic fiber blanket, the setup was left barer for test C to be able to manage the wires for conductivity measurements. The lower infiltration height for the C series is likely due

to heat loss and temperature and solidification-related limit of the setup. To reach the maximal infiltration height, isothermal conditions should be provided at a larger scale.

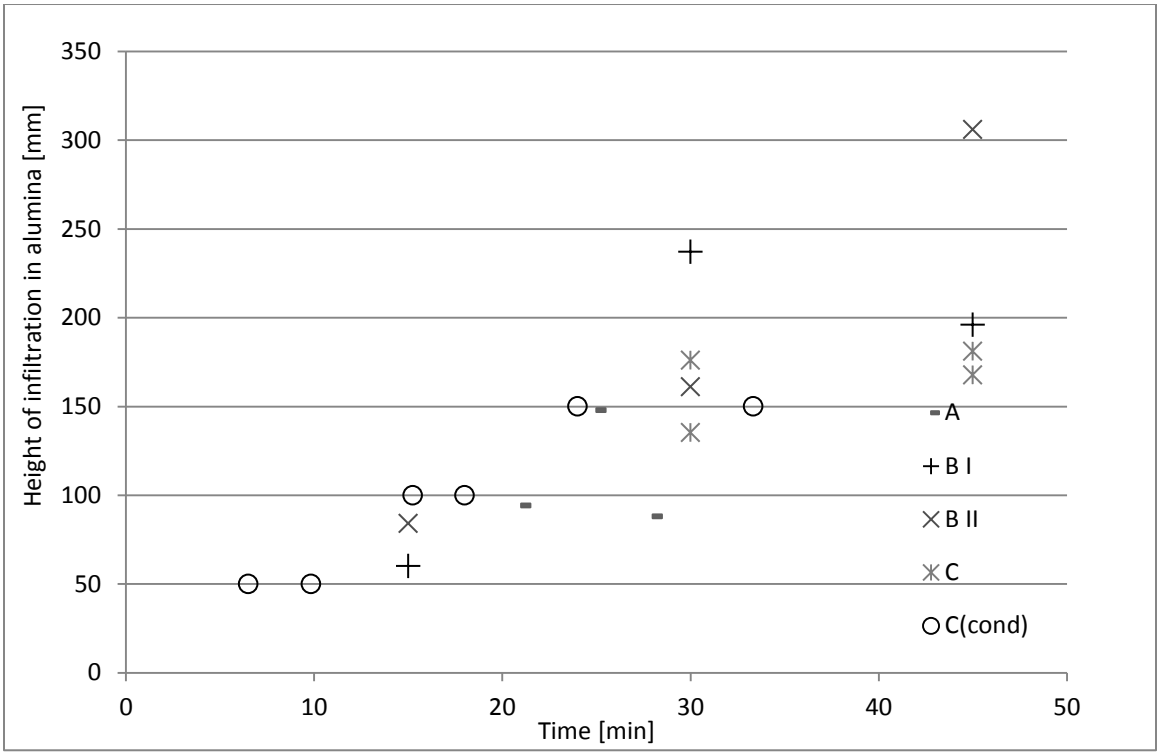

Figure 86: Infiltration height in alumina powder

We attempted to theoretically estimate the height of capillary rising in the alumina powder bed. For all intents and purposes, the average pore diameter of a powder is often substituted by the average particle size. The diagram below presents the dynamics of capillary rising of cryolitic bath in capillary tubes with diameter in the range of particle size of alumina powder (Figure 87), according to the Lucas-Washburn equation [104] (Equation 19).

$$\frac{dh}{dt} = \frac{r\gamma \cos\alpha}{4\mu}\frac{1}{h} - \frac{\rho_l g r^2}{8\mu}$$

Equation 19: Lucas-Washburn equation

Where h(t) is the meniscus height, ϒ is the surface tension, α is the contact angle, r is the capillary radius, ρ_l is the density of the liquid and μ (Pa s) is the dynamic viscosity of the liquid.

Assuming 100 micron diameter and isothermal conditions, the bath level would reach its maximum level above 200 mm in a capillary tube, in 5 minutes.

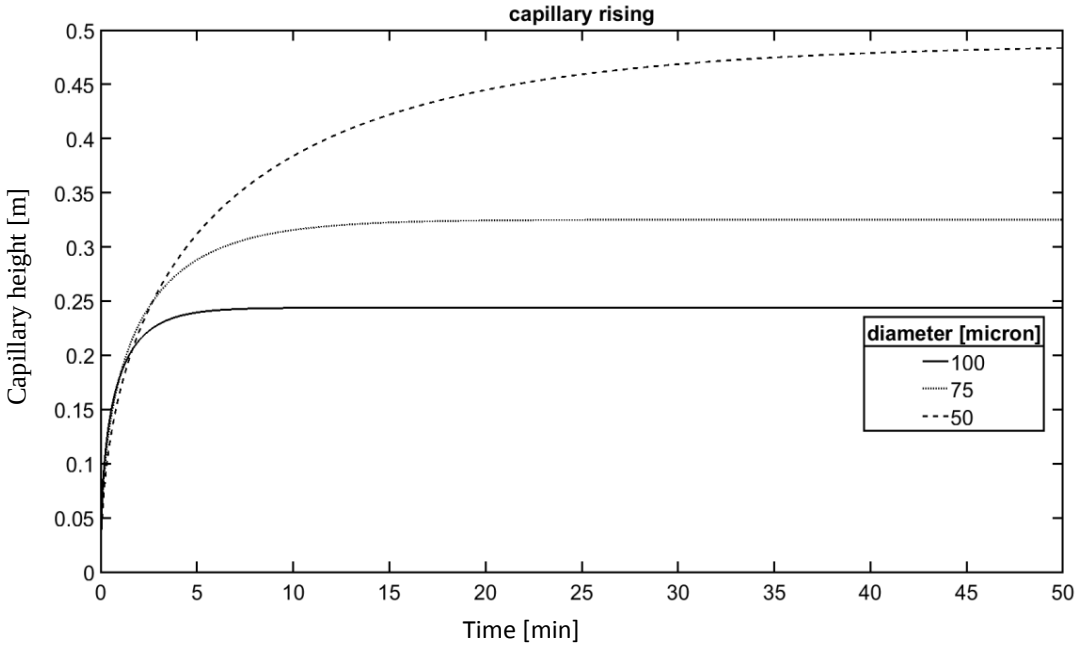

Figure 87: Capillary rising in vertical tube, contact angle 30°

4.3.2.2 Density

The apparent density of the infiltrated alumina was calculated from the mass, infiltration height and the internal diameter of the tube (Figure 88). The expected limit of apparent density is 2.5 g/cm^3; assuming that alumina transforms into alpha phase, no dissolution, and all the pores are filled with bath. Apparent density increases with the infiltration height. This tendency corresponds to the expectations. Alumina on the lower portion of the tube is exposed to fresh bath. As the electrolyte travels upwards, it gets saturated with alumina, therefore the upper portions would be less likely to dissolve. As the alumina dissolves, the solid fraction decreases, and the bath (with lower density than alumina) can take up relatively more space, henceforth the lower apparent density.

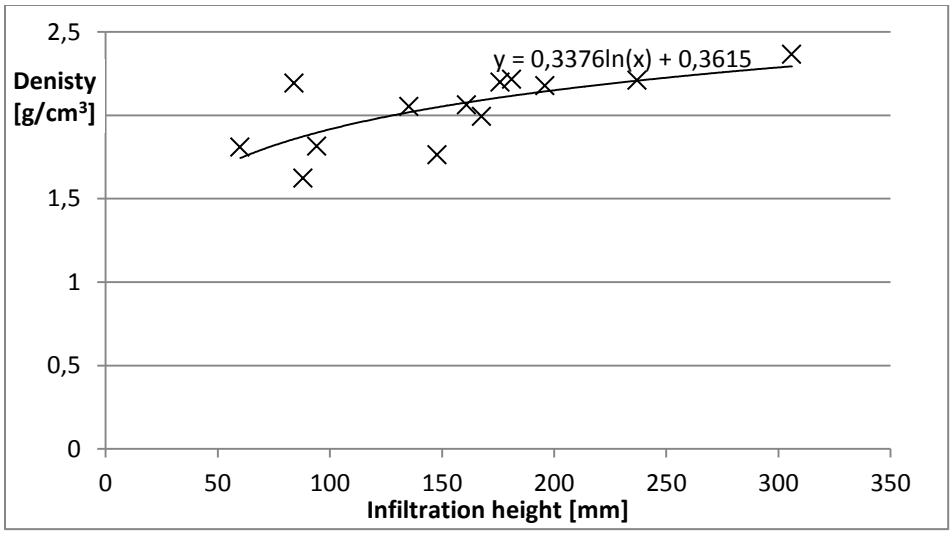

Figure 88: Apparent density of infiltrated alumina

From the tubes from series B, horizontal slices were cut, 2 cm and 10 cm from the bottom. The density of the samples was measured by Archimedes method (grav) and calculated from the thickness and mass of the slices (geom) (Figure 89). In some of the samples, smaller or larger holes were visible indicating that the dissolution was in a relatively advanced state in those areas. This explains the discrepancy between the results achieved with different methods. While small holes can be explained by the shrinkage of bath during solidification and cooling, larger holes might indicate that the bath had retracted either during the test, or at the removal of the tube from the bath.

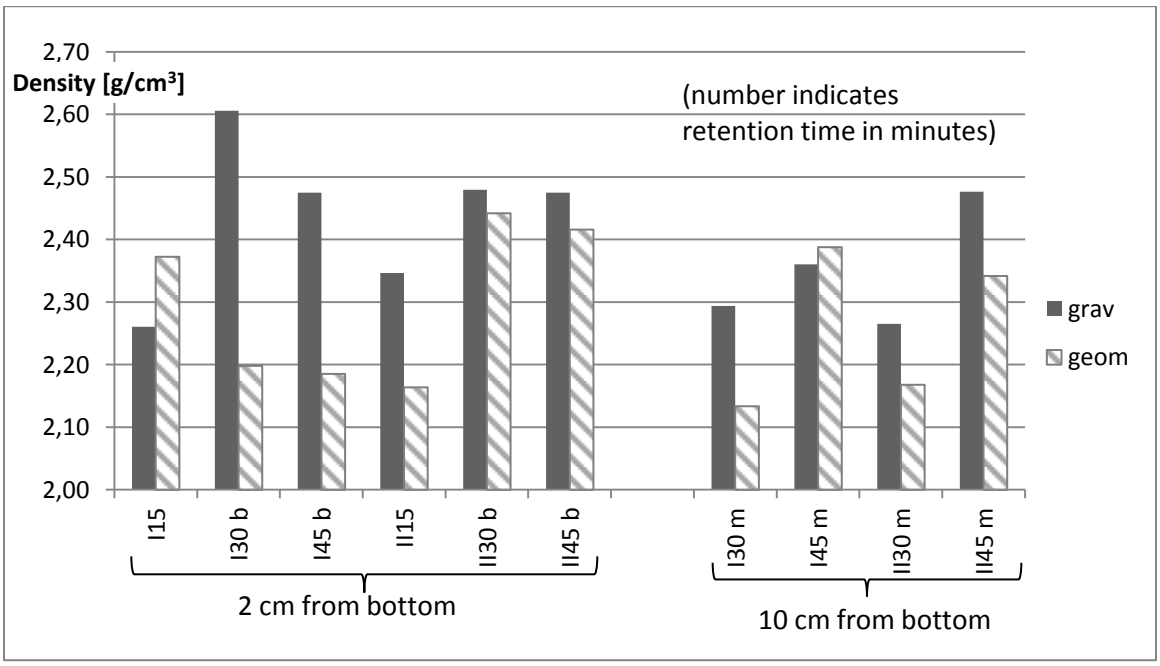

Figure 89: Density of infiltrated alumina, series B

Even in a small diameter tube, the dissolution was not homogenous across a horizontal (transversal) section. Bath would first break through points where the structure of the powder is loose. The initial fresh bath would dissolve some of that powder ensuring that the loose structure gets even looser, the convection is easier and the transport of alumina is faster in those areas.

The density above 2.5 g/cm^3 in some cases indicates that the alumina was compacted over course of the experiment, and locally, the solid (alumina) fraction surpassed the original value (approximately 0.25).

4.3.3 Secondary alumina

The secondary alumina available for experiments provided by Rio Tinto Aluminium was distinctly floury in nature, and contained stones of unknown origin, several millimetres in size, possibly common gravel. It was questionable if that secondary alumina was indeed a good representative of industrial standard. Consequently, we stopped conducting experiments with it, with the exception of the second test in series A, with 28 minutes retention time (Figure 90).

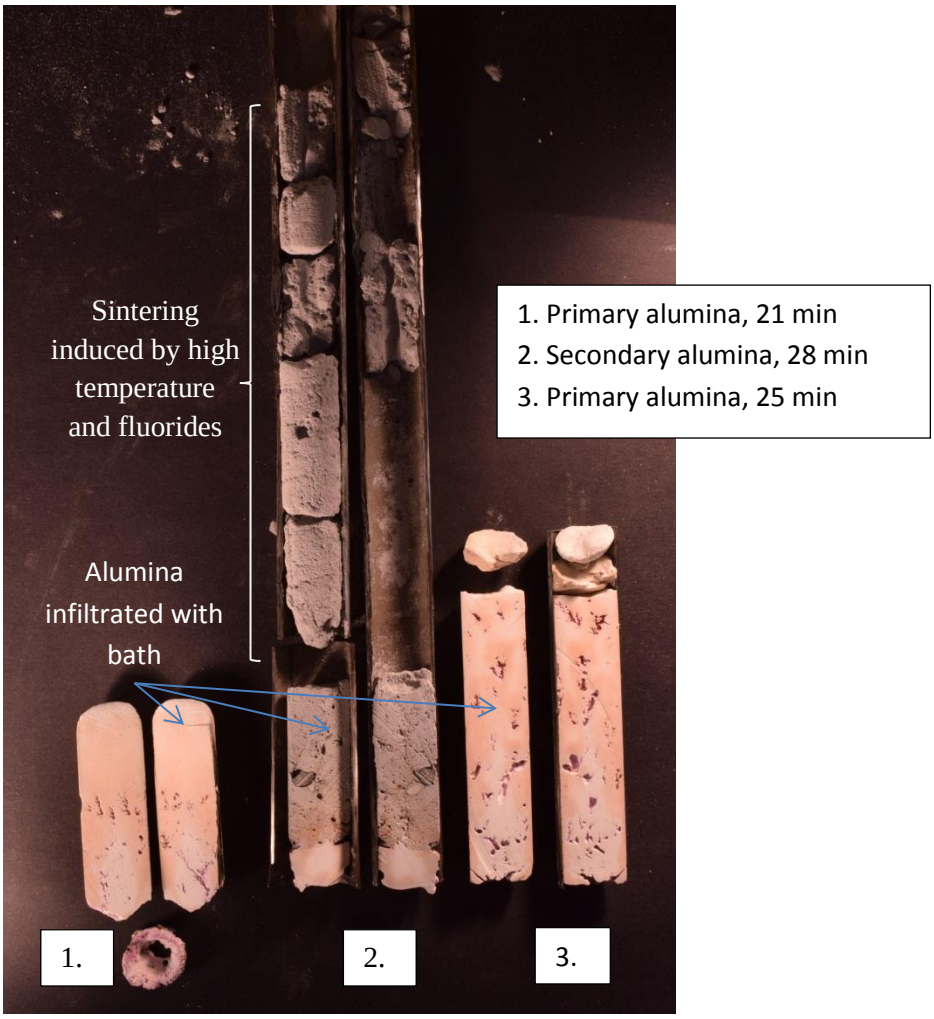

Figure 90: Photo of cross-cut samples from series A, infiltrated alumina in tubes ©Csilla Kaszas

Several differences were observed between primary and secondary alumina during the experiment:

- Release of volatiles
- Sintering above bath level
- Apparent density
- Infiltration height

In the course of the preliminary experiments, untreated (non-dried) alumina was fed into the tubes. As the alumina warmed up, the moisture evaporated, and the vapour bubbles rose through the alumina to the opening of the tube, carrying some of the fluidised powder, pushing it out of the tube and over the edges, much like water boiling in a vertical tube. This bubbling occurred two times for fresh alumina, likely corresponding to the desorption of physically and chemically adsorbed water around 150 °C and 400-500 °C. It was decided that the alumina should be preheated both to eliminate this effect, and to aid and accelerate the infiltration process. Primary alumina preheated to 500 °C did not reproduce the double gas release;

however secondary alumina did. As it was pointed out in the literature review, the desorption of fluorides occurs around 700 °C. In the presented conditions, the quantity of fluorides and their rate of release were strong enough to produce the same effect as the desorption of water in fresh primary alumina.

The results of the temperature measurements during these tests show that the temperature difference between the center and the side of the tube was smaller for secondary alumina, which was the result of mixing and agitation caused by the volatiles (Figure 91).

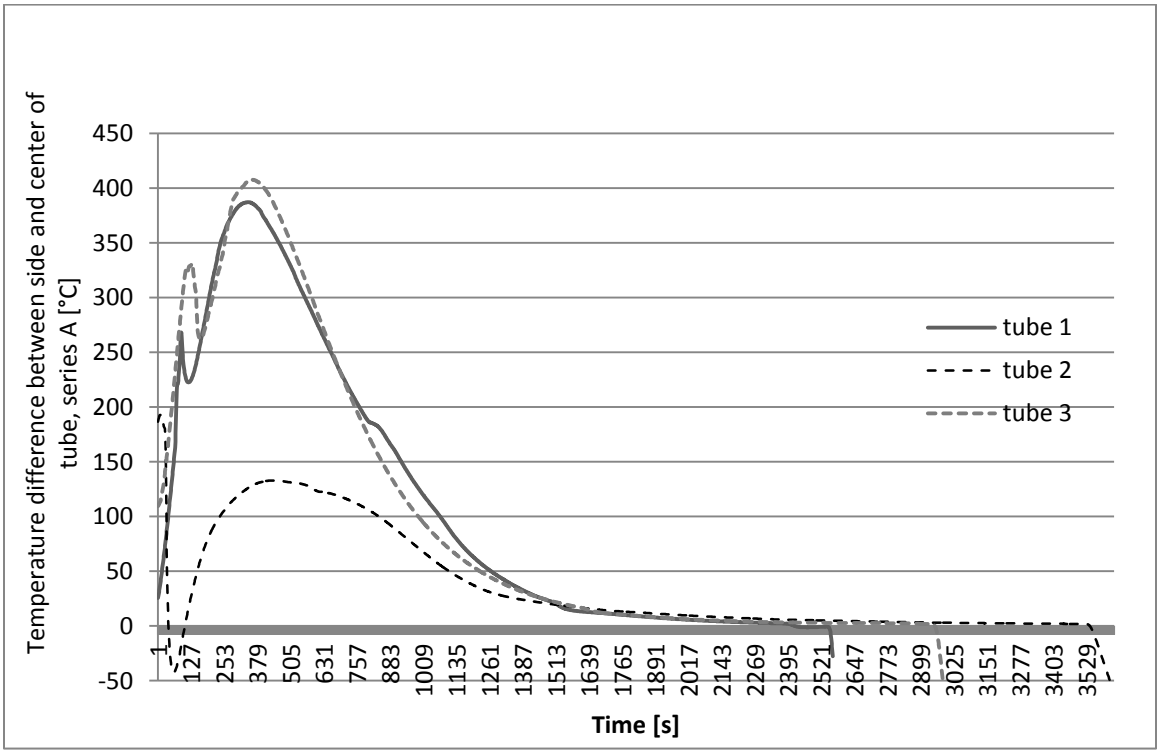

Figure 91: Temperature difference between side and center of tube filled with alumina

Another goal of our experiments was to investigate if different zones of infiltration could be distinguished. For compressed discs, the front of infiltration composed of sintered alumina, with traces of bath. For primary alumina in the steel tubes, the front of infiltration was similar, but somewhat thicker, probably due to the looser and less homogeneous nature of the non-compacted powder. The rest of the alumina remained loose, non-sintered powder and was poured out easily. A separate test was conducted with a steel tube and primary alumina to study the sole effect of bath fumes. The bottom of the tube was closed with a fine stainless-steel mesh and the bottom was set 3 cm above the bath level to expose the powder to the fumes for 30 minutes. The result was a poorly distinguishable, weakly sintered alumina layer of 2-3 mm thickness. However, when the test was repeated with secondary alumina, its fluoride content catalysed the sintering at a lower temperature, which, under the same conditions, resulted in more than 20 cm of sintered powder above the alumina infiltrated by the bath. The density of the sintered powder was 0.7 g/cm^3.

The density of the bottom part, imbibed by bath was lowest from all the samples, barely above 1.6 g/cm^3. We propose that the low apparent density is the result of the release of volatiles and recrystallization occurring simultaneously. Both the desorption of fluorides and the sintering commence around 700 °C, the particles are agitated by the gas and the structure is loosened – meanwhile the developing alpha crystals bind the neighbouring particles in this temporarily loosened state, rendering the apparent density of both sintered alumina and infiltrated alumina relatively low. It is also possible that the walls of the relatively narrow tube supported the loosened powder, helping to it to keep its apparent density low.

The infiltration height was also the lowest. It can be presumed that the carbon particles present in the alumina decrease the apparent contact angle between the powder and the bath.

4.4 Disintegration: sintering vs dissolution

Initial raft formation occurs when the powder is cold enough to freeze the surrounding liquid. As we show later on (5.3), some powder agglomerates would disintegrate gradually and easily as the solidified liquid melts back and the particles on the bottom get surrounded by liquid. While the resultant force for the rest of the raft is still zero, the buoyant and surface tension forces keep the particles held together by frozen bath afloat, the position of bottom particles, now surrounded by liquid shall be determined by the forces acting upon them individually. In the lack of a mechanical connection or cohesive forces between these particles and the raft, the denser particles will sink in the less dense liquid, triggering the disintegration of the raft (Figure 92).

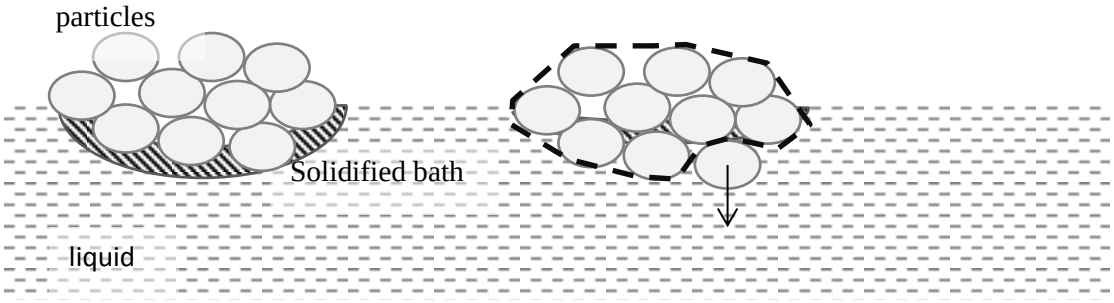

Figure 92: Disintegration of a raft ©Csilla Kaszas

Beside the detachment of fully infiltrated parts, a non-sintered powder raft would also be able to adapt to the deformation and movement of the liquid surface (Figure 93). A strongly sintered alumina raft does not adapt to the deformations of the liquid surface, but a weakly sintered may still can, either by the detachment of certain parts, or by adapting to the movement to the liquid surface, as fresh powder would.

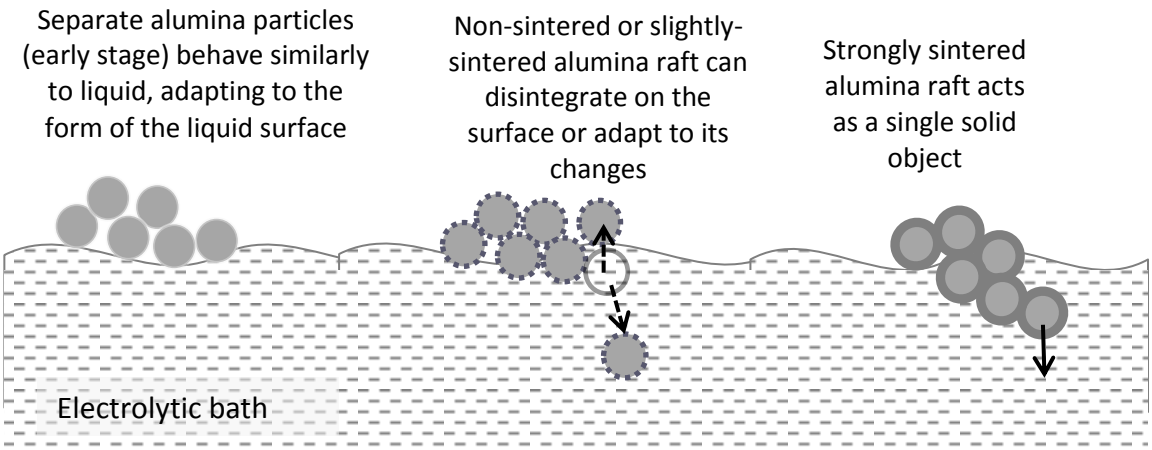

Figure 93: Effect of surface movement on raft disintegration or sinking ©Csilla Kaszas

In case of an alumina raft, the continued mechanical connection between adjacent particles is assured by the recrystallization of the transitional phases of alumina into alpha phase. The infiltrated parts of the raft could not be detached from the bulk until this bond is broken. The bond might be broken simply by the resultant force of gravitational and buoyant forces acting on the bottom particles – or it can be aided by the drag force if the liquid is agitated.

While agitation certainly helps, a strongly sintered alumina raft might never disintegrate, unless the bath is not saturated by alumina. Dissolution weakens the bonds created by recrystallization, and at some point, the connections might get weak enough to be broken by the aforementioned forces, and the raft would start to disintegrate.

Dissolution rate is a data much sought after in the field of aluminium electrolysis. However, looking at the bigger picture, if a raft can disintegrate, the dissolution of a single particle is practically guaranteed – and the disintegration depends on the balance of sintering and dissolution. Therefore, we should look at the dissolution rate more like a piece in the disintegration puzzle – and not like the endgame. The rate controlling factor in the overall dissolution process is the rate of fragmentation that opens up fresh contact surfaces between the solid alumina and the bath.

Some properties and conditions aid or hinder disintegration in ways that are easily understandable. Bath agitation has been discussed earlier. Alpha alumina does not recrystallize; therefore less new connections are established in powders with large alpha content, and the powder sinters poorly. Preheating of the alumina and large superheat of the bath leads decreased bath solidification and the period in which sintering takes place before dissolution would start is shorter.

The literature on the behaviour of secondary alumina did not provide conclusive explanations for the difference in its behaviour in comparison with primary alumina. Experiments discussed in

the previous subchapter have highlighted some of these differences. In order to isolate the influence of carbon content, further tests were prepared.

4.4.1 Carbon content

To investigate separately the influence of carbon, powder mixtures were prepared with primary alumina dosed with 0.5% and 1% fine carbon powder, scratched from an anode. Two set of tests were conducted on two days with fresh bath. 2.5 g alumina was added at a time, increasing the alumina content of the bath in 0.5 % steps. The order of the experiments is presented below.

Table 12: Carbon content of injected alumina

	1st	2nd	3rd	4th	5th
Day 1	0	0.5	1	0	0
Day 2	1	0	0	0.5	1

While the samples were dosed with fine carbon dust, it is worth mentioning that secondary alumina contains both fine and larger carbon particles (Figure 94).

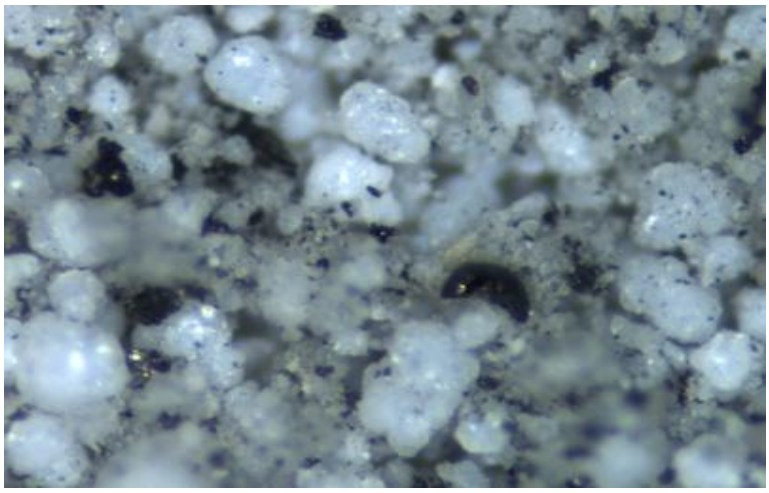

Figure 94: Microscopic image of secondary alumina ©Csilla Kaszas

4.4.1.1 Results

The flotation time and characteristic behaviour are arranged by carbon content of the powder and order of injection. With repeated injections, the alumina content of the bath increases, decreasing liquidus temperature and increasing superheat.

	Carbon content: 0		0.5-1%	
	Time on the surface [s]		Time on the surface [s]	
1st	24	Sinks as raft	123	Dissolves on surface
2nd	85	Sinks as raft	70	Edges disintegrate in clumps gradually
3rd	42	Sinks as raft	360	Dissolves on surface
4th	27	Sinks as raft	343	Dissolves on surface
5th	38	Sinks as raft	460	Dissolves on surface

Table 13: Behaviour of alumina on the bath surface with or without added carbon

Clippings from the video recordings are presented below (Figure 95).

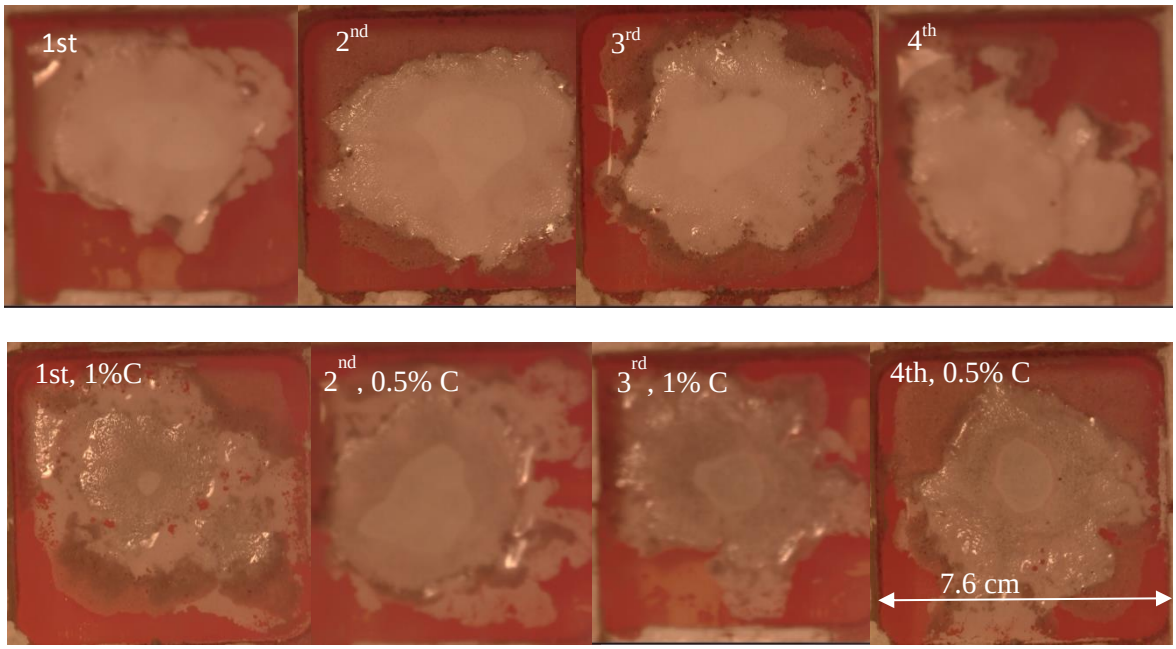

Figure 95: Alumina rafts 10 s after injection (camera was out of focus on the 1st day) ©Csilla Kaszas

To better illustrate the difference in behaviour, the video recordings of the experiments were processed with Matlab® Image Processing Toolbox™. In each frame, the areas of the rafts were calculated using the dimensions of the crucible as reference (Figure 96).

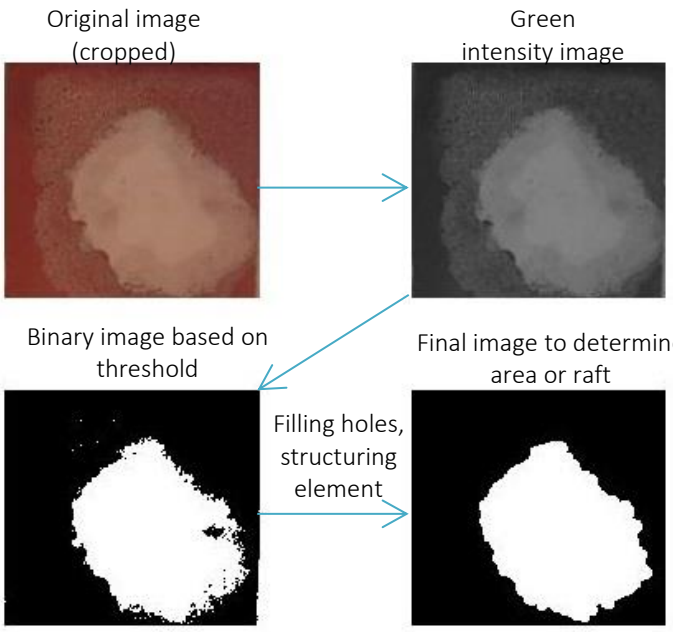

Figure 96: Treatment of images of alumina rafts with Matlab ©Csilla Kaszas

The image processing permits to calculate the area of the raft's surface in every frame of the recording. Valuable information can be obtained regarding the dynamics of raft disintegration that is not included in the flotation time only. The selected diagram (Figure 97) displays the impact of carbon content in alumina. Conducted with the same conditions (bath composition, temperature, height of injection, quantity of alumina), the area of the primary alumina raft only slightly decreased then it sunk in one piece after 23 seconds – while the same powder with added carbon continuously shrunk, and disintegrated and dissolved on the surface.

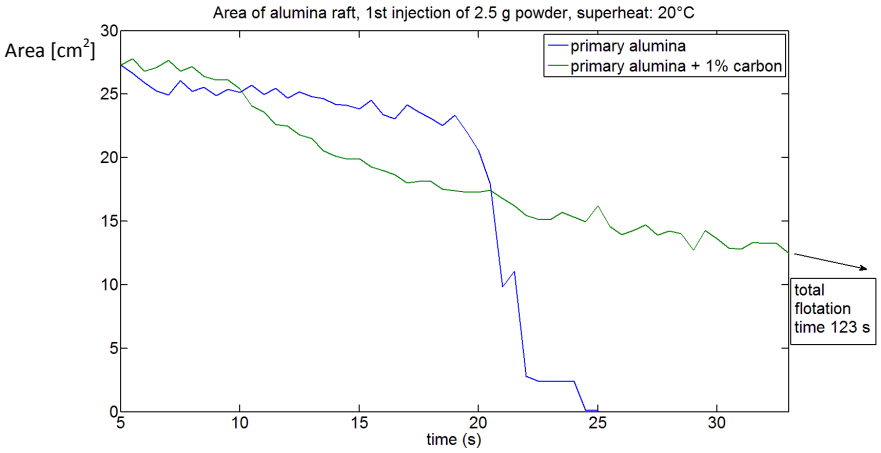

Figure 97.: Result of image processing, disintegration of alumina rafts, 1st injection

Admittedly, top view is not ideal for the observation of the disintegration and dissolution of an alumina raft. While the side view in an expensive quartz crucible ensures the detection of any dispersion along the bottom, from the top view, only the subtle changes of the edges of the rafts indicate what is happening on the bottom. Drawing conclusions from the development of raft areas should be done with care, results can be misleading as the shapes of the rafts are not uniform, and some rafts may thin out more around the edges than others. For this reason, while it could be attempted, it would be unwise to turn the shrinkage of surface area into dissolution (or rather, disintegration) rate.

4.4.1.2 Discussion

These experiments were inspired by the work of Chinese researchers [61] [63], especially the reasoning they offered to explain the differences between primary and secondary alumina. According to them, it is the oxidation of carbon and the release of heat and gas that bursts the raft apart and causes secondary alumina to disintegrate faster. This theory was dubious, for a number of reasons.

To begin with, there should be oxygen present for the oxidation to happen. In industrial cells, the atmosphere above the rafts is anode gas, consisting mostly of carbon-dioxide, containing little oxygen. Experimental cells with carbon crucibles, such as ours, are protected with argon gas. Carbon particles may float on the surface without burning out quickly, and yet, alumina with carbon did disintegrate better than primary alumina.

Another factor that discredits the former reasoning is that during the experiments in the present subchapter, and the experiments with secondary alumina in the previous subchapter, the alumina powder kept its grey colour, therefore the carbon was still present and did not burn out.

We propose that the carbon in the alumina partially blocks the sintering; the weaker bonds are easier to either break or dissolve.

Carbon may act against sintering in two possible ways, either mechanically or chemically. It is possible that by simply being present as a foreign material when the alpha alumina platelets form, the newly developing crystals cannot fuse together with a carbon particle in-between. If that is the case, any foreign material that is not dissolved or molten in the cryolitic bath may have the same effect. However other potential additives that are inert in the eletrolyte are few and far between – and expensive.

In either case, alumina dosed with carbon behaves in the cryolitic bath much like any regular cold powder in water would, supporting the idea that carbon acts by negating the sintering and not by exploding the powder.

The carbon present in the powder would rise to the surface and form a scum, the influence of which has been discussed in the previous chapter.

5 Phenomena at the bath-metal interface

5.1 Steady-state flotation

5.1.1 Equivalent system for liquid-liquid interface

The mathematical model of flotation discussed earlier (2.1) was developed to liquid-gas interfaces, where the effect of the upper fluid was neglected. Since on the bath-metal interface, the densities of the liquids are fairly close to each other, disregarding the effect of the upper fluid would be unacceptable. The buoyant force or pressure exerted by the fluid can be accounted for by the introduction of the equivalent density (ρ*). By subtracting the density of the fluid from the density of the solid and the density of the liquid, the resultant force on the solid in this equivalent system stay equal to the original (Equation 20) (Figure 98).

$$\boldsymbol{V\rho_s g = V_l\rho_l g + V_f\rho_f g + F_s}$$

$$\boldsymbol{V = V_l + V_f}$$

$$\boldsymbol{V(\rho_s - \rho_f)g = V_l(\rho_l - \rho_f)g + F_s}$$

Equation 20: Formulation for the development of the concept of equivalent density

Where V is the volume of the solid, V_l and V_f are the volume of displaced liquid and fluid.

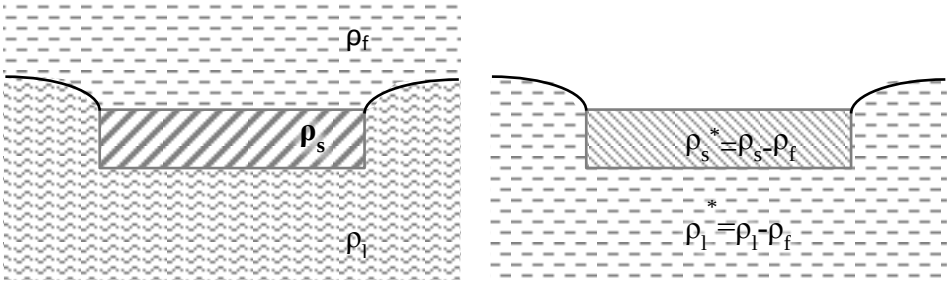

Figure 98: Modification of flotation model to account for the upper fluid ©Csilla Kaszas

The equivalent density was used to calculate the flotation limit for the BMI, but for the sake of comprehension, the results were translated back to the actual apparent density of the agglomerates.

5.1.2 Model results

The mathematical model was run with the parameters of the equivalent system and the results for the conditions of flotation of alumina on the bath-metal interface are presented below.

The contact angle at the triple line of alumina-aluminium-cryolitic bath was first measured by Dewing; the contact angle he found was 176° [105]. It was also measured later by Utigard. He found it ranging between 150° and 170°, with an average value of 158° [39]. While both used sessile drop method, Dewing`s angle measurements were conducted at room temperature, by cutting the crucible after the setup was cooled down and the liquids solidified, while Utigard used X-ray radiographic techniques to observe the drop`s profile in situ.

In any case, the exact value of contact angle changes little the flotation limit of spheres, in the given range, and it does not change the flotation limit of discs whatsoever, as the angle of the interface at the triple line has been limited at 0° for discs (Figure 99).

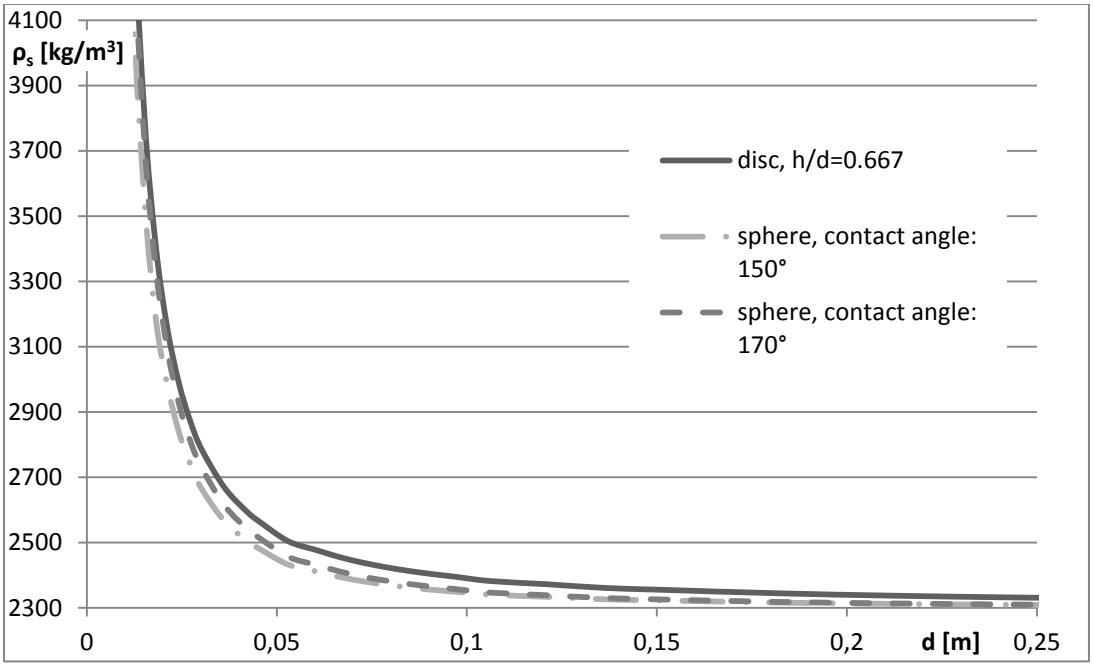

Figure 99: Flotation limit on bath-metal interface

Low height-diameter ratio (h/d) promotes flotation, but even relatively thicker agglomerates have a chance of staying trapped on the BMI, as long as they are only a few centimeters in diameter (Figure 100).

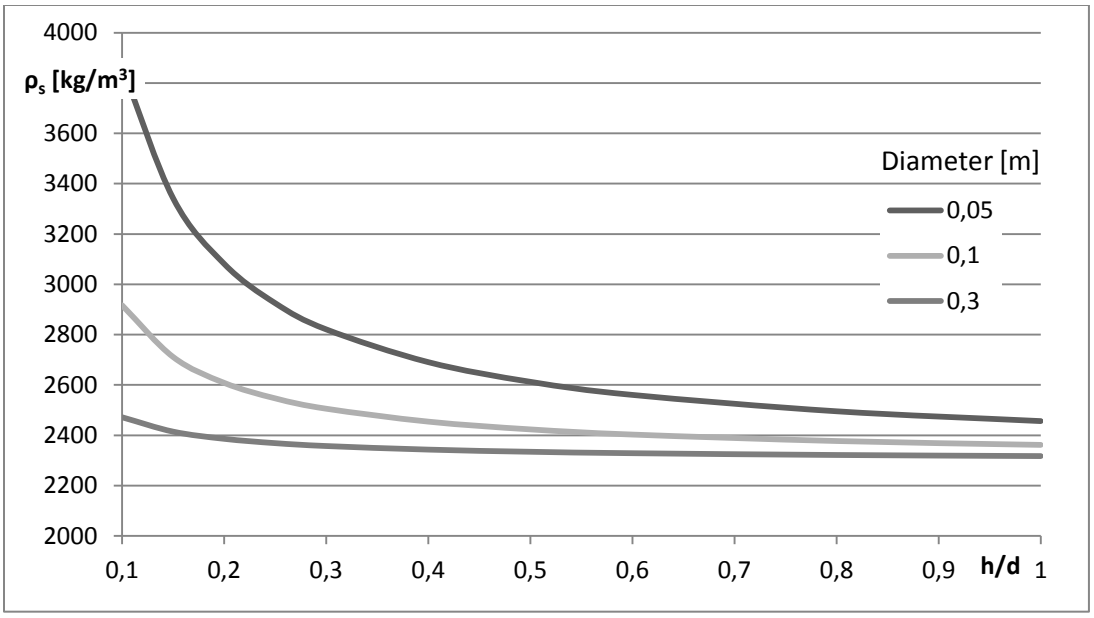

Figure 100: Dependence of flotation limit of discs on height-diameter ratio, on BMI

The bulk density of SGA before injection is around 1 g/cm^3. Pieces of alumina rafts, or whole rafts themselves may sink as their density reach 2.1 g/cm^3, containing alumina, bath, and gas in the un-infiltrated pores. Assuming that the alumina keeps its original porosity, and all the pores get infiltrated with liquid bath, the density would become 2.6 g/cm^3. At that density, the bath-metal interface is capable of supporting an agglomerate of more than 1.5 cm of thickness, regardless its diameter. Agglomerates can get compacted over time, but they have an upper density limit of 3.99 g/cm^3, the density of solid (pore-less) alpha alumina. Even with that extreme density, the BMI can uphold an agglomerate at least 3 mm thick (Figure 101).

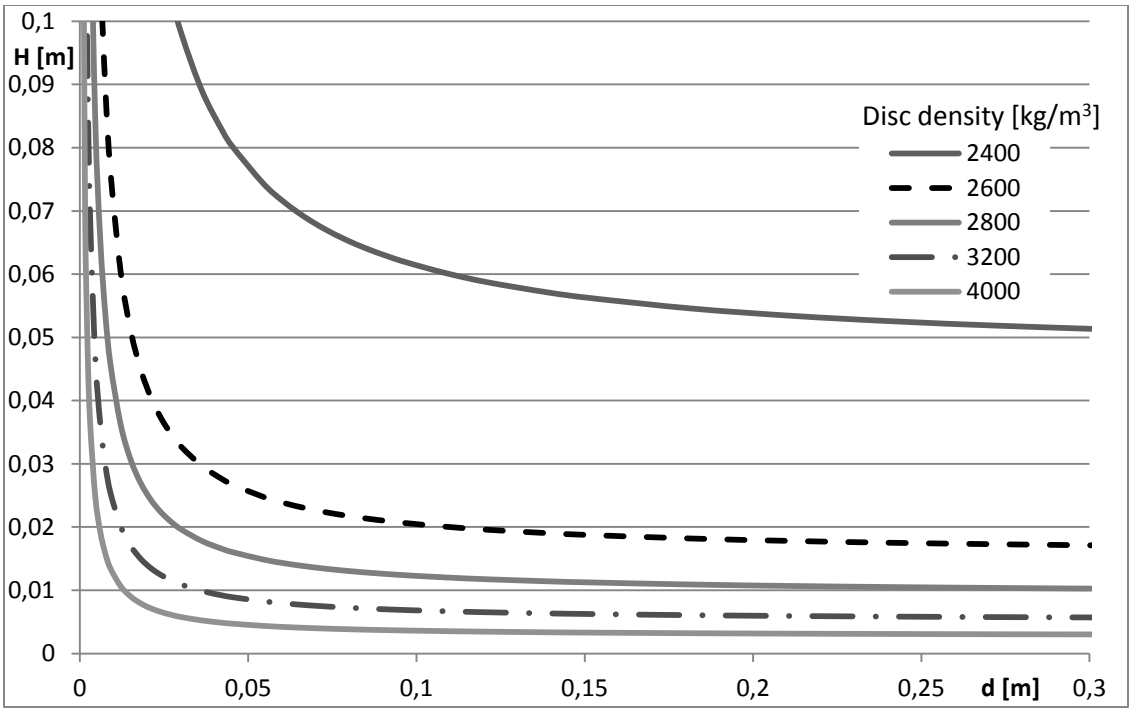

Figure 101: Maximal thickness of disc shape agglomerate on the BMI

To put it in the other way, potentially more meaningfully, the mass of agglomerate the bath-metal interface can uphold can be measured in kilograms (Figure 102).

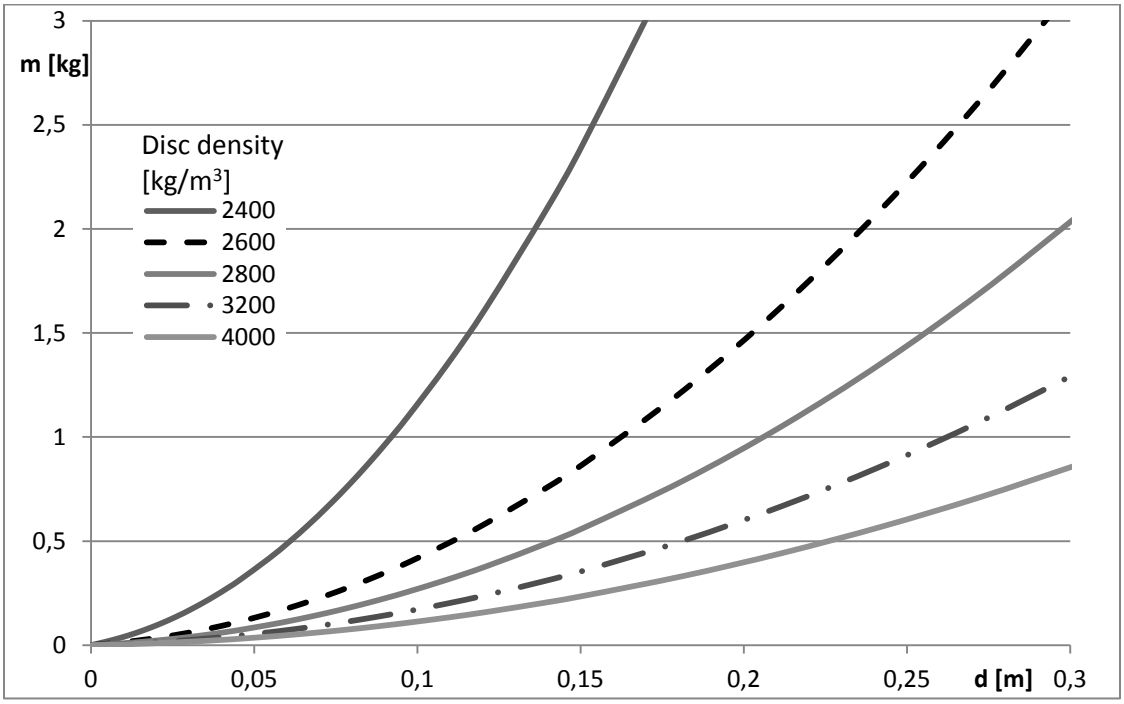

Figure 102:Mass limit of disc-shaped agglomerates on the BMI

The flotation on the bath-metal interface has been investigated before. Thonstad applied Maru's approximation for maximal radius of a floating spherical object that is independent of the contact angle. His equation has been used to calculate the flotation limit of solid alumina agglomerate on the bath-metal interface, presumably with a density of solid alpha alumina, 3.99 g/cm^3. 7.5 mm was calculated as the critical radius [66], which corresponds to the results of the present flotation model.

Solheim investigated the flotation of disc-shaped agglomerates on the bath-metal interface. He derived the meniscus height assuming flat solid surface, and permitted negative angle at the triple line including unstable floating positions [65].

5.2 Dynamic model of flotation and piercing of the interface

The surface penetration and flotation of particles are of particular interest in the mineral industry, [106] [107] [108], where flotation is used to separate the valuable ores from waste, and it is actively aided by bubbles. Studies on flotation quickly turn to half-empirical calculations, which, given that the conditions are so different, might be misleading and unhelpful if attempted to apply on the flotation of alumina on bath-metal interface. Fundamental/theoretical studies meanwhile focus on the surface penetration of spheres, following the triple line advancement and changes in dynamic contact angle with high speed cameras [109] [110] [111].

The behavior of the alumina on the bath surface has been discussed in detail earlier. It was shown how its low bulk density and low temperature results in the flotation of SGA. If these conditions are taken as given, there is no doubt that the alumina powder will settle on the surface, reaching close to steady state flotation without sinking; therefore to analyse the possibility of interface penetration due to the initial velocity of the powder is not expected to bear fruits of any particular interest. The piercing of the bath-metal interface by an agglomerate or a piece of crust, dislodged by the crust breaker, is a different issue.

In this chapter a simplified model of interface penetration is presented, based on the static model of flotation presented in (link). The objective of this extension of the model is to give a rough measure of the necessary velocity or apparent density of an alumina agglomerate to penetrate the interface and sink – or to stay afloat.

5.2.1 Additional parameters and assumptions in the dynamic model

When an object is in relative motion inside a fluid, there are additional effects at work beside those in the case of static flotation. The liquid's resistance to the object can be represented by drag force, while the inertia of the liquid displaced by the moving object is represented by the associated mass. Before the contact angle reaches its equilibrium state, it might change depending on the movement of the liquid surface and the wetting of the object. The object arrives to the interface with a certain velocity – a kinetic energy that should be dissipated before the interface is penetrated, if the object were to stay afloat.

The extended force balance of the dynamic flotation model is presented below (Equation 21).

$$\dot{\boldsymbol{v}} \cdot (\boldsymbol{m} + \boldsymbol{m_a}) = \boldsymbol{F_g} + \boldsymbol{F_b} + \boldsymbol{F_s} + \boldsymbol{F_d}$$

Equation 21: Extended force balance for dynamic model of interface penetration

Where v is the velocity of the sinking body, $\dot{\boldsymbol{v}}$ is its acceleration, m is the mass of the sinking body, m_a is the associated mass and F_d is the drag force.

Explicit finite difference method was used to obtain numerical approximation for the motion of the sinking object in time. The object was given its initial position and velocity. In each advancing time step, the acceleration is calculated from the resultant force and the total mass – which determines the new position of the object, in relation to the undisturbed interface.

The different terms of the equation are elaborated in the following section, including the physical phenomena they represent and their approximation for the mathematical model.

5.2.1.1 Shape and surface tension

While it is possible to follow the descent of a spherical solid body into an interface, imposing a contact angle and calculate the relative immersion, angle of the interface and meniscus height, it was not the route taken. If the agglomerates were spheres, the former method would have been worth the computational demand. However, agglomerates are of irregular shape. For the ease of calculation, cylinder shape was used to calculate the resultant force of surface tension and the meniscus height. The height-diameter ratio is a variable in the calculations, with a reference value of 2/3 to represent an equivalent sphere. This can apply to fallen pieces of crust or smaller agglomerates from the raft. However, the matter of the fact is, rafts themselves are flat, if not disc-like objects, and the parts detaching themselves from the raft are sometimes also flat, almost like flakes. While they would be unlikely to arrive in a perfectly horizontal position to the bath-metal interface, the edge reaching the interface would be subjected to force which would possibly rotate the agglomerate to the position which is assumed in the model: the bottom of the disc parallel to the BMI (Figure 103).

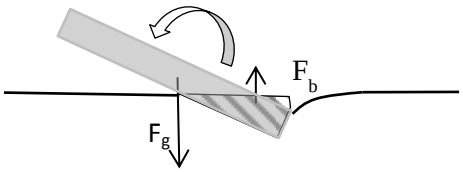

Figure 103: Flat disc arriving at the interface with an angle©Csilla Kaszas

When the interface is attached to a corner of the disc, the angle was determined from the meniscus height, so the resultant force of surface tension could be calculated. When the triple

line is on the sides, a contact angle is applied on the surface and the triple line moves for the next time-step.

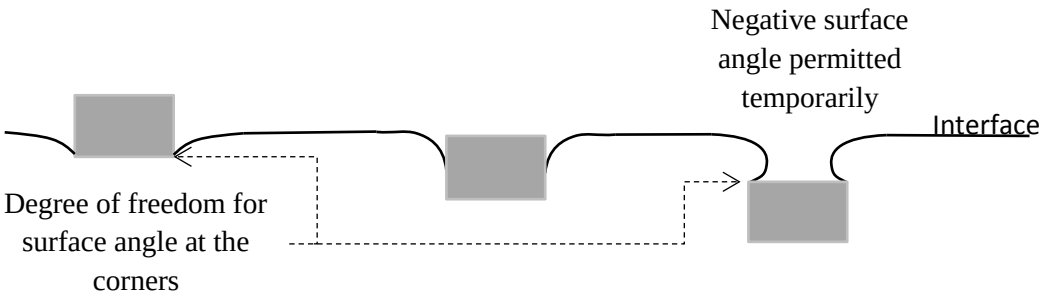

Figure 104: Different stages of interface penetration ©Csilla Kaszas

While in the static model, negative surface angle was not accepted as a stable state; in the dynamic model it was permitted, which in some cases might lead to a higher density limit for flotation in the dynamic model.

5.2.1.2 Contact angle

The contact angle in dynamic conditions changes with the direction of the movement: advancing and receding contact angle. The advancing contact angle is larger, while the receding is smaller than the static contact angle – more so with increasing velocity. Advancing and receding contact angles can be measured, but they are associated with a constant speed, which is not the case when a solid body is dropped onto an interface. Another possible issue is the wetting state of the surface, as the liquid fills the grooves on the uneven surface the contact angle decreases with time on a newly-wetted surface [112].

In the numerical simulation, when the object is sinking into the lower liquid for the first time, 180° contact angle is imposed, in the model. The wetting line is recorded, and it provides another point of freedom for the surface angle, between the static contact angle and 180° when the object rises back from the initial impact. Then, the static contact angle is imposed on the wetted surface. If the object moves past the point when the static compact angle can be applied with the triple line remaining on the wetted zone, and the top of the disc has not been in contact with the lower liquid, the line of wetting and the triple line advances but only half of what it were if the static contact angle was applied. There is a limit for the velocity of the advancement of the triple line and the wetting process, it does not occure instantenously. This approach in the model works to that effect. The velocity of the triple line is limited in other numerical simulations [113].

While the previous considerations are important when the solid is wetted by the liquid, it is not the case with alumina and liquid aluminium. The measured contact angles between alumina and the bath-metal interface are fairly close to 180°, therefore it is not expected that the

rudimentary approach to the variation of contact angle on the side would make a significant effect.

For the top edge of the disc, at initial impact, the theoretical minimum surface angle was allowed, as seen in chapter 2 (Figure 9), which is in accordance with the former assumption that the initial contact angle is 180°. If the object bounced back and descended a second time, then the surface angle was limited by the contact angle, in accordance with Gibbs extension (Figure 11) – or the theoretical minimum surface angle, which might be a stricter restriction for small diameters.

Unless otherwise specified, the contact angle applied in the model for the bath-metal interface was 170°.

5.2.1.3 Drag force

Drag force acts opposite to the relative motion of an object moving with respect to a surrounding fluid. The drag force is the result of the friction between the solid and the liquid (viscous drag) and also the pressure difference along the solid body caused by the movement (pressure drag). Its general form is the following

$$F_d = \frac{1}{2}\rho v^2 C_d \mathrm{A}$$

Equation 22: Drag force

Where v is the speed of the object relative to the fluid, A is the cross sectional area, and C_d is the drag coefficient, depending on the shape of the object and the Reynolds number.

The drag force is usually investigated for conditions where the solid is completely immersed in the liquid. On the liquid-fluid interface, a linear relationship was assumed between the immersion level (the position of the triple line) and the drag force.

At low Reynolds number, the model follows Stokes' law and the drag coefficient is calculated as 24/Re for disc shape. At large Reynolds number, the drag coefficient is constant, 1.17 for discs in normal flow relative to its flat side. In the transitional zone, this simplification leads to the underestimation of the drag force.

Even though the basic shape applied in the model was thought as an equivalent sphere, the drag coefficient is that of a disc. It is because we can safely assume, that even if a roughly spherical piece of raft or crust would fall onto the interface, it would be coarse and irregular, therefore the drag coefficient of a sphere would surely underestimate the actual drag coefficient.

5.2.1.4 Associated mass

A solid body penetrating into a liquid displaces some of the liquid volume, which ultimately has a dampening effect on its movement. The displaced volume of liquid was calculated in every time step. 0.5 was chosen for the associated mass coefficient (C_a) [114] [109].

$$m_a = C_a \rho_l V_d$$

Equation 23: Associated mass

In the calculation of the volume of displaced liquid, not only the volume, displaced by the object itself, was considered, but also the volume displaced by the curved interface. As the object sinks below the undisturbed interface, the sum of all displaced volume becomes larger than the volume of the objects, as it drags a certain quantity of the upper liquid below the line of the interface. The volume was calculated as the area of the base of the disc, multiplied by the distance between the undisturbed level of interface and the top or bottom of the disc – respectively for the displaced upper fluid, or bottom liquid (Figure 105).

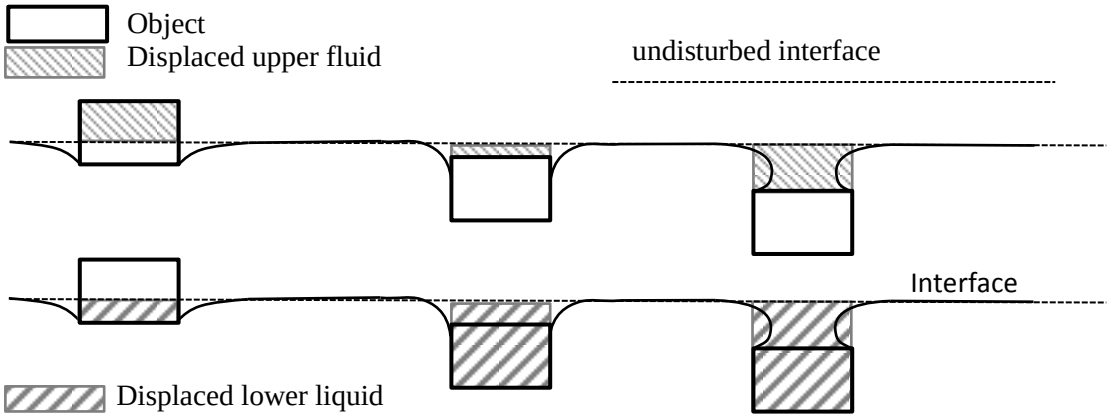

Figure 105: Displaced volume at different stages of sinking ©Csilla Kaszas

When the displaced volume increases during a time step, its dampening effect is considered according to the conservation of momentum.

5.2.1.5 Meniscus height and surface angle

To decrease the computational demand of the model, the meniscus height was calculated at four different surface angles, and linear interpolation was used to estimate the meniscus height from the surface angle, or vice versa, for the in-between values (Figure 106).

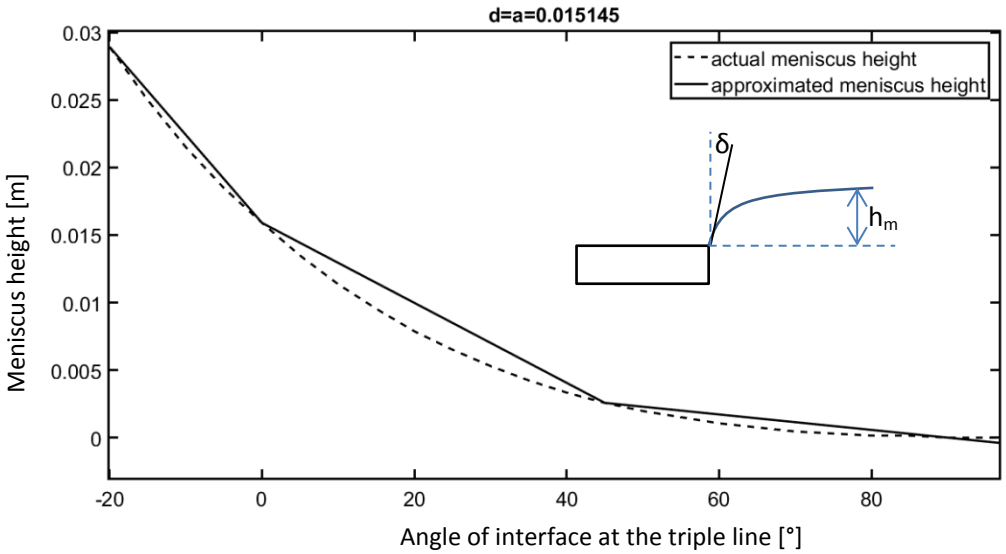

Figure 106: Approximation of meniscus height and angle of interface for dynamic interface penetration model

The four reference points are: minimal angle of the interface (dependent on diameter, as seen in Chapter 2), 0°, 45° and 90°. Between 0 and 90°, the meniscus height is consistently overestimated, while above 90° it is underestimated. On negative contact angles, the error may go either way, depending on the value of minimal interface angle, therefore dependent on the diameter of the object. While in the presented figure, on the discussed zone, the estimated meniscus height is larger than the value calculated by solving the differential equation for the surface, for large objects when the surface angle can decrease as low as -90°, the meniscus height is underestimated for negative contact angles.

5.2.2 Results

5.2.2.1 Impact

The model predicts whether an agglomerate with a certain diameter, density, bath-height ratio, initial velocity would penetrate the interface or stay afloat. To provide an inside glimpse of the workings of the model, discussed previously, two groups of diagrams are shown: the first is the impact of an agglomerate that does sink (Figure 107), the second on the other hand stays afloat (Figure 108). The internal variables in the model, the angle of the interface, the triple line length, and the calculated forces at each time step are presented, beside the position of the agglomerate as a function of time. Zero position is designated to the object touching the interface, when the bottom edge reaches the level of the liquid metal.

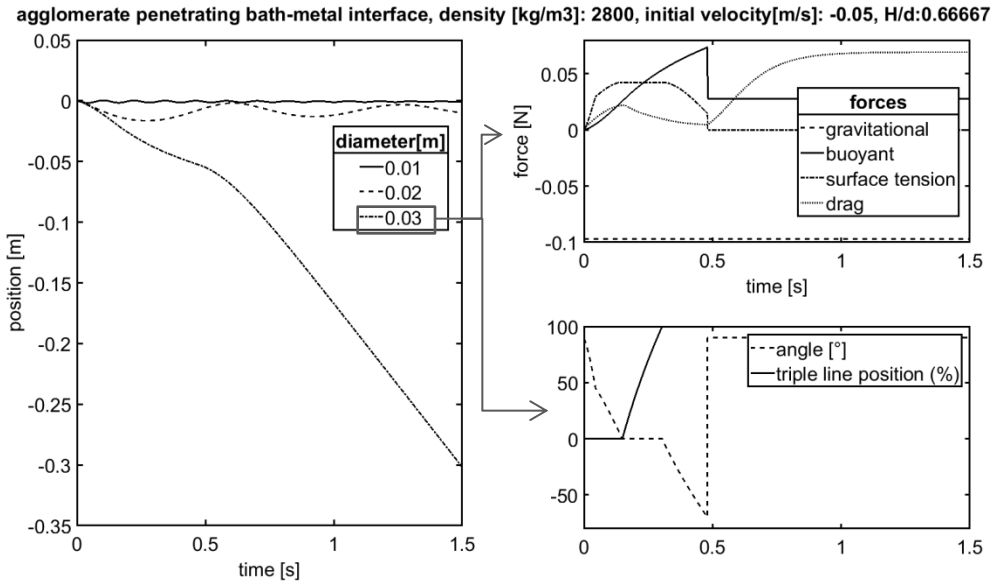

Figure 107: Agglomerate impact on bath-metal interface (sinking)

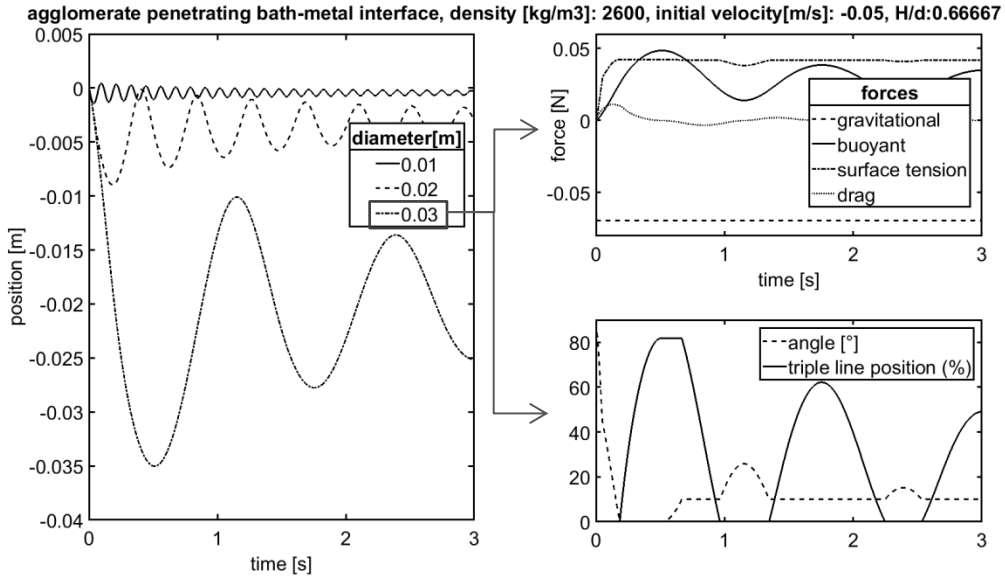

Figure 108: Agglomerate impact on bath-metal interface (floating)

Objects that are held back keep oscillating with decreasing amplitude on the BMI. Interface penetration can occur at the end of the initial sinking period, or (for small contact angles) the objects can bounce back once and sink at the second descending period.

5.2.2.2 Critical velocity for quasi-spherical objects

The critical conditions for sinking were investigated, for different combinations of velocity, density, size, the combination that represents the divisive line between sinking and floating was found.

When the object's height-diameter ratio is fixed at 2/3, the results of the dynamic model are comparable to their static counterparts (Figure 109) (Figure 99). Even with zero initial velocity, the two diagrams would not be exactly the same, for two reasons: one is that in the dynamic model negative surface angles were permitted, the second is that the initial velocity is defined at the position indicated in a pictogram in Figure 109, and not at the object stable floating position.

Agglomerates, smaller than a centimeter, would likely stay afloat, given the possible density of an agglomerate is limited; while those, larger than 6 cm, would probably sink even if their density just slightly exceeds the density of the liquid metal.

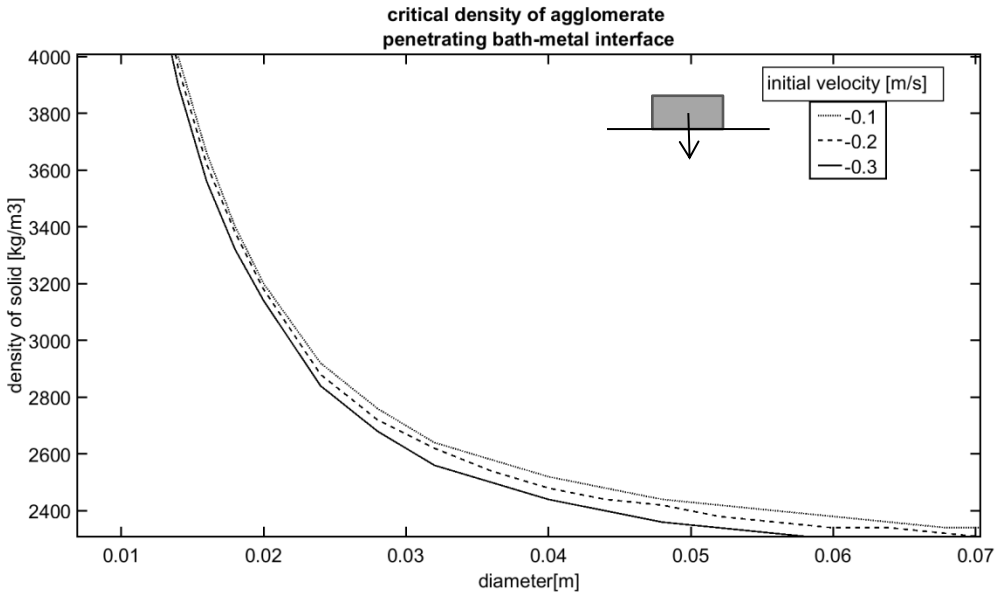

Figure 109: Critical density for agglomerate penetration on BMI, H/d=2/3

Critical velocity (minimum velocity for interface penetration/ maximum that permits flotation) is only applicable for solid densities larger than the density of the bottom liquid. It decreases with increasing density. The model shows an almost linear relationship until the object's density approaches its critical density and the tangent of the curve is increasing (Figure 110).

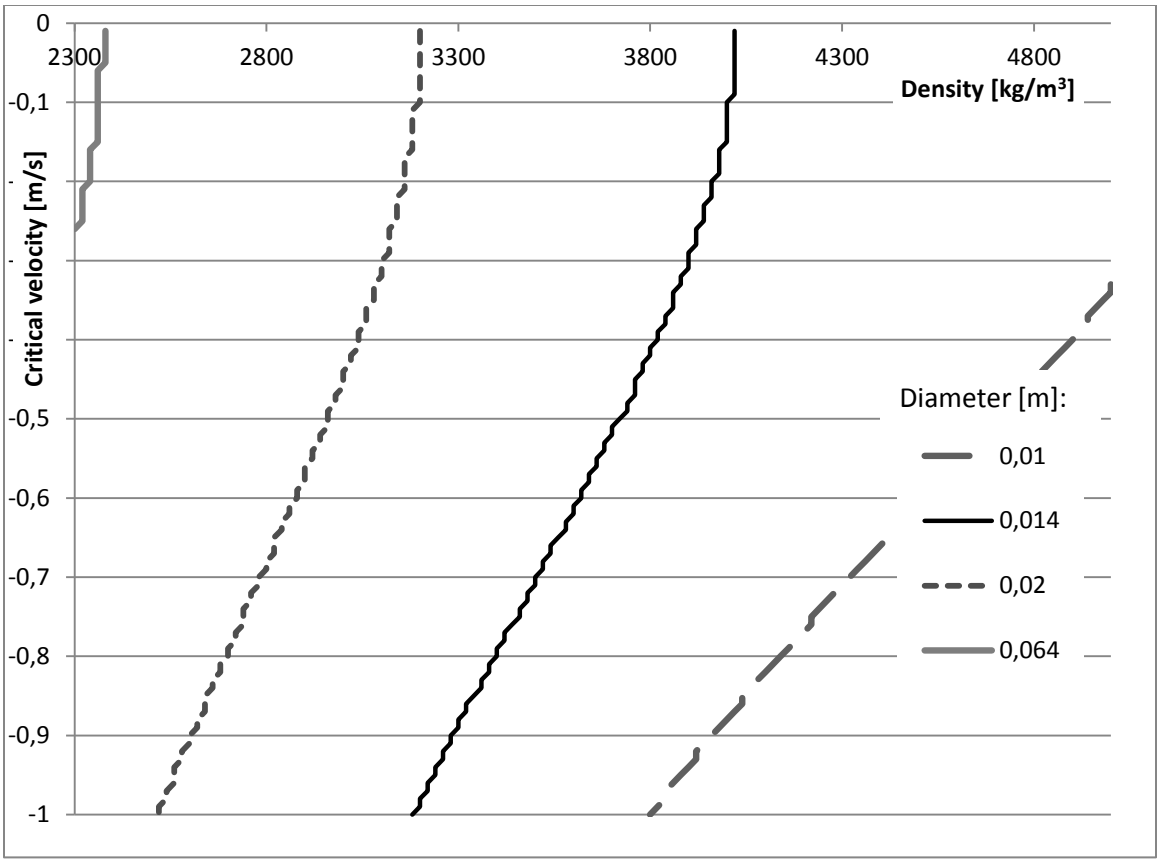

Figure 110: Critical velocity for agglomerate penetration on BMI, H/d=2/3

5.2.2.3 Velocity on bath-metal interface

Initial velocity can be treated as another input in the model along with the parameters of the agglomerate. But, assuming an agglomerate starts sinking from the bath surface with the initial velocity of zero (as opposed to a crust falling into the bath from above, or the crust breaker pushing the raft below the surface), the descent of the agglomerate and the velocity with which it arrives to the bath-metal interface can be calculated, using the same mathematical model, with the exclusion of surface tension force. The velocity at the bath-metal interface depends on the diameter and density of the agglomerate, and the bath height. As the bath is relatively shallow, considering the expected size of agglomerates, their velocity is not expected to surpass 1m/s. Small agglomerates, with a few centimeters of diameter would reach their settling velocity before they reach the bath-metal interface (Figure 111).

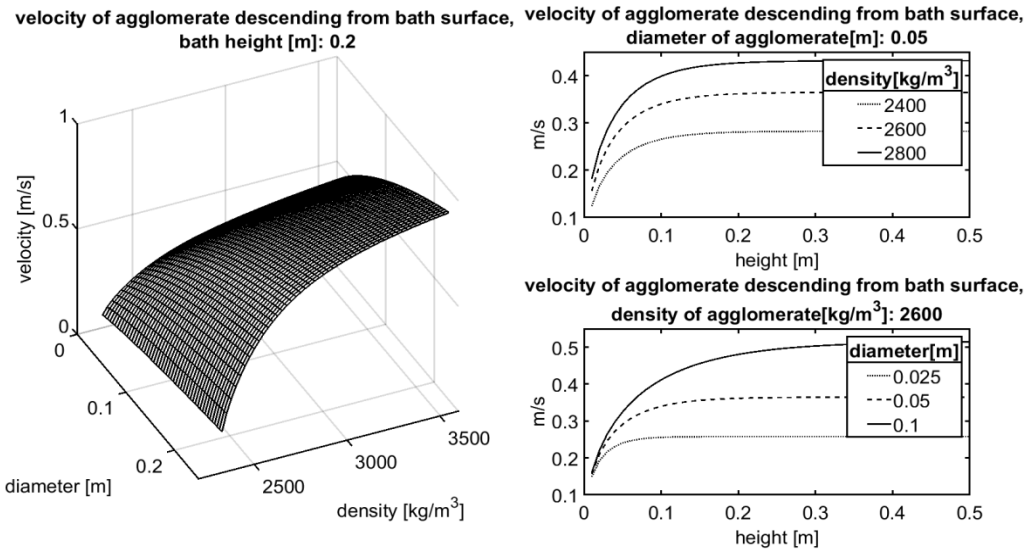

Figure 111: velocity of agglomerate descending from bath surface onto bath-metal interface

5.2.2.4 Results with constant bath height and zero initial velocity

Assuming the agglomerates get detached from the raft with zero initial velocity and descend through 20 cm cryolitic bath, one variable is eliminated from the model and the results can be presented in a concise form.

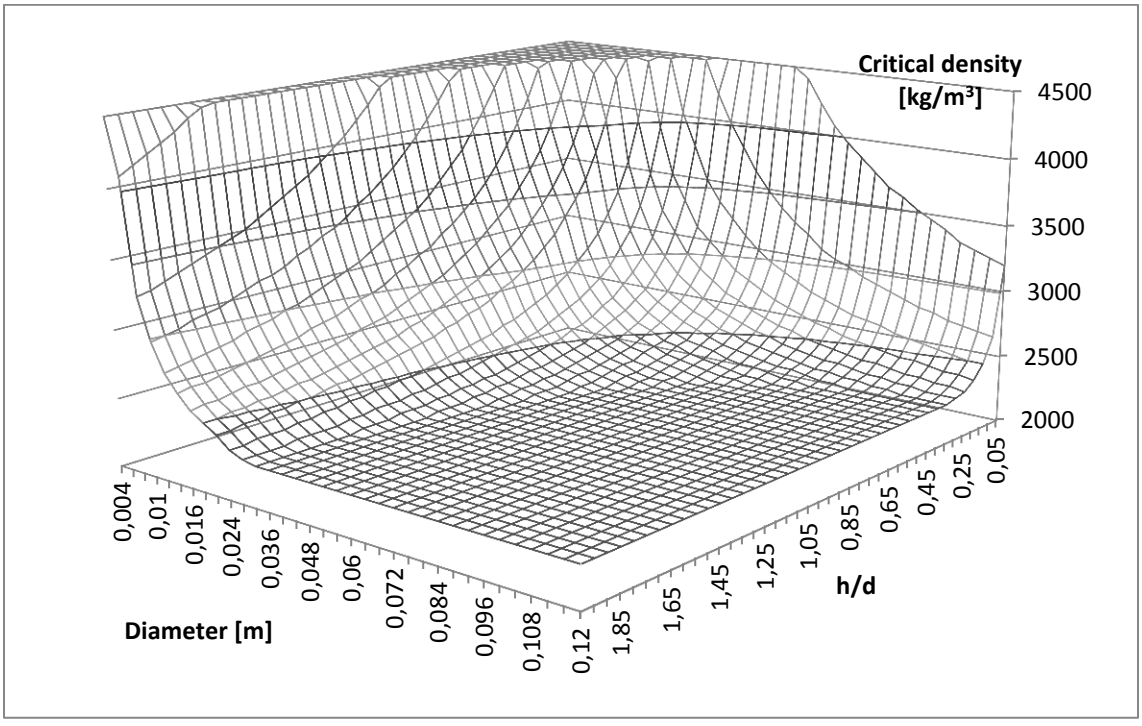

Figure 112: Critical density of interface penetration, fixed bath height

The results as function of diameter with fix height-diameter ratio can be observed later on as well (Figure 116 Figure 119). The critical density decreases with increasing height-diameter ratio until it sets at 2300 kg/m^3(Figure 113).

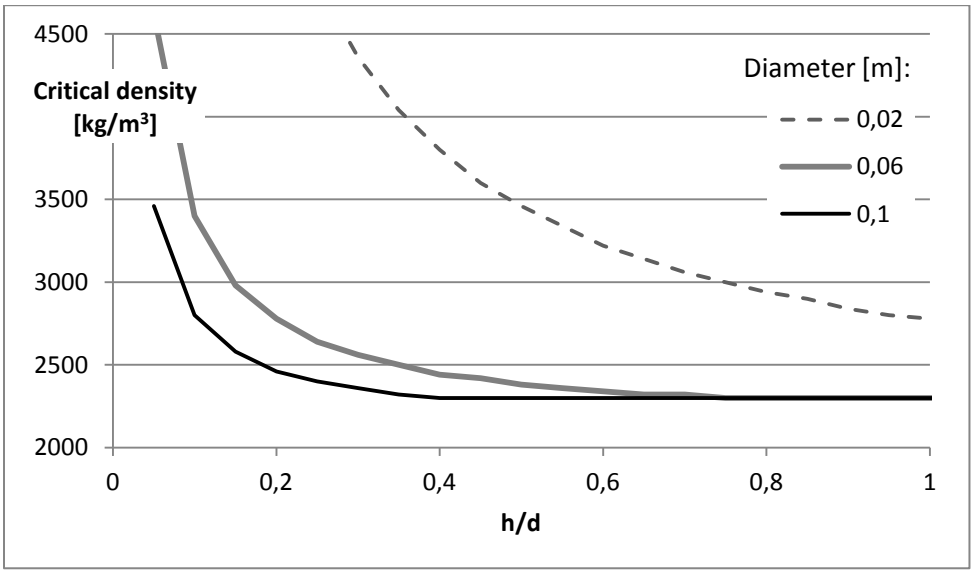

Figure 113: Critical density of interface penetration, influence of relative thickness

Instead of the height diameter ratio, the actual thickness of an agglomerate can be investigated as well. This point of view brings closer the plotlines; and provides an opportunity to have a better grasp the size of object that may stay afloat on the bath-metal interface (Figure 114).

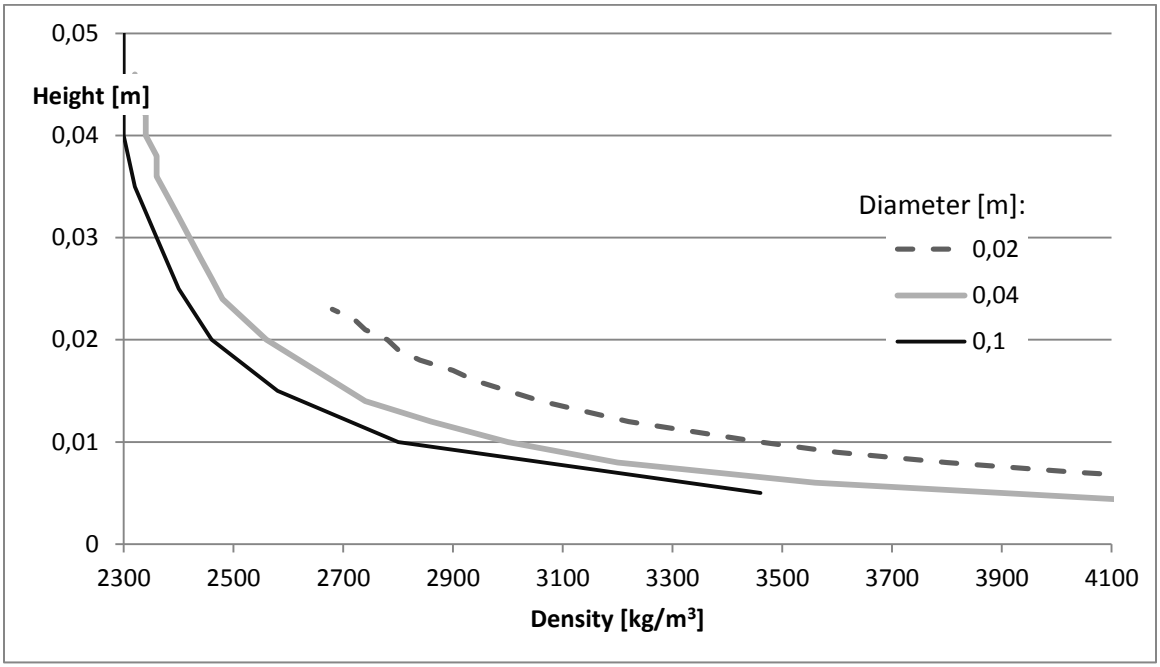

Figure 114: Critical thickness for interface penetration

Studying the maximal mass of an agglomerate that stays afloat, we may find for example that the BMI can support an agglomerate with the diameter of 0.1m and density of 2400 kg/m^3 up to 1.35 kg in static conditions (Figure 102), however if it sinks through 0.2m of cryolitic bath before impact, the penetration limit drops below 0.5 kg (Figure 115).

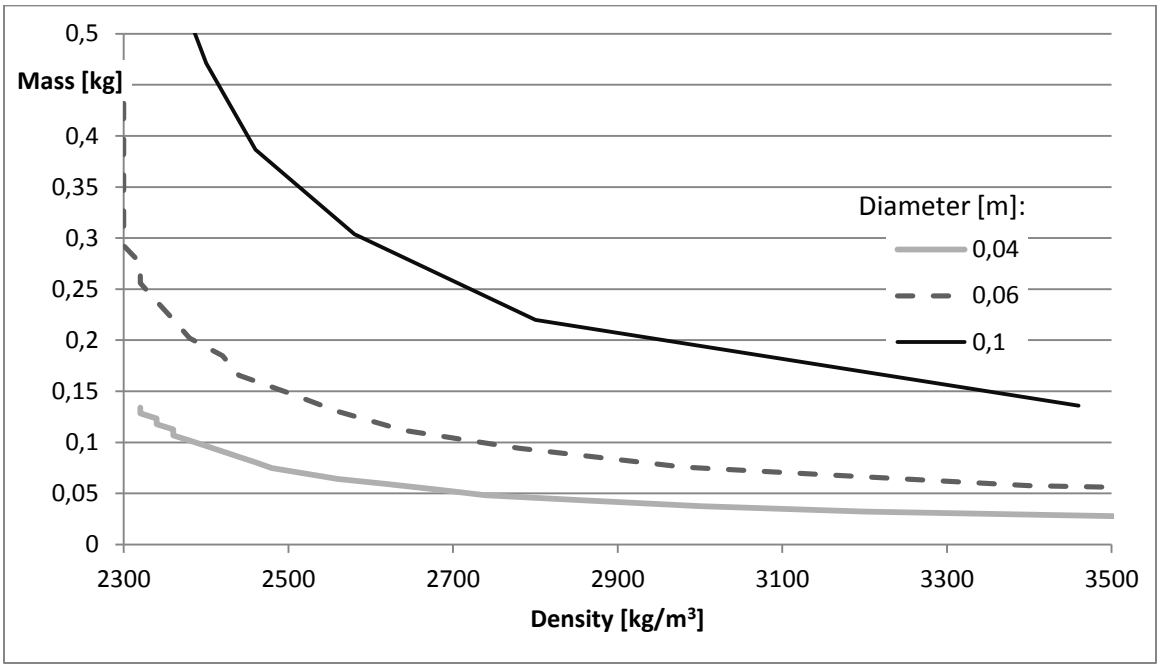

Figure 115: Mass limit of interface penetration

5.2.2.5 Effect of contact angle

Interface penetration occurs at the initial impact for the presented case (Figure 107) – as a matter of fact, for 170° contact angle, if interface penetration happens, it is expected to happen at first impact. The contact angle between alumina and the bath-metal interface is so close to perfect non-wetting, that the shift from 180° to 170° takes place after the first sinking period, by the time, the inertia of the initial drop is dampened. Even if the contact angle were set to 150°, the lowest value of contact angle between alumina and the bath-metal interface, it has barely any influence on the model results (Figure 116). When the contact angle is imposed on the side of the object, the resultant force of the surface tension is 98% and 87% of its maximal value, for 170° and 150° contact angles respectively. This would be a roughly 10% difference. However, the surface tension is not the only force one hindering the interface penetration, there is the buoyant force. In addition to that, the degree of freedom for the top edge of the disc ensures that in both cases the interface angles can reach the vertical 0°, which provide the maximum resultant force of the surface tension. In case of a smaller, but still large contact angle (150°), the object could spend relatively more time in this sweet zone, close to the vertical angle while the triple line is attached to the top edge. For 170°, the interface angle reaches and drops below 0° sooner. The overall effect, of course, is still decreasing critical density with decreasing contact angle, but at the given range, it is quite subtle.

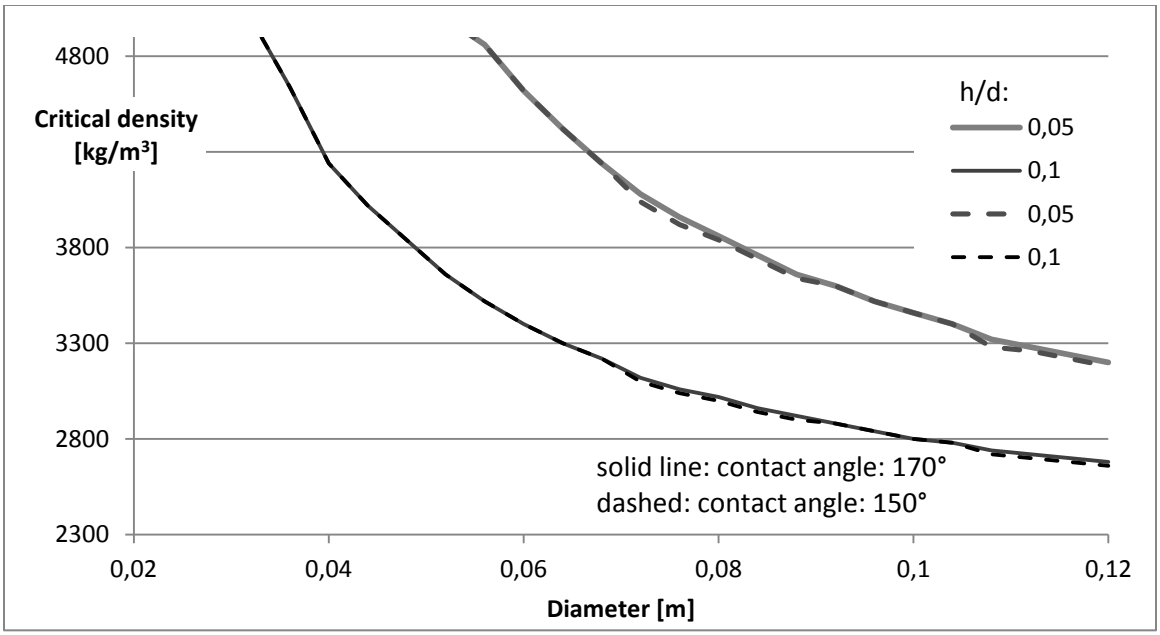

Figure 116: Effect of contact angle on the critical density for interface penetration

To be able to appreciate more the influence the contact angle has on the limit of interface penetration, a larger domain should be investigated, closer to the line separating wetting and non-wetting characteristics (Figure 117).

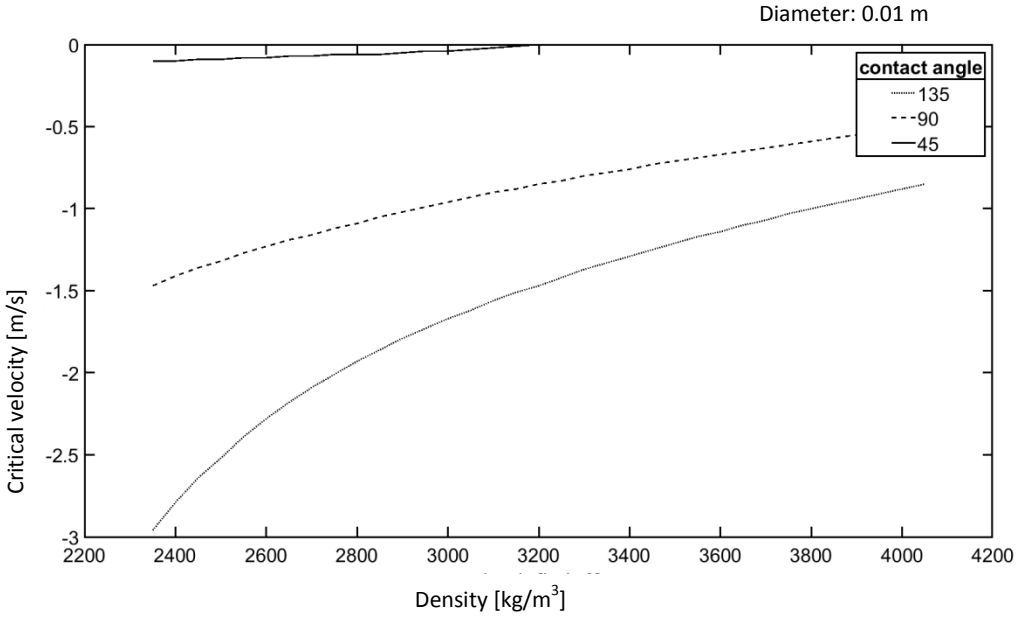

Figure 117 : Influence of contact angle on critical velocity of interface penetration (wetting-non-wetting)

5.2.2.6 *Interface angle at top edge*

In the model, and the result presented earlier, the assumption was made that the interface can bend backwards in dynamic conditions, something that was not accepted for the disc flotation model in static conditions. As this part of the model is especially debatable, the effect of setting a stricter limit on the interface angle was investigated (Figure 118).

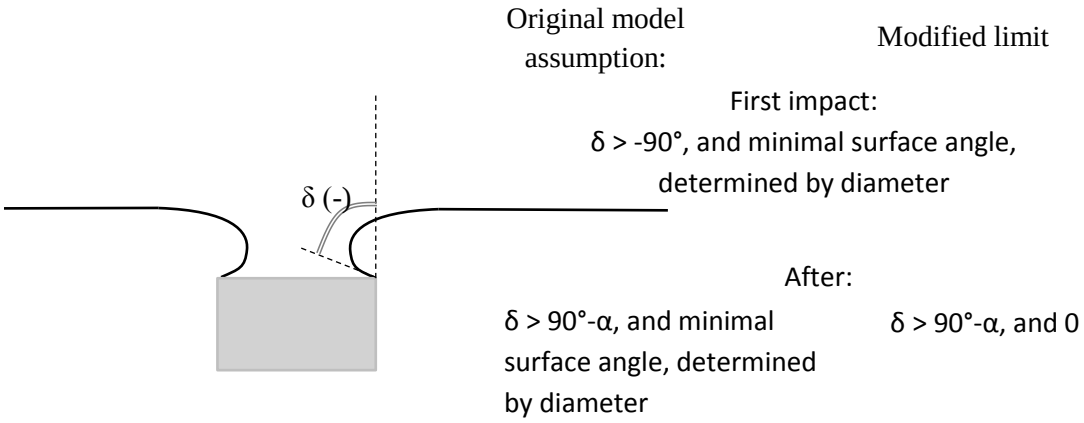

Figure 118: Limits for the interface at the triple line for various stages ©Csilla Kaszas

The modification has more significant effect than the 20° decrease in contact angle had before. For the investigated zone, the change is resulted in a 4% decrease in critical density on average, with the maximum alteration of 13% (Figure 119). As the model was not meant to predict with exactitude the conditions of interface rupture, the modified model should be considered as a more conservative estimate.

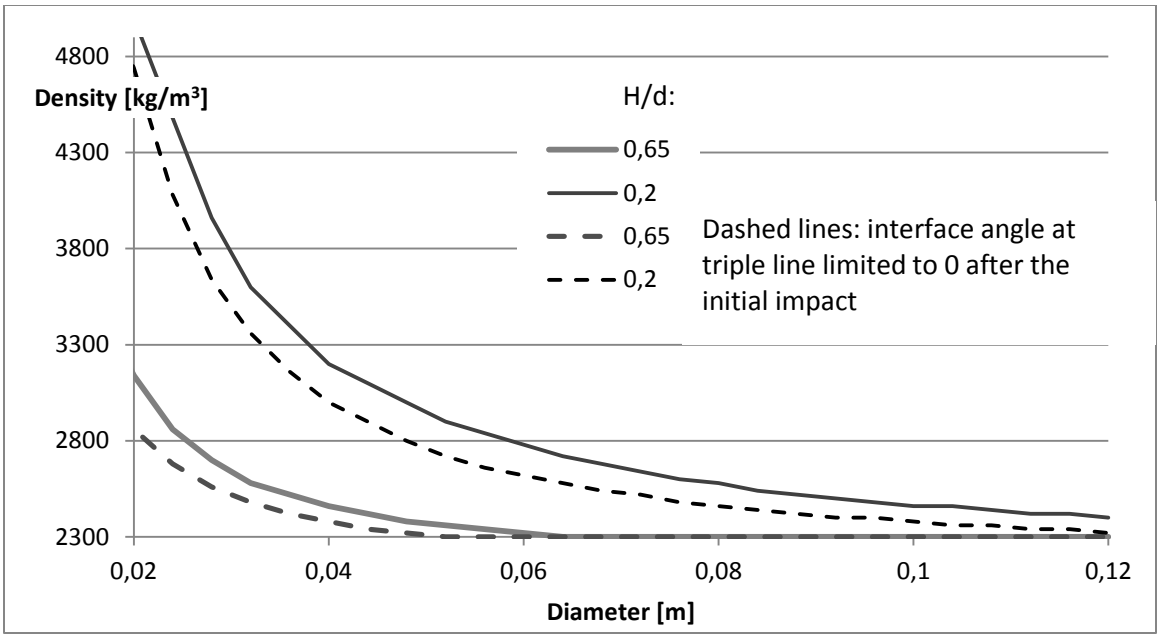

Figure 119 : Effect of limited interface angle

5.2.3 Comparison of model with experiments

Experiments for the interface penetration of alumina on the bath-aluminium interface were prepared in the laboratory. To counter the effect of the large contact angle between aluminium and the carbon crucible, which would result in the liquid metal to form a large droplet with a curved surface on the bottom of the cell, the lower half of the crucible was lined with titanium-diboride to ensure a flat interface. However, at the insertion of aluminium, the cryolitic bath was clouded with reflective aluminium particles and visual observation of the interface was unmanageable.

5.2.3.1 Experiments with micro-beads

At the UQAC`s laboratory, experiments for surface penetration has been conducted with test objects sold as micro-beads, glass beads with a plastic coating. The density of the beads was measured at 2500 kg/m^3, with pycnometric method. Water was used as the liquid for the surface penetration experiments.

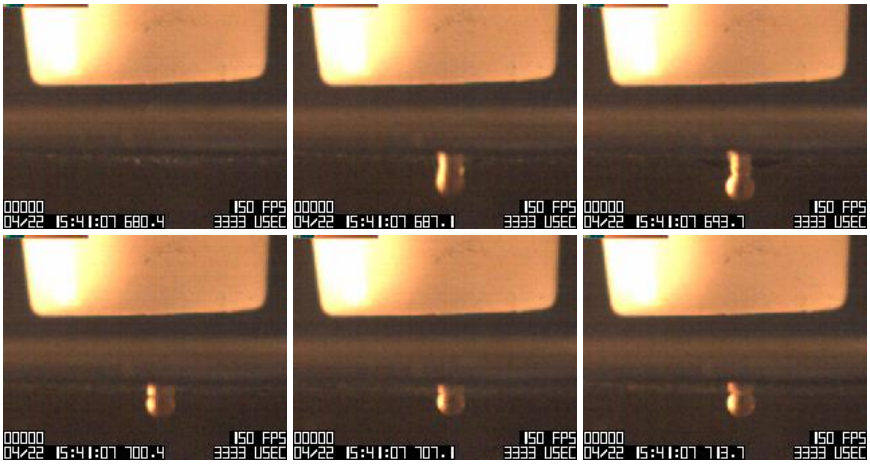

Figure 120: Micro-bead dropped on water surface, 1/150 s timestep ©Csilla Kaszas

Two different sized objects were used; the beads were dropped from four heights (Figure 120). The results are summarized below (Table 14).

Table 14: Penetration of water surface by micro-beads, test results

Sinking/number of attempts	Diameter [mm]	
Drop height [m]:	0.8	1.15
0.01	0/1	1/4
0.017	0/4	3/6
0.0235	1/4	4/4
0.028	4/4	

The model results for the various diameters and injection heights are presented below. To substitute the spherical object, the diameters were kept as measured and 2/3 height-diameter ratio was used. The static contact angle was visually estimated at 70°.

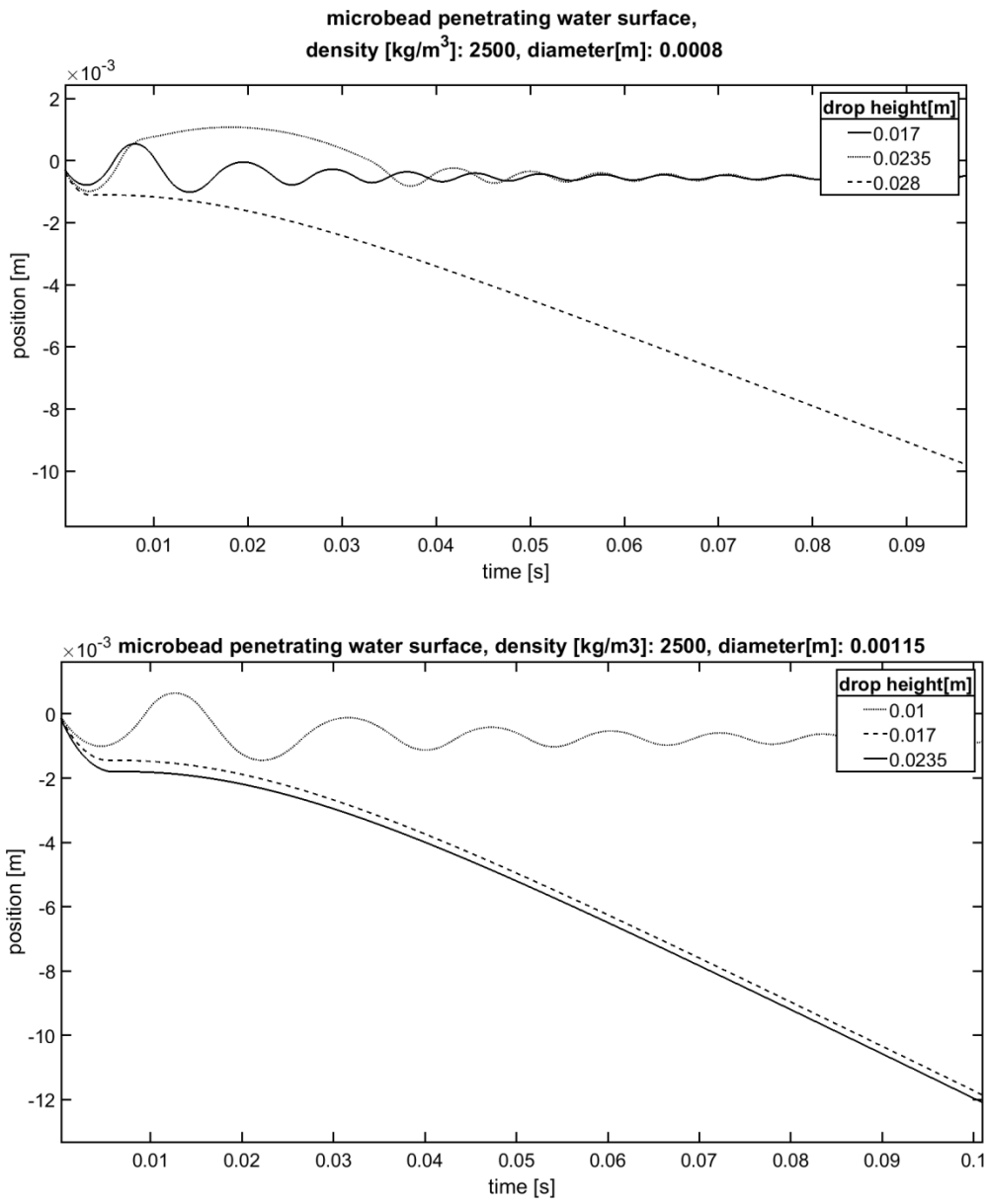

Figure 121: Micro-bead dropped on water surface, model results

The model predicts similar outcomes for the different injection heights as those observed: for the smaller bead, sinking when dropped from 2.8 cm, floating for lower injection heights (Figure 121). For the larger object, the test results had been somewhat ambiguous, with 3 out of 6 attempts resulting in sinking at 1.7 cm drop height, for which the model predicted sinking.

As the initial contact angle is 180° in the model, and it is imposed on the object for the initial sinking phase, the simulation overestimated the surface tension force. It would have been expected that the model should predict floating in cases when the object in reality sunk. The accurate prediction of the model in spite of the overestimated surface tension force suggests

that the associated mass coefficient is underestimated. It is supported by the fact that while according to the model, the test object would have bounced back from the surface in case of the 0.8 mm bead and 2.35 cm drop height, it was not observed visually.

5.2.3.2 Comparison with data from literature

Ozawa and Mori conducted experiments on the mechanism of surface penetration with spherical objects on the surface of mercury [109]. They used object with lower densities than their fluid, and two different outcome of the drop: one when the object bounces back from the surface, than rests on it, the other when the object dips below the surface, and resurfaces covered with a layer of mercury.

As previously, the spherical test object is substituted in the model with a disc with a 2/3 height-diameter ratio. The densities, surface tension and contact angle are the same values found in the article. The presented model works with the assumption that the surface angle at the triple line cannot descend below 0° (the surface cannot bend back above the object), as it was found it provided results close to the test results for the objects with larger densities (stainless steel and hastelloy B) (Figure 122).

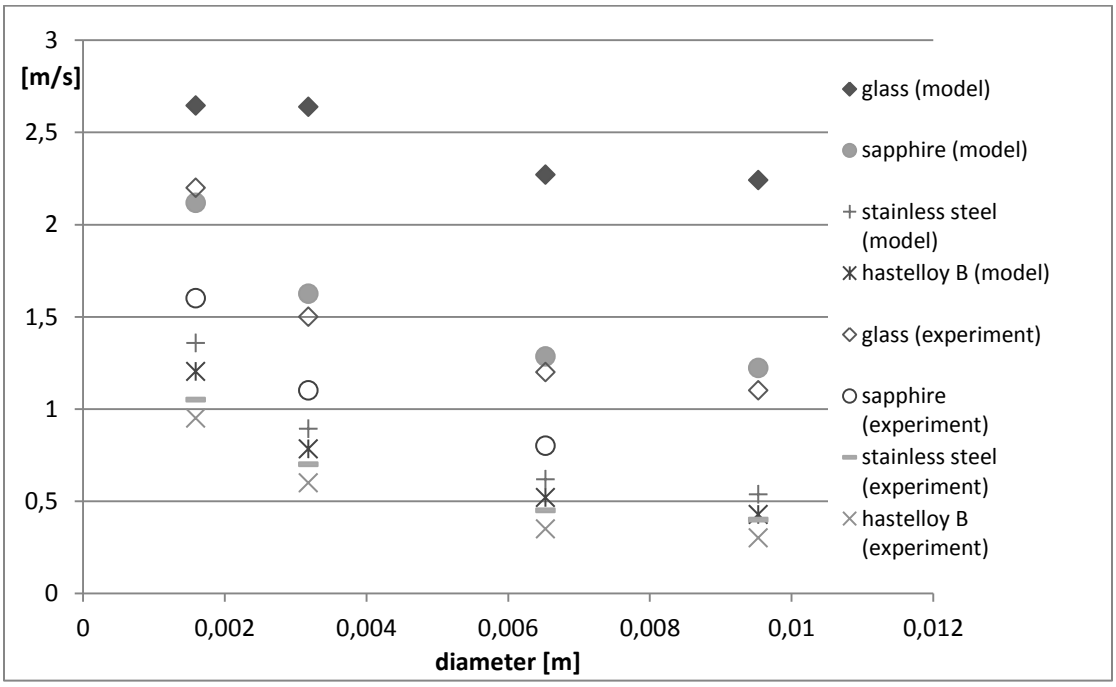

Figure 122: Critical velocity of surface penetration, comparison of model with experiments from literature [109]

5.3 Experiments with analog systems

Due to the lack of experiments on the bath-metal interface, the study of analog models is of special importance for this area.

5.3.1 Similarity conditions

To build an analog, low temperature, hydrodynamic model of an aluminium electrolysis cell, which permits to conduct a large number of experiments and observe the effect of different parameters of injection of powder at a reasonable cost, there are some obvious criteria that need to be met. Two immiscible liquids (at, or close to room temperature) are required to represent the molten bath and the liquid aluminium. They should be transparent to permit visual observation. A powder, soluble in the upper liquid, but not in the other liquid below, should stand for alumina.

Examining the terms of the non-dimensional form of the flotation equation (Equation 12, Equation 13) several more requirements are revealed.

$$\cos(\delta(x))$$

The angle of the interface at the contact line depends highly on the contact angle. The contact angle of alumina at the bath-metal interface has been measured (5.1.2); it is close to 180 °– perfect non-wetting. The contact angle measurement between alumina and cryolitic bath has been formerly presented in this work, it was found to be around 30°.

$$\frac{\rho_s}{\rho_l}$$

The ratio of the solid and the liquid represents the ratio of the gravitational force and the buoyancy. The question arises here, what kind of solid density should be applied here, as we have a powder, or porous solid. Preferably, since the pores will be filled with the liquid, changing the apparent density, both the bulk density and the skeletal density should be considered – or any of the two, and their ratio: consequently, the porosity of the powder. It should be noted that SGA has a multiscale porosity, there is not only inter-particle porosity: the space between the grains; but the particles themselves are porous as well.

$$\frac{h_m}{R} \cong \left(\frac{\gamma}{\rho_l R^2 g}\right)^{1/2}$$

While the meniscus height is not necessarily equal to the capillary length, the latter provides the order of magnitude for the possible value of the former. The squared ratio of characteristic size and capillary length is known as Eötvös or Bond number – mostly used for bubbles and drops.

$$\frac{\gamma}{\rho R^2 g}$$

Another group emerges from the second term of the original dimensionless equation, resembling to the former – but as it can be expressed as the combination of Bond number and density ratio, it is redundant.

Regarding the dynamics, the inertial viscous forces should be considered. There is a variety of dimensionless numbers from which two should be selected: Capillary number (viscous forces vs surface tension), Weber (inertial force vs surface tension force), Reynolds (inertial forces vs viscous forces).

$$Ca = \frac{\mu v}{\gamma}$$

$$Re = \frac{\rho v L}{\mu}$$

$$We = \frac{\rho v^2 L}{\gamma}$$

Water is a straightforward choice for one of the liquids. Compared to other potential materials for the analog model, like oils, it has a relatively large surface tension, like the electrolytic bath, and it is a good solvent, therefore it provides a large selection of materials to represent alumina.

Ethyl trichloro-acetate is a transparent liquid, with a density of 1.38 g/cm^3 at 25 °C. It is immiscible in water and although it is irritant (GHS classification – H301, H315, H319, H335), it is not very dangerous. Unfortunately, it is not a cheap substance, and as it is slightly soluble in water, so there is a slow but steady evaporation loss during experiments.

Several powders were tested to model the alumina. The main issue is the unusual pore structure of smelter grade alumina powder. As the gamma alumina particles are porous, the overall porosity of the powder is around 75%. For comparison, random loose packing of monodisperse solid spherical particles provides porosity around 40-44%. While some alimentary powder could have fitted the profile, the visibility was another requirement – and a priority. Therefore monosodium-glutamate was selected, and to account for the effect of the pore structure, alongside the commercially available powder with elongated particles, ground powder was also tested. Tri-sodium citrate is also a quite suitable alternative regarding its skeletal density and solubility in water (and also its price and availability), but the more spherical shape of the particles (compared to the MSG whiskers) lead to a slightly smaller porosity.

Table 15: Dimensionless numbers in the electrolysis cell and the analog model

Dimensionless number		Electrolysis cell	Water- ethyl trichloro-acetate - MSG	Trisodium citrate
Density ratio	Free surface	3.9/2.1 – 3.75/2.1 = 1.8	1.6/1 = 1.6	1.7
	Interface	(3.9-2.1)/(2.3-2.1) = 9	(1.6-1)/(1.38-1)=1.6	1.8
				Scaling for the model
Bond number $(L/a)^2$	Free surface	L/ 2.5-2.6 mm	L/ 2.7 mm	$L_m=1.04L_0$
	Interface	L/ 15 mm	L/ 2.5 mm	$L_m=0.167L_0$
Porosity of solid		75%	45-50%	
Particle size/characteristic length or: number of particles in a bath				
Contact angle	Free surface	Wetting	Wetting	
	Interface	Non wetting	Non-wetting	
Capillary number	Free surface	0.0241·v	0.0139·v	$v_m=1.7v_0$
	Interface	0.0062·v	0.0167·v	$v_m=0.37v_0$
Reynolds number	Free surface	6·10^5·v·L	1·10^6·v·L	$v_m=0.58v_0$
	Interface	8.6·10^5·v·L	3.45·10^6·v·L	$v_m=1.5v_0$

The skeletal density of solid was considered to calculate the density ratio. On the free surface, the density ratio of the model and the electrolysis cell are quite close (1.6 and 1.8), but not on the interface. However, if the bulk density of the raft or agglomerate were considered, the density ratio of the analog model would fit better the density ratio on the interface – and less on the surface.

The Bond number shows that on the free surface, the same size of powder batch can be used in the model as in the electrolysis cell, so an industrial feeder could be repurposed as it is in model where water represents the electrolyte. Meanwhile, on the interface, the characteristic size of an agglomerate should be sixth of that in an aluminium electrolysis cell.

The chosen independent dimensionless numbers accounting for the dynamics are the Reynolds number and the capillary number. As it can be seen in the table, these numbers propose different ideal scaling for the model, both on the surface and the interface. An analog model will never be perfect, one can do nothing more than to select the most prominent forces and make compromises on other fronts.

5.3.2 Small model with monosodium-glutamate, water and ethyl trichloroacetate

Due to the cost of ethyl trichloroacetate, two-phase experiments were conducted in a small crucible with an internal width of 24 mm, and height of 38 mm, with the injection of 0.6 cm^3 powder – proportional to the crucible size. Four cases are presented here, with two different particle size and powder temperature. Adding room temperature powder into water would correspond to the injection of extremely preheated alumina, where raft formation could barely occur. To account for the large temperature difference between alumina and bath, and provide similar conditions in the analog model, the powder was cooled with liquid nitrogen.

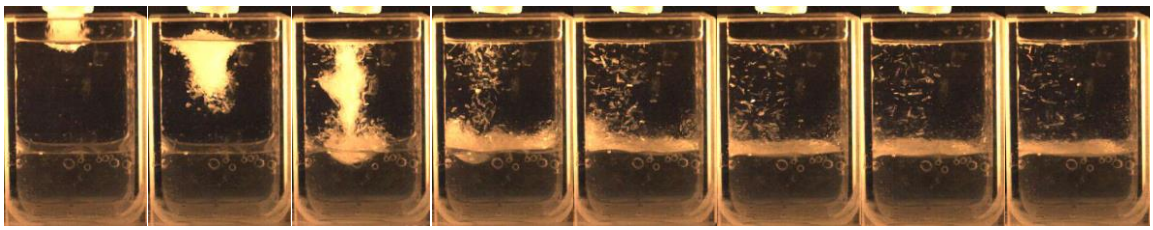

0 s 0,2 s 0,4 s 0,6 s 0,8 s 1s 1,2 s 1,4 s

Figure 123: Injection of room temperature MSG ©Csilla Kaszas

The first presented case (Figure 123) is the injection of room temperature powder, with large particle size (length: 1-3 mm, width 0.1-0.3 mm). At the injection, the powder was slightly slowed down by the surface. The particles first arriving to the surface and pushed under by the impact wetted and sunk first, followed closely by the bulk of the powder. Partial spreading on surface can be observed 0.2 s after the injection, the undeveloped raft kept some of its shape during sinking; but the infiltration and disintegration was extremely rapid. Single particles remained afloat after bulk sunk, dissolving and settling gradually to the interface.

The impact of the bulk on the interface is visible at 0.4-0.6 seconds, but at 1.4 seconds, the interface is practically flat, holding up some undissolved MSG particles. The MSG is distributed unevenly on the interface; it pulls down meniscus on the left side of the container where the bulk of the powder had drifted.

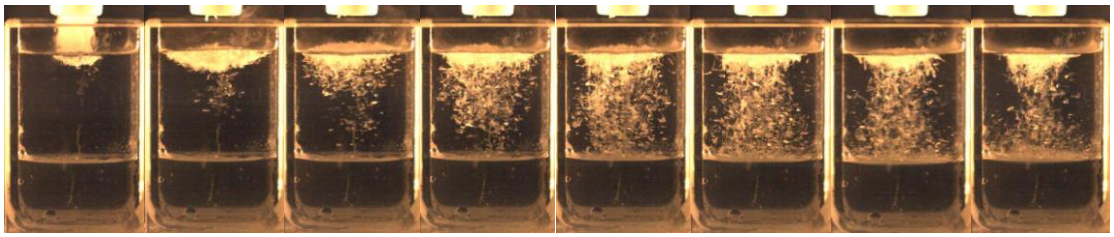

0 s 0,2 s 0,4 s 0,6 s 0,8 s 1s 1,2 s 1,4 s

Figure 124: Injection of MSG cooled with liquid nitrogen ©Csilla Kaszas

To account for the relatively low temperature of the alumina fed into the electrolysis cell, compared to the temperature of the cryolitic bath, the MSG was cooled with liquid nitrogen to a temperature of -196 °C. Complete raft formation can be observed on the corresponding photos (Figure 124). The freezing delays the infiltration; therefore the apparent density of the powder remains lower than the density of the liquid. The powder cannot sink, but it relaxes on the surface creating a saucer-shaped bottom with a heap of powder with small slope on top. Disintegration starts at the bottom – with the particles that were first in contact with the room temperature water. Gradual, elongated disintegration can be observed, without large clumps. The particles are settling on the interface, without visibly bending it.

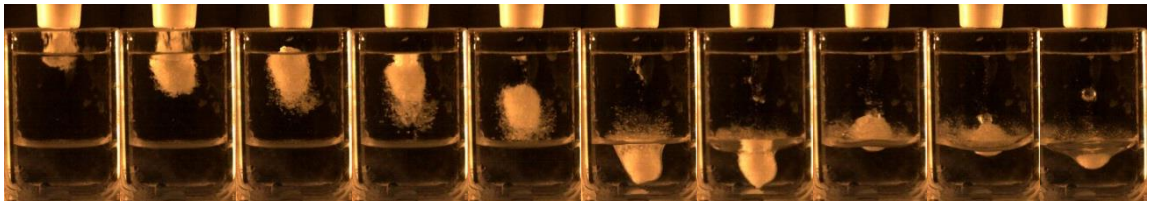

0 s 0,2 s 0,4 s 0,6 s 0,8 s 1s 1,2 s 1,4 s 1,6 s 1,8 s

Figure 125: Injection of room temperature ground MSG ©Csilla Kaszas

The commercial MSG was ground in a mortar with a pestle. As observed on an optical microscope, the average particle size of the ground powder was smaller than 0.1 mm. The smaller particles have a larger surface area relative to their mass, so the cohesive forces on the surface are more significant, resulting in a tendency of the powder to clump.

Unlike in its original form before, the ground MSG remained in a cluster during the injection. The powder pierced through liquid surface, but the bulk of the powder was slowed down by buoyancy and surface tension around 0.4-0.6 seconds. The contribution of the surface tension is noticeable by the reflection of the water surface bending downwards around the powder at 0.6 sec. A cloud of separated particles sinks toward the interface while the bulk is hold back.

The clump of powder piercing into interface reached the bottom of the crucible, held back and started to oscillate at the interface.

Due to the fact that the powder sunk rapidly, it carried some air in-between the particles. The air bubble, formed from by gas occupying pores at the moment of sinking, pushed out by the infiltrating water, detached itself from the clump at 1.6 s, as the batch of powder started sinking again. At the last photo in the sequence flotation of interface is visible due to interfacial tension, contributing in the flotation of the agglomerate.

Some powder was held up by the surface after the bulk sank (0.8-1.2s)

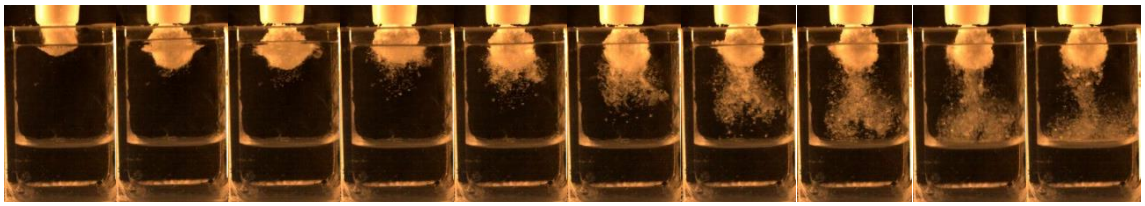

0 s 0,2 s 0,4 s 0,6 s 0,8 s 1s 1,2 s 1,4 s 1,6 s 1,8 s

Figure 126: Injection of ground MSG powder, cooled with liquid nitrogen ©Csilla Kaszas

When cooled with liquid nitrogen, the ground powder has similar clumping tendency as it had at room temperature. The infiltration was hindered by ice forming over the pores on the surface of the clump. The disintegration was delayed, not just in comparison to the room temperature powder, but also to the cooled regular MSG. Likely, it is due to the smaller particle size, which decreases thermal conductivity, and also the smaller pores resulting in slower rate of infiltration.

5.3.3 Larger quantities of MSG injections

Based on the dimensional analysis, if we wanted to create a faithful analog model for alumina feeding in an electrolysis cell, the characteristic length – the radius of the injected lump – should be close to that in the electrolysis cell. Ideally, that would mean the injection of 0.5-2 liters of powder. Although we did not get that far, a larger setup was created using one liquid, water only. To account for the anode gas agitating the electrolytic bath, air was introduced at the bottom of two polycarbonate boxes partially immersed into the water, at the two sides of the filmed area.

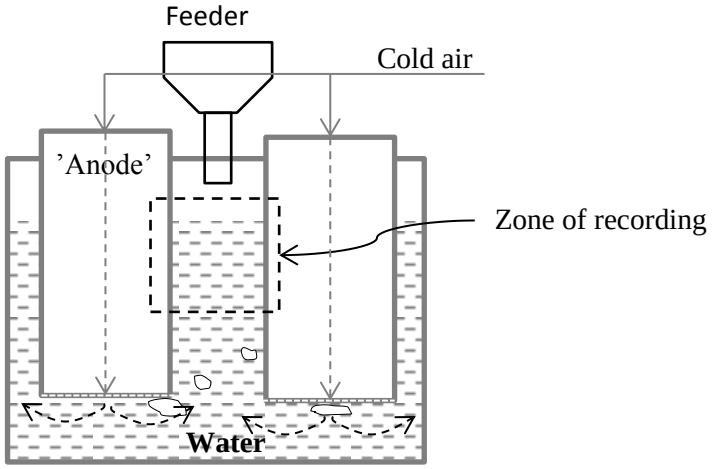

Figure 127: Sketch of analog setup with 'anodes' ©Csilla Kaszas

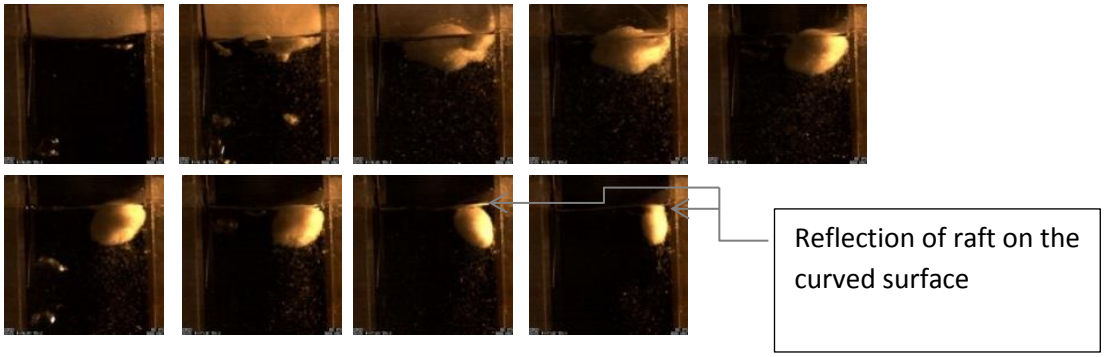

Figure 128: Injection of 30 ml cold MSG, 0.5 minute time step ©Csilla Kaszas

While some problems with handling occurred with small quantities of cold powders, they were most prominent with larger quantities, which resulted in a staggered injection of the powder, lasting for more than half minute. Small chunks had detached themselves in the initial state, because due to staggered injection the raft was not one homogenous piece, some parts floated away before another part of the batch arrives, leaving a discontinuity – or a weaker connection in-between.

The main raft stayed afloat for minutes, gradually disintegrating without clumps. The dense particles get detached when they are no longer attached to the bulk either by ice, or by a liquid bridge. Since the completely infiltrated, dense border of the raft can get detached, the apparent density of the remaining clump decreases, leaving it floating on the surface. While at the beginning it was due to the buoyant force, the influence of the surface tension can be observed 3.5-4 minutes after the injection, as the curved meniscus above the raft reflects the color of the object into the camera.

5.3.4 Various phenomena observed in analog experiments in relevance to the electrolysis cell

5.3.4.1 Resurfacing clumps

While one might think, that if a clump of powder detached itself from the surface and sunk, it will not stop until the interface, the fact is, it can still rise back due to either the formerly mentioned phenomena, the detachment of the completely wetted particles decrease the apparent density of the clump itself. The convection generated by the bubbles in the liquid can also aid to either slow down, or carry back the clumps, or single particles toward the surface.

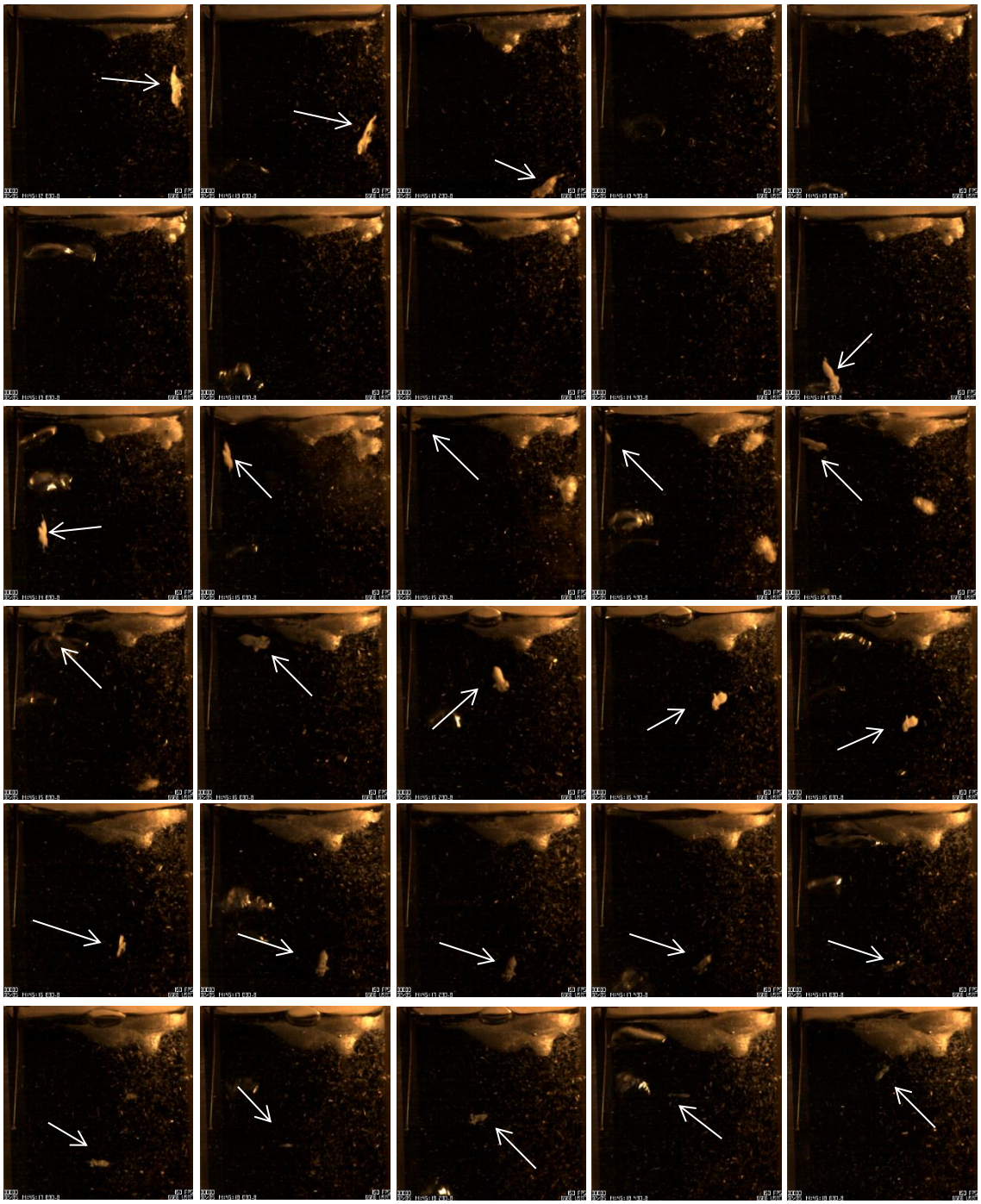

Figure 129: Resurfacing clumps, MSG 30ml (02.05), time step 0.2s ©Csilla Kaszas

When 30 ml monosodium glutamate was added, cooled by liquid nitrogen, due to the jamming during feeding, first a few, separate rafts were form. One of those started sinking before the bulk of the powder arrived; as another small incoming batch disturbed the surface. The agglomerate sank and disappeared for a second, then resurfaced on the left side of the setup

(Figure 129). It spent a couple of seconds hovering in the water column, while the big salt-raft disintegrates gradually. Judging by the appearance of the resurfacing agglomerate, it is unlikely to contain air, and the shift in the density is due to dissolution of the monosodium glutamate (decreasing apparent density) and the melting of ice (increasing apparent density). These two effects balance the apparent density close to the density of the water for this to occur. For an alumina agglomerate, both the density of alumina and density of frozen bath exceed the density of the cryolitic bath, therefore if the agglomerate does not contain un-infiltrated pores with trapped gas bubbles, the same phenomena would not happen.

Air however would get entrapped even with the injection of simple pore structure as that of MSG and sodium citrate. The following images demonstrate the resurfacing of agglomerates in analog experiments that visually release bubbles while sinking and could potentially be still holding some air or nitrogen as they resurface, aided by the convection induced by bubbles in the model.

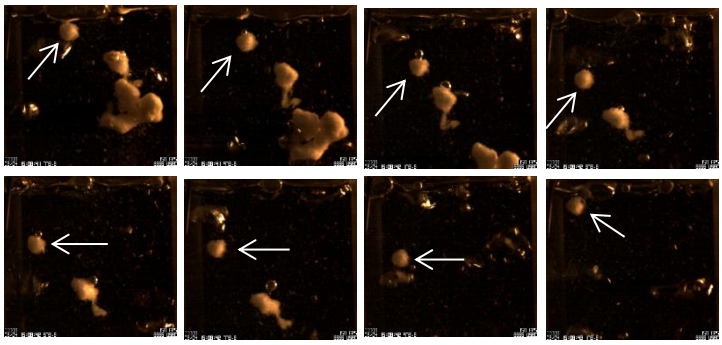

Figure 130: Resurfacing clumps, sodium-chloride (0204), time step 0.2s ©Csilla Kaszas

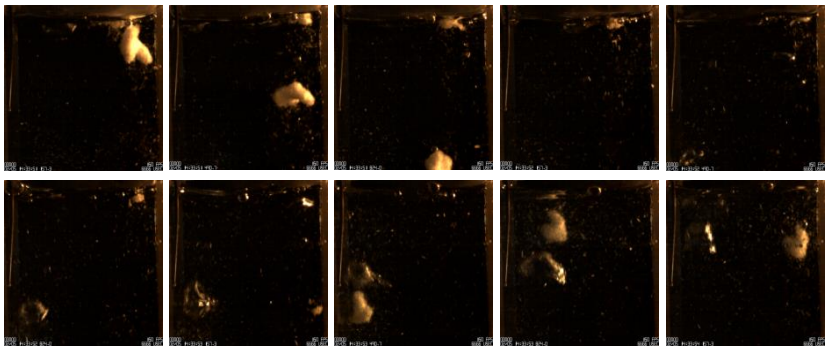

Figure 131: Resurfacing clumps, MSG 1/4 tsp (0205), time step 0.3s ©Csilla Kaszas

There are other examples of this behavior (Figure 130, Figure 131), in these instances, the clumps resurface in the wake of a rising bubble, or being pushed upwards by them.

5.3.4.2 *Piercing interface without large impact*

While a clump arriving to the interface with a high velocity can certainly pierce through it, particles can also pass it without a lot of kinetic energy. The accumulation of solids would also strain the interface until its eventual breakup, but there is a third possible cause for this, presented on the next figure.

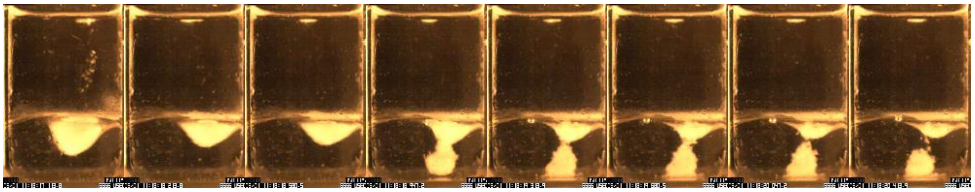

0 s 1 s 2 s 3 s 4 s 5 s 6 s 7 s

Figure 132: Accumulation of particles penetrating the liquid-liquid interface ©Csilla Kaszas

While the clump seemed to be settling on the interface for a couple of seconds, a part of the clump pierces through at 3 seconds with no apparent reason (Figure 132). It is likely caused by the reorganisation of the particles, as in granular material, the weight distribution depends on how the particles are arranged, therefore the shifting of the particles, however subtle, can lead to the clump weighing more heavily to one area of the surface. This theory is supported by the appearance of a small bubble on the interface, leaving the (now rearranged) clump as the interface is pierced through. In conclusion, that means that even though theoretically the interface would be able to hold up a certain amount of infiltrated powder, a part of the clump might pass through anyway.

5.3.5 Limitations of analog models

Analog models give the opportunity to observe powder-liquid interactions in a way that would be hard to achieve in an electrolysis cell. Although there are many similarities, the chosen materials also have several limitations.

The density of ice is lower than density of water; therefore the solidification contributes to the flotation in the model, unlike the frozen bath around the alumina in the electrolytic bath. One component systems, like water, have a single melting point, while the electrolyte usually contains several additives leaving the liquidus and solidus temperature around 200 K apart. When the temperature is between liquidus and solidus, the bath is in the mushy zone, which does not appear in the analog model.

Cooling the powder with liquid nitrogen is feasible, but the condensation of the moisture content of the air can bind the particles, leading to clumping and jamming, making it hard to handle. Another potential consequence of using liquid nitrogen is that there could remain residual liquid between the particles. The evaporation of the liquid nitrogen when the powder is injected in the bath can mimic the evaporation of the moisture content in the alumina;

however, the quantity should be controlled. Another additive to this effect might be sodium bicarbonate, although the production of carbon-dioxide would not be as rapid.

A peculiarity of SGA is its high (75%) porosity, which is crucial if the analog model should work on both of the interfaces (bath surface and bath-metal interface). Water-soluble powders with this high porosity are not readily available, although they can be manufactured.

Sintering, as the result of the recrystallization of gamma-alumina, when it is exposed to high temperatures and fluorides, is also quite unique for alumina. While some other phenomena in other powders can result in similar clumping behaviour, the similarities do not extend to the disintegration of the raft or agglomerate, which is most importantly under our scrutiny.

Conclusions

The behavior of smelter grade alumina injected into the cryolitic bath had been studied extensively, with special regard to the flotation behavior of the formed raft.

A mathematical model was developed to investigate the conditions of static flotation of axisymmetric objects on a liquid surface (2). Two geometries, disc and sphere, were considered. The model was based on the force balance that contains the gravitational force, resultant force of surface tension, and the buoyant force, accounting for the meniscus height for the sake of calculating the latter. The model was specifically applied to the parameters encountered in an aluminium electrolysis cell, to analyze the flotation limit of alumina rafts, forming on the bath surface upon the injection of alumina powder (2.2.2), and also the flotation of agglomerates on the bath-metal interface (5.1.2). The flotation limit was defined as the maximum density for a floating object of a given size; alternatively, the flotation limit could be formulated as the maximum size of a floating solid for a given density. It was shown how the expected shape, size and density of alumina rafts and agglomerates could influence their flotation. Realistic sizes of alumina batches were considered and the effect of spreading on the flotation was presented. The maximal diameter for the flotation of spherical objects of solid corundum on the bath surface was calculated to be 1.8 mm, on the bath-metal interface 15 mm; for a spherical raft with a density of 2.3 g/cm^3, 5.3 mm flotation limit was determined on the bath surface. Small height-diameter ratio for disc-shaped objects promotes the flotation, for h/d ratio less than 0.1, the maximal density for potential flotation on the bath surface surpasses 2.3 g/cm^3, with diameters above 50 mm.

The alumina-bath contact angle was an essential parameter to determine the conditions of flotation on the bath surface. As it has not been found in the literature, it has been measured in the frame of this work (3.3.1.2), and was found to be between 29 and 34°.

The mathematical model of static flotation has been extended into a dynamic model for the bath-metal interface (5.2); the drag force and associated mass were included and Newton`s second law applied. The critical conditions for interface penetration have been estimated for agglomerates with different densities and thickness-diameter ratio. The model has been compared to test results from both literature and our work. It was found for example that an agglomerate of 2 cm diameter could be captured on the bath-metal interface, with up to 2.8 g/cm^3 density, even if it were just as thick as wide.

Analog experiments were also conducted in a model using water as bath, ethyl-tricloroacetate as liquid aluminium and monosodium-glutamate as alumina (5.3). The salt cooled with liquid nitrogen formed a raft similar to that of alumina dried at high temperature and devoid of moisture. The salt raft disintegrated similarly to alumina rafts dosed with carbon dust. When the powder was cooled, the raft dispersed slowly, and the salt that was not dissolved, settled on the interface evenly. One would probably expect the liquid-liquid interface to rupture under a big impact, or a large accumulation of particles. However, one example shows that it does not have

to be either of this: a small accumulation of powder can pierce the interface locally, leading the way for other particles to follow.

Several small-scale experiments with primary smelter grade alumina and cryolitic bath were conducted. Moisture content was identified as the most important parameter that influences the shape and structure of the forming raft (3.2.3). Rapidly evaporating moisture spreads the powder on the surface, creating a thinner raft, longer triple line, therefore promoting flotation. The breaking of solidified bath is often attributed to the evaporation. While in certain cases, it is a possibility, we would propose, that during raft formation, the evaporating moisture prevents the formation of solid (pore-less) frozen bath, promoting infiltration. It was also found that the evaporating moisture is a major contributor to the initial dispersion of the powder upon injection. It is based on the observation that in analog experiments with cold powders there was no initial dispersion upon feeding, and there was also no significant initial mass loss when the alumina was previously dried at 550 °C – unlike with the alumina that was dried at only 150 °C. The evaporation does not only change the shape and macroscopic structure of the powder, but also its microstructure (4.2). The porosity analysis of leached raft samples, that preserved the underlying alumina structure showed differences in the evolution of pore size distribution depending on the initial moisture content of the alumina. For pore width below 25 nm, the pore size distributions showed the same tendencies, with less incremental pore are for the raft created with completely dry alumina. Fore larger pore sizes, the pore size distribution of the sample made with non-dried alumina deviated from the other two.

The thermal properties of SGA were measured to establish a thermal model for rafts (4.1.2). The effective thermal conductivity was increasing linearly between 350-850 °C, from 0.15 to 0.3 W/mK. A two-level thermal conductivity model was also developed and applied to represent the inter- and intra-particular porosity of alumina. A two-dimensional, cylindrical model was developed to predict the evolution of temperature in space and time, the infiltration and the consequent increase of apparent density of alumina rafts. The results have been compared with experiments, conducted with compressed alumina discs as artificial rafts. The theoretical limit of flotation has not been reached with the compressed discs, but the contribution of the surface tension to the flotation was shown.

The experiments brought attention to the influence of solid particles on the bath surface on flotation which justifies further investigations (3.3.3).

Researchers are mostly occupied with the overall dissolution rate of smelter grade alumina. Dissolution occurs on all contact surfaces between alumina and bath; however the bath that infiltrated the raft gets saturated quickly. The dissolution in reality is stimulated by the disintegration of the raft, the detachment of infiltrated parts around the bottom that exposes new areas to the main body of bath. Consequently, the detachment of these relatively dense parts also decreases the apparent density of the remaining raft, promoting flotation. For smelter grade alumina, principally primary SGA, what hinders disintegration is sintering: bonds between particles created by gamma-alpha phase transformation. What, in time, can weaken these

bonds well enough for the gravity or liquid flow to drag certain clumps from the bottom of the raft, is local dissolution. Therefore, it is proposed that the goal of research should be to determine the rate of raft disintegration, and local dissolution should be considered and studied a process parallel but opposing to sintering, as the balance of dissolution and sintering is what determines the disintegration of the raft, and leads to its overall dissolution.

A series of experiments were conducted with primary alumina doped with carbon dust (4.4.1). It has been observed that the rafts formed by this alumina stayed afloat until disintegration on the surface. While it has been previously noted by other researcher that carbon helps dissolution, they explained it by the burning of carbon and development of carbon-dioxide gas. In the presented experiments, there is no visible burning and agitation due to gas formation, the alumina preserved its grey coloration during the test. The prolonged flotation indicates that the heavily infiltrated parts can detach themselves from the bottom of the raft without pulling the entirety of the raft with them. Alumina dosed with carbon behaves similarly to regular cold powders in water, where sintering is not present. Therefore we propose that the carbon dust blocks sintering, prevents the formation of strong connections during recrystallization and this is how it promotes the disintegration of the raft.

Although there were few experiments conducted with secondary alumina (4.3.3), the results draw attention to the fact learned from the literature that both the desorption of fluorides, and the recrystallization starts at the same temperature interval, around 700 °C. The escaping fluorides agitate the powder, while the bonds are forming, and the resulting alumina structure is of unusually low density and less strongly sintered. The latter can be also attributed at least partially to the carbon dust content of secondary alumina.

Bibliography

[1] P. Homsi, Alumina Requirements for Modern Smelters, Australian Aluminium Smelter Technology Course; 575-618 University of New South Wales, Kensington, 1995.

[2] S. J. Lindsay, "SGA requirements in coming years," in *TMS Light Metals*, 2005.

[3] V. Martinent, "A new method for smelting grade alumina (SGA) characterization," in *TMS Light Metals*, 2004.

[4] A. M. Archer, "Consideration in the selection of alumina for smelter operation, pp 569-573," in *TMS Light Metals*, 2013.

[5] Y. Bertaud and A. Lectard, "Aluminium Pechiney specifications for optimising the aluminas used in sidebreak and point feeding reduction pots," in *TMS Light Metals, pp 667-686*, 1984.

[6] N. Wai-Poi and B. J. Welch, "Comparing alumina specifications and smelter expectations in cells," in *TMS Light Metals, pp345-350*, 1994.

[7] R. K. Jain, S. B. Tricklebank, B. J. Welch and W. D. J., "Interaction of aluminas with aluminium smelting electrolytes," in *TMS Light Metals, pp 609-622*, 1983.

[8] S. Rolseth, R. Hovland and O. Kobbeltvedt, "Alumina agglomeration and dissolution in cryolitic melts," in *TMS Light Metals, pp 351-357*, 1994.

[9] J. B. Metson and al, "Alumina Phase Distribution, Structural Hydroxyl and Performance of Aluminas in the Reduction Cell," in *TMS Light Metals, pp 129-131*, 2005.

[10] T. Ashida and al, "New Approaches on Phase Analysis of Amelter Grade Aluminas," in *TMS Light Metals pp 93-96*, 2004 .

[11] L. M. Perander, Z. D. Zujovic, T. F. Kemp, M. E. Smith and J. B. Metson, "The Nature and Impacts of Fines in Smelter-Grade Alumina," *JOM,* no. 61, pp. 33-39, 2009.

[12] M. A. Llavona and R. Zapico, "Effect of Residual Hydrate on Properties of Metalurgical Grade Aluminas," in *TMS Light Metals pp 93-96*, 2005.

[13] T. Jun and al, "Microstructure analysis of aluminum hydroxide and alumina," in *TMS Light Metals pp 111-114*, 2005 .

[14] J. M. Andersson, Controlling the Formation and Stability of Alumina Phases, Linköping

Studies in Science and Technology Dissertation No. 987, 2005.

[15] O. Ducreux and al, "Air and Gas Drying with Activated Alumina," Axens IFP Group Technologies, 2012. [Online]. Available: cabestisrl.com.ar/AirGas%20Drying%20Brochure.pdf. [Accessed 12 May 2017].

[16] A. Serbezov, "Adsorption Equilibrium of Water Vapor on F-200 Activated Alumina," *ournal of Chemical & Engineering Data,* vol. 48, no. 2, pp. 421-425, 2003.

[17] B. Whittington and D. Ilievski, "Determination of the gibbsite dehydration reaction pathway at conditions relevant to Bayer refineries," *Chemical Engineering Journal,* vol. 98, no. 1-2, pp. 89-97, 2004.

[18] B. Zhu and al, "Dehydration reactions and kinetic parameters of gibbsite," *Ceramics International,* vol. 36, no. 8, pp. 2493-2498, 2010.

[19] R. G. Haverkamp, J. B. H. M. M. Metson and B. J. Welch, "Adsorption of Hydrogen Fluoride on Alumina," *Surface and Interface Analysis,* vol. 19, pp. 134-144, 1992.

[20] A. R. Gillespie, M. M. Hyland and J. B. Metson, "The Surface Chemistry of Secondary Alumina from Dry Scrubbing Process," in *TMS Light Metals*, 2000.

[21] Y. Yang, B. Gao, J. Yu and Z. Wang, "Fluoride Desorption of Secondary Alumina at High Temperatures," *Electrochemistry - Tokyo -,* vol. 81, no. 7, pp. 535-537, 2013.

[22] R. G. Haverkamp and al, "The Influence of Fluorination on the Dissolution Rate of Alumina in Smelter Electrolyte," in *TMS Light Metals 265-370* , 1994.

[23] D. C. Ginnings and R. Corruccini, Enthalpy, Specific Heat, and Entropy of Aluminum Oxide from 0° to 900° C, U. S. Department of Commerce National Bureau of Standards Research Paper RP1797 Volume 38, June, 1947.

[24] G. T. Furukawar and al, "Thermal Properties of Aluminum Oxide From 0° to 1,200° K," *Journal of Research of the National Bureau of Standards,* vol. 57, no. 2, p. 2694, 1956.

[25] K. M. Krupka and al, "High-temperature heat capacities of corundum...," *American Mineralogist,* vol. 64, pp. 86-101, 1979.

[26] R. W. Powell and al, Thermal Conductivity of Selected Materials, National Standard Reference Data-Series- National Bureau of Standards - 8 , 1966.

[27] S. S. Sih and J. W. Barlow, THE PREDICTION OF THE THERMAL CONDUCTIVITY OF POWDERS, 397-401 , 1995.

[28] L. Huang and M. S El-Genk, "Thermal conductivity measurements of alumina powders and molded Min-K in vacuum," *Energy Conversion and Management,* vol. 42, no. 5, pp. 599-612, 2001.

[29] M. Llavona and al, "Density, Hardness and Thermal Conductivity of Hall-Heroult Crusts," in *TMS Light Metals 429-437* , 1990.

[30] M. Llavona and al, "Formation and Characterization of Aluminium Electrolysis Crusts," in *TMS Light Metals 439-446* , 1990.

[31] T. Ostvold and al, "Sintering and Heat Conductivity of Alumina," in *TMS Light Metals 127-131* , 1997.

[32] K. Rye and al, "Heat Transfer, Thermal Conductivity, and Emissivity of Hall-Heroult Top Crust," in *TMS Light Metals 441-449* , 1995.

[33] Walker, Alumina in aluminium smelting and its behaviour after addition to cryolite-based electrolytes, PhD thesis, University of Toronto, 1993.

[34] J. Thonstad and al, Aluminium Electrolysis - The Fundamentals of the Hall-Herould Process, Dusseldorf: Aluminium-Verlag, 2001.

[35] K. Grjotheim and H. Kvande, Introduction to Aluminium Electrolysis, Aluminium-Verlag, 1993.

[36] V. Danek and e. al, "Surface Tension of Cryolite-based Melts," *Canadian Metallurgical Quarterly,* vol. 34, no. 2, pp. 129-133, 1995.

[37] M. Kucharik and R. Vasiljev, "Surface Tension of the System NaF-AlF3-Al2O3 and Surface Adsorption of Al2O3," *Z. Naturforsch,* vol. 61a, pp. 389-398, 2006.

[38] M. Vermot Des Roches, Modeles de tension de surface pour les sels fondus et les metaux..., Universite de Montreal, 2018.

[39] T. Utigard and J. M. Toguri, "Interfacial Tension of Aluminum in Cryolite Melts," *Metallurgical Transactions B,* vol. 16B, p. 338, 1985.

[40] L. A. Issaeva and e. al, "Rates of dissolution of commercial aluminas with different physical properties," *Light Metals,* pp. 507-513, 1998.

[41] X. Wang, "Alumina dissolution in cryolitic melts: A literature review," *Light Metals ,* pp. 41-54, 2000.

[42] G. R. Haverkamp and J. B. Welch, "Modelling the dissolution of alumina powder in cryolite," *Chemical Engineering and Processing,* vol. 37, pp. 177-187, 1998.

[43] V. Dassylva-Raymond and al, "Modeling the behavior of alumina agglomerate," *TMS Light Metals,* pp. 603-607, 2014.

[44] A. I. Berezin and L. A. Iseava, "A model of dissolution and heating of alumina charged by point-feeding system in "Virtual Cell" program," in *TMS Light Metals*, 2005.

[45] S.-q. Zhan, M. Li, J.-m. Zhou, J.-h. Yang and Y.-w. Zhou, "Analysis and modeling of alumina dissolution based on heat and mass transfer," *Trans. Nonferrous Met. Soc. China 25(2015) 1648−1656.*

[46] S.-q. Zhan, M. Li, J.-m. Zhou, J.-h. Yang and Y.-w. Zhou, "CFD simulation of dissolution process of alumina in an aluminum reduction cell with two-particle phase population balance model," *Applied Thermal Engineering 73 (2014) 805-818.*

[47] E. Yalamac, A. Trapani and S. Akkurt, "Sintering and microstructural investigation of gamma-alpha alumina powders," *Engineering Science and Technology, an International Journal 17 (2014) 2-7.*

[48] R. M. German, "Sintering Trajectories: Description on How Density, Surface Area, and Grain Size change," *JOM, Vol. 68, No. 3, 2016,* pp. 878-885.

[49] D. W. Townsend and L. G. Boxall, "Crusting Behavior of Smelter Aluminas," in *TMS Light Metals pp 649-665*, 1984.

[50] J. Gerlach and G. Winkhaus, "Interactions of Alumina with Cryolite-based Melts," in *TMS Light Metals pp 301-313*, 1985.

[51] R. Oedegard, S. Roenning, S. Rolseth and J. Thonstad, "On Alumina Phase Transformation and Crust Formation," in *TMS Light Metals pp 695-709*, 1985.

[52] T. J. Johnston and N. E. Richards, "Correlation between alumina properties and crusts," in *TMS Light Metals pp623-639*, 1983.

[53] T. Eggen, S. Rolseth, K. A. Rye and J. Thonstad, "Alumina crusting in molten cryolitic melts. Part I: Penetration of molten electrolyte into alumina," in *TMS Light Metals*, 1992.

[54] O. Kobbeltvedt, Dissolution kinetics for alumina in cryolitic melts. Distribution of alumina in the electrolyte of industrial aluminium cells., Norwegian University of Science and Technology, Department of Electrochemistry, 1997.

[55] N. P. Ostbo, Evolution of Alpha Phase Alumina in Agglomerates upon Addition to Cryolitic Melts, Norwegian University of Science and Technology, Department of Materials Technology and Electrochemistry, 2002.

[56] A. J. Becker, T. R. Hornack and T. J. Steinback, "In-situ properties of crusts formed with five ores in a Soderberg smelting cell," in *TMS Light Metals pp 41-50*, 1978.

[57] X. Liu, S. F. George and V. A. Wills, "Visualization of Alumina Dissolution in Cryolitic Melts," *TMS Light Metals,* pp. 359-364, 1994.

[58] T. A. Utigard and al, "Visualization of the Hall-Heroult Process," *TMS Light Metals,* pp. 233-240, 1994.

[59] Y. Yang and al, "The Formation and Dissolution of Crust Upon Alumina Addition into Cryolite Electrolyte," *JOM, The Minerals, Metals & Materials Society,* vol. 67, no. 9, 2015.

[60] Y. Yang and al, "Study on the Dissolution of Alumina in Cryolite Electrolyte Using the See-Through Cell," *Light Metals 2015,* pp. 582-587, 2015.

[61] Y. Yang and al, "Dispersion Caused by Carbon Dioxide During Secondary Alumina Dissolution: A Lab-Scale Research," *Metallurgical and Materials Transactions B,* vol. 45B, p. 1150, 2014.

[62] Z. Y. Z. Qiu, B. Gao, Z. Wang, S. Sun and W. Li, "Dissolution of Alumina in Molten Cryolite (A Video Recording Study)," in *TMS Light Metals pp 467-471*, 1999.

[63] Y. Yang, B. Gao, Z. Wang, Z. Shi and X. Hu, "Mechanism of Dissolution Behavior of the Secondary Alumina," *Metallurgical and Materials Transactions B,* vol. 44B, pp. 1296-1304, 2013.

[64] A. R. Johnson, "Alumina crusting and dissolution in molten electrolyte," in *TMS Light Metals pp 373-378*, 1981.

[65] A. Solheim and S. Rolseth, "Some surface and interfacial phenomena encountered in aluminium electrolysis," *TMS, Light Metals,* pp. 469-474, 2001.

[66] J. Thonstad and Y.-X. Liu, "The effect of alumina layer at the electrolyte/aluminium interface," *TMS Light Metals,* pp. 303-312, 1981.

[67] A. Solheim, "Crystallisation of Cryolite and Alumina at the Bath-Metal Interface in Aluminium Reduction Cells," in *TMS Light Metals*, 2002.

[68] R. Keller, "Alumina Dissolution and Sludge Formation," in *TMS Light Metals pp513-518*,

1984.

[69] P.-Y. Geay, B. J. Wlech and P. Homsi, "Sludge in Operating Aluminium Smelting Cells," in *TMS Light Metals*, 2001.

[70] R. Keller, "Alumina Dissolution and Sludge Formation Revisited," in *TMS Light Metals pp 147-150*, 2005.

[71] J. S. Hove and H. Kvande, "Centre-break Alumina Feeding and Sludge Control of Prebaked Cells," in *TMS Light Metals*, 1983.

[72] J. Thonstad, P. Johansen and K. E. W., "Some Properties of Alumina Sludge," in *TMS Light Metals pp 227-239*, 1980.

[73] L. A. Isaeva, A. B. Braslavskii and P. V. Polyakov, "Effect of the Content of the Alpha-phase and Granulometric Composition on the Dissolution Rate of Alumina in Cryolie-Alumina Melts," *Metallurgy of Nonferrous Metals,* vol. 50, no. 6, pp. 35-40, 2009.

[74] A. N. Bagshaw and B. J. Welch, "The Influence of Alumina Properties on its Dissolution in Smelting Electrolyte," in *Essential Readings in Light Metals*, 2016, pp. 783-787.

[75] N. Wai-Poi, R. G. Haverkamp, S. Kubler, H. Muller-Steinhagen and B. J. Welch, "Thermal effects associated with alumina feeding in aluminium reduction cells," in *TMS Light Metals*, 1994.

[76] J. Tessier, G. P. Tarcy, E. Batista and X. D. P. Wang, "Improvement of alumina dissolution rate through alumina feeder pipe modification," in *TMS Light Metals*, 2013.

[77] A. Solheim, "A novel design criterion for alumina feeders in aluminium electrolysis cells," in *TMS Light Metals*, 2014.

[78] O. Kobbeltvedt, S. Rolseth and J. Thonstad, "On the mechanism of alumina dissolution with relevance to point feeding aluminium cells," in *TMS Light Metals*, 1996.

[79] C. Kaszas, L. Kiss, S. Guerard and J.-F. Bilodeau, "Behavior of powders on the surface of a liquid," *TMS Light Metals,* pp. 639-644, 2015.

[80] P. Singh and D. D. Joseph, " Fluid dynamics of floating particles," *Fluid Mechanics ,* vol. 530, pp. 31-80, 2005.

[81] P. Singh and D. D. a. A. N. Josep, "Dispersion and attraction of particles floating on fluid–liquid surfaces," *Soft Matter,* no. 6, p. 4310–4325, 2010.

[82] V. M. Starov and al, Wetting and Spreading Dynamics, Surfactant Science Series vol 138, CRC Press, 2007.

[83] S. Gurupatham and al, "Breakup of particle clumps on liquid surfaces," *Powder Technology,* vol. 217, p. 288–297, 2012.

[84] S. Gurupathama and e. al, "Particles dispersion on fluid–liquid interfaces," *Particuology ,* no. 9, p. 1–13, 2011.

[85] P. Singh and al, "Spontaneous dispersion of particles on liquid surfaces," *PNAS,* vol. 106, no. 47, p. 19761–19764, 2009.

[86] T. H. Nguyen and al, "An analysis of the thermodynamic conditions for solid powder particles spreading over liquid surface," *Powder Technology,* vol. 201, pp. 306-310, 2010.

[87] E. J. C. P. S. Jambon-Puillet, "Wrinkles, folds, and plasticity in granular rafts," *Phys. Rev. Materials 1, 042601,* 2017.

[88] G. Morris and e. al, "Particles in thin liquid films and at interfaces," *Current Opinion in Colloid & Interface Science,* 2015.

[89] V. N. Paunov and e. al, "Lateral Capillary Forces between Floating Submilimeter Particles," *Journal of Colloid Interface Science ,* no. 157, pp. 100-112 , 1993.

[90] P. A. Kralchevsky and N. D. Denkov, "Capillary forces and structuring in layers of colloid particles," *Current Opinion in Colloid & Interface Science ,* no. 6, 2001.

[91] P. A. Kralchevsky and K. Nagayamaa, "Capillary interactions between particles bound to interfaces, liquid films and biomembranes," *Advances in Colloid and Interface Science ,* no. 85 , pp. 145-192, 2000. .

[92] K. D. Danov and P. A. Kralchevsky, "Capillary forces between particles at a liquid interface: General theoretical approach and interactions between capillary multipoles," *Advances in Colloid and Interface Science ,* no. 154 , p. 91–103, 2010.

[93] E. Jambon-Puillet, C. Josserand and S. Protiere, "Drops Floating on Granular Rafts: A Tool for Liquid Transport and Delivery," *Langmuir,* vol. 34, no. 15, pp. 4437-4444, 2018.

[94] D. Vella and e. al, "Elasticity of an interfacial particle raft," *Europhys. Lett.,* no. 68 (2), p. 212–218 , 2004.

[95] L. I. Kiss and W. Chen, "Determination of the Thermophysical properties of solid and granular materials in the 200-1200 °C range," in *TEMPMEKO '99*, Delft, 1999.

[96] R. S. Rayleigh, "On the influence of obstacles arranged in rectangular order upon the properties of a medium," *The London, Edinburgh, and Dublin Philosophical Magazine and Journal of Science ,* vol. 34, no. 211, pp. 481-502, 1892.

[97] P. Garcia Coque, M. M. Llavone, L. F. Blanco and J. P. Sancho, "Porosity of industrial aluminas," in *TMS, Light Metals*, 1992.

[98] S. S. Sih and J. W. Barlow, "The Prediction of the Emissivity and Thermal Conductivity of Powder Beds," *Particulate Science and Technology,* vol. 22, no. 3, pp. 291-304.

[99] D. Demange and al, "New Methods for Measuring the Thermal Emissivity of Semi-transparent and Opaque Materials," in *Quantitative InfraRed Thermography*, ONERA, France, 2006.

[100] R. Bardestani, G. S. Patience and S. Kaliaguine, "Experimental methods in chemical engineering: specific surface area and pore size distribution measurements - BET, BJH snd DFT," *The Canadian Journal of Chemical Engineering,* vol. 97, no. 11, pp. 2781-2791, 2019.

[101] F. Chevarin and al, "Active pore sizes during the CO2 gasification of carbon anode at 960C," *Fuel,* vol. 178, pp. 93-102, 2016.

[102] F. Chevarin and al, "Substrate effect of coke particles on the structure and reactivity of coke/pitch mixtures in carbon anodes," *Fuel,* vol. 183, pp. 123-131, 2016.

[103] N. R. Dando and S. J. Lindsay, "The Competitive Adsorption of HF and SO2 on Smelter Grade Alumina," in *Light Metals (TMS)*, 2016.

[104] E. W. Washburn, "The Dynamics of Capillary Flow," *Physical Review,* vol. 17, no. 3, p. 273, 1921.

[105] E. W. Dewing and P. Desclaux, "The Interfacial Tension Between Aluminum and Cryolite Melts Saturated with Alumina," *Metallurgical Transactions B,* vol. 8, no. 3, pp. 555-561, 1977.

[106] L. Wang and al, "A review of entrainment: Mechanisms, contributing factors and modelling in flotation," *Minerals Engineering,* vol. 70 , p. 77–91, 2015.

[107] D. Chipfunhu and al, "The dependency of the critical contact angle for flotation on particle size – Modelling the limits of fine particle flotation," *Minerals Engineering,* vol. 24, p. 50–57, 2011.

[108] P. B. Kowalczuk and al, "Maximum size of floating particles in different flotation cells," *Minerals Engineering,* vol. 24, p. 766–771, 2011.

[109] Y. Ozawa and K. Mori, "Critical Condition for Penetration of Solid Particle into Liquid Metal," *Transactions ISU,* vol. 23, pp. 769-774, 1983.

[110] D. Liu, Q. He and G. Evans, "Capture of impacting particles on a confined gas–liquid interface," *Minerals Engineering,* vol. 55, p. 138–146, 2014.

[111] D. Liu and al, "Penetration behaviour of individual hydrophilic particle at a gas–liquid interface," *Advanced Powder Technology,* vol. 21 , p. 401–411, 2010.

[112] E. B. Web and B. Shi, "Early stage spreading: Mechanisms of rapid contact line advance," *Current Opinion in Colloid & Interface Science,* vol. 19, pp. 255-265, 2014.

[113] T. Oda, N. Satofuka and H. Nishida, " Numerical analysis of particle behavior penetrating into liquid by level set method," in *Proceedings of the Second International Conference on Computational Fluid Dynamics, ICCFD, Sydney, Australia*, 2002.

[114] W. Koo and J.-D. Kim, "Simplified formulas of heave added mass coefficients at high frequency for various two-dimensional bodies in a finite water depth," *International Journal of Naval Architecture and Ocean Engineering,* vol. 7, no. 1, pp. 115-127, January 2015.